Vision-Based Control of Unmanned Aerial Vehicles for Automated Structural Monitoring and Geo-Structural Analysis of Civil Infrastructure Systems

by

Hao Zhou

A dissertation submitted in partial fulfillment
of the requirements for the degree of
Doctor of Philosophy
(Civil Engineering)
in the University of Michigan
2021

Doctoral Committee:

Professor Jerome Lynch, Co-Chair
Associate Professor Dimitrios Zekkos, Co-Chair
Associate Professor Dimitra Panagou
Associate Professor Jeffrey Scruggs

Hao Zhou

zhh@umich.edu

ORCID iD: 0000-0003-1623-8833

Dedication

To Mom and Dad,

for encouraging me to go on every adventure.

Acknowledgements

I extend my deepest gratitude to my advisor, Professor Jerome Lynch, for helping and supporting me both academically and personally over the course of my doctoral study. Professor Lynch provided constant motivation, valuable insight, gentle direction, and the resources I needed to succeed. I would also like to express my profound gratitude to my co-advisor, Professor Dimitrios Zekkos, who has guided my growth as a student and provided compassion and encouragement throughout my doctoral research. I sincerely thank the rest of my PhD advising committee, Professor Jeffrey Scruggs and Professor Dimitra Panagou, for sharing their unique perspectives on this dissertation and their guidance in my course work. I am also grateful for the generous support and advice provided by other faculty members in both CEE and Robotics, particularly Professor Dmitry Berenson, Doctor Peter Gaskell, and Doctor Lissa MacVean. Additionally, I would like to thank my faculty advisor during my undergraduate study at Peking University, Professor Pu Chen, for his mentoring and inspiration.

This dissertation work is dedicated to my parents, who have always loved me unconditionally and whose good examples of work ethic have taught me to put every effort into the things I aspire to achieve. My heartfelt appreciation also goes to my girlfriend Jiayang, who has been the best cheerleader in my trying moments. Her support and encouragement have helped me overcome many obstacles during the challenges of graduate school and life.

I am blessed to have many incredible friends at Ann Arbor; special thanks are owed to them. I thank all members of the Laboratory of Intelligent Systems Technology (LIST) for their friendship and company that have made the past few years in the basement more fun and enjoyable, particularly Rui Hou, Omid Bahrami, Katherine Flanigan, Wentao Wang, Peng Sun, William Greenwood, Cassandra Champagne, Gabriel Draughon, Kidus Admassu, Yilan Zhang, Mitsuhito Hirose, Andrew Burton, Nephi Johnson, and Sean O'Connor. Many thanks are owed to my fellow graduate students from the Michigan Robotics Institute for the intellectual and social interactions that have made the doctoral journey so much more memorable. In particular, I would like to thank Kevin French, Zhen Zeng, Yukai Gong, Matthew Romano, Jeremy Castagno, Yu Yao, Brian Bittner, Lixing Huang, and Lichao Xu. Some of my sweetest memories of Ann Arbor will be of my time spent with various friends on the basketball courts at NCRB, CCRB, and IMSB. I am particularly thankful to Feng Lu, Zongyang Hu, Chenghang Liu, Gongfan Chen, Yanbo Li, Gaorui Guo, Xing Chen, Yuan Liang, Jingyi Shi, Chunan Ye, Yifeng Tang, Linfeng Li, Haoyue Tang, Xiaosong Du, Chuxi Wei, Yuren Zhong, and Xintao Yan, for the endless laughter, shouting, and goofiness. Additionally, I am grateful to Zhicheng Ouyang, Baixu Chen, Yejun Lao, Da Li, Bohan Huang, Jiecao Yu, Jingyuan Zhang, Xiaotong Sun, Haochuan Lu, Dehui Zhang, and Zhixiong Yin, for staying by my side and sharing my highs and lows.

Finally, I would like to acknowledge the gracious support from the technicians in CEE, particularly Bob Spence, Steve Donajkowski, and Ethan Kennedy. I deeply appreciate their assistance in material fabrication and equipment testing.

This research was sponsored and supported by the National Science Foundation (NSF) under grant numbers 1362513, 1442773, 1446521, and 1831347. Additional support was provided by the Office of Naval Research (ONR) under Grant Number N00014-21-1-2033. Any opinions, findings, and conclusions or recommendations expressed in this dissertation are those of the author and do not necessarily reflect the views of the NSF or the ONR.

Table of Contents

List of Tables

List of Figures

List of Acronyms

1D, 2D, 3D	one-dimensional, two-dimensional, three-dimensional
3DR	3D Robotics
ADC	analog-to-digital converter
AFPN	Air Force Print News
AI	artificial intelligence
ASCE	American Society of Civil Engineers
BDA	battle damage assessment
CAGR	compound annual growth rate
CAN	controller area network
CES	Consumer Electronics Show
CG	center of gravity
CLA	control law accelerator
COTS	commercial off-the-shelf
CPS	cross-power spectrum
CPU	central processing unit
CRA	Computing Research Association
CRMP	Common Receiver MidPoint
DART	downfall air receiver technology
DJI	Da-Jiang Innovations
DRDY	data ready
DTM	digital terrain model
EKF	extended Kalman filter
eMMC	embedded MultiMediaCard
EO	electro-optical
EPM	electropermanent magnet
ER	electrical resistivity
ESC	electronic speed control

ETHW	Engineering and Technology History Wiki
EVM	evaluation model
FAA	Federal Aviation Administration
FDD	frequency domain decomposition
FFT	fast Fourier transform
FIR	finite impulse response
FLIR	forward looking infrared
FoV	field of view
FPU	floating-point unit
FPV	first-person view
FSM	finite-state machine
GCS	ground control station
GDP	gross domestic product
GNSS	global navigation satellite systems
GP	Gaussian process
GPIO	general-purpose input/output
GPR	ground-penetrating radar
GPS	global positioning system
GPU	graphics processing unit
GUI	graphical user interface
HD	high definition
HPF	high-pass filter
HSV	hue, saturation, value
I^2C	inter-integrated circuit
IE	impact echo
IIR	infinite impulse response
IMU	inertial measurement unit
INS	inertial navigation systems
IoT	Internet of things
IR	infrared
ISR[1]	intelligence, surveillance, and reconnaissance
ISR[2]	interrupt service routine

KF	Kalman filter
LiDAR	light detection and ranging
LiPo	lithium-ion polymer
LIST	Laboratory of Intelligent Systems Technology
MARS	midair retrieval system
MASW	multichannel analysis of surface waves
MAVLink	micro air vehicle link
MBZIRC	Mohamed Bin Zayed International Robotics Challenge
MCU	modified microcontroller unit
MEMS	micro-electro-mechanical systems
MIT	Massachusetts Institute of Technology
ML	machine learning
MOx	metal oxide
MSN	mobile sensor network
MVDL	minimum-variance distortionless look
NAS	national airspace system
NDT	non-destructive testing
NED	North-East-Down
NIS	normalized innovations squared
NMEA	National Marine Electronics Association
NRC	National Research Council
NSF	National Science Foundation
ONR	Office of Naval Research
OpenCV	Open Source Computer Vision Library
OS	operating system
PC	personal computer
PEC	pulsed eddy current
PGA	programmable-gain amplifier
PID	proportional-integral-derivative
PIG	pipeline inspection gauge
PNC	particle number concentration
PnP	Perspective-n-Point

PPS	pulse-per-second
PSD	power spectral density
PWM	pulse-width modulation
RABIT	Robotics Assisted Bridge Inspection Tool
RADAR	radio detection and ranging
RAS	robotics and autonomous systems
RAVEN	Real-time indoor Autonomous Vehicle test ENvironment
RC	radio-controlled
remote ID	remote identification
RGB	red, green, blue
RMSE	root mean square error
ROI	region of interest
ROV	remotely operated vehicles
RTCM	Radio Technical Commission for Maritime Services
RTK	real-time kinematic
RTOS	real-time operating system
S2	Skydio 2
SAR	search and rescue
SASW	spectral analysis of surface waves
SBC	single board computer
SfM	structure from motion
SHM	structural health monitoring
SITL	software in the loop
SLAM	simultaneous localization and mapping
SNR	signal-to-noise ratio
SPAC	spatial autocorrelation
SPI	serial peripheral interface
SPS	samples per second
SWM	surface wave method
TI	Texas Instruments
ToF	time of flight
TTFF	time to first fix

UART	universal asynchronous receiver/transmitter
UAV	unmanned aerial vehicle
UAVaaS	UAV as a service
UMV	unmanned marine vehicle
UPenn	University of Pennsylvania
USB	universal serial bus
USW	ultrasonic surface waves
UTM	unmanned aircraft system traffic management
VIO	visual-inertial odometry
WSN	wireless sensor network
WWI	World War I
WWII	World War II

Abstract

The emergence of wireless sensors capable of sensing, embedded computing, and wireless communication has provided an affordable means of monitoring large-scale civil infrastructure systems with ease. To date, the majority of the existing monitoring systems, including those based on wireless sensors, are stationary with measurement nodes installed without an intention for relocation later. Many monitoring applications involving structural and geotechnical systems require a high density of sensors to provide sufficient spatial resolution to their assessment of system performance. While wireless sensors have made high density monitoring systems possible, an alternative approach would be to empower the mobility of the sensors themselves to transform wireless sensor networks (WSNs) into mobile sensor networks (MSNs). In doing so, many benefits would be derived including reducing the total number of sensors needed while introducing the ability to learn from the data obtained to improve the location of sensors installed. One approach to achieving MSNs is to integrate the use of unmanned aerial vehicles (UAVs) into the monitoring application. UAV-based MSNs have the potential to transform current monitoring practices by improving the speed and quality of data collected while reducing overall system costs. The efforts of this study have been chiefly focused upon using autonomous UAVs to deploy, operate, and reconfigure MSNs in a fully autonomous manner for field monitoring of civil infrastructure systems.

This study aims to overcome two challenges pertaining to UAV-enabled wireless monitoring: the need for high-precision localization methods for outdoor UAV navigation and facilitating modes of direct interaction between UAVs and their built or natural environments. A vision-aided UAV positioning algorithm is first introduced to augment traditional inertial sensing techniques to enhance the ability of UAVs to accurately localize themselves in a civil infrastructure system for placement of wireless sensors using an MSN architecture. Multi-resolution fiducial markers indicating sensor placement locations are applied to the surface of a structure, serving as navigation guides and precision landing targets for a UAV carrying a wireless sensor. Visual-inertial fusion is implemented via a discrete-time Kalman filter to further increase the robustness of the relative position estimation algorithm resulting in localization accuracies of 10 cm or smaller. The precision landing of UAVs that allows the MSN topology change is validated on a simple beam with the UAV-based MSN collecting ambient response data for extraction of global mode shapes of the structure. The work also explores the integration of a gripper with a UAV that facilitates the picking up and dropping of payloads with a ferrous surface. Specifically, the work explores the use of a magnetic gripper to drop defined weights from an elevation to provide a high energy seismic source for MSNs engaged in seismic monitoring applications. The dissertation reveals a 70% success rate in picking up payloads in an autonomous manner. Leveraging tailored visual detection and precise position control techniques for UAVs, the work illustrates the ability of UAVs to—in a repeated and autonomous fashion—deploy wireless geophones and to introduce an impulsive seismic source by dropping a weight from a defined elevation for in situ shear wave velocity profiling using the spectral analysis of surface waves (SASW) method. The dispersion

curve of the shear wave profile of the geotechnical system is shown nearly equal between the autonomous UAV-based MSN architecture and that taken by a traditional wired and manually operated SASW data collection system. The developments and proof-of-concept systems advanced in this study will extend the body of knowledge of robot-deployed MSN with the hope of extending the capabilities of monitoring systems while eradicating the need for human interventions in their design and use.

Chapter 1 Introduction

1.1 Robotic Automation Technologies for Infrastructure Monitoring and Management

Civil infrastructure systems such as buildings, bridges, tunnels, dams, pipelines, and power plants represent an important asset of the society ensuring economic prosperity and social welfare. Consequently, the preservation and maintenance of existing civil infrastructure is crucial to enable, sustain, and enhance societal quality of life. The recent American Society of Civil Engineers (ASCE) Report Card for America's Infrastructure in 2021 has renewed attention to the condition of infrastructure in the United States. The report card gives the nation's infrastructure a C- grade overall but some infrastructure systems receive a lower grade including dams (D), levees (D), roads (D), and stormwater systems (D), just to name a few (ASCE 2021a). It is estimated that failure to invest in the aging infrastructure would cost the United States more than $10.3 trillion in gross domestic product (GDP) by the year 2039 and more than 3 million jobs in 2039 (ASCE 2021b). Preventing these high economic costs can be addressed through improvements in inspecting and maintaining civil infrastructure systems. Among modern infrastructure maintenance practices, structural health monitoring (SHM) has played an increasingly critical role in ensuring the safety and integrity of in-service structures.

SHM entails deploying sensors temporarily or permanently installed in various locations in a civil infrastructure system to collect data on its response and load environment. SHM also entails building analytical frameworks to extract value from the collected load and response time histories in the form of identified damage and deterioration (Farrar and Worden 2010). The information obtained from SHM can be used to verify structural properties, assess damage levels (namely, damage detection), plan timely preservation and maintenance activities, and predict future structural behavior and condition (namely, prognosis). By providing accurate and timely structural condition information to infrastructure owners and managers, SHM is rapidly becoming an essential component of structural asset management methods necessary to ensure sustainable and resilient civil infrastructure.

In traditional SHM system designs, sensor measurements are stored within a central data repository with communication between the repository and sensors established through the use of coaxial wiring. While wired communications are a secure and reliable means of transferring data, the installation of wires in large and complex structures can be expensive and labor-intensive. For example, the installation of a 12-channel wired structural monitoring system in a mid-rise building in 2002 for seismic monitoring cost up to $50,000 (roughly $4,200 per channel) (Çelebi 2002). Wired monitoring systems installed in the Tsing Ma suspension bridge in Hong Kong were estimated to cost in excess of $20,000 per sensing channel (Farrar 2001). In 2003, the costs for purchasing and deploying 40 permanent seismic stations, as part of the USArray network designed to examine Earth's subsurface structure, were estimated to be $4.6 million (NRC 2006).

Wireless telemetry offers an alternative approach to transferring data in an SHM system; this can lower system costs while making systems more scalable (Sohraby, Minoli, and Znati 2007). Exploiting the latest advances in micro-electro-mechanical systems

(MEMS), microprocessors, and radio technologies, wireless sensors are essentially mobile data collection nodes capable of collecting data from traditional sensors (e.g., accelerometers, strain gages) and communicating sensor data wirelessly (Lynch and Loh 2006). Compared to conventional tethered monitoring systems, the time and cost to install wireless sensors have been shown to be significantly reduced (S. Kim et al. 2007). When integrated with cloud computing platforms, data management for wireless sensor networks (WSNs) is more efficient and secure (Zhang et al. 2016). Another attractive functional attribute of wireless sensors are their onboard computation capabilities. These resources allow them to perform data interrogation tasks at the point of data collection. The benefit of onboard computing is the conversion of raw, high-bandwidth data into compressed information to be transmitted, thereby reducing data volumes to be transmitted (Bajwa et al. 2006). The use of wireless transmission of processed data helps to ensure the scalability of SHM systems for large and complex civil structures over long-term periods of monitoring.

Within the research community, wireless SHM systems have been installed and validated on a diverse set of civil infrastructure systems. Straser (1998) presented his early endeavors in designing and prototyping a wireless accelerometer system on the Alamosa Canyon Bridge in the state of New Mexico. The SHM system highlighted capabilities of both periodic monitoring and detection of extreme events such as earthquakes. Similarly, Lynch et al. (2006) successfully demonstrated a short-term deployment of a wireless monitoring system comprising 14 accelerometers in the Geumdang Bridge in South Korea. The wireless monitoring system was capable of accurate estimation of modal parameters of the bridge using the collected time-history acceleration responses. Buildings are important to our everyday lives but are subjected to hazards such as strong winds and severe earthquakes. To mitigate these hazards, risk monitoring of buildings using a network of wireless sensors was proposed and validated on a two-story steel structure by Kurata et al. (2005). These wireless sensors called MOTE (Wait et al. 2002) were able to detect damages in different stories during shaking table tests. To aid in monitoring and designing of wind turbines, Swartz et al. (2010) reported on their use of wireless sensors including accelerometers and strain gauges to collect high-quality response data from three operational turbines and perform complete modal analysis of them. Ship hull monitoring benefits the prediction of ship responses and the assessment of the hull's fatigue life. Johnson et al. (2018) validated their design of a wireless hull monitoring system and an associated analytical framework that was able to collect hull measurements and assess the performance of a vessel over its full life cycle.

While the advancement of sensing technology has unquestionably improved the way infrastructure systems are monitored, the vast majority of the current field deployed monitoring and SHM systems are stationary, meaning that their sensors (wired or wireless) are installed in a fixed location permanently with a geometric layout tailored to the objectives the monitoring system. Even though wireless sensors could be moved with great ease, they rarely are ever moved after installation as has been the case in the previously cited wireless monitoring studies. Therefore, a large array of sensors is needed to densely instrument a civil structure as is often required in order to achieve damage detection due to the local nature of damage and damage's impact on measurements. This is unfortunate as an early promise of wireless sensing was the freedom afforded by being untethered.

A wireless sensor network can be upgraded to a mobile sensor network (MSN) by including mobile sensing nodes that are designed to be moved over time (Akyildiz et al. 2002; Zhu 2014). The monitoring process starts by deploying the MSN nodes in a localized neighborhood of a large structure to collect sufficient measurements within this area. The MSN is then moved to the next region of interest (ROI) with a different configuration. This procedure is repeated until the entire structure has been monitored by sensors. By monitoring a portion of the structure in a ROI for a period of time, a smaller number of nodes are required to achieve high spatial density, as shown in Figure 1-1. By reducing the number of sensing nodes needed in the MSN architecture, the overall cost of the monitoring system is reduced, thereby potentially driving greater adoption of sensors for SHM. Another advantage of a mobile, deployable sensing system compared to its fixed-location counterparts is the ability to adapt its sensing topology to structural changes and loading events as they emerge. For example, if damage is discovered at one location, sensors used at other locations can be moved to densify measurements at locations where more data is needed to quantify the damage. Statically placing an array of sensors in structures without any future topological modifications can be ineffective due to the fact that the location and timing of events of interest (i.e., structural damage) are usually unknown a priori (Huston et al. 2003). This uncertainty of when and where to measure often times puzzles the designers and users of SHM systems. If wireless sensors are rapidly moved to more advantageous positions when emergent structural damage is detected, the structural parameters associated with damage can be measured and recorded in a more timely and detailed fashion.

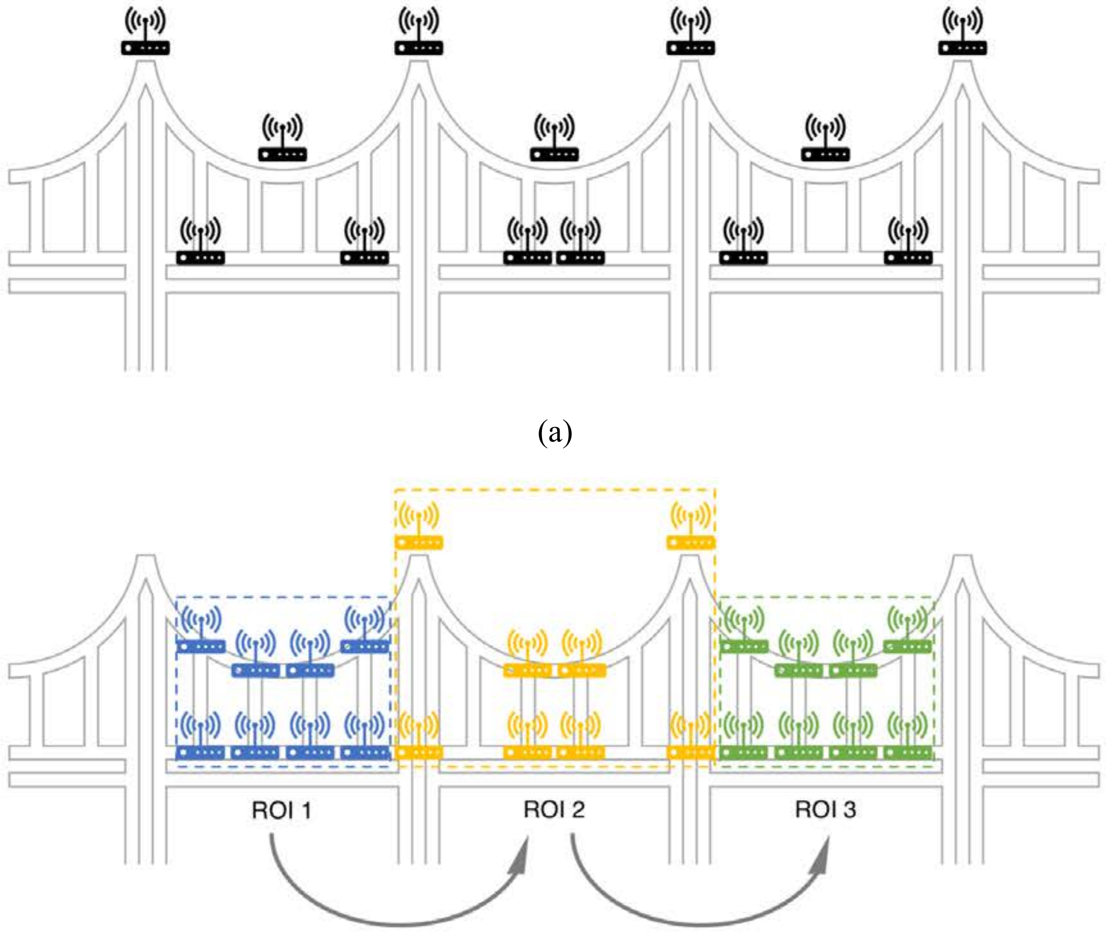

(a)

(b)

Figure 1-1. Comparison of a static wireless sensor network and a “mobile” wireless sensor network deployed on a bridge: (a) a static sensor network comprising 13 sensing nodes installed at fixed locations with relatively low spatial resolution; (b) a mobile sensor network of eight nodes but movable from location to location in three regions of interest thereby offering high spatial resolution to the data collected.

To realize the benefits of mobile sensing networks, inducing the mobility of the sensors is of utmost importance. Manual movement by human installers is a straightforward solution. While humans have unique advantages in installing and uninstalling sensors, they also suffer from several disadvantages. First, manual sensor deployment processes can pose safety risks to the installer. For example, workers installing sensors on high bridges are exposed to dangers such as climbing potentially unstable structures and being suspended from significant heights. Another challenge is the general accessibility of many operational infrastructure systems. For example, traffic control can be necessary to ensure safe access to transportation structures where sensors are installed. Also, some infrastructure systems may be located in remote regions with site access difficult. Finally, human-operated sensor deployments and reconfigurations can have high costs associated with them including the cost of labor, operational shutdown of the structure (resulting in revenue loss such as in wind turbines), and human mistakes due to bias and fatigue.

Mounting wireless sensors onto robots is another option to achieve sensor mobility that is driving recent excitement. Advances in robotics have made robots increasingly feasible for autonomous field services. Modern robotic systems are gradually achieving performance similar to humans while enabling extended uses in contexts where human accessibility is impractical. By including a mobile robot as an integral part of the sensing system, a number of the aforementioned challenges with manual installation of sensors in structures can be overcome or at least reduced. In particular, robots can be used to—possibly in an autonomous manner—first deploy and later move sensors around complex environments (Wang and Wu 2007), deliver power to sensors (Griffin and Detweiler 2012), calibrate sensor error (Gong, Yuan, and Ni 2000), detect sensor failure (Goel et al. 2000), collect sensor data (Kumar, Rus, and Singh 2004), and perform inference for decision-making (Chung and Burdick 2007). The integration of robots into SHM systems holds tremendous promise and has only recently been explored (Sony, Laventure, and Sadhu 2019). They can be the key ingredient to realizing MSN architectures that drive high levels of spatial efficiency of SHM systems.

1.1.1 Opportunities and Benefits

The increasing demands to maintain and preserve our crucial civil infrastructure systems to ensure safe and efficient operation has driven the field to explore monitoring solutions (including SHM) to collect quantitative data related to the response of infrastructure. Concurrently, the field is also exploring robotics as a way to eliminate the need for human actors in the process including robotic approaches to replacing human inspectors (Lattanzi and Miller 2017). Clearly, robots also hold great potential to play a role in the deployment and operation (including topology adaptation associated with MSN solutions) of structural monitoring solutions. Richardson et al. (2017) in the white paper on robotics for resilient infrastructure envisioned a society where “infrastructure engineering is undertaken with zero disruption to human activity and zero environmental impact”. An extension of this visionary view of the future are robots that play a major role in automating infrastructure SHM solutions. The emergence and development of robotics and autonomous systems (RAS), defined as technological systems that can sense, analyze, interact with, and manipulate their physical environments (Marvin et al. 2018), are opening new research directions across the full spectrum of infrastructure management methods including inspection, maintenance, and repair using autonomous ground, maritime, and aerial robots. Potential advantages of RAS over traditional human-based practices in wide use today include, but are not limited to:

- increased inspection productivity and higher overall safety, especially in situations where human accessibility to infrastructure is difficult or dangerous;
- greater accuracy in data collection that goes beyond the capabilities of humans;

- proactive and repetitive activities able to free humans from undertaking dirty, mundane, and dangerous inspection and repair tasks;
- improved efficiency and reduced costs derived from automation;
- greater asset manager insight and judgment derived through the integration of artificial intelligence (AI) and machine learning (ML) algorithms to automate the collection and processing of data.

The RAS field is growing at an accelerated pace that is producing new technologies and automation methods, all of which benefit the use of RAS in civil infrastructure applications. For example, the RAS global market is projected to reach \$145.5 billion by 2026, progressing at a compound annual growth rate (CAGR) of 24.6% (KBV Research 2020). In the United States, the position paper 'A Roadmap for US Robotics: From Internet to Robotics', classifies robots aiming for infrastructure inspection, maintenance, and rehabilitation under the domain of professional service robots and predicts this specific domain to grow by 30% annually (CRA 2016).

Already, RAS technology has been adapted to achieve more efficient monitoring, repair, and control of civil infrastructure systems and has changed the way humans interact with their built environments. Infrastructure inspection robots have been the most commonly studied RAS-based solution in the infrastructure field. Among all civil engineering structures, storage tanks have relatively simple shapes enabling early development efforts in the field of robotic inspection of storage tanks. Neptune, a crawler robot designed by Schempf et al. (1995) for filled tank inspection, used magnetic switching treads to attach the robot to the vertical walls of the storage tanks. Onboard cameras and ultrasonic sensors capable of operating fully immersed in fluids (e.g., water, oil) were used by the robot to determine the state of corrosion of the tank floor and sidewalls. The benefits of this RAS solution were that tanks were no longer required to be emptied, cleaned, or vented before a human inspector could gain access to its inside space and to perform visual inspection. Similarly, Kalra et al. (2006) developed a wall climbing robot utilizing the same magnetic adhesion mechanism of Schempf et al. (1995) to inspect storage tanks from the outside. The robot navigated on the tank external walls with an embedded autonomous surface coverage algorithm and carried an ultrasonic sensor to uncover possible structural defects. Another simple structure that has been studied by researchers for RAS inspections are building facades. The robot developed by Inoue et al. (2010) was attached to tiled building surfaces while hanging from two wires suspended from a hanger truck. Acoustic analysis involving the use of a hammer to strike the tile face was adopted by the robotic system to detect the existence and extent of tile exfoliation on the structure facade.

Several researchers have successfully used RAS platforms to monitor the structural behavior of more complex structures such as bridges, pipelines, and tunnels. The inspection of cables of suspension bridges is critical to the safety of the overall bridge system but often poses safety risks to bridge inspectors and maintenance crews. Recognizing the inherent difficulties of manual inspections, Cho et al. (2013) studied the use of a cable climbing robot for visual inspection of the hanger cables in suspension bridges. The robot featured three identical locomotion modules assembled circumferentially around the cable, each providing functional mechanisms such as adhesion, mobility, and landing. While climbing up and down a cable, the robot transmitted in real time its position on the cable and 360° visual images of the cable surfaces for onsite inspectors to observe. Moving beyond visual inspections that can only identify structural distress visible on bridge surfaces, researchers have also developed robot-based non-destructive testing (NDT) methods able to reveal damages beneath structural surfaces. RABIT (Robotics Assisted Bridge Inspection Tool), a concrete bridge deck monitoring system developed by Gucunski et al. (2015), utilized four NDE technologies: electrical resistivity (ER), impact echo (IE), ground-penetrating radar (GPR), and ultrasonic surface waves (USW) method. These technologies complemented each other to enhance the characterization of different types of bridge deck deterioration including corrosion, delamination, and overall concrete quality degradation. In another example, Zhu et al. (2012) prototyped a climbing robot equipped with magnetic wheels capable of adhering to and navigating on a steel bridge. The robots carried accelerometers as their payload and measured structural vibrations at high spatial resolution. The results were used to perform modal analysis and system identification of the bridge for global-based damage detection purposes.

Structural condition assessment of underground pipelines is of utmost importance because of the deterioration processes (e.g., aging, corrosion, and fissures) induced by both natural (e.g., corrosive environments) and man-made impacts (e.g., operational loading). However, pipeline inspections have long posed access difficulties for human inspectors requiring removal of pipe sections and high replacement costs. RAS solutions are a promising alternative and have been studied intensively for use in pipeline networks with widely varying pipe types and diameters. In fact, the use of “PIGs” (pipeline inspection gauges) which are non-robotic data collection platforms used to inspect industrial pipelines has always placed pipelines at the vanguard of SHM innovation (Quarini and Shire 2007). Extending on PIGs for data collection, KANTARO, an autonomous mobile robot developed by Nassiraei et al. (2007), was able to move in straight sewer pipes with a diameter range of 0.2-0.3 m and capable of maneuvering past a number of different pipe bends. The onboard sensor suite contained in their solution included a laser scanner for detecting navigational landmarks and a fisheye camera to assist with assessing pipe state and fault detection. From the collected images, nine different fault types could be detected including crack and water infiltration, among others. Other than optical sensors, specialized inspection sensors for measuring the internal geometry of a pipe have also been used such as electromagnetic sensors tailored for ferrous pipes. One example of this mechanism can be found in the works of Valls Miro et al. (2018), where the authors mounted pulsed eddy current (PEC) sensors onto a robot for estimating pipe wall thickness and identifying wall loss patches in cast iron pipes. The robot highlighted special Mecanum wheels that allow movement and control in both the longitudinal and circumferential pipe detections. A Gaussian process (GP) model was also developed to produce detailed density maps of the pipe inner surface from the robot's limited set of inspection data.

Tunnels require regular inspections but the environment inside is usually constrained to human inspectors to safely operate in. Potential hazards include exposure to dust, absence of natural light, and tunnel users (such as cars, trucks, and trains for transportation tunnels). In response to this problem, Yu et al. (2007) developed a robotic inspection system for measuring cracks in concrete tunnels. The mobile robot was controlled to keep a constant distance from the tunnel walls while acquiring image data using an onboard camera. The authors also proposed an autonomous crack detection method based on Dijkstra's shortest path algorithm (Dijkstra 1959), which yielded high recall scores but low precision scores. Another recent example of robotic tunnel inspection was the ROBO-SPECT system developed by Menendez et al. (2018). Composed of a mobile vehicle, a crane, and a robotic arm, ROBO-SPECT was able to position its onboard sensors (e.g., cameras, ultrasonic sensors, lasers) near the tunnel lining with high accuracy and detect deformations of the tunnel; the system also included a camera enabling extra teleoperation modes for inspectors.

There have also been budding efforts within the research community to extend RAS's role in SHM to not only inspect structures and collect condition and response data from them, but to carry out maintenance and repair tasks as well. Power lines are an example that can benefit from the developments of RAS solutions. Teleoperated or autonomous robots have been explored for inspection and maintenance of transmission lines, especially those in hard-to-reach locations such as along cross sections of roads, over rivers, and through mountainous terrain. Insulator contamination from dust, vegetation, and salt is one of the main causes of the power failure and requires routine cleaning predominantly done by water jets. Cho et al. (2006) introduced specialized robots to handle the task of cleaning insulators in transmission lines. The robot utilized a clamping mechanism to attach to a transmission line while using a rotating brush and a circular motion apparatus to clean the insulation of the wires. A megohmmeter sensor and an impact generating device were also used to measure insulation resistance and to detect cracks that can lead to long-term insulator failure. Another common damage on overhead transmission wires are broken strands which are often caused by mechanical loading, lightning strikes, electrical arcing, and long-term fatigue accumulation. The level of damage associated with wire strands cannot be quantified from the ground, but robots can be sent to inspect and make repairs to damaged sections. The LineScout robot developed by Canada's Hydro-Québec Research Institute is a leading unmanned RAS platform in this area (Pouliot, Richard, and Montambault 2015). The three-frame mobile platform design (i.e., a wheel frame, a gripper frame, and a center frame) allowed the robot to undertake inspection and repair tasks while rolling along a power line and crossing most obstacles (e.g., transmission towers) found on the grid infrastructure. Installed with a programmable pan-and-tilt camera and a dedicated repair tool, LineScout supported visual inspection of line components and installation of a clamp to secure the broken strands around the wire.

In summary, this section has highlighted some of the key studies performed to date in RAS platforms applied to infrastructure monitoring and repair with particular emphasis on storage tanks, buildings, bridges, pipelines, tunnels, and electrical transmission systems. Other civil infrastructure have also seen a growing body of research into using RAS for maintenance operations include in house roofs (Romano et al. 2019), levees (Akiyama et al. 2021), and even ship hulls (Prabakaran et al. 2020). The field of RAS solutions for infrastructure is still in its infancy, but looking chronologically, the increase in research efforts has given impetus to future platforms serving as commercially viable solutions that can augment and potentially replace traditional human-based urban infrastructure practices. More broadly, robots are likely to be solutions that proactively navigate around cities of the future to gather data from different assets, undertake reasoning about the condition of infrastructure, observe how people use their infrastructure, and perform maintenance and repair work on them with limited or no human assistance.

1.1.2 Technological Challenges

The ability of infrastructure robots to move freely within a structure, especially in difficult-to-reach areas, is both a primary motivation behind their use as mobile data collecting agents as well as a critical technological challenge. Understanding and implementing different robotic locomotive mechanisms to allow access to all portions of a large and complex structure is one of the key design elements of robots for structural applications. Various locomotive mechanisms have been proposed by engineers to allow robots access to different types and areas of structures. In general, they can be categorized into ground-based, crawling, climbing, marine, or aerial propulsion (Lattanzi and Miller 2017). Ground-based locomotion based on motorized wheels provides a stable instrument platform and lends itself well to uses on flat surfaces such as roadways and tunnels. Crawling and climbing robots are able to access hard-to-reach areas of structures such as vertical surfaces and high-elevation cables but require much more power for adhesion and motion than ground-based wheeled systems do. Unmanned marine vehicles (UMVs) and unmanned aerial vehicles (UAVs) provide perhaps the most locomotive flexibility but impose limited payload capacity and reduced stability when faced with environmental disturbances such as waves and wind gusts, respectively. The choice of locomotive mechanism calls for a balance between payload capacity, platform stability, the needs for overcoming environmental disturbances, and public safety requirements (especially for UAVs). There is potential for research into how this compromise can be diminished utilizing technology advances. For instance, higher-payload-capacity robotic platforms and lighter-weight sensors would expand the range and duration of robots used for sensing. Also, advanced controller and actuator designs for robots would enhance their stability and resilience when operating in harsh and complex outdoor environments.

Another ongoing challenge tied to the varied and complex infrastructure environment is the sophisticated autonomy and efficient planning algorithms needed for robots to navigate in it. The problem of a robot navigating an unknown environment is described as the simultaneous localization and mapping (SLAM) (Durrant-Whyte and Bailey 2006; Bailey and Durrant-Whyte 2006). While roaming an unknown environment, the robot seeks to build a map of the environment, and at the same time it wishes to determine its location relative to this map given noisy data collected from onboard sensors. The SLAM problem is especially challenging to solve in many civil infrastructure systems with very complex geometries (e.g., steel truss bridges with dense truss elements) and tight, confined interior spaces (e.g., enclosed buildings, trunnels, pipelines). While recent progress has been made, current methods can only handle simple tasks in structured, static, and limited-scale environments. There is a need for more theoretical research on mapping unstructured, dynamic, and large-scale environments as are often posed by infrastructure in a more real-time and robust fashion (Stachniss, Leonard, and Thrun 2016). Robust motion planning and object avoidance methods are another major research need in the community. These methods must be capable of real-time operation and provide safety and robustness guarantees in close proximity to moving objects such as humans. At present, teleoperation is still the predominant choice when operating a robot in unknown and unstructured environments such as those that occur in post-disaster scenarios (Queralta et al. 2020). A principled integration of SLAM and motion planning techniques is required to reach the level of full autonomy for robots to explore the environment safely and become helpful partners to humans.

There is substantial need for more research on how to perceive and represent damage consistently and accurately with robot-based monitoring systems. Because of the inherent localization and navigation inaccuracies of autonomous robots (Kümmerle et al. 2009; Delmerico and Scaramuzza 2018), sensor data acquired from mobile robotic platforms can be inaccurate, incomplete, or intermittent depending on navigation inaccuracies and the application. Variable environmental conditions such as weather and the time of day can substantially degrade the usefulness of commonly adopted sensors. For instance, laser range finders (such as light detection and ranging (LiDAR)) may fail in the presence of rain or fog; visual measurements using cameras are also highly susceptible to weather but also to changes in lighting and shadows. There is a distinct need to determine acceptable accuracy metrics for robotic measurements, without which it will be difficult for infrastructure owners or operators to justify and allow the use of robots for monitoring and condition assessment.

The limited battery life and onboard storage space of mobile robots also pose challenges regarding sufficient spatial coverage of the system, especially in a large-scale infrastructure system (Franco and Buttazzo 2015; Nagarajan et al. 2019). While complete coverage of the structure is not always necessary, more work is required on assimilating local information collected by robots with global knowledge of the structure to make structure-specific assessments. The massive amount of data produced in long-term applications (especially those using LiDAR and cameras) is another impediment to automated monitoring (Krishnappa and Turner 2014; Cura, Perret, and Paparoditis 2017). More research is needed to develop scalable data management systems and automated robot-level information retrieval approaches to reduce the amount of data that needs to be stored and analyzed.

While the majority of current research (e.g., Debenest et al. 2008; Leon-Rodriguez, Hussain, and Sattar 2012; La et al. 2013; Debenest, Guarnieri, and Hirose 2014; Schäfer et al. 2016) on infrastructure robots is centered on structural inspection applications, there is potential for research into robot interaction with the physical systems to broaden a robot's role from sensing and gathering data from its surrounding environment to physically interacting with it. Achieving dexterous manipulation like that of a human in a robot for use in the field environment, especially in large and heavy structures, is likely a longer-term goal that requires significant innovation. Perhaps the biggest impediment to implementation of interactive robots is the absence of a robust and skillful manipulator ensuring the accomplishment of the manipulation task. Given the promise of robotic manipulation, it is an active research area in the robotics field (Berenson et al. 2009; Alonso-Mora et al. 2015; Erhart and Hirche 2015; Sui et al. 2017; Fan et al. 2018). Some of the important issues include the modeling of the interfaces that exist between the robot and the environment along the execution of the robot's motion (Kuffner and Xiao 2016). A major difficulty is the integration of a robotic manipulator with a moving platform. Designers of such joint systems must account for the dynamics of both components (i.e., robot platform and an attached manipulator) and build sophisticated controllers to stabilize them in the face of external environmental disturbances. To date, the difficulties of simultaneous mobility and manipulation have led to limited research efforts in the automation of infrastructure repair in general, but some work has been reported on a small set of simple structures such as power lines (Pouliot, Richard, and Montambault 2015) and ship hulls (Hachicha et al. 2019). Also, the manipulators used have had very simple mechanistic designs including the use of open/close grippers (Zhou et al. 2016) and magnetic latches (Stibinger et al. 2021), etc.

The need for flexible mobile robotic systems for infrastructure systems propels UAVs to the front of all other robotic platforms that can be considered (Lattanzi and Miller

2017). A large number of civil engineering researchers and practitioners are adopting UAVs because they have matured into versatile data acquisition platforms that can be safely and easily deployed via flight. Compared to manned aircraft, UAVs are much smaller, more agile, and orders of magnitude cheaper, allowing them a greater range of movement and easier access to traditionally hard-to-reach areas such as remote sites and confined spaces. Carrying a wide variety of sensors onboard, UAVs are able to collect data that is difficult to obtain using conventional sensing strategies. Recent development of UAV autonomy further allows them to be programmed to execute missions autonomously. The benefits presented by UAVs makes them potentially invaluable tools for infrastructure monitoring applications. In the context of the aforementioned challenges with RAS solutions, UAVs offer the best opportunity for addressing those challenges. This dissertation will use UAVs as the primary RAS platform to explore the potential for RAS solutions for structural monitoring and geo-structural analysis.

1.2 UAVs: High-Precision and Purpose-Built Mobile Sensing Platforms

Widely referred to by the public as drones, UAVs are aircraft that can either fly autonomously or be remotely piloted by either a human operator or a ground control station (GCS); that is, without an on-board human pilot in control. UAVs are often small platforms and have lower costs compared to traditional aircraft. In recent years, UAV technology has gained increasing interest from both academic and industrial uses given their versatility. UAVs have become central to the functions of various businesses (e.g., real-estate, agriculture) and governmental organizations including defense organizations (Floreano and Wood 2015). Today, UAV models are available in varying grades ranging from small consumer models designed for aerial photography and first-person view (FPV) entertainment (Kim et al. 2018), mid-sized professional drones meant to patrol borders (Bein et al. 2015), report oil spills (Gómez and Green 2017), survey wildlife (Linchant et al. 2015), and regulate fisheries (Raoult and Gaston 2018), all the way to massive enterprise-level platforms created for specific purposes such as precision agriculture (Mogili and Deepak 2018) and firefighting (Innocente and Grasso 2019). In the United States, the Federal Aviation Administration (FAA) which regulates the airspace in which drones fly, forecasts that by the end of 2024, around 828,000 UAVs will be deployed for commercial use, which is more than twice as large as the number of 385,000 in 2019 (FAA 2020a). In addition, while the pace of recreational registration ownership has slowed down over the past few years, the recreational UAV fleet are expected to attain its peak at around 1.48 million units by 2024. Globally, the UAV market is estimated to grow from $22.5 billion in 2020 to $42.8 billion in 2025 at a CAGR of 13.8% (Schroth 2020).

1.2.1 The Evolution of UAV Technology

Headlines featuring UAVs and drones have become a common occurrence in recent times. For example, Amazon’s Prime Air drone made its first delivery in the United Kingdom in 2016, bringing the company “one step closer to making 30-minute package delivery by drone a reality” (Popper 2016). Other Internet corporate giants like Google (Project Loon) and Facebook (Internet.org) have also been developing balloon or UAV-based wireless networks to bring low-cost internet access to unserved or underserved regions around the globe (Richards 2014). While these headlines might make UAVs seem like a new and young technology, the reality is that UAVs are a fairly old and mature technology first explored in the military and later adopted in civilian applications.

The UAV technology we see today is an outcome of a complex evolutionary process that has its roots in the military with development starting more than a century ago. UAVs were first introduced in the early 1900s as practice targets for training military personnel mostly in the United States (Shaw 2014). During World War I (WWI), UAVs were imagined as radio-controlled aircraft capable of carrying explosives. They were intended for use as flying bombs or aerial torpedoes (a forerunner of today's cruise missiles), that could be delivered behind enemy lines. Integrating wood and fabric airframes with sensors such as gyroscope and propeller revolution counters, the most advanced UAVs at that time could carry payloads of almost 200 pounds of explosives along a distance of approximately 40 miles (Keane and Carr 2013). However, WWI UAVs faced two operational problems: (1) difficulties with launching and recovery, and (2) struggles to determine the flight characteristics of the airframe to stabilize it during flight (Pearson 1969). In the period between the two wars and into World War II (WWII), there was a continued effort to perfect radio-controlled weapon delivery using UAVs. In 1937, the U.S. Navy developed a UAV called Curtiss N2C-2 requiring two remote control pilots, one seated in a field cart and the other in a companion aircraft that flew alongside the UAV (Fahrney 1980). The pilot on the ground could control the UAV during takeoff and landing while the second pilot in the plane could take control of the UAV when it was airborne. Although these operations seem inefficient today, N2C-2 represented a noteworthy step in the development of radio-controlled UAV technology. The most remarkable UAV event during WWII was the emergence of the German V-1 Doodlebugs, the world's first successful cruise missile. The V-1 flying bomb was equipped with an autopilot whose guidance system used a pair of gyroscopes to monitor yaw and pitch, a barometric device to measure altitude, a small propeller attached on the nose of the missile serving as an air-log to measure the distance the missile had travelled, and a magnetic compass to keep the missile heading along a predetermined bearing to the target (Zaloga 2011). The sensor suite in V-1 was quite innovative and functioned as a prototype of modern-day inertial navigation systems (INS).

With the start of Cold War, UAVs were seen as a viable platform to gather intelligence, surveillance, and reconnaissance (ISR) data. The transition of UAV from being a munition conveyance system to a remote sensing platform greatly extended its field of use in military applications. In 1973, Israel developed its first military UAV, the Tadiran Mastiff, for surveillance and scouting purposes. The Mastiff had over seven hours of flight time and a data-link system capable of streaming live video of targeted areas (Tucker et al. 2008). Around the same time, reconnaissance UAVs were deployed by the U.S. Army in the battlefields of Vietnam. These UAVs were used to take photos from low and high altitudes for the purpose of strike planning and post-strike battle damage assessment (BDA). Statistics showed that a total of 3,435 operational reconnaissance UAV missions were flown across southeast Asia between 1964 and 1975. Around one-third of these missions were carried out by various models of the Ryan Model 147 Lightning Bug (Clark 1999). The Ryan 147 featured a midair retrieval system (MARS) where a helicopter could catch it while in its parachute descent and return it undamaged (Wagner and Sloan 1992). In 1986, the United States and Israel jointly developed one of the most versatile UAV platforms at the time, the RQ-2 Pioneer. The RQ-2 was equipped with three sensor packages including an optical camera, a forward looking infrared (FLIR) sensor, and an electro-optical/infrared (EO/IR) dual-sensor. The camera or EO sensor was suited for daytime operations, while the FLIR or IR sensors enabled usage at night by establishing images from heat signatures (Major 2012).

Fusing surveillance and lethality, weaponized UAVs were introduced in the 1990s and since then have been heavily invested in to provide offensive capabilities without committing humans to dangerous situations. With the help of UAV pioneers like Abraham Karem, the United States developed the famous MQ-1 Predator drone in 1994 (Whittle 2013). The Predator had a wingspan of 55 feet, a gross weight of 2,249 pounds, and could reach top speeds of 135 mph. Equipped with various cameras and radio detection and ranging (RADAR) sensors, and up to two Hellfire air-to-surface missiles, the Predator provided the warfighter persistent ISR information together with a kill capability (Whittle 2015). Thirteen years later in 2007, a larger, heavier, and more powerful successor to the MQ-1 Predator was introduced called the MQ-9 Reaper. The Reaper was able to cruise at almost three times the speed of the Predator and carry 15 times more ordnance (AFPN 2006). The Predator and Reaper created the public image of modern military drones striking targets worldwide. The rapid proliferation of UAV technology has changed the character of warfare. As of 2020, more than 10 countries have conducted UAV strikes, and about 40 countries maintain armed UAVs in their arsenals (Bergen, Salyk-Virk, and Sterman 2020). Today, UAV technology in the military sector is much more advanced than any other sector. Many of the technological innovations of military UAVs remain top secret and unknown to the public.

The military development of UAV technology over the previous century make the introduction and adoption of UAVs for civilian applications inevitable. UAVs have been common as a hobbyist pursuit for decades with the general public building and flying radio-controlled (RC) aircraft such as fixed wing planes and traditional helicopters. However, one of the first uses of UAVs for non-military, and non-hobbyist use was recorded as early as 2006, when the FAA issued a certificate of authorization allowing Predators to be used for search and rescue (SAR) for survivors of disasters (Robinson 2006). The past 15 years has seen a rapid advancement of the civilian UAV technology ecosystem and a corresponding exponential growth of civilian UAV applications. Consumers use them for aerial photography and FPV cinematography (Mollica 2020) while government agencies use them for border patrol (Haddal and Gertler 2010), traffic monitoring (Kanistras et al. 2013), and disaster management (Erdelj et al. 2017); private businesses use them for facility inspection (Jordan et al. 2018), cargo delivery (Yoo, Yu, and Jung 2018), and industrial warehousing (Fernández-Caramés et al. 2019). The evolution of civilian UAV technology has had four major phases of development (Figure 1-2):

1. development of stable and reliable flight controls;
2. integration of onboard sensors for effective data collection;
3. advancement of UAV intelligence and data management tools;
4. customization for specialized functionality and UAV-as-a-service (UAVaaS).

The following subsections highlight these four phases and their current status of development.

1.2.1.1 Stage 1: Development of Stable and Reliable Flight Controls

The first fundamental challenge began with the understanding of vehicle flight dynamics and the ability to keep the UAV bodies aloft reliably and with adequate control.

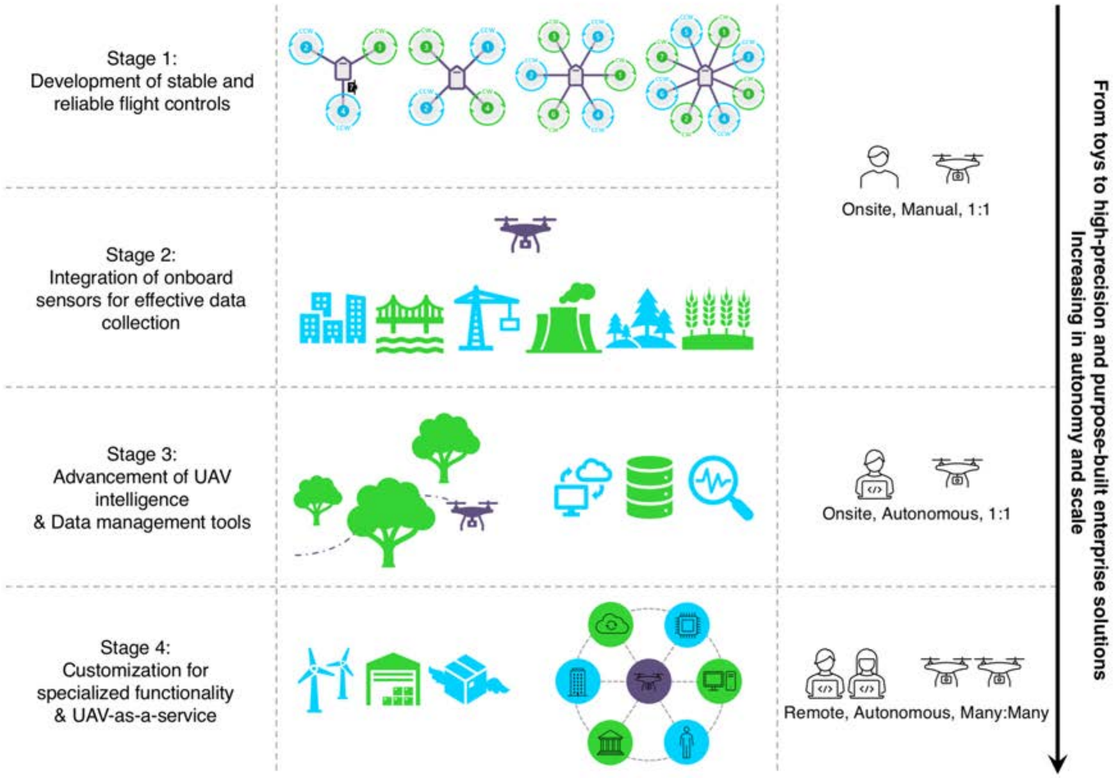

Figure 1-2. Four major stages of the evolution of civilian UAV technology.

Multiple research groups around the globe published a large amount of papers at this stage, demonstrating state-of-the-art technologies for vehicle modeling, state estimation, and control (Bouabdallah, Murrieri, and Siegwart 2004; Tayebi and McGilvray 2006; Huang et al. 2009; Mahony, Kumar, and Corke 2012; Brescianini and D’Andrea 2016). Academic researchers tested their flight control algorithms intensively in both simulation and experiment using real UAVs on the field. Real-life testing environments were established indoors utilizing high-accuracy optical motion-capture systems, such as Real-time indoor Autonomous Vehicle test ENvironment (RAVEN) at Massachusetts Institute of Technology (MIT) (How et al. 2008), the GRASP Multiple Micro-UAV Testbed at the University of Pennsylvania (UPenn) (Michael et al. 2010), and the Flying Machine Arena at ETH Zurich (Lupashin et al. 2014). Among the various airframe choices for UAVs, multirotor designs gained the most attention due to the simple rotor mechanics required for control and stability of their frames in flight. Based on the number and configurations of motors, multirotors are named tricopter, quadcopter, hexacopter, or octocopter when referring to 3-, 4-, 6-, 8-rotor rotorcraft, respectively. Quadcopters dominate the mainstream consumer market and became known to the public after various TED talks presented by UAV pioneers Dr. Vijay Kumar at UPenn (Kumar 2012; 2015) and Dr. Raffaello D'Andrea at ETH Zurich (D'Andrea 2013; 2016). These talks impressively demonstrated the ability of quadcopters to perform aggressive maneuvers and work in concert with one another to perform intricate tasks. These early demonstrations showed the maturity of control algorithms used to control UAVs with such precision and agility.

At the same time, the UAV industry outside of academia was going through a rapid evolution with many startups building prototypes that could be general purpose or were designed for specific applications (Giones and Brem 2017). An example of an entrepreneurial startup was 3D Robotics (3DR), co-founded in 2009 by Chris Anderson and Jordi Muñoz (Shontell 2014). The company targeted the manufacture of versatile UAVs with an open-source software platform that could enable a wide range of capabilities developed by developers and UAV end users. Although the company ultimately failed as a commercial UAV manufacturer, it pivoted into providing software solutions to the construction industry in 2016 (Mac 2016). Nonetheless, its open-source UAV software ArduPilot (ArduPilot.org) remained in active development and has become one of the most well-accepted UAV autopilot systems in current use globally (Benowitz 2021). Another startup entrant at this stage was the French company called Parrot. In 2010, Parrot released AR.Drone at the Consumer Electronics Show (CES) 2010 in Las Vegas. The navigation and control design of the vehicle involved collaborations with the company's academic partner MINES ParisTech (Bristeau et al. 2011). The AR.Drone could be safely piloted by an app installed on a smartphone. The commercial efforts of 3DR and Parrot attested to the ability of UAVs to be reliable solutions with accessible software architecture that allowed end users to use UAVs in a wide range of applications. This dissertation will use a 3DR UAV at the core of its research.

1.2.1.2 Stage 2: Integration of Onboard Sensors for Effective Data Collection

When looking at the hardware components layout of a typical civilian-use quadcopter in Figure 1-3, it is clear that the commercial UAV industry has taken advantage of technological advances in sensing. Specifically, the miniaturization of electronic components (e.g., MEMS-based inertial measurement units (IMUs), electronic speed controls (ESCs)), faster and more powerful processing units (e.g., 32-bit floating-point unit (FPU) computers), lighter and stronger materials (e.g., carbon fiber structures), among other advancements, made it possible to design and build small UAVs with a wide range of functionality at a modest cost. However, it was not until the Chinese company Da-Jiang Innovations (DJI) releasing its Phantom product line in early 2013 that UAV technology truly went mainstream in the commercial market. The Phantom incorporated a global positioning system (GPS) sensor and could resist windblasts when used outdoors due to its robust flight controller (Mulcahy 2013). Most importantly, the UAV came off the shelf with a 2-axis professional Zenmuse gimbal that can hold a GoPro Hero3 action camera. The unique combination of a stable UAV and a high-quality camera quickly drove widespread adoption in the field of aerial photography/videography. Unlike the all-in-one and ready-to-fly solutions provided by DJI, the PX4 team led by Dr. Lorenz Meier at ETH

Figure 1-3. Typical hardware components and their layout on a typical 4-rotor civilian UAV (similar layouts would be found in 3-, 6-, and 8-rotor UAVs).

Zurich took a different approach by delivering an open-hardware autopilot compatible with user customizable sensor peripherals. In 2013, the PX4 team partnered with 3DR to develop Pixhawk (pixhawk.org), an advanced hardware flight controller designed to serve the needs of the hobby, academic, and industrial UAV user communities (Auterion 2020). The PX4 team offered its own complete flight control stack PX4-Autopilot, but Pixhawk could also be paired with other autopilot software such as ArduPilot (Ebeid, Skriver, and Jin 2017). Pixhawk greatly improved the reliability of UAV flight control while allowing for ease of use for users willing to customize their own sensor suite on board.

During the phase of commercial drones like DJI Phantom coming to market, onboard sensors for UAVs capable of collecting data in a range of applications emerged. Fastening a camera to a UAV is the dominant configuration in the literature. UAVs were used to monitor and survey wildlife populations in hard-to-reach areas with a high-resolution digital camera (Hodgson et al. 2016). Similar image-based inspection/monitoring UAVs equipped with digital cameras were widely deployed in many applications such as boarder surveillance (Haddal and Gertler 2010), traffic management (Salvo, Caruso, and Scordo 2014), geotechnical site modeling (Zekkos et al. 2018), road maintenance (Inzerillo, Di Mino, and Roberts 2018), building/bridge monitoring (Eschmann et al. 2012; Chen et al. 2019), and railway operation (Li et al. 2020). These camera-based UAV solutions all aimed to replace costly human teams these applications typically used. There were also efforts to integrate more sophisticated cameras (i.e., non-optical cameras) into UAV systems. For example, multispectral cameras installed on UAVs allowed farmers to determine crop classification, monitor crop growth, assess fertilizer responses, and forecast crop yields (Lottes et al. 2017; Schut et al. 2018). SAR UAVs permitted rescue organizations to quickly detect and geo-localize human during a disaster relief effort with the help of thermal IR cameras (Rudol and Doherty 2008; Burke et al. 2019). UAVs equipped with specialized FPV cameras expanded into recreative space and found new uses such as live streaming extreme sports (X. Wang, Chowdhery, and Chiang 2017; Fincky 2019), hosting virtual tours (Song and Ko 2017; Beautiful Destinations 2019), and FPV racing (Bloomberg Quicktake 2016; Barin, Dolgov, and Toups 2017). Another popular sensor payload on a UAV is LiDAR that was mainly used for survey and mapping. In the forestry industry, UAV-LiDAR systems were used to measure tree location, height, and crown width with high spatial accuracy (Wallace et al. 2012). In glaciology, an airborne LiDAR flown by UAVs was deployed to make observations of land and sea ice for mapping surface elevation and topography (Crocker et al. 2012). As a means to develop

3D models that could quantify terrain changes, camera and LiDAR data obtained from a UAV measuring its position in space were taken advantage of to obtain 3D point clouds and to generate digital terrain model (DTM) outputs (Fuad et al. 2018). Other UAV sensors were also reported in the literature for specific aims, such as particle number concentration (PNC) monitors for air pollution monitoring (Villa et al. 2016), metal oxide (MOx) gas sensors for gas leakage localization (Rossi and Brunelli 2016).

1.2.1.3 Stage 3: Advancement of UAV Intelligence and Data Management Tools

While remotely controlled UAVs have tremendous commercial value, their operations are manual meaning a skilled human operator and oftentimes visual observers are required. Manual UAVs are difficult to fly and easy to crash, reducing their effectiveness and scalability as a viable data collection platform. The human operator can be expensive and erodes some of the cost efficiencies of UAVs. Limited autonomy is granted usually by providing GPS waypoints for the UAV to follow from point to point. Although the global navigation satellite systems (GNSS) enabled successful commercialization of some autonomous outdoor UAV applications, GPS typically has low accuracy (roughly, in meters) and is unavailable (or unreliable) in confined, cluttered, or indoor environments. As a result, even the most highly trained pilots avoid flying UAVs in close proximity to their targets to avoid crashing. In fact, in civil infrastructure applications, vortex shedding by large structures on even lightly windy days can present demanding disturbances that pose a serious risk to UAVs.

The next generation of the UAV technology is based on autonomous operations; this requires higher precision flight controls with more advanced computing hardware and real-time software supporting those flight control laws. Although full automation (level 5) is not likely to happen in the next few years, recent advances have shown promise in key areas such as environment mapping (Newcombe, Lovegrove, and Davison 2011; Pizzoli, Forster, and Scaramuzza 2014; Greene et al. 2016), path planning (Ratliff et al. 2009; Oleynikova et al. 2017; B. Zhou et al. 2019), obstacle avoidance (Ragi and Chong 2013; Ma et al. 2016; Y. Lin and Saripalli 2017), and object tracking (Hare et al. 2016; Bertinetto et al. 2016; Gordon, Farhadi, and Fox 2018). Multiple research groups have proposed different UAV platforms installed with various onboard navigation sensors tailored to solve the SLAM problem (Shen, Michael, and Kumar 2011; Tomic et al. 2012; Sa et al. 2017). In the meantime, the industry is also pushing forward fully autonomous flight technology that can navigate UAVs in unknown, cluttered environments. The California-based UAV manufacturer Skydio is one of the leaders in creating intelligent UAVs capable of safe operations in cluttered flight environments. In 2019, the company released its Skydio 2 (S2) drone featuring six navigation cameras and an Nvidia Tegra TX2 with 256 GPU cores that runs a state-of-the-art autonomy engine. The autonomous flight stack utilizes visual-inertial odometry (VIO) for state estimation and deep-learning-based algorithms for depth estimation and obstacle avoidance (Robotics Today 2021). The S2 is able to see and understand its surroundings, plan a flight path through them, and constantly avoid obstacles in any direction. Two particular industrial applications for S2 have been bridge 3D inspection (Skydio 2020a) and roof scanning (Skydio 2020b).

With the widespread use of UAVs as data collection platforms in civilian applications comes the problem of data management, including services for data storage, aggregation, processing, visualization, and sharing. As organizations start to scale their

UAV programs, they typically grow acutely aware of the high volume of data UAVs collect demanding cost-efficient data management solutions. Specific challenges include organizing massive amounts of aerial data (e.g., camera imagery, LiDAR point clouds) in a local machine or a cloud database, fusing other relevant data, utilizing AI and ML algorithms to derive benefits from the UAV-collected data such as feature recognition and defect detection, and establishing collaborative data management platforms that allow multiple workgroups to interact and share key insights from UAV data.

1.2.1.4 Stage 4: Customization for Specialized Functionality and UAV-as-a-Service

As the precision of UAVs increase and their customization is easier (and cheaper) to do, it will be increasingly feasible to introduce new functionality in a broad array of niche spaces for UAVs. UAV manufacturers have been faced with the task of tweaking their designs and developing purpose-built enterprise solutions. An example is SkySpecs, a startup based at Ann Arbor that offers automated inspection services to identify maintenance issues for wind farms (Adler 2018). SkySpecs develops customized UAVs with high tolerance for strong winds which can maintain precise location, control, and image capture while navigating around a wind turbine with high levels of vortex shedding. Standard commercial solutions would fail in this task because turbines are located in windy locations and the rapidly changing wind speed and direction around turbine blades makes UAV stabilization and control extremely difficult (Froese 2018). Another example of a customized UAV is the Elios drone from the Swiss company Flyability (Palomba 2017). Carrying a ball-shaped protective frame around itself, Elios is able to bounce off and roll around obstacles without the risk of crashing, thereby enabling inspections inside tight spaces such as conduits, sewers, bunkers, chimneys, and other hard-to-reach locations

(Flyability 2016). An attractive feature of the cage surrounding the UAV is that it rotates independently of the UAV itself, meaning the UAV body and the onboard camera can stay upright even after it comes into contact with an obstacle. High-precision UAVs have also shown great promise in the logistics industry. Currently inside warehouses, many companies including Verity (verity.ch), Vtrus (vtr.us), Eyesee (eyesee-drone.com), and doks.innovation (doks-innovation.com) report to have implemented UAVs for inventory management. In order to successfully implement UAVs in warehouses, these companies utilize vision-based SLAM technology for precise indoor navigation (due to the denial of GPS in these settings) enabling the UAV to create a 3D map of its surrounding and locate itself inside the map in real time (Wawrla, Maghazei, and Netland 2019). Externally, UAVs have been also explored for product delivery. For example, the American drone delivery company Zipline manufactures and operates its self-designed fixed-wing UAVs to deliver medical product such as blood and vaccines to remote regions (Lydgate 2018). The UAV features a quickly swapped battery for rapid turnaround between flights and can cruise at a top speed of 100 km/h before dropping its onboard medical supplies (up to 1.75 kg) based on use of a parachute. The company have also invented a unique launching and catching system for the UAV that ensures quick response and safe landing (Real Engineering 2019).

UAVs can be used to provide services in an on-demand and pay-as-you-go manner. The idea of UAVaaS rather than requiring individuals to purchase their own UAVs reduces the cost and risks of owning, licensing, operating, and maintaining UAVs (Yapp, Seker, and Babiceanu 2016). UAVaaS providers host both hardware and basic software on behalf of their customers, freeing up users to focus on thought-provoking tasks that require creativity, critical thinking, and human judgement. Integration of UAVaaS with existing business intelligence systems enables deeper insight and quicker decision-making by integrating and analyzing data from multiple organizations. Another advantage of the UAVaaS infrastructure is its adaptability and scalability. For example, UAVs can be flown in a manner that serves more than one user (Loke 2015).

On account of the risks of causing damage to individuals and property, a prerequisite for the UAVaaS infrastructure is absolute safety and security. Currently, regulators in the United States are looking to deploy an unmanned aircraft system traffic management (UTM) system to allow safe operations of multiple beyond visual line-of-sight UAVs (i.e., fully autonomous UAVs) and manage the increased airspace traffic at low altitudes, indicating a major influx of UAVs coming into the market in the near future (FAA 2020b). The first step to building a UTM and at later stage integrating UAVs into the national airspace system (NAS) is to set up rules and a method for UAVs to be identified and communicated with by other parities (including agents in the commercial airline industry), commonly known as remote identification (remote ID). The FAA released final rules of remote ID on December 28, 2020 requiring most UAVs operating in U.S. airspace to have remote ID capability, making way for UAV services in the future to move to completely autonomous flights at scale and with order that ensures public safety (FAA 2021).

1.2.2 Limitations of Existing UAV Systems for Infrastructure Monitoring

Over the past decade, the fast-paced development of UAVs has spawned a diverse set of applications in the realm of civil infrastructure systems. Fundamentally, UAVs are revolutionizing the field by providing previously unobtainable data collection capabilities that surpass conventional civil engineering methods in terms of ease, accuracy, and affordability (Greenwood, Lynch, and Zekkos 2019). UAVs are finding use in inspecting existing structures (Chan et al. 2015), documenting construction progress (J. J. Lin, Han, and Golparvar-Fard 2015), surveying geotechnical sites (Turner, Lucieer, and De Jong 2015), performing post-disaster reconnaissance (Zekkos et al. 2016), and estimating traffic flow (Ke et al. 2018), among others. In fact, any application that could utilize a mobile data acquisition platform could conceivably include UAVs as an integral data collection component.

To date, UAVs have been predominantly used in the civil engineering domain based on Stage 2 phase of development, to collect data most often with a human operator in control and with a camera used for data collection. UAV-based photogrammetry is widely used and currently the main means of assessing civil infrastructure systems (Ham et al. 2016). Leveraging computer vision techniques, a significant amount of research has focused on taking photographs and videos of structures with a UAV that can be used for onsite evaluation or subsequent virtual offsite assessment (Sankarasrinivasan et al. 2015; Ellenberg et al. 2016; Gopalakrishnan et al. 2018). Vision-based monitoring poses many challenges regarding storage and processing of the enormous number of images collected, manual labelling of ground-truth for deep learning-based algorithms, and assimilation of data from image sequences, among others (Spencer, Hoskere, and Narazaki 2019). For structural analysis applications, although recent research work has successfully demonstrated the feasibility of vision algorithms for measuring modal information (Yoon et al. 2017; Hoskere et al. 2019), accurate displacement information is hard to obtain due to limited camera resolution and poor UAV motion accuracy. The role of UAVs also can go well beyond photogrammetry driven by manual operations by offering UAVs the possibility to carry and install other sensor types to be deployed onto the structure for data collection. In the case of structural modal analysis, traditional motion sensors such as accelerometers are more effective and reliable in recording vibrations of a structure than a remote UAV with cameras.

The issue of poor positioning accuracy of UAVs in most civil applications is due to the use of black-box commercial UAVs by these teams with general-purpose flight controls and reliance on GPS and IMU navigation. Maintaining stability and spatial accuracy for UAVs in outdoor environments is a major challenge because of their susceptibility to environmental disturbances. The majority of civil engineering UAV research programs therefore use remotely operated vehicles (ROVs), eschewing autonomy for human-controlled navigation. Although limited autonomy is provided in some applications by offering GPS waypoints for the UAV to follow, GPS signals are only available outdoors and typically are insufficiently accurate resulting in positioning errors at the meter-scale level. There are clear opportunities to enhance the autonomy of UAVs in both outdoor and indoor environment by exploiting more advanced Stage 3 UAV technologies such as SLAM and visual odometry. To move to Stage 3 and 4 phases of development, higher performing controllers are needed and better positioning technology that offers positioning at the cm-level accuracy level (and not GPS m-level accuracy).

Despite the abundance of research work exploring the coupling of UAV mobility and sensing capability, the majority of these studies have been limited to observing infrastructure from afar yet avoiding direct contact with the structure. Within the civil engineering research community, UAVs are primarily used for flythroughs for applications of inspection or surveillance while minimizing interactions with the physical structure being studied. By allowing the UAV to physically interact with and manipulate its physical environment, an entirely new set of applications in the civil engineering domain can be envisioned. First, providing UAVs with the ability to perch on beams or rods can greatly increase their flight time and hence the overall endurance of their missions. This can be especially valuable in applications where UAVs are placing MSN nodes at optimal sensing locations. Moreover, if perch locations are equipped with charging stations, UAVs can be recharged during missions to reach an extended lifespan. Currently, limited onboard batteries used to power UAVs result in short (< 1 hour) flight times. When UAVs are large and carry more payloads, these flight times reduce in proportion to the total UAV weight (Greenwood, Lynch, and Zekkos 2019). Second, empowering UAVs to grasp objects would enable new and exciting applications for civil infrastructure monitoring. UAVs can be used to deploy sensor payloads and modify their spatial configurations when needed as part of an MSN monitoring architecture. Modular structures can be assembled or disassembled by a team of cooperative UAVs installed with grippers. Robotic manipulation also gives UAVs access to payloads that are potentially beneficial to geotechnical applications such as a drop weight for earth subsurface investigation (Zekkos et al. 2014; Greenwood et al. 2018).

In conclusion, while Stage 2 UAV technologies have already stimulated many innovative uses of UAVs in the civil engineering domain, there are still challenges facing the field to developing and implementing more advanced Stage 3 and Stage 4 technologies for automated civil infrastructure monitoring. The existing challenges or limitations of currently adopted UAV systems can be summarized as:

- UAV outdoor navigations have low positioning accuracy (meter level) due to heavy reliance on GPS signals.
- None of the prior UAV applications have high degrees of autonomy (they use manual flights and belong to Stage 2 efforts).
- UAVs are mainly used for flythroughs avoiding direct contact and interactions with their built or natural environments.
- The majority of studies in the field use UAVs to payload non-contact sensors (e.g., cameras) with limited detection capability of structural behavior and severe control limitations.
- Multiple UAVs deploying MSNs suffer from time synchronization issues due to low performing time synchronization algorithms which are OK for low dynamic applications (e.g., modal analysis of structures) but NOT OK for high dynamic applications (e.g., dispersion analysis of seismic sites).

1.3 Dissertation Goal and Objectives

In response to the limitations of RAS solutions in general (as identified in Section 1.1.2) and UAV-based civil infrastructure monitoring technologies in particular (as identified in Section 1.2.2), the overarching goal of this dissertation is to empower structural and geotechnical monitoring applications by advancing a UAV autonomy framework tailored for these applications, with a focus on using vision for accurate UAV position control. Towards this end, several multi-rotor UAVs will be equipped with onboard computers and visual cameras to—in an autonomous fashion—explore structures, deploy wireless sensors onto ROIs within structures, provide impulse excitations by dropping weight payloads, and reconfigure MSN topologies by moving wireless sensors to

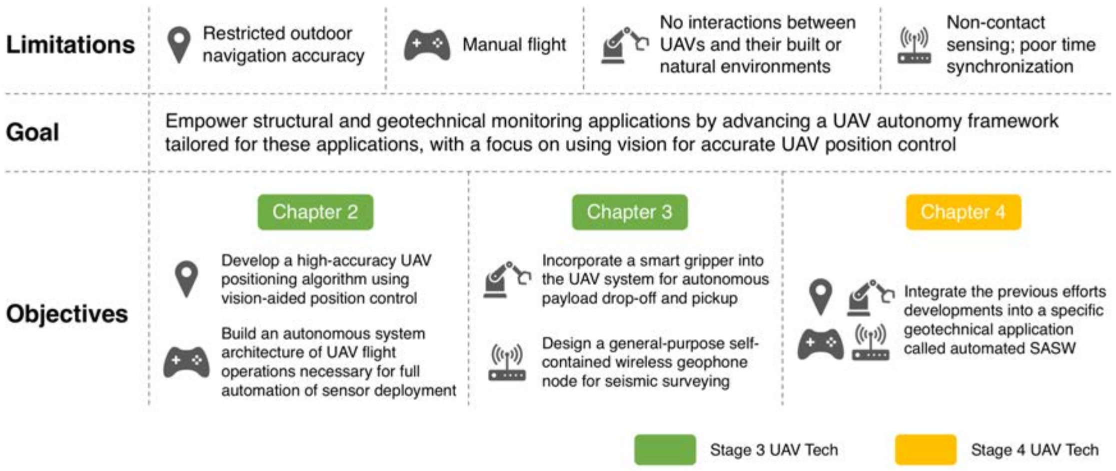

Figure 1-4. Goal and primary research objectives of UAV-enabled automated civil infrastructure monitoring.

subsequent ROIs. Two real-life applications of the UAV autonomy framework are demonstrated, one entails conducting modal analysis of a beam structure using UAV-moved wireless accelerometers, and the other involves autonomous earth subsurface characterization with UAV-deployed wireless geophones and impulsive sources. To the best of the author’s knowledge, the UAV autonomy framework and its validation on real-world civil infrastructure applications are the first of their kind and represent the huge potential of automation in civil infrastructure monitoring applications.

Figure 1-4 outlines the primary research objectives of this dissertation and illustrates how each chapter addresses the limitations of existing UAV systems for automation of structural monitoring. This doctoral research has three primary research objectives. First, it is clear that the accuracy of current UAV navigations in outdoor environments has to date been limited as a result of strong dependence upon GPS signals. To address this challenge, the first objective of this study is to develop a high-accuracy UAV positioning algorithm for autonomous outdoor flights using vision-aided position control of UAVs. Multi-resolution fiducial markers are proposed for attachment to structures to serve as navigation reference targets. Also, to advance the ability for UAVs to interact with their environments, UAV payloads are painted with unique colors for visual detection and aerial grasping. Tailored computer vision algorithms are designed to recognize fiducial markers and colored patterns to estimate the relative pose (i.e., position and orientation) of the UAV relative to these visual patterns. Vehicle state estimation will be implemented based on visual and inertial fusion using a discrete-time Kalman filter (KF). Combined with cascaded position and attitude proportional-integral-derivative (PID) controllers, the accuracy of UAV positioning will be substantially improved to cm-level which will outperform GPS-only navigation. The efficacy of the proposed vision-based control method for autonomous UAV flights and several novel structural monitoring applications driven by the precision control of UAVs will be validated in this dissertation.

With the achievement of a UAV platform that reaches a high degree of spatial accuracy, the second objective of this study is to build a fully autonomous system architecture of UAV flight operations necessary for full automation of infrastructure monitoring. This dissertation accomplishes this objective by creating dedicated finite-state machines (FSMs) for different applications that enable flexible organization and robust management of all aspects of the automation process of UAVs working together. The vast majority of UAV use in civil infrastructure to data have been a single UAV performing mission tasks; in contrast, this dissertation shows the utility of UAV fleets working collectively. This empowers MSN-applications for infrastructure monitoring. The FSM design for each UAV accounts for the collective action of the UAV-based MSN in the design of each UAV FSM. For example, in the application of UAV-based autonomous

MSN deployment and reconfiguration, the complicated mission is split into manageable pieces by the FSM such as searching for a sensor installation location while exploring a structure, flying to the installation location, assessing the location of other UAVs of an MSN, and performing a precision landing of the UAV for sensor placement. Transitions between separate tasks and terminations of them are well defined, ensuring safe, reliable, and efficient flight operations. The FSMs are embedded in the UAV's onboard computer, rendering the UAV a completely self-operating intelligent agent independent of off-board instructions from a human pilot or a GCS. The powerful computing capability of the onboard computer greatly facilitates the UAV's onboard decision-making ability, which is crucial to autonomous operations of any kind.

Leveraging the vision-aided precision control of UAVs and UAV autonomy framework, the last objective of this study is to devise novel methodologies for automation of field monitoring and demonstrate the value of the proposed UAV system. For this purpose, UAVs designed in this study are primarily used to deploy wireless sensor networks and reconfigure their geometries. While generic wireless monitoring systems have been deployed on large structures and in geotechnical field applications, this dissertation emphasizes the automated deployment of wireless monitoring systems in structural monitoring and geotechnical site investigation applications using autonomous UAVs. A considerable fraction of the research effort has been dedicated to the design and implementation of UAV-sensor pairs for each application. For instance, the proposed wireless geophone node is the first modular, low-cost, and open-source seismic sensing technique of its kind and is also capable of being deployed by a mobile UAV for shear wave investigation of field sites. The UAV-enabled sensor deployment strategy is unique in its ability to deploy wireless sensors rapidly with a high spatial accuracy by virtue of the agility and accurate positioning of the UAV. It gives new meaning to sensor network deployment as part of an MSN architecture and adds to the limited body of knowledge of automated monitoring of civil infrastructure using RAS.

1.4 Dissertation Outline

The outline of the dissertation is now delineated. Chapter 2 demonstrates the feasibility of using vision-based autonomous UAVs to deploy wireless sensor networks for structural monitoring purposes, which falls into the realm of applications of Stage 3 UAV technology. While GPS-based waypoint navigation is available for automating UAV flight operations, such positioning tools do not provide the accuracy necessary for precision placement of sensor payloads on structures. In this chapter, computer vision-based pose estimation is used to improve the accuracy of UAV localization for sensor placement. Multi-resolution fiducial markers applied to the surface of the structure are adopted as navigation and precision landing targets that identify sensor placement locations. Visual and inertial measurements are fused by means of a discrete-time Kalman filter to further increase the robustness of the relative position estimation algorithm that is included in the PID control law used for UAV landing. Field experiments are conducted to validate the proposed vision-aided control of the UAV for sensor placement; the UAV is able to land on a predefined landing point within 10 cm. UAVs moving wireless accelerometers to locations on a beam structure are used to experimentally show the validity of automating UAV sensor placement for modal analysis using reconfigurable sensor network topologies.

Chapter 3 is devoted to the development and validation of two crucial hardware components that are essential for automated geo-structural analysis such as earth subsurface characterization. In this chapter, the UAV is explored to deploy seismic sources, as a substitute for traditional human-based methods, by autonomously picking up and dropping off a heavy weight. This is particularly valuable in areas where human accessibility is difficult or impractical such as those that occur in post-disaster scenarios. Following the same vision-aided control strategy of the UAV introduced in Chapter 2, this chapter extends the UAV’s visual perception ability with a tailored color blob detection algorithm so that the UAV can track the weight’s location after dropping it. This is essential for processing shear wave data because the distance between the impulse source and sensor is needed. The second piece of hardware presented in this chapter is a self-contained wireless geophone node with the capability of recording high-resolution seismic waves and precisely time-stamping the collected time histories. The open-software approach adopted in the design of the wireless sensor node renders it much more affordable when compared to its commercial counterparts without sacrificing performance and functionality.

Chapter 4 extends the efforts and accomplishments made in Chapter 2 and Chapter 3 to geotechnical applications and introduces a RAS solution to seismic surveying using the spectral analysis of surface waves (SASW) method. The autonomous robotic system is designed for uses in remote or dangerous sites without any human intervention. The RAS developed in this chapter is an application of Stage 4 UAV technology and covers the full spectrum of a seismic survey including sensor installation, seismic source deployment, and data acquisition. Three autonomous UAVs are employed in the RAS solution with two of them deploying a pair of wireless geophone nodes and the third one impacting the ground surface by dropping an instrumented weight from significant heights. The work shows excellent positioning of all three UAVs relative to a cube-shaped anchor that is located at the sensors' midpoint. The work also verifies the quality of the data collected by building an in situ dispersion curve of the field site and comparing it against one constructed from data collected by a commercial wired seismic monitoring system.

Chapter 5, the final chapter of the dissertation, presents a dissertation summary including highlights of key intellectual contributions achieved and a discussion focused on future extensions of the research needed to realized Stage 4 UAVs for civil infrastructure monitoring applications.

Chapter 2 Autonomous Wireless Sensor Deployment with UAVs for Structural Monitoring Applications

2.1 Introduction

Adoption of sensing is growing increasingly attractive in a wide range of civil engineering applications due to the reduction of sensor cost, the integration of wireless communication that make deployments easier, and the improvement of analytical frameworks that extract value from collected data (Law and Lynch 2019). This has made monitoring common in many field applications such as SHM. In SHM applications, dense sensor arrays are often needed which can drive system costs high. For example, long-span bridges could require hundreds of sensors to ensure sufficient spatial coverage for SHM (Jang et al. 2010). If sensors could be moved, the density of permanent sensors could be reduced, thereby lowering system monitoring costs while rendering systems more flexible to adapt to the needs of the SHM application. To date, the placement of sensors on a structure are done manually with the assumption that they do not move. However, autonomous robotic systems could be developed for the initial placement and later movement of sensors which would make monitoring systems more flexible and cost-effective.

UAVs could potentially be one such solution that offer mobility to sensors that allow for the collection of data that is difficult to obtain using conventional stationary monitoring approaches. The data collection capabilities of UAVs have already proven valuable in many civil engineering applications such as infrastructure inspection, traffic monitoring, and remote sensing (Greenwood, Lynch, and Zekkos 2019). For instance, in earthwork survey projects, Siebert et al. (2014) showed that a camera-equipped UAV conducting photogrammetric surveying is able to provide more accurate spatial measurements while requiring less time to collect than traditional ground-based real-time kinematic (RTK) GPS surveying. To complement conventional oil and gas pipeline monitoring methods (e.g., periodic inspections by foot patrols, air surveillance using light aircraft or helicopters), Gómez et al. (2017) explored the use of UAV systems equipped with active/passive sensors that can inspect pipelines for damage. Computer vision methods offer a promising approach to identifying the condition of infrastructure with inexpensive cameras installed on the UAV. For example, recent studies have demonstrated several innovative applications of UAVs equipped with cameras (e.g., optical, infrared) to conduct infrastructure monitoring such as delamination detection of concrete bridge decks (Escobar-Wolf et al. 2018), modal analysis of a pedestrian suspension bridge (Hoskere et al. 2019), and visual inspection of a steel girder bridge (Fujino and Siringoringo 2020). In all of these applications, the UAV systems are primarily used as a mobile data collection platform to observe the system from afar and make no direct contact with the structure. Also, navigation of the UAV is controlled by either a human pilot operating the UAV or using a GPS module providing waypoint coordinates for autonomous flight operations. Both navigation methods lack accuracy and struggle to give desirable or reliable measurements for cases where precise spatial control of the UAV is required. The utility of UAVs could be further enhanced if they not only carry sensor payloads, but also have the ability to deploy sensors. This can be especially valuable in applications where data collection may be required over a longer period of time (e.g., days, years) than what current UAV flight endurances allow (e.g., minutes, hours). In the literature, the idea of using robots to deploy mobile sensor networks in structures has been developed and validated by several researchers. Huston et al. (2004) studied the use of a mobile robot that was able to crawl along bridge girders while measuring girder flange thickness with an ultrasonic sensor. Zhu et al. (2012) prototyped a climbing robot equipped with magnetic wheels capable of adhering to and navigating on a steel bridge. The robots carried accelerometers as a robot payload and moved around the bridge to sample structural vibrations. In this paper, aerial delivery of sensing payloads based on computer vision and position estimation is proposed as part of an autonomous UAV sensor deployment system. Aerial deployment has advantages over prior wheel-based robots including more freedom to move and a more efficient approach to sensor deployment.

Precision control of a UAV to land on desired positions (i.e., within 0.5 m or less) is necessary for effective sensor placement. GPS-based waypoint navigation techniques used in other SHM applications (e.g., collection of imagery data) are insufficient due to UAV positioning errors being as large as meters that would result in inaccurate and unsuccessful sensor placement. Modern computer vision object detection and pose estimation algorithms are a promising alternative to GPS. Autonomous landing of UAVs using vision as the primary data source is currently an active topic of research. Among early investigations, printed patterns have been used to mark the landing target. Saripalli et al. (2003) demonstrated vision-based autonomous landing of a model helicopter on an “H”-shaped pad; landing position accuracy was reported to be within 40 cm. To extend the detection distance, Merz et al. (2006) proposed an autonomous precision landing method featuring a landing pattern consisting of five circle triplets of different size (with their radii varying from 2 to 32 cm) with the same center point; touch down precision of 42 cm was reported. Lange et al. (2009) designed a landing pattern with several concentric white rings on a black background and was able to hover a Hummingbird quadcopter above the pattern with a maximum deviation of 23 cm over 5 minutes. One drawback of the printed patterns used in the aforementioned works is that they lack generality. The fact that they lack an extensible design limits their usage when multiple landing targets in a structure are required. Also, the detection performance of a UAV using these markers under challenging scenarios such as low lighting has not been rigorously analyzed. To address these challenges, researchers have developed fiducial marker systems with a large number of distinguishable features that perform robustly under challenging field conditions (e.g., ARToolKit (Kato and Billinghurst 1999), ArUco (Garrido-Jurado et al. 2014), AprilTag (Olson 2011)). With a known pattern and size, a fiducial marker can be used to calculate the location and orientation of cameras observing them. Borowczyk et al. (2017) gave a demonstration of autonomous landing of a DJI M100 quadcopter on a moving vehicle with a speed of up to 50 km/h. The landing pad featured a 30×30 cm^2 AprilTag for visual estimation and a mobile phone for transmitting the GPS and IMU data of the moving vehicle. To keep track of the single AprilTag, both a gimbal-mounted camera and a fixed bottom facing camera were installed onboard the UAV. Although good performance was achieved, the system required two cameras. Chaves et al. (2015) accomplished autonomous landing of a UAV (Parrot AR.Drone) on a Segway using a landing platform with four AprilTags: one large marker in the center for initial detection and three small markers on the side for fine pose control at close range when completing the landing maneuver. The drawback of this system is that computations were not done on the UAV so a separate laptop was needed to run the system code and a wireless connection was used by the laptop to stream commands to the UAV. To further extend the detection range, Araar et al. (2017) designed a landing pad using a total of 28 AprilTags with bigger tags surrounding smaller ones. They used an AR.Drone 2.0 quadrotor for experimental validation and reported an 8 cm landing error from the pad center on a stationary target and a 13 cm error on a moving target; similar to Chaves et al. (2015), all computations were run on a separate laptop computer. The past works of precision landing of UAVs using fiducial markers reveal that a single fiducial marker does not provide the range necessary for detection from afar while being sufficiently small for close-range navigation. Also, landing pads with too many markers demand a long computation time or the use of powerful computers on the UAV. In this paper, a simple yet universal landing pattern design for different detection ranges is proposed for detection by a UAV onboard computer in near real-time to be used by a UAV controller during precision landing.

In this study, multi-rotor UAVs are explored for autonomously deploying wireless sensors for structural monitoring applications. The work emphasizes the integration of precise landing and mission management capabilities within the onboard computer of the UAV for truly autonomous operations. Figure 2-1 provides the operational principles of the autonomous UAV-based sensor deployment system proposed including the use of fiducial-based landing pads for placement of a wireless sensor that can be moved from location to location. The proposed landing pad design is easily adjustable and able to provide reliable visual estimation by the UAV (using an onboard computer) during the

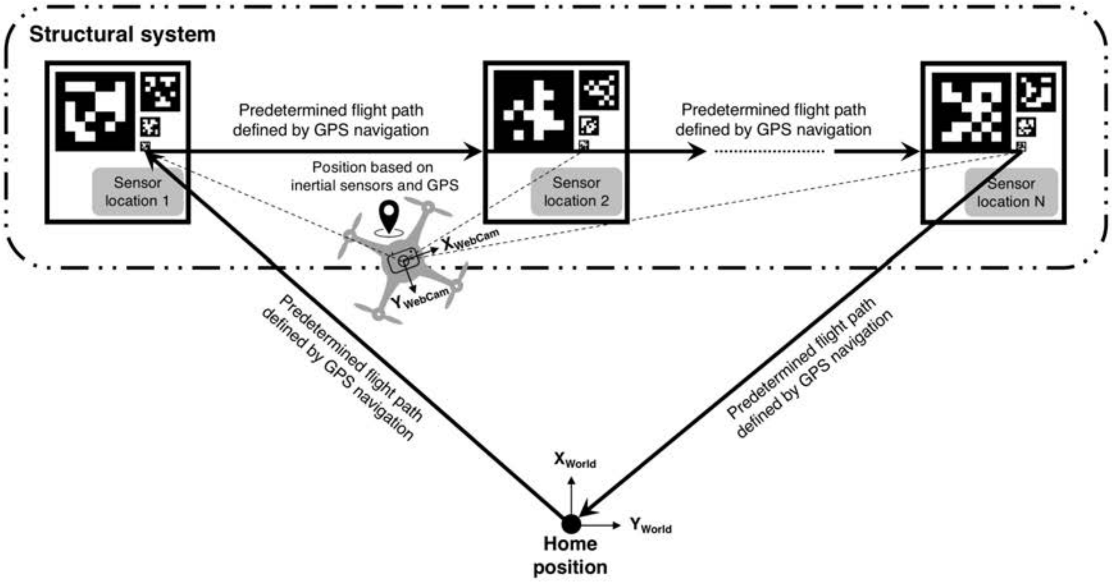

Figure 2-1. Overview of the proposed autonomous UAV system for wireless sensor deployment: UAV autonomously explores a structure, finds target landing patterns, performs precision landing, attaches sensor payload onto the structure, collects sensor measurements, repeats the process until all deployment locations are covered, and returns home.

entire landing process, thereby ensuring an accurate placement of the sensor payload. The envisioned applications include movement of sensors (e.g., accelerometers) on a structure for structural monitoring (with locations predetermined and marked with landing pads). The work aims to make three major intellectual contributions. First, a computer vision approach using four AprilTag markers for a single landing pad is created to trade off precision with onboard computational time for real-time control of the UAV landing. Second, a fully autonomous system architecture is advanced to control UAV flight operations and sensor placement using only the onboard computing resources of the UAV. Third, the integrated UAV system is demonstrated to autonomously perform modal analysis of a simply supported beam where the only human intervention is impacting the beam with a modal hammer (which emulates ambient vibrations). This work evaluates the precision and repeatability of the autonomous landing process for sensor placement. The work also showcases the quality of the sensor data collected by performing complete modal analysis of the monitored structure using the reconfigurable sensor networks.

2.2 UAV Platform: Hardware and Software

2.2.1 UAV Hardware

In this study, two UAV platforms are used: a 3D Robotics (3DR) X8 octocopter and a Lumenier QAV210 quadcopter (Figure 2-2). The X8 has an "X" shape similar to a typical quadcopter but features two motors spinning in opposite directions on each of the four arms (thus eight motors in total). The X8 has a durable aluminum frame that is mechanically sturdy, yet light weight. Eight Sunnysky 2206-12 800 Kv motors are installed and give the X8 more lift to carry nearly a 1 kg payload. The eight motors also provide redundancy offering enough lift and control should a motor burn out on a mission. The X8 is powered by a 16,000 mAh 4S 20C LiPo battery and can stay aloft for about 15 minutes. The QAV210 UAV has a much smaller size with a diagonal length of 210 mm (where the name "QAV210" comes from). The QAV210 has a symmetric carbon fiber frame design featuring four efficient Lumenier RX2206-11 2350 Kv motors. The QAV210 has a payload capacity of 300 grams and a flight endurance of about 10 minutes using two 2,200 mAh 3S 40C LiPo batteries in parallel. In this study, the heavy-duty X8 is mainly used for thorough testing of the UAV control algorithms with a heavy payload carried on board, while the mini QAV210 is used during the experiments related to delivering light-weight wireless sensor nodes onto a narrow beam to validate system integration and autonomy.

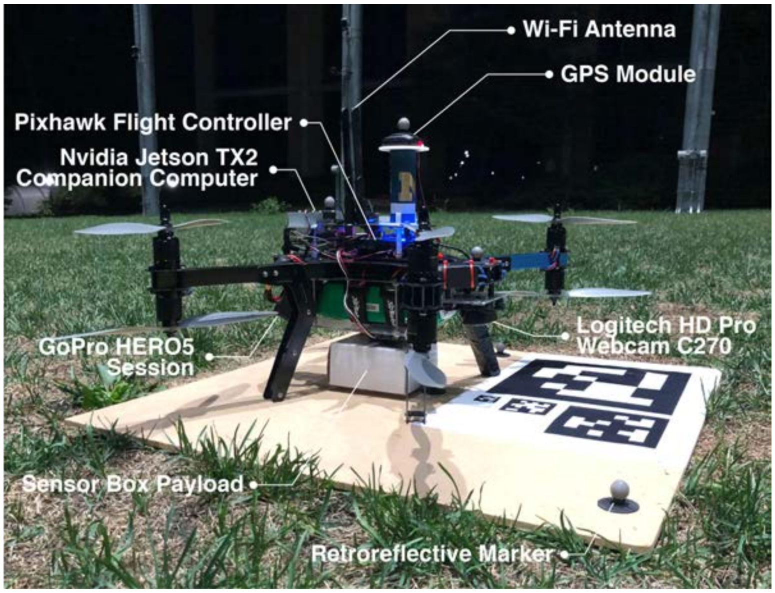

(a)

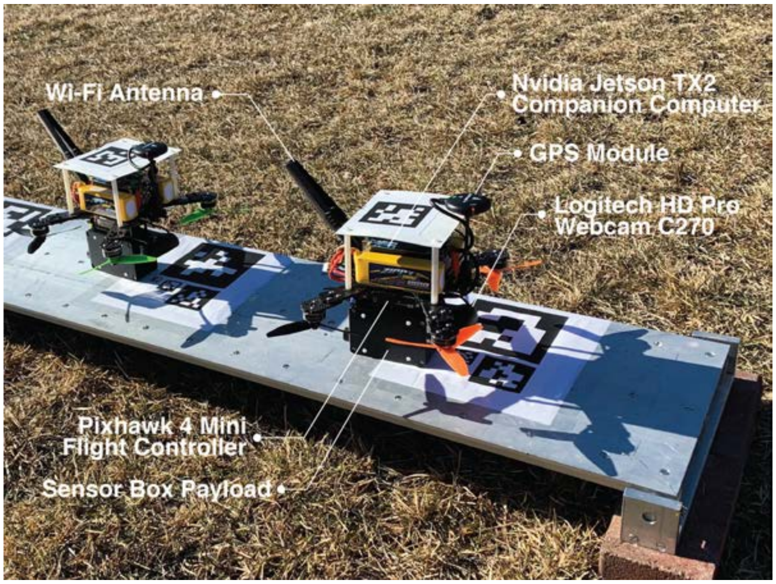

(b)

Figure 2-2. Customized multi-rotor UAVs used in this study: (a) the 3DR X8 octocopter sitting on the landing pad with a sensor box attached (retroreflective passive markers are installed on both the UAV and the landing pad for pose tracking using the Qualisys motion capture system in M-Air); (b) two Lumenier QAV210 quadcopters carrying wireless sensor payloads on a simply supported aluminum beam (AprilTag markers are put on the beam to detect landing spots and on top of each UAV for visual identification of UAV positions on the beam).

The X8 comes preinstalled with an original 3DR Pixhawk flight controller first released in 2013 (Rees 2013). The Pixhawk has a 32-bit STM32F427 ARM Cortex-M4 processor with 256 KB RAM and 2 MB Flash, and operates at 168 MHz. The flight controller includes sensors for inertial measurements including two gyroscope/accelerometer sensors (TDK InvenSense MPU6000 gyroscope/accelerometer, and STMicroelectronics L3GD20H gyroscope/LSM303D accelerometer), a 14-bit STMicroelectronics LSM303D magnetometer, and MEAS MS5611 barometer. The Pixhawk also provides many connectivity options including five universal asynchronous receiver/transmitters (UARTs), two controller area network (CAN) ports, and one inter-integrated circuit (I^2C) interface. An external u-blox LEA-6H GPS module is paired with the Pixhawk for outdoor navigation. For the QAV210, its small frame size requires a flight controller with a scaled-down form factor. In this study, a Holybro Pixhawk 4 Mini is chosen. The Pixhawk 4 Mini has only half the footprint of the Pixhawk but has higher computing performance. The Pixhawk 4 Mini features an upgraded 32-bit STM32F765 Arm Cortex-M7 processor running at 216 MHz with 512 KB RAM and 2 MB memory. The enhanced onboard sensor suite includes an InvenSense ICM-20689 and Bosch BMI055 gyroscope/accelerometer pair, an iSentek IST8310 magnetometer, and the same MS5611 barometer as the 3DR Pixhawk. The external GPS sensor is also upgraded to a u-blox Neo-M8N module. Both flight controllers have a FrSky XSR receiver connected via SBus so that a user can manually command the vehicle using a RC transmitter that operates on the 2.4 GHz radio frequency.

To expand the onboard computational capabilities of both UAVs, a more powerful single-board computer (SBC) is integrated. The Nvidia Jetson TX2 is selected as the companion computer to perform tasks on the UAVs that are computationally resource intensive. The TX2 is equipped with a 256-core Pascal graphics processing unit (GPU), a dual-core Nvidia Denver 2.0 central processing unit (CPU), a quad-core ARM Cortex-A57 CPU, and 8 GB 128-bit LPDDR4 memory. In addition, the TX2 includes Wi-Fi communication capabilities. A small carrier board (Connect Tech's Orbitty Carrier) to which the TX2 module is attached is selected. This small carrier board (87×50×15 mm^3) takes little space on the UAV but offers a variety of interface communication ports (one universal serial bus (USB), two UARTs, one I^2C, and four general-purpose input/outputs (GPIOs)). Communications between the Pixhawk flight controller and the TX2 is established using a serial connection (UART) with a baud rate at 921,600. A ground-based personal computer (PC) is also used to communicate with the Nvidia Jetson TX2 through its 5 GHz Wi-Fi interface. The flight controller takes commands from the TX2 in the form of MAVLink messages (MAVLink 2010) posted over the UART port. At any time, a human pilot can retake control of the UAV by commanding the flight controller through the FrSky Taranis X9D transmitter (although this will not be needed in this study). The complete system hardware architecture is shown in Figure 2-3.

The camera is another critical component for the precise control of both UAVs. A downward facing Logitech C270 high definition (HD) web camera is connected to the bottom of the UAV and attached directly to the TX2 via USB. This low-end webcam is purposely chosen due to its lack of auto-focus functionality which could create blurry images when the UAV is moving at high speeds. Although the auto-focus function found in high-end webcams could be disabled, field tests have shown that this low-cost webcam outperforms top-of-the-line webcams by consistently providing clear, sharp images ideal

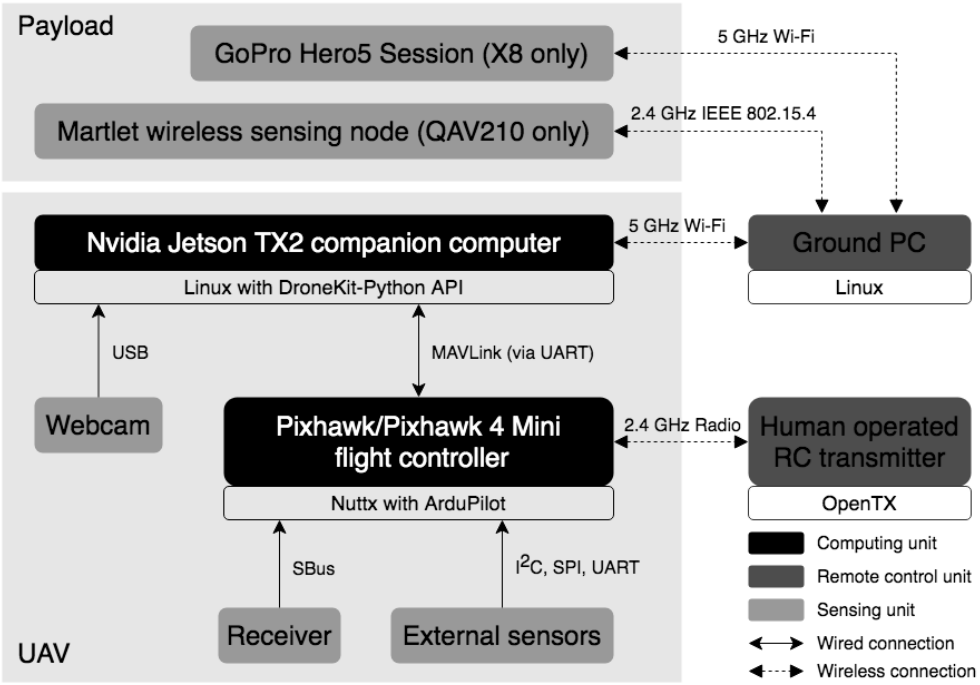

Figure 2-3. UAV system hardware architecture showing system components, embedded software and communication links.

for visual position estimation. Despite the camera's ability to record 720p HD video clips, image resolution is set to a much lower 640×480 px^2 resolution so that images can be processed in real-time on the TX2. The camera is mounted beneath the front of the UAV using rubber dampers that dampen vibrations. The use of a gimbal is intentionally avoided to ensure an unfiltered view of the ground is obtained from which the pose of the UAV can be estimated. An additional camera (GoPro HERO5 Session) is included in the X8 for flight video logging only during validation experiment (and not for use in pose estimation during landing); this GoPro communicates directly with the Ground PC using a 5 GHz Wi-Fi connection.

The Martlet wireless sensing node (Kane et al. 2014) (Figure 2-4(a)) developed at

(a) (b) (c)

Figure 2-4. The wireless sensing node to be attached on the bottom of the QAV210: (a) Martlet wireless node baseboard; (b) inside of the sensing enclosure (left: the Martlet baseboard together with the ADC daughter board; right: the Crossbow accelerometer); (c) exterior of the sensing enclosure.

the University of Michigan is selected as the primary data collection platform for accelerometers used to measure structural vibrations. The computing core of the Martlet is a 16-bit Texas Instruments (TI) TMS320F28069 modified microcontroller unit (MCU) with a clock frequency up to 80 MHz. An attractive feature of the MCU is its dual-core design. The main CPU is able to handle regular single-precision floating-point calculations, while a 32-bit control law accelerator (CLA) is used for complex double-precision floating-point computations. The Martlet contains a 9-channel dual sample-and-hold 12-bit analog-to-digital converter (ADC) capable of sampling analog signals at a maximum sampling frequency of 3 MHz. An ADC sensor interface board (Figure 2-4(b)) is attached on top of the Martlet baseboard to provide bandpass filtering and amplification of input analog signals (100 Hz cut-off frequency and 1× gain in this study). Wireless communication between the Martlet and a ground-based PC is established through a power amplified TI CC2520 2.4 GHz IEEE 802.15.4 transceiver integrated with Martlet. A customized enclosure (Figure 2-4(c)) is designed to house the Martlet and a Crossbow CXL02LF1 accelerometer (Figure 2-4(b)) with 2 g range and 1 mg RMS noise floor. The sensor enclosure is firmly attached to the bottom of the QAV210 and will be moved to different locations on the beam structure together with the vehicle.

2.2.2 Embedded Software Architecture

Embedded software is needed to automate the operations of the UAVs for the deployment of wireless sensors used for monitoring civil engineering systems. Software is written for the two onboard computing elements of the UAV: the TX2 companion computer and the Pixhawk flight controller. High-level flight planning like mission management and compute-intensive tasks like visual pose estimation will be executed using the TX2, while position and attitude control of the UAV are implemented on the flight controller. Figure 2-5 shows the layout of the software architecture distributed across the two computing elements. To speed up the development of the UAV, the open-source ArduCopter firmware from the ArduPilot project (ArduPilot 2011b) is selected to run on the Pixhawk flight controller as the real-time flight control stack. ArduCopter provides reliable and responsive flight control operations for UAVs in a full range of flight modes including manual and automatic flight operations. High-level control abstractions and interfaces are well documented that enable customized flight features and the development of complex use cases. ArduCopter also has well defined communication interfaces that allow a companion computer (like the TX2) to gain access to flight data and to allow extra computing power to handle computationally intensive tasks not easily executable on the flight controller. The ArduPilot project also offers several simulators (e.g., SITL (for software in the loop), Gazebo) (ArduPilot 2011c) to test the behavior of the UAV prior to going to the field thereby lowering the risks of testing in the field.

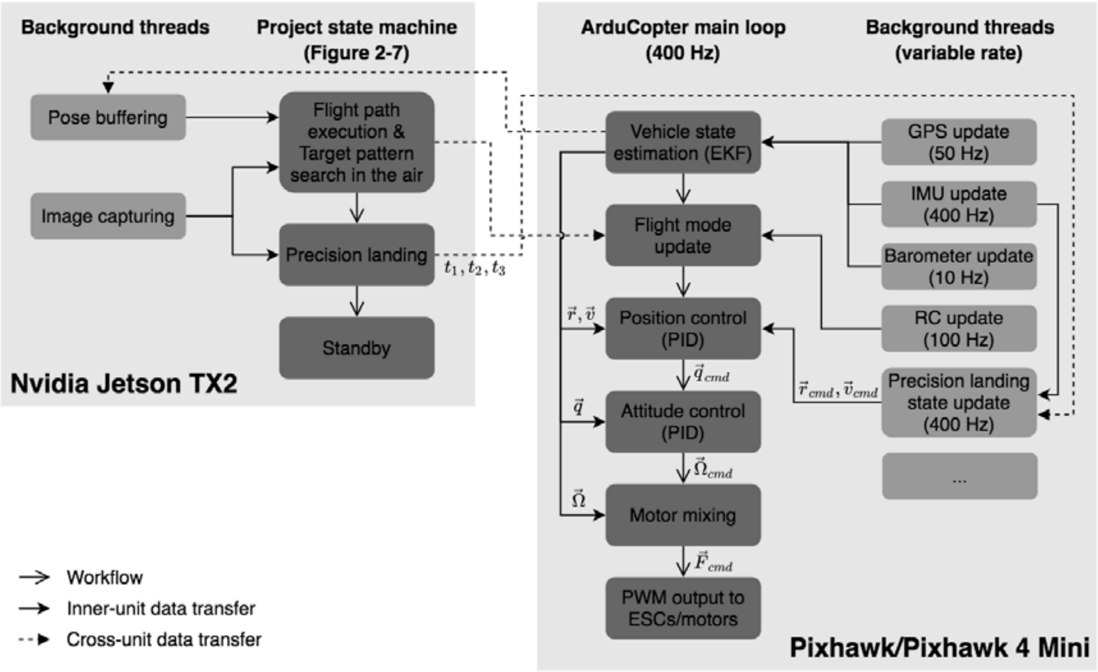

Figure 2-5. Software architecture for the UAV platform where the TX2 provides high-level mission management and image processing while the Pixhawk flight controller is responsible for vehicle state estimation and control.

The main loop (Figure 2-5) of the ArduCopter flight code includes a 24-state extended Kalman filter (EKF) (ArduPilot 2011a; Pittelkau 2003) for vehicle state estimation (e.g., vehicle attitude $\vec{q} = [q_0\ q_1\ q_2\ q_3]^T \in \mathbb{R}^4$, vehicle velocity in the global North-East-Down (NED) frame $\vec{v} = [v_N\ v_E\ v_D]^T \in \mathbb{R}^3$, vehicle position in the NED frame $\vec{p} = [p_N\ p_E\ p_D]^T \in \mathbb{R}^3$, gyro bias offsets in the UAV's local body frame $\overrightarrow{b_g} = \left[b_{gX}\ b_{gY}\ b_{gZ}\right]^T \in \mathbb{R}^3$, gyro scale factor in the local IMU frame $\overrightarrow{s_g} = \left[s_{gX}\ s_{gY}\ s_{gZ}\right]^T \in \mathbb{R}^3$, acceleration bias in vehicle body Z direction $b_{aZ} \in \mathbb{R}^1$, earth magnetic field in the NED frame $\overrightarrow{m_e} = [m_N\ m_E\ m_D]^T \in \mathbb{R}^3$, body magnetic field $\overrightarrow{m_b} = [m_X\ m_Y\ m_Z]^T \in \mathbb{R}^3$, wind velocity $\overrightarrow{v_w} = [v_{wN}\ v_{wE}]^T \in \mathbb{R}^2$). In this study, the vehicle attitude $\vec{q}$, velocity $\vec{v}$, and position $\vec{p}$ will be used for control of the UAV. The EKF is designed to linearize the nonlinear UAV flight dynamics and sensor measurement equations using IMU deadreckoning to propagate the state and onboard sensor (e.g., GPS, barometer) measurements to update the state estimation. Advantages of the EKF include being able to switch between sensors (in case a sensor fault is identified) and the estimation of external flight variables such as gyro and accelerometer biases and wind speed leading to better flight performance. The ArduCopter main loop is run on the Pixhawk at 400 Hz including the EKF filter. A number of background threads are running constantly on the flight controller to provide input to the EKF algorithm including updates of the GPS (50 Hz), barometer (10 Hz), and IMU (400 Hz). As a result, the EKF provides estimations of the UAV attitude, position, and velocity using available flight data at the 400 Hz main loop execution rate.

To control UAV motions for autonomous flight, ArduCopter implements a cascaded control structure with a position controller followed by an attitude controller. The first step of the control solution is the "flight mode update" which is used to offer a target mode for the UAV. For example, the "Land" mode reduces vehicle altitude to the ground level, the "Alt Hold" mode holds altitude and only allows movement in the horizontal plane, the "RTL" mode returns the vehicle to the launching point, etc. Flight mode update can be informed by a command from a radio controller when in manual mode or, as is done in this study, issued by the external onboard computer (i.e., the TX2) as part of a state machine associated with automated flight operations. Depending on the flight mode, the flight controller utilizes different control strategies. The "Land" mode is most pertinent to this study and the control logic behind precision landing is described here (Figure 2-6). The outermost control loop is the position controller that is based on a proportional-integral-derivative (PID) controller design. The position controller takes in a target vehicle position $\vec{r}_{cmd}$ and velocity $\vec{v}_{cmd}$ from the precision-landing Kalman filter (which will be illustrated

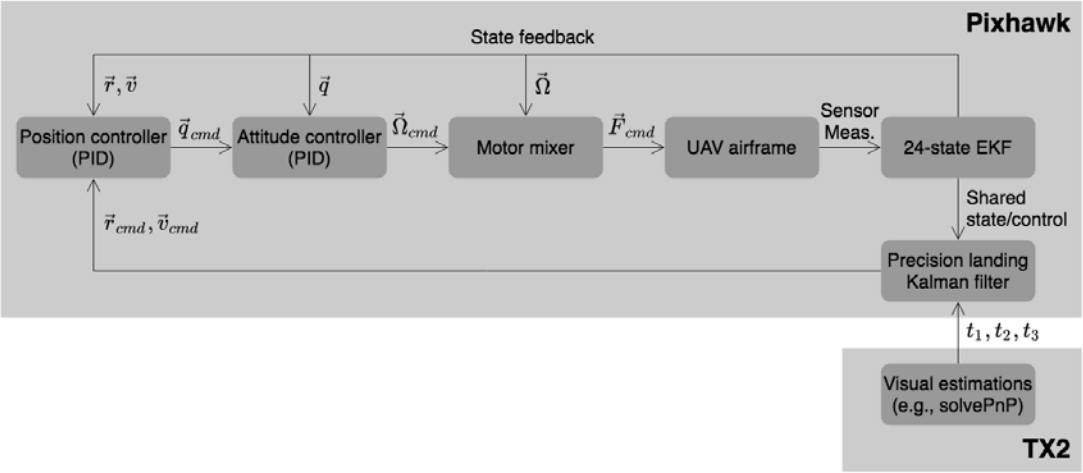

Figure 2-6. Cascaded control of the UAV during a precision landing maneuver.

in the next section) and the vehicle's actual position $\vec{r}$ and velocity $\vec{v}$ from the 24-state EKF to generate a target vehicle attitude $\vec{q}_{cmd}$ that will be fed into the attitude controller. Similarly, the attitude controller adopts a PID design for each angle axis and outputs desired angular body rates $\vec{\Omega}_{cmd}$ (i.e., $[\Omega_{cmdX}\ \Omega_{cmdY}\ \Omega_{cmdZ}]^T \in \mathbb{R}^3$ along the three axes of the vehicle's body frame) for the vehicle. At the end of the ArduCopter main loop, outputs from the attitude and position controllers are converted to absolute motor outputs (i.e., pulse-width modulation (PWM) values) for the specific frame type (e.g., quad, X8) and sent to the ESCs which command each motor with a PWM output, $\vec{F}_{cmd}$ (i.e., $[F_1\ F_2 \dots F_n]^T \in \mathbb{R}^n$, where n is the number of motors). It should be emphasized that the contributions of this work lay mainly on the TX2 side, where visual estimation of the UAV's relative position to the landing pad is provided based on computer vision methods. In contrast, the Pixhawk is used as coded with an addition of a Kalman filter for precision landing and fine tuning of the PID control parameters for precision control of the UAV.

The Nvidia Jetson TX2 companion computer running Linux (Ubuntu 16.04) constitutes the other significant part of the UAV software system. The main thread embedded on the TX2 is a finite-state machine (FSM) for automated flight operations including where and when to place wireless sensors on a structural system. As will be described in the next section, the FSM is primarily focused on implementing a target search for identifying sensor locations and performing precision landing of the UAV while ensuring flight safety and efficiency. To do this, the UAV's bottom mounted camera interfaced to the TX2 will be used to search for landing locations identified with fiducial markers and to improve UAV positioning during precision landing. The DroneKit-Python API (DroneKit 2014) is set up on the TX2 to establish communication between the Pixhawk flight controller and the TX2 using the MAVLink communication protocol. Through this low-latency communication protocol, the TX2 is able to get real-time access to the vehicle's state and to command vehicle movement and operations to the flight controller.

2.3 Methodology

2.3.1 Sensor Deployment State Management

This study is focused on full automation of UAVs for deployment of wireless sensors for structural monitoring applications. The major intellectual merit of the work is embodied in the methodology associated with automation of sensor deployment and redeployment. At the core of the work is the creation of an FSM embedded in the UAV onboard computer (i.e., TX2) that choreographs each step of the fully autonomous sensor deployment. The deployment strategy (Figure 2-1) will be based on a structure with pre-determined sensor locations defined by fiducial markers. The role of the UAV is to deploy sensors to the locations predetermined by precise landing and placement. Once sufficient data is collected, the sensor is retrieved by the UAV and taken to another installation location. This deployment strategy will be executed by the UAV using the FSM embedded in the onboard TX2 computer.

The FSM approach partitions the autonomous sensor deployment method into a set of well-defined operational states with deterministic transitions between them. As shown in Figure 2-7, the task of deploying a wireless sensor node is split into manageable pieces such as searching for the target landing pattern in the air, hovering above the landing pattern, and performing a precision landing of the UAV for sensor placement. The FSM guides the UAV to first take off from the home position to a target height and to fly a predetermined flight path while searching for the desired fiducial marker on the structure that indicates the installation location of the wireless sensor (e.g., sensor location 1 in Figure 2-1). If the desired landing pattern is found, a precision landing maneuver based on computer vision is performed to precisely land on the target pattern for precise placement of the sensor. After desired measurements are taken, the UAV takes off and searches for the next installation location (e.g., sensor location 2 in Figure 2-1). The UAV will repeat this procedure until all required locations are visited, at which point the UAV will return to its home position. A challenge with UAVs in general is their limited battery energy; this requires an efficient FSM that does not waste scarce energy. Certain states in the FSM presented in Figure 2-7 are only granted a limited time for the UAV to stay in so that battery life is not wasted. For example, if the UAV has spent an unreasonably long time searching for landing patterns due to situations like bad GPS data or strong winds, the FSM would command the vehicle to land immediately to save battery life.

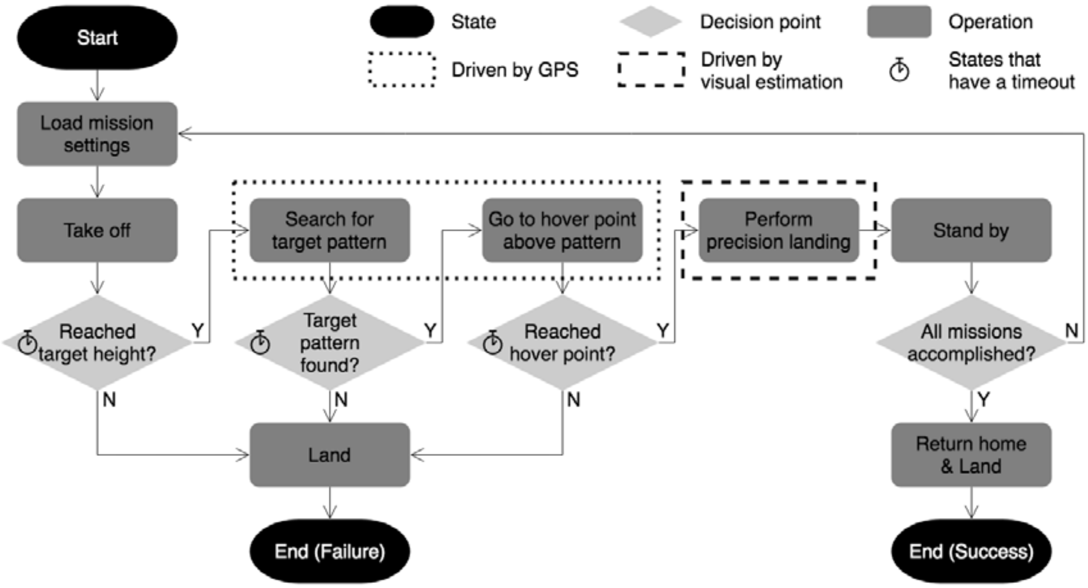

Figure 2-7. Finite-state machine for the UAV-based sensor placement mission; certain operations are only granted a limited time to stay in for battery life preservation (Note: reliability and flight protection are provided by issuing an immediate land command whenever things go wrong).

In the flight operations dictated by the FSM, the UAV will rely on two primary sources of data for spatial pose estimation: vehicle state estimation data (e.g., vehicle position $\vec{r}$, velocity $\vec{v}$, attitude $\vec{q}$) queried by the TX2 companion computer from the flight controller and camera images viewing the landing pattern which are a set of unique fiducial markers. The TX2 has a flight path defined by GPS waypoints that is communicated point by point to the flight controller over the MAVLink communication interface. The GPS data is sufficiently accurate (i.e., within meters) for guiding the UAV over large distances but too coarse for precision landing. Once the fiducial markers corresponding to a desired landing location is found, the UAV uses the TX2 computer to estimate with greater precision (i.e., within centimeters) the UAV position $\vec{r}$ and orientation $\vec{q}$ using camera images of the fiducial markers and a Kalman filter. Once the landing pattern is detected, the cascaded position and attitude controller (Figure 2-6) inside the Pixhawk controls the

UAV to land using the estimated UAV pose relative the landing pattern as an input to the control law. The processing of the camera images and relative pose estimation are done by the TX2 computer using tailored software written in Python and executed by the Linux OS of the TX2. The fusion of the camera estimates and other sensor data such as IMU-based measurements is implemented via a second Kalman filter (i.e., independent of the EKF) embedded in the Pixhawk flight controller by the author; this Kalman filer in written in C++.

2.3.2 Landing Pattern Design and Detection

2.3.2.1 Need for Tags of Variable Sizes

Being able to detect the landing pattern defined by fiducial markers is fundamental to the automated sensor deployment FSM. Specific challenges include keeping the visual target within the camera's limited field of view (FoV), robust detection of the landing pattern using low-resolution images, and use of the fiducial markers for UAV state estimation for precision landing. A multi-resolution tag pattern is designed to address these challenges. During a precision landing task, ground areas covered by the UAV's downward facing camera is limited by the camera's FoV and the height, dz, of the UAV. A camera from a higher altitude with a wider FoV has better coverage of the ground. More specifically, as shown in Figure 2-8, the maximum lateral and longitudinal ground distance covered by the camera, dx and dy, can be calculated as:

$$\begin{aligned} dx &= 2 \cdot dz \cdot \tan\left(\frac{FoV_x}{2}\right), \\ dy &= 2 \cdot dz \cdot \tan\left(\frac{FoV_y}{2}\right), \end{aligned} \tag{2-1}$$

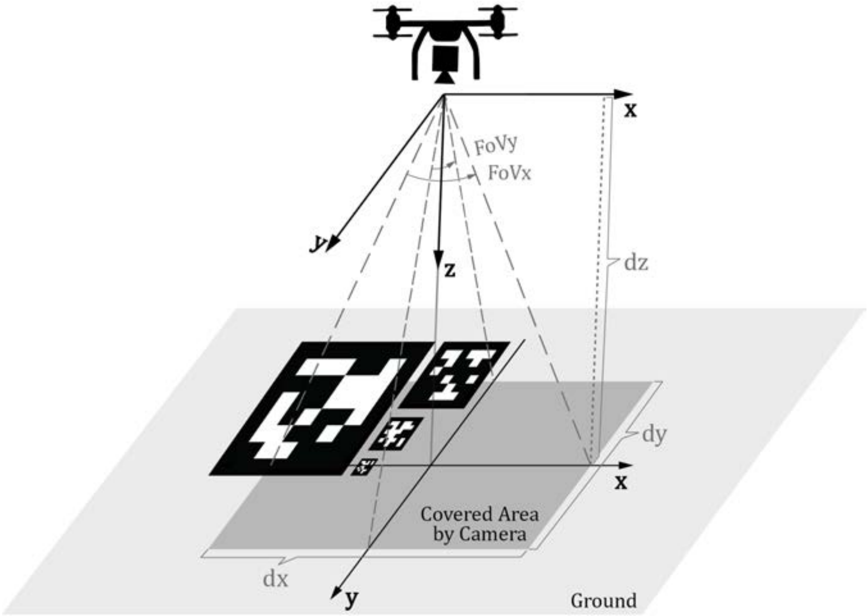

Figure 2-8. Diagram illustrating camera's limited field of view. Area covered on the ground by a downward facing camera is restrained by the camera's FoV and the height of the camera (in this case, only the two smallest tags stay completely in the camera's FoV).

where FoV_x and FoV_y are the camera's field of view along the x and y axis, respectively. The designed landing pattern includes fiducial markers of different sizes which are intentionally positioned as guides to the UAV at different distances from the target during landing, leading to better precision. Bigger markers allow the UAV to detect landing spots from high altitudes, but smaller markers are needed to ensure precision during landing. As the UAV descends, bigger tags gradually leave the camera's FoV while smaller ones become detectable, thereby providing a continuous navigation guide for the UAV.

2.3.2.2 AprilTag Fiducial Detection System

The AprilTag fiducial detection system is chosen for the design of the landing pad due to its robust performance with respect to suboptimal lighting conditions, occlusion,

1	1	0	1	0	1
0	1	1	1	0	1
0	1	1	0	0	0
1	0	1	0	0	0
0	1	0	1	1	0
0	0	0	1	0	0

(a) (b) (c)

Figure 2-9. AprilTag detection process: (a) line segments detection; (b) quad detection; (c) payload decoding.

and motion blur (Olson 2011). These black and white, QR-code-like square tags contain identification information (tag ID) and provides full pose estimation of a calibrated camera with respect to a tag. The AprilTag detection system is composed of two major components: tag detector and coding system. The detector's job is to estimate the position of potential tags in an image and the coding system enables encoding/decoding of distinguishable IDs. The detection process starts with detecting line segments by grouping together pixels with similar gradient directions and magnitude (Figure 2-9(a)). Sequences of line segments that form a 4-sided shape (i.e., possible tag boundaries) are then identified based on a recursive depth-first search method (Figure 2-9(b)). The final stage of the detection algorithm is payload decoding, where bits from the tag-relative payload field are extracted one by one (Figure 2-9(c)). Once the data payload is determined, the coding system determines whether it is a valid tag or not. The AprilTag encoding scheme utilizes a modified lexicographic coding system that ensures minimum Hamming distance between codewords while rejecting simple patterns that commonly occur in natural scenes (Olson 2011). Different families of tags are provided by the AprilTag coding system, depending on the size of the tag (e.g., 4×4, 5×5, 6×6 grids) and the minimum Hamming distance between codewords. In general, families with smaller grid size (and hence larger pixel size) enable detection from afar while those with a larger grid size allow larger Hamming distance thereby providing higher identification accuracy. In this study, the Tag36h11 AprilTag family (6×6 codewords with a 11 bits minimum Hamming distance) is adopted for its high detection accuracy with low processing time. A Python module is implemented in the UAV TX2 to detect the AprilTag (Swatbotics 2016).

2.3.2.3 Superiority of a Fixed Landing Point over Floating Landing Points

When using a multi-resolution AprilTag landing pattern, several tags may be detected at the same time from an image. Different strategies can be applied regarding which detected tags to use for precision landing. In previous work (Zhou, Lynch, and Zekkos 2019), the smallest AprilTag among all detected is set as the active one and the landing point is assigned as the center of the active tag (Figure 2-10(a)). This method is time efficient but struggles to produce smooth landing trajectories. The suboptimality of this strategy can be explained by the following. When a switch of active AprilTag happens, the sudden change of the target landing point could drive the UAV to make a dramatic horizontal move in the air, which could further result in a large camera tilt angle and possibly a permanent loss of the landing patten. During development and testing, it has been found that when the UAV is not well tuned (i.e., PID parameters are not well tuned so that the UAV cannot track its desired position or velocity tightly), visual loss of the landing pattern occurs frequently. One way to alleviate this problem is to organize different tags in a carefully designed pattern. For instance, having tags arranged in a circular pattern with smaller ones sitting closer to the center of the circle (Figure 2-10(a)) outperforms a pattern with randomly placed tags. This patten design is still suboptimal though. As smaller

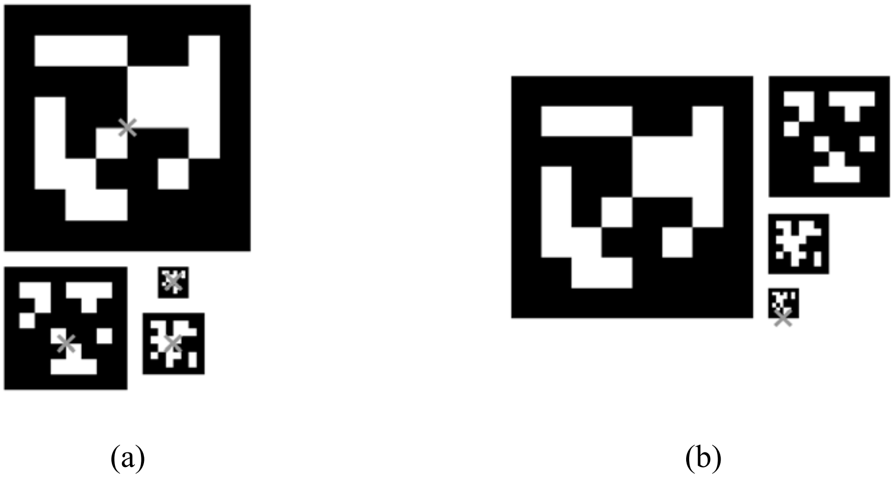
(a)

(b)

Figure 2-10. Two landing pattern designs and their associated landing points shown as gray crosses: (a) a design with four AprilTags placed in a circular pattern (note: the floating landing point is assigned as the center of the smallest Apriltag among the detected); (b) The landing pattern adopted in this study with a fixed landing point defined at the middle of the bottom edge of the smallest AprilTag.

tags come into view, chances are the active tag would bounce between different tags, which could cause oscillations and other unexpected behavior of the UAV. In this study, a new strategy that abandons the switching of active tags is proposed. All tags identifiable in an image are employed to construct a fixed landing point, and the UAV estimates its pose relative to this single reference point. In this way, all kinds of landing pattern can be used as long as all the tags stay relatively close to each other (so that when a bigger tag leaves FoV, smaller ones become detectable) and the predetermined fixed landing point is near the smallest tag (because the smallest tag needs to stay in FoV to provide guidance at the final stage of landing). In this study, a landing pattern with the appearance of Figure 2-10(b) is adopted. The pattern contains four different levels of tag resolution with the fixed landing point defined at the middle of the bottom edge of the smallest AprilTag. Detection range is easily configurable by using different sizes of print.

2.3.3 Visual Position Estimation

Having detected the landing pad and identified the pixel coordinates of the detected AprilTags' feature points (i.e., tag center and corners), estimation of the relative position of the UAV relative to the landing point is now possible. Towards this end, a robust relative position estimation method relying on both IMU and vision data is developed. To compensate for cases where visual localization data is not available, a Kalman filter is next implemented to provide continuous estimation of the UAV position relative to the landing point.

2.3.3.1 Relative Position Estimation

Figure 2-11 presents the method for positioning the UAV with respect to the landing point M. In this study, a superscript on the location variable denotes the reference frame (e.g., P^A denotes the coordinates of point P with respect to frame A). Three main coordinate frames and transformations between them are illustrated in Figure 2-11. The global North-East-Down frame, denoted *Ground*, is located at the UAV's home position P (i.e., where it takes off). The North direction (x_P) is provided by the magnetometer sensor onboard the vehicle. The *UAV* body frame is set at its center of gravity (CG), point Q, with the x_Q axis pointing between two of the arms towards the front of UAV, the y_Q axis pointing to the right, and the z_Q axis pointing to the bottom of the UAV. A *Camera* frame $O(x_O, y_O, z_O)$ is defined at the optical center O. Common practice is to set x_O to right of the camera, y_O down, and z_O outwards from the camera lens. The objective is to find the relative position of the landing point M with respect to the UAV's CG, point Q, in the *Ground* frame. Because the UAV's coordinates in the *Ground* frame (i.e., Q^{Ground}) is

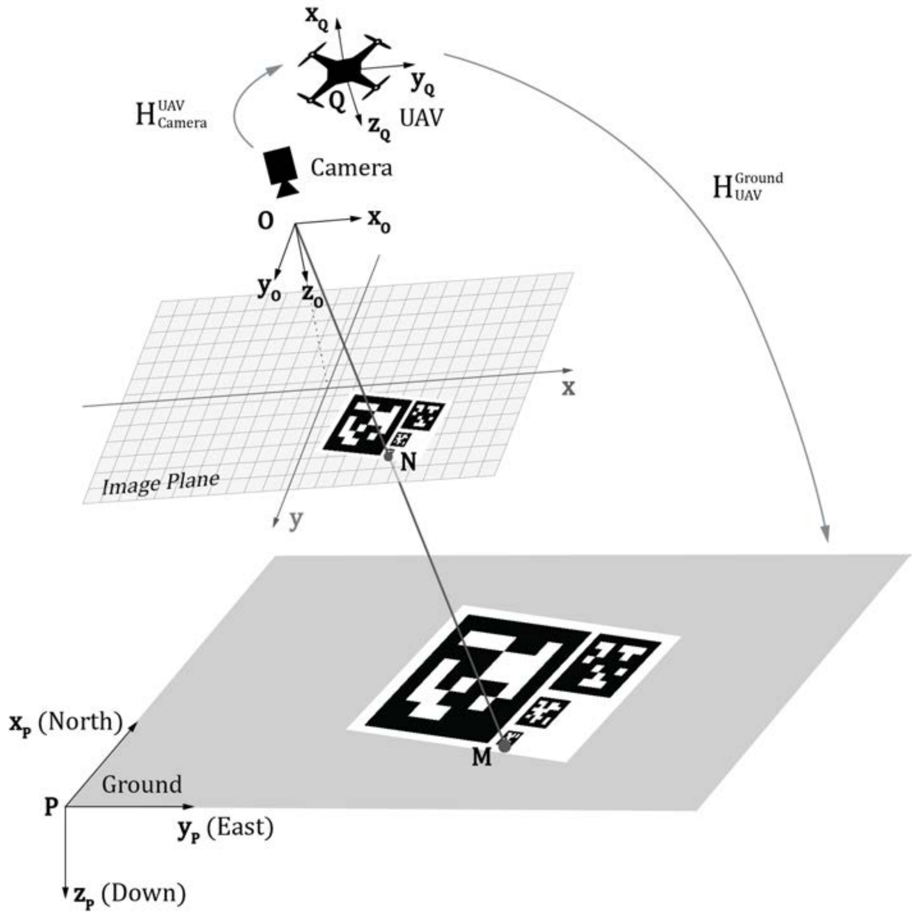

Figure 2-11. Diagram illustrating how to compute the relative position of the landing point M with respect to the UAV's CG, Q, in the *Ground* frame.

provided as state estimations by the 24-state EKF implemented in the Pixhawk flight controller, the objective then becomes to find M's coordinates in the *Ground* frame (i.e., M^{Ground}).

The first step is to compute the landing point M's representation in the *Camera* frame, M^{Camera}. To this end, a pinhole camera model (Figure 2-12) is adopted to construct the mathematical relationship between coordinates of point M in a 3D world frame and the 2D coordinates of its projection point denoted as point N in the image pixel frame. Four coordinate systems are defined in the pinhole model of Figure 2-12. The *Camera* reference

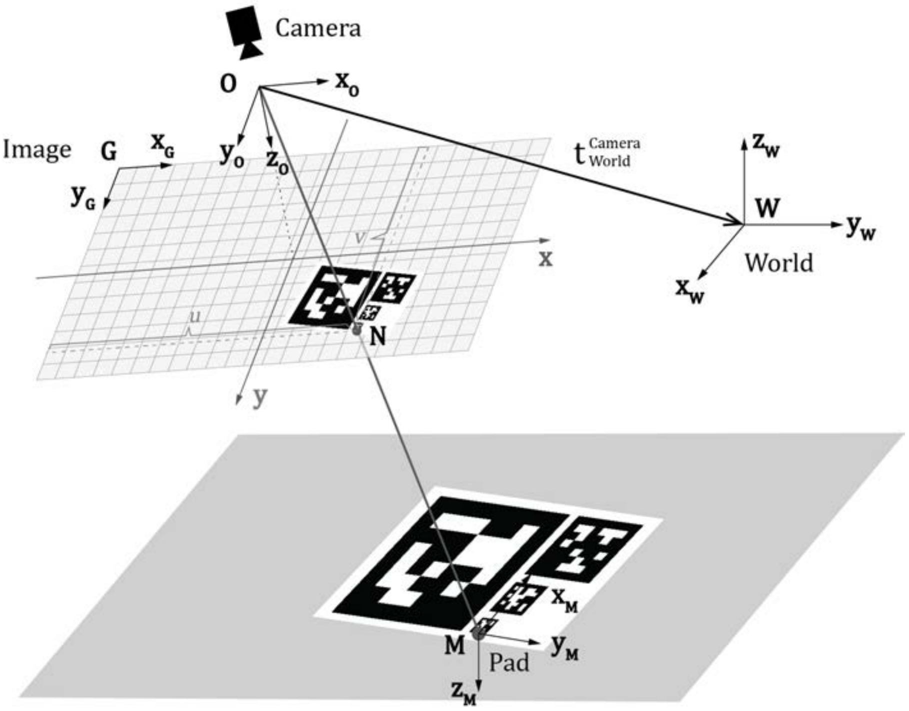

Figure 2-12. Pinhole camera model showing the landing point M in the 3D *World* frame and its projection point N in the *Image* plane through the camera lens center O.

frame is as defined in Figure 2-11. The *World* frame $W(x_W, y_W, z_W)$ is the frame of reference for absolute positioning. The *Image* coordinate frame, denoted as $G(x_G, y_G)$, is defined with the origin G at the top-left corner of the image with x_G pointing to the right. The fourth reference frame *Pad*, denoted as $M(x_M, y_M, z_M)$, is defined at the landing point M. In the *Pad* frame, x_M points up, y_M points to the right, and z_M points inward to the pad. Both the x_M and y_M axes are parallel to tag boundaries.

The pinhole camera model can be formulated as (see Appendix A.1 for details):

$$cN^{Image} = K[R^{Camera}_{World}|t^{Camera}_{World}]M^{World}, \tag{2-2}$$

where $c \in \mathbb{R}$ is a scaling factor, $K \in \mathbb{R}^{3\times3}$ is the camera intrinsic matrix, $[R^{Camera}_{World}|t^{Camera}_{World}] \in \mathbb{R}^{3\times4}$ is the camera extrinsic matrix representing the relative rotation and translation of frame *World* with respect to frame *Camera*, $N^{Image} = [u\ v\ 1]^T \in \mathbb{R}^{3\times 1}$ and $M^{World} = [x\ y\ z\ 1]^T \in \mathbb{R}^{4\times 1}$ are homogeneous coordinates of point N and M, respectively. The camera intrinsic matrix, K, is based on the camera optics and is a constant matrix that only needs to be found once. Equation (2-2) can be expanded as:

$$c\begin{bmatrix} u \\ v \\ 1 \end{bmatrix} = K\begin{bmatrix} r_{11} & r_{12} & r_{13} & t_1 \\ r_{21} & r_{22} & r_{23} & t_2 \\ r_{31} & r_{32} & r_{33} & t_3 \end{bmatrix}\begin{bmatrix} x \\ y \\ z \\ 1 \end{bmatrix}. \tag{2-3}$$

Note that the translation vector t_{World}^{Camera} can be interpreted as the coordinates of the origin of the *World* frame with respect to the *Camera* frame (Figure 2-12). By purposefully defining the *World* frame exactly as the *Pad* frame, the landing point M becomes the origin of the *World* frame, and M's representation with respect to the *Camera* frame is simply t_{World}^{Camera}, i.e.,

$$M^{Camera} = t_{World}^{Camera} \triangleq [t_1\ t_2\ t_3]^T. \tag{2-4}$$

M^{Camera} represents all the necessary information about the landing point that can be obtained from a single image needed for control of the UAV to land with precision on the pad. Specifically, M^{Camera}, or the translation vector t_{World}^{Camera}, defines the relative distances, Δx, Δy, and Δz, of the camera with respect to the landing pad that will be used to control the UAV landing with the control law aiming to drive t_{World}^{Camera} to zero.

The problem of estimating the pose of a calibrated camera (with known intrinsic matrix, K) based on a set of n reference 3D points and their corresponding 2D projections is commonly referred to as the Perspective-n-Point (PnP) problem. Mathematically, the PnP problem can be defined as given a set of n 3D world coordinates-2D image coordinates pairs, determine the camera extrinsic matrix $[R_{World}^{Camera}|t_{World}^{Camera}]$ (Equation (2-2)). Existing solutions to the PnP problem can be classified into two methods: optimization-based iterative methods (solved by minimizing a properly defined cost function, e.g., Lu, Hager, and Mjolsness 2000) and closed form methods (solving the equation directly, e.g., Lepetit, Moreno-Noguer, and Fua 2009). Making use of the open-source computer vision library, OpenCV (Bradski 2000), an iterative method called solvePnP (OpenCV 2019) is selected here. The cost function used by solvePnP is the reprojection error, which is defined as the sum of squared distances between the observed projection points and those calculated in each iteration. Solutions of the extrinsic matrix $[R_{World}^{Camera}|t_{World}^{Camera}]$ that minimize the reprojection error are found based on the well-known Levenberg-Marquardt algorithm (Levenberg 1944; Marquardt 1963).

The compute-intensive solvePnP algorithm is implemented in the TX2. After obtaining the translation vector t_{World}^{Camera} (i.e., t_1, t_2, and t_3) from each image, MAVLink messages encoding t_1, t_2, and t_3 are sent from the TX2 to the flight controller (Figure 2-6). These visual estimations are used as a measurement update for a precision-landing Kalman filter that will be illustrated next.

Once M^{Camera} is computed, a set of homogeneous transformations can be applied to get M^{Ground} based on rigid motions between different frames:

$$M^{Ground} = H_{UAV}^{Ground} H_{Camera}^{UAV} M^{Camera}, \tag{2-5}$$

where M^{Ground} and M^{Camera} are 4×1 homogeneous coordinates augmenting the original 3×1 coordinates by a fourth component of 1. A homogeneous transformation matrix H_B^A

(4×4) is nothing but a compact way to include both the relative rotation R_B^A and translation t_B^A between two frames A and B, i.e.,

$$H_B^A = \begin{bmatrix} R_B^A & t_B^A \\ 0 & 1 \end{bmatrix}. \tag{2-6}$$

H_{UAV}^{Ground} comes from the attitude and position estimations for the UAV in real time, and H_{Camera}^{UAV} is a preset constant dependent on how and where the camera is mounted on the UAV.

On a side note, the rotation matrix R_{World}^{Camera}, or specifically R_{Pad}^{Camera}, produced by the solvePnP algorithm is utilized to line up the *Camera* frame and the *Pad* frame such that the camera's x_O axis coincides with the pad's y_M axis. Before precision landing starts, the vehicle is commanded to yaw an appropriate angle based on this rotation matrix. In this way, the orientation of the UAV is deterministic with respect to the landing pad when it lands.

2.3.3.2 Kalman Filter for Landing Position Estimation

The IMU can be further exploited to increase the robustness and accuracy of the vision-based relative position estimation. Visual and inertial fusion has been an active topic of research to address accurate and reliable localization and mapping in a wide range of robotic oriented applications. The rich information contained in images in a longer time window, together with the accurate short-term estimates by gyroscopes and accelerometers complement each other, making visual and inertial measurements ideal for fusion. Existing approaches found in the literature can be broadly classified into two categories: batch nonlinear optimization methods (Leutenegger et al. 2015; Forster et al. 2016; Qin, Li, and

Shen 2018) and recursive filtering methods (Mourikis and Roumeliotis 2007; Bloesch et al. 2015). The optimization methods jointly minimize errors from both the IMU and vision measurements, while filter based methods commonly use IMU measurements for state propagation with updates originating from visual observations. Nonlinear optimization methods are higher performing but their increased accuracy comes at a cost of more computational resources. Hence, a recursive linear Kalman filter is adopted in this work due to its simplicity and the flight controller's limited computing power.

A standard visual-inertial filtering method requires a state vector involving states of both the vehicle and the landing pad (e.g., their positions and velocities). When visual data is not available, state estimation for the UAV is provided by the 24-state EKF implemented in the Pixhawk flight controller stack. When an image is available, the original 24-dimension state vector would be augmented to include the landing pad's states. This approach would require a large number of modifications to the original flight controller EKF codebase shown in Figure 2-5. Alternatively, a less accurate but more efficient approach taken herein is adding a second Kalman filter for relative position and velocity estimations of the landing pad while leaving the state estimates for the UAV from the original 24-state EKF filter unchanged. State estimations from the 24-state EKF can be used as inputs to the second Kalman filter, while visual estimation results from the previous section will be used as measurement updates (Figure 2-6).

The second Kalman filter is established as follows. As the dynamics of the UAV are loosely coupled in the x_P, y_P, and z_P directions in the *Ground* frame, they are modeled independently during the precision landing process. In the z_P direction, a standard landing maneuver is commanded. On the horizontal plane, two discrete Kalman filters are used independently: one in the x_P (North) direction and another in the y_P (East) direction. Without loss of generality, the Kalman filter in the x_P direction is illustrated. The states of the Kalman filter are the relative position and relative velocity of the landing pad with respect to the UAV, $s = [x^{rel}\ v^{rel}]^T$. The next state s_{k+1} is propagated from the currents state s_k using the following motion model:

$$\begin{aligned} s_{k+1} = \begin{bmatrix} x_{k+1}^{rel} \\ v_{k+1}^{rel} \end{bmatrix} &= \begin{bmatrix} 1 & \delta t \\ 0 & 1 \end{bmatrix} \begin{bmatrix} x_k^{rel} \\ v_k^{rel} \end{bmatrix} + \begin{bmatrix} 0 \\ \delta v_k^{rel} \end{bmatrix} + \begin{bmatrix} 0 \\ \delta v_{noise}{}_k^{rel} \end{bmatrix} \\ &\triangleq F_k s_k + G_k u_k + q_k. \end{aligned} \tag{2-7}$$

The Kalman filter assumes a constant relative speed in δt, which is reasonable because the filter is updated at 400 Hz. The controlled input $u = [0\ \delta v^{rel}]^T$ is the negative of the UAV's velocity change over the timestep δt . The process noise $q_k = [0\ \delta v_{noise}{}_k^{rel}]^T \sim N(0, Q_k)$ is set to be the estimated accelerometer noise times δt. Both δv^{rel} and $\delta v_{noise}{}^{rel}$ comes directly from the original 24-state EKF. Relative distance is measured and updated when visual data arrives. The measurement model is simply:

$$m_k = x_{meas}{}_k^{rel} = [1 \quad 0] \begin{bmatrix} x_k^{rel} \\ v_k^{rel} \end{bmatrix} + \delta m_{noise}{}_k^{rel} \triangleq H_k s_k + r_k, \tag{2-8}$$

where m_k comes from the relative position estimates described in the previous section. The measurement noise $r_k = \delta m_{noise}{}_k^{rel} \sim N(0, R_k)$ is assigned to be 2% of the UAV's distance to landing point. The Kalman filter is solved with the following prediction and update steps.

$$\begin{aligned} \text{Prediction:} \quad \hat{s}_{k+1} &= F_k s_k + G_k u_k, \\ \hat{P}_{k+1} &= F_k P_k F_k^T + Q_k; \end{aligned} \tag{2-9}$$

$$\begin{aligned}\text{Update:}\quad K_{k+1} &= \hat{P}_{k+1}H_{k+1}^{T}[H_k\hat{P}_{k+1}H_{k+1}^{T} + R_{k+1}]^{-1},\\ \gamma_{k+1} &= m_{k+1} - H_{k+1}\hat{x}_{k+1},\\ s_{k+1} &= \hat{s}_{k+1} + K_{k+1}\gamma_{k+1},\\ P_{k+1} &= (I - K_{k+1}H_{k+1})\hat{P}_{k+1}(I - K_{k+1}H_{k+1})^{T}\\ &\quad + K_{k+1}R_{k+1}K_{k+1}^{T}.\end{aligned} \tag{2-10}$$

The Kalman filter predicts the state mean, $\hat{s}_{k+1}$, and the state covariance matrix, $\hat{P}_{k+1}$, before updating the state mean, s_{k+1}, and state covariance matrix, P_{k+1}, with the Kalman gain, K_{k+1}, and innovation, γ_{k+1}.

The discrete Kalman filter is run on the Pixhawk flight controller since the real-time operating system provides a precise time base. The use of a Kalman filter allows compensation for bad visual localization data or even the loss of it. Erroneous and inaccurate state estimates are detected based on the normalized innovations squared (NIS) metric (Bar-Shalom, Li, and Kirubarajan 2004). The NIS check for Kalman Filters is based on the assumption that under nominal conditions, the normalized innovations will have unit variance. If NIS exceeds a predefined threshold, the measurement is likely to be imprecise or erroneous and thus cannot be used for the update of the filter states. In cases when a visual update if unavailable, for example, if the camera fails to detect the landing point in a blurry image, the filter will only predict for this iteration and compensates in the next update step for the then longer time interval. This allows the system to recover from several dropped camera frames.

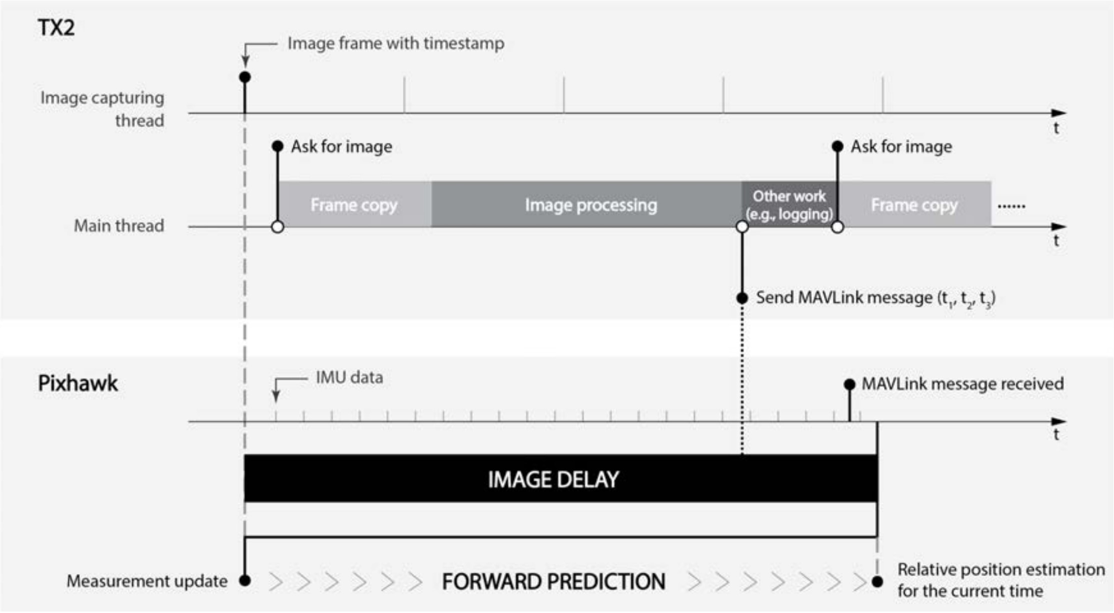

Figure 2-13. Diagram showing visual-inertial synchronization. The total image delay is the lapse of time from the camera shutter time to the moment the Pixhawk executes a measurement update. Kalman filter is run on a delayed time horizon on the Pixhawk. Results from the Kalman filter are further predicted forward to produce state estimations for the current time utilizing an IMU buffer.

2.3.3.3 Visual-Inertial Synchronization

Conducting image capture and processing as close to real-time as possible is critical for a healthy Kalman filter. High latency could result in incorrect position estimations. A seemingly simple frame polling command from the TX2 to the camera introduces latency because polling involves image processing in the camera, USB transfer of the image, and image decoding by the TX2. To reduce latency present in the polling process, an image capture background thread is adopted by the TX2 that continually polls the camera and labels each resulting frame with a timestamp. Image processing is carried out in the main thread with landing point estimations transferred to the flight controller via the MAVLink protocol when available. Because of the latency present in the camera image pipeline, an observation of the landing pad is received by the filter framework with a delay. To synchronize inertial and visual data, a buffer of IMU measurements is maintained since the IMU data is updated faster (400 Hz) than the image measurements (about 30 Hz). Once the Pixhawk receives a visual position estimate, it performs an update step of the Kalman filter on the delayed time horizon, and then predict forward to the current time using the buffered IMU data. Figure 2-13 illustrates the data fusion process.

2.4 Experiments and Results

Two different sets of experiments were designed to quantitatively assess the proposed UAV-based vision system for precision placement of wireless sensors on structures. The first round of experiments focused on testing each individual system component such as position estimation of the UAV relative to the landing pattern and the control method used for precision landing of the UAV. These experiments were conducted using the 3DR X8 UAV mainly due to its sturdy frame design (allowing for possible crashes during experimental validation) and relatively long flight times (15 minutes with a 1 kg payload). The second round of experiments were intended to validate the concept of deploying sensors on a structure in a modular fashion. Two UAVs carrying cameras and wireless sensors with accelerometers were used to perform modal analysis of a beam structure. The case study featured fully autonomous operations of two QAV210 UAVs carrying a Martlet wireless sensor node that is programmed to safely land on a simply supported beam with a restricted surface area. The two UAVs are programmed to move the sensors so as to accurately identify the beam mode shape.

Field experiments were performed in M-Air, a netted outdoor flying lab (22.4×36.6×15.2 m^3) designed for UAV research located on the campus of the University of Michigan. A Qualisys motion capture system is permanently integrated into M-Air and includes 30 cameras installed around the facility to provide accurate (mm-level) tracking of object motion. Retroreflective passive markers were mounted on the objects of interest, in this case, this study's UAV and landing pads (Figure 2-2(a)), for tracking purposes. The cameras' threshold was adjusted so that only the bright reflective markers were captured. UAV and landing pad positioning data were reported by the Qualisys IR system in real-time at 60 Hz and were used as ground truth for the validation studies.

2.4.1 UAV System Component Testing

For testing and validation purposes, the landing pattern was designed with four AprilTags (Figure 2-10(b)) with side lengths of 22.4 cm, 11.2 cm, 5.6 cm, and 2.8 cm. The largest AprilTag could be reliably detected from as high as 12 m from the air. The smallest ApilTag fits into the X8 camera's FoV even when the UAV sits on the ground over the landing spot (there is a 9.2 cm distance between the camera and the ground).

2.4.1.1 SolvePnP Validation

First, the performance levels of relative position estimation method proposed in Section 2.3.3.1 were evaluated. Two types of test flights were performed to quantify the performance of the solvePnP algorithm for estimating the relative position of the landing point, M, with respect to the camera lens of the UAV (i.e., M^{Camera}). In the first round of test flights, the UAV was kept in a relatively close position above the AprilTag landing pattern with the UAV continuously estimating its position relative to the landing point, M. The Qualisys IR motion capture system was used to determine the relative position of the UAV with respect the landing pattern as ground truth. The second round of testing centered on how distance affects the estimation accuracy of the embedded algorithm. In these tests, the UAV took off from the landing pad and rose up to about 12 m.

Test results for two of the flights are shown in Figure 2-14. Estimations of M^{Camera} (t_1, t_2, and t_3 from solvePnP) are shown in red plus signs and ground truth measurements from the motion capture system are shown in solid blue lines. Figure 2-14(a)-(c) shows results of a flight where the UAV was flown relatively close to the landing pattern at a height of roughly about 1.4 m, while Figure 2-14(d)-(f) shows another flight where the UAV was slowly flown away from the landing pattern getting to a height of more than 12 m. In both test flights, the solvePnP algorithm is able to provide estimations that follow the ground truth tightly in all three directions, which demonstrates the accuracy of the algorithm. Root mean square error (RMSE) for the estimations are shown in Table 2-1. For the first test flight, RMSEs in all three directions are well under 3 cm, which indicates the ability for the UAV to precisely land.

The second test flight shows that the landing pattern can be detected by the camera from as far away as 12 m. However, as the distance between the camera and landing point (i.e., $\left\|\overrightarrow{OM}\right\|$) grows larger, the estimation accuracy decreases. The accuracy of the position estimation algorithm was assessed as a function of the relative distance $\left\|\overrightarrow{OM}\right\|$. Figure 2-15 presents the estimation errors with respect to the relative distance in all three directions. Also shown in the figure is the number of AprilTags detected and used to compute the relative distances indicated by blue stars. As shown, only one AprilTag is detected when the vehicle is far from the pattern ($\left\|\overrightarrow{OM}\right\| > 6.0$ m) and close to the pattern ($\left\|\overrightarrow{OM}\right\| < 0.6$

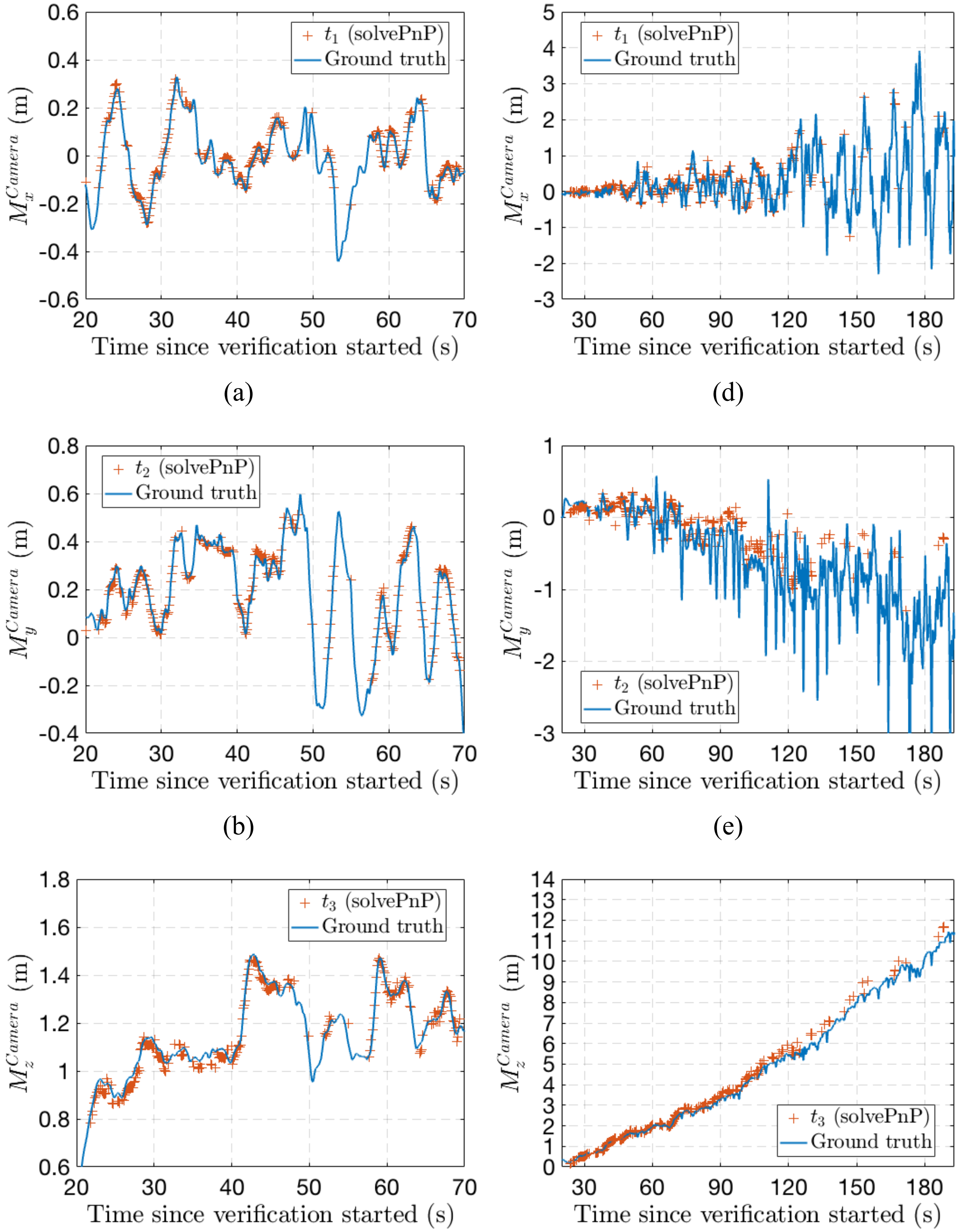

Figure 2-14. Estimation of M^{Camera}: (a)-(c) UAV flown relatively close to landing pattern at a distance roughly about 1.4 m; (d)-(f) UAV took off from the landing point and slowly flown away.

Table 2-1. RMSEs of the solvePnP position estimation algorithm (Units are in meters).

	$M_x^{Camera}\ (t_1)$	$M_y^{Camera}\ (t_2)$	$M_z^{Camera}\ (t_3)$
1st Flight (Figure 2-14(a)-(c))	0.0107	0.0165	0.0269
2nd Flight (Figure 2-14(d)-(f))	0.0637	0.1282	0.2008

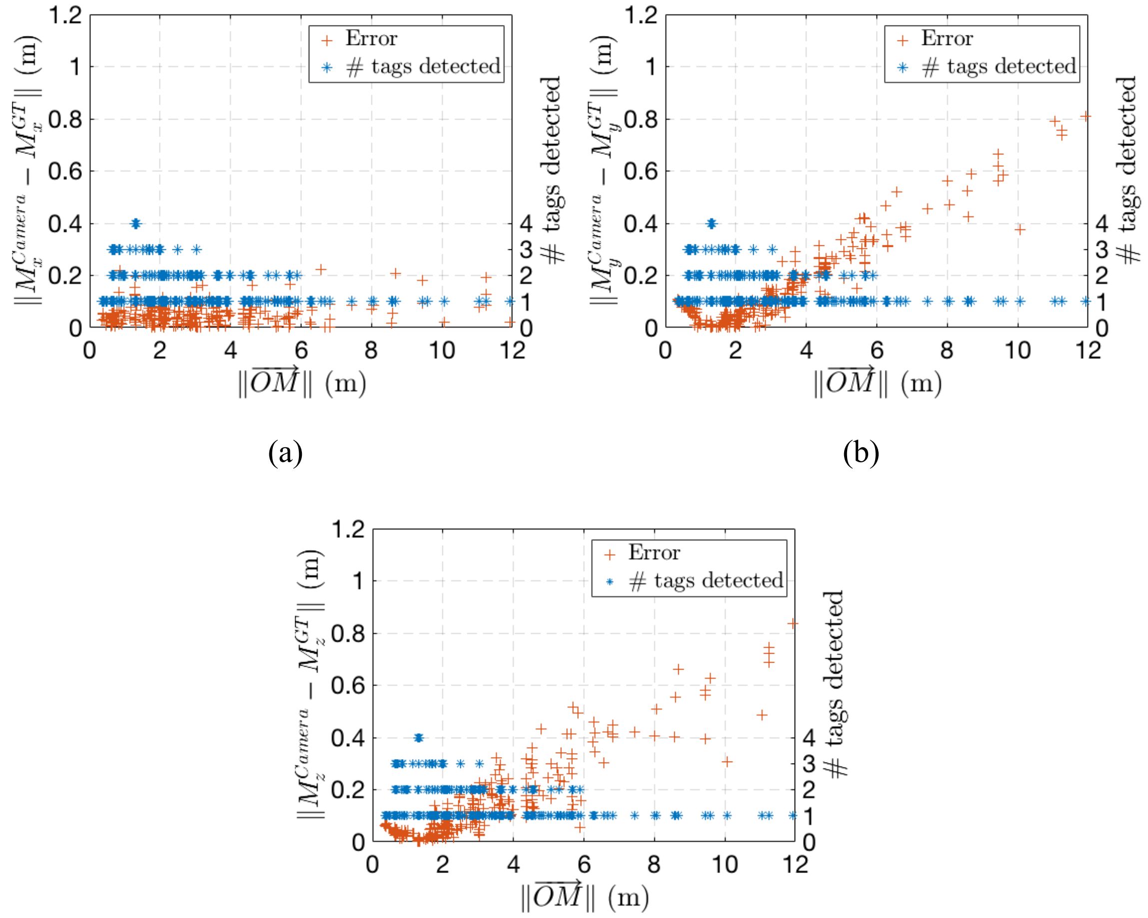

(a)

(b)

(c)

Figure 2-15. Estimation errors with respect to the relative distance between the UAV and the landing pattern. Overlayed on the figure is the number of AprilTags detected and used to compute relative distances.

m), which proves the necessity of the inclusion of all four AprilTags in the landing pattern. Figure 2-15(b) and Figure 2-15(c) shows a clear correlation between the number of detected tags and the estimation accuracy. When all four AprilTags in the pattern are detected ($\|\overrightarrow{OM}\| \approx 1.6$ m), the estimation error is the smallest (close to zero). Another interesting finding is that comparing Figure 2-15(a) and Figure 2-15(b), when $\|\overrightarrow{OM}\|$ is relatively large, the estimation errors in the *Camera*'s x_O direction are smaller than those in the y_O direction. This is possibly due to the landing pattern's larger overall length in the x_O direction (thus more accurate pixel coordinates of the feature points and better distance estimation).

2.4.1.2 Image Transmission Delays

It is important for attitude data from the Pixhawk flight controller and the camera-based estimation of the UAV position relative the landing pattern to be synchronized. The UAV was flown over a landing pattern and the time delay between image capture (i.e., opening of the camera shutter) and transmission of extracted UAV position information (i.e., t_1, t_2, and t_3) from the TX2 to the Pixhawk over the MAVLink interface was calculated. This delay is shown in Figure 2-16 as the solid red curve with cross markers. The delay, which is 31.5 ms on average, is mostly due to the time needed to load the image from the camera and process the image. The processing time for the TX2 to process the image of the landing pattern is shown as the green curve with plus markers in Figure 2-16. The computation time is on average 13.9 ms and less variable. Also, this computation time is not affected by the number of AprilTags (indicated by blue star markers in Figure 2-16) used in calculation of the UAV relative position. There is a high level of variability in the total delay (red curve with cross markers) not seen in the computation time (green curve with plus markers) of the UAV position estimation. This variability is associated with

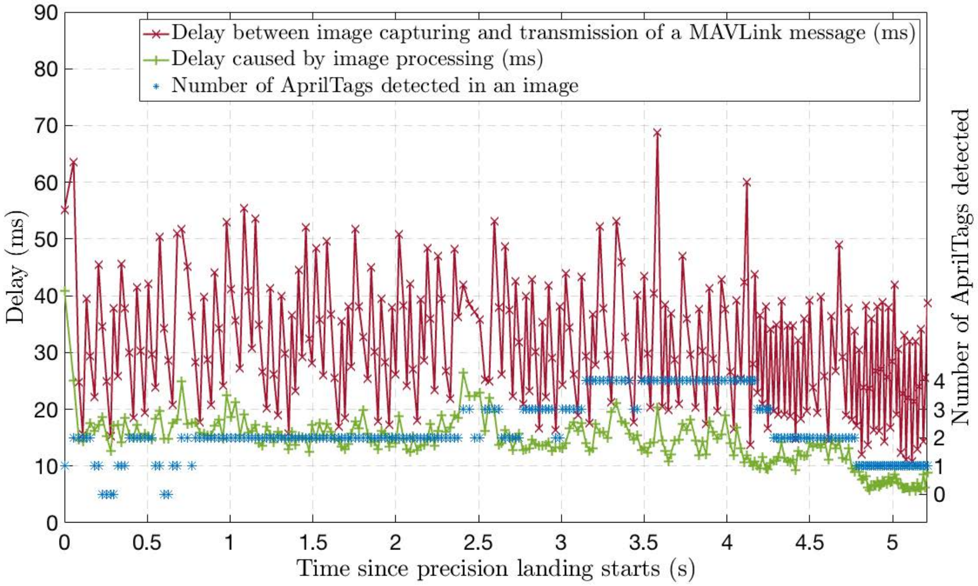

Figure 2-16. Image data transmission delay: the total delay equals the delay from image capturing to the transmission of a MAVLink message by the TX2 (red curve, on average 31.5 ms) plus the actual transmission time of the message from the TX2 to the Pixhawk (about 17.8 ms, not shown in the figure). IMU buffer size is set to 20 to compensate for the delayed visual measurement.

stochastic delays of the TX2 operating system (which is not a real-time operating system) when servicing the MAVLink interface and executing image capturing in the background.

Once the relative position estimate is determined, the TX2 will transmit its relative position to the Pixhawk controller. The MAVLink interface operates at a baud rate of 921,600 and requires about 17.8 ms to transmit its data. If average total delay of the TX2 getting an image from the camera, calculating the relative UAV position using the image, and sending out the relative position is 31.5±11.1 ms, then the total delay for the Pixhawk controller is 49.3±11.1 ms. With the Pixhawk generating attitude data at 400 Hz and an average delay of image data at 49.3 ms, then an IMU buffer (discussed in Section 2.3.3.3) is programmed to have 20 or more data points.

2.4.1.3 Precision Landing

Next, the UAV's capability of precision landing was tested thoroughly. Figure 2-17 shows a sequence of snapshots from the onboard webcam during a typical precision landing. Detected AprilTags are highlighted in each image with the corners and centers of each detected tag marked by orange dots. Based on these feature points, pixel coordinates for the fixed landing point M are computed and marked with a red cross. M^{Camera} is further extracted using the direct method and shown on top of each frame (t_1, t_2, t_3 in green). As shown in the sequence of snapshots, only the largest AprilTag among the four is detectable at the very beginning of the landing process when the UAV is at about 4.43 m above the pattern (Figure 2-17(a)). Smaller AprilTags gradually come into the camera's FoV as the UAV descends. At the height of about 1.14 m, all four AprilTags are successfully detected (Figure 2-17(c)). After that, larger AprilTags slowly leave the camera's FoV and only the smaller AprilTags contribute to visual estimations and provide guidance to the landing vehicle. Figure 2-17(f) shows the camera view when the vehicle lands. Relative horizontal distance from the camera lens to the desired landing point at this final stage is only about 0.02 m.

Figure 2-18 illustrates state estimation results from the discrete Kalman filter during one typical landing. The Kalman filter shows good performance along the whole landing trajectory. Relative distance estimations (red curves) in both the Ground frame's x_P (North) and y_P (East) directions follow the ground truth (blue curves) well. Green vertical lines indicate the moments when a visual measurement is received by the Pixhawk and used to update the Kalman filter. When visual measurements are not available (e.g., during

(a) (b)

(c) (d)

(e) (f)

Figure 2-17. A sequence of images captured by the webcam during precision landing (computed landing point M and visual estimations from the direct method are presented in each image), roughly: (a) 4.43 m; (b) 3.46 m; (c): 1.14 m; (d) 0.73 m; (e) 0.61 m; (f) 0.10 m height.

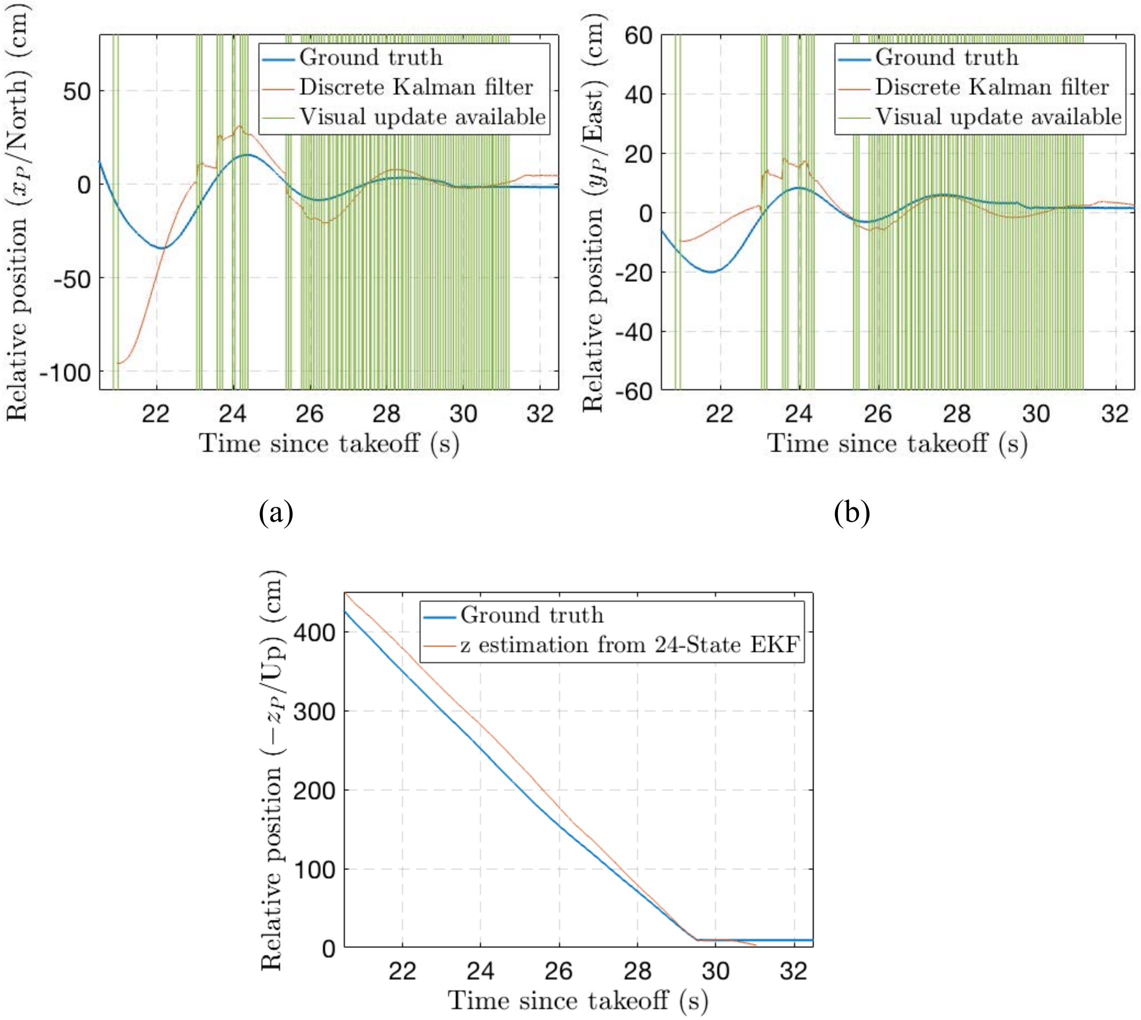

(a)

(b)

(c)

Figure 2-18. Relative distance estimations in the *Ground* coordinate system during a typical precision landing: (a) x_P (north); (b) y_P (east); (c) $-z_P$ (up).

21-23 s in Figure 2-18(a) and Figure 2-18(b), the landing pattern leaves the camera's FoV due to the UAV's aggressive maneuvers to correct its position), the Kalman filter is still able to provide estimations by only executing the prediction step.

A set of landings are performed 25 times to assess the repeatability of the landing and to quantify landing precision. Figure 2-19 illustrates these 25 landing trajectories and their associated landing locations with respect to the desired landing point. The trajectory

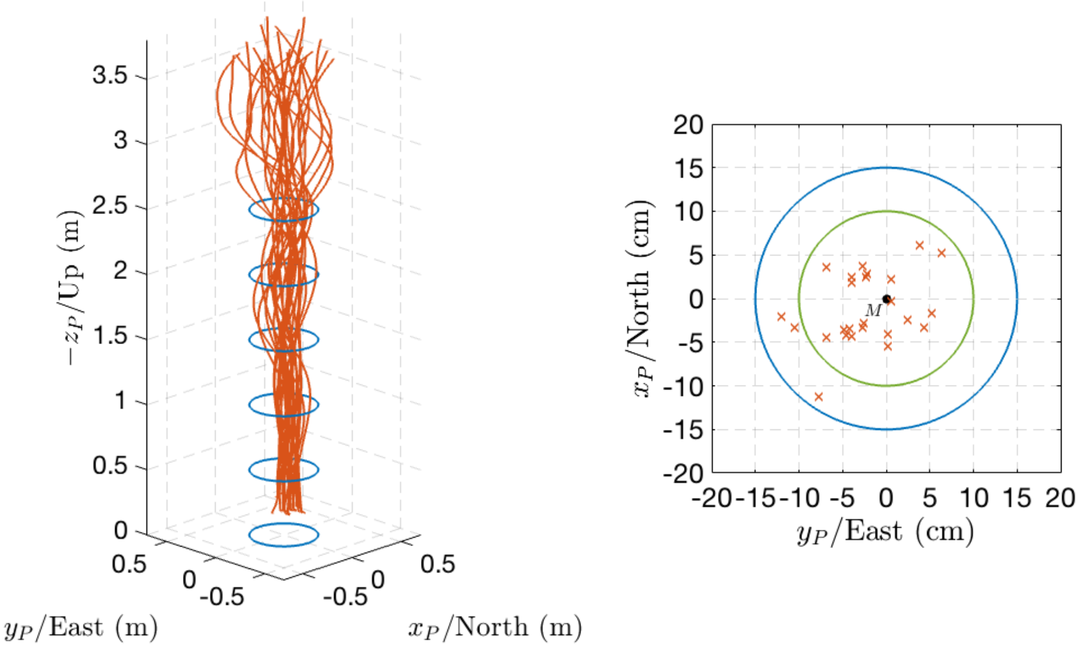

(a) (b)

Figure 2-19. 25 landing trajectories and their associated landing spots: (a) landing trajectories captured by Qualisys IR system in red with blue circles indicating a deviation of 25 cm from the desired landing point in the horizontal plane; (b) landing accuracy with landing positions indicated by red crosses.

data shown in Figure 2-19(a) are recorded by the motion capture system. Below a height of about 2.5 m, all of the landing trajectories are within a deviation of 25 cm from the desired landing point in the horizontal plane. All 25 landing maneuvers are able to land the vehicle on the pad within 15 cm from the desired landing point, among which 22 are in a circle with a radius of 10 cm as shown in Figure 2-19(b).

2.4.2 Case Study: Autonomous Modal Analysis of a Structural Beam

The objectives of the second case study are to evaluate the feasibility of UAVs to: (1) autonomously place wireless sensor nodes on a simply supported beam structure; (2) localize the sensors on the structure; (3) collect ambient acceleration data from the structure; and (4) perform modal analysis of the beam. Towards this end, experiments were performed in M-Air using a simply support aluminum beam (182.5 cm long, 30.5 cm wide, and 0.6 cm thick). Three different sets of landing patterns are attached on the beam along its longitudinal length representing target sensor locations equidistant from one another. Two QAV210 UAVs were adopted to each carry a sensor enclosure containing a Martlet sensing node and an accelerometer sensor. The sensor enclosure is firmly mounted on the bottom of the UAV and moves from location to location on the beam surface as the UAV takes off and lands. Attached on top of each UAV is another distinct AprilTag used for localization of the UAV-sensor pair on the beam using tailored visual algorithms. Figure 2-20 shows the setup of the case study.

The experiment is performed in several steps. First, *UAV 1* takes off, searches in the air for the landing pattern of *sensor location 1*, and delivers the sensing node onto the beam by landing on the pattern. Once *UAV 1* lands, *UAV 2* takes off, flies above the beam and *UAV 1*, and delivers its wireless sensing node to *sensor location 2*. While *UAV 2* is in the air, it is also able to register the position of the landed *UAV 1* using camera data of the AprilTag on top of *UAV 1*. This allows the precise location of *UAV 1* on the beam to be determined. Soon after the landing of *UAV 2*, a human operator strikes the beam with a modal hammer while both UAVs command their wireless sensing nodes to collect and transmit acceleration data to a ground PC. The hammer impulse is equivalent to white noise ambient excitation expected in a real, operational structure. *UAV 1* then takes off again and moves from *sensor location 1* to *sensor location 3*. Position registration of *UAV 2* is accomplished during this process using images of its overhead AprilTag captured by *UAV*

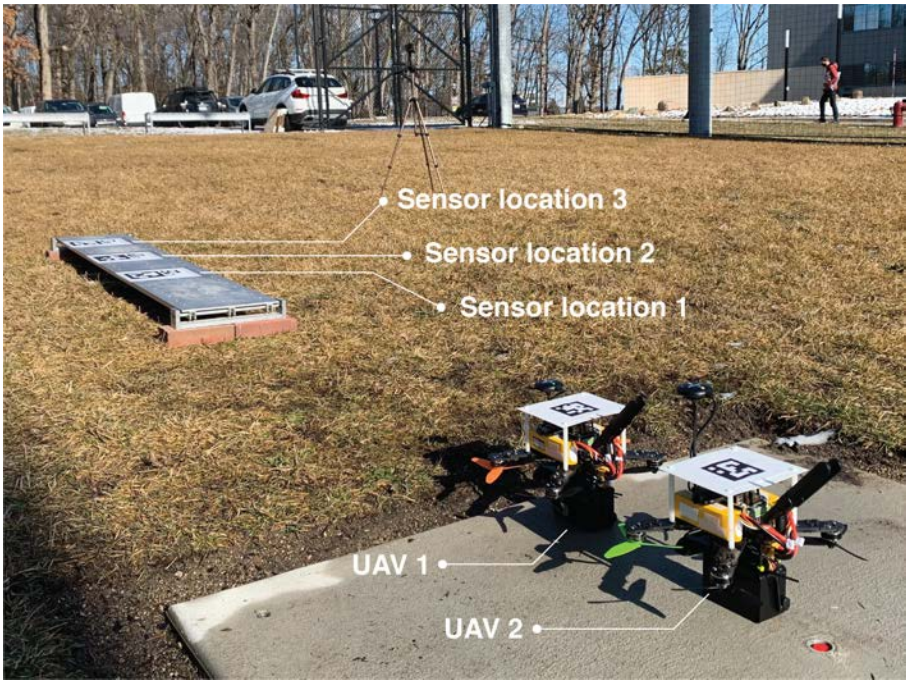

(a)

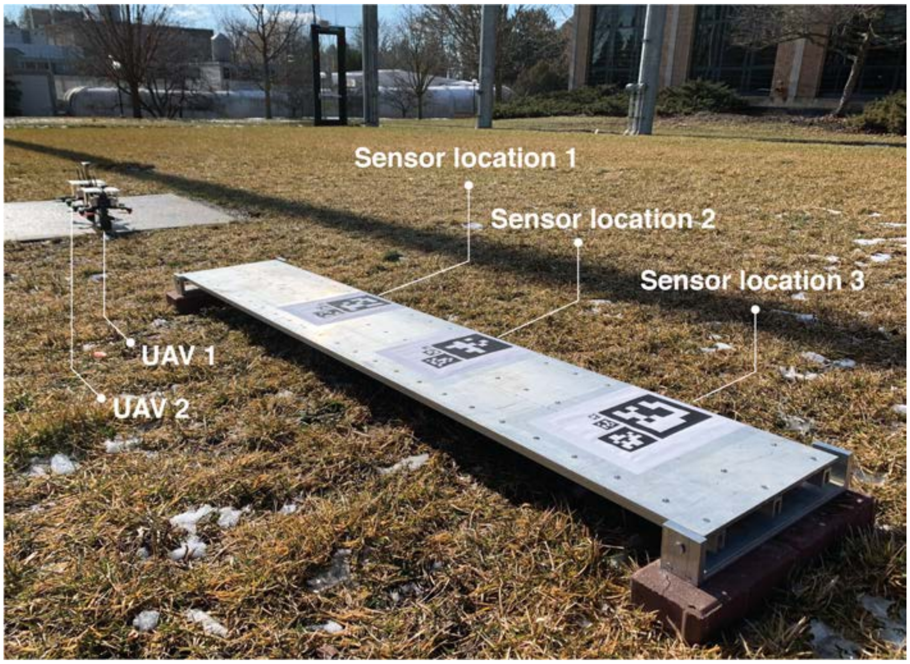

(b)

Figure 2-20. Experiment setup of the case study: (a) two QAV210s sit on the ground, ready to deliver wireless sensors measuring structural acceleration; (b) landing patterns on beam where acceleration measurements are desired.

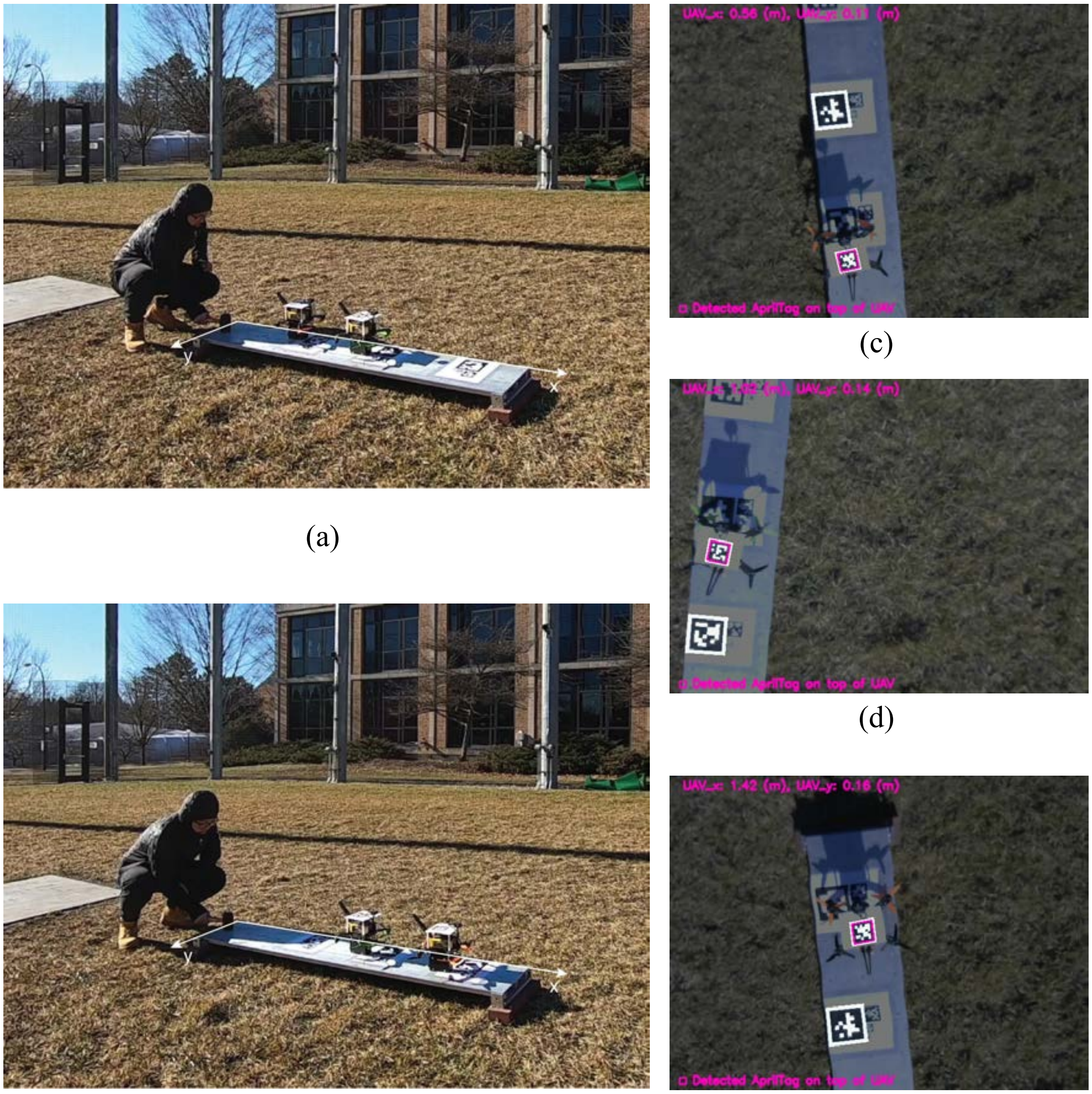

(a) (b) (c) (d) (e)

Figure 2-21. Case study procedures: (a)-(b) human operator striking the beam with two QAV210s landing on it; (c)-(e) spatial registration of UAV landed on the beam with (x, y) coordinates expressed in the frame shown in (a)-(b).

1. Upon landing of *UAV 1*, the human operator excites the beam again and data collected by the accelerometers now at different locations on the beam are transmitted back to the ground PC. Lastly *UAV 2* is commanded to fly over *UAV 1* and leave the beam in order to register *UAV 1*'s last position. At the final stage of the experiment, modal analysis of the

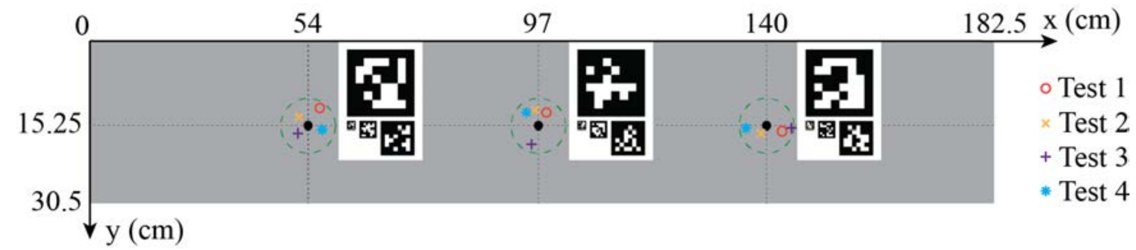

Figure 2-22. Spatial registration of wireless accelerometers.

beam is performed using the acceleration response data collected at the three locations along the beam length. The frequency domain decomposition (FDD) (Brincker, Zhang, and Andersen 2000) method is used to assemble two-point mode shapes for each sensor configuration; overlap in the mode shapes allow them to be stitched together to from global modes of the beam structure. The experiment is fully autonomous with the human operator only intervening to impulse the beam structure which would not be necessary in applications in real civil engineering structures with ambient vibrations.

As shown in Figure 2-21(a)-(b), the two QAV210s successfully positioned the Martlet wireless sensing nodes on the beam after carefully following each operation in the FSM. Position registration of the UAV is accomplished by detecting both its overhead AprilTag and at least one more AprilTag on the beam at the same time (See Appendix A.2 for details). Computed UAV positions are shown in the top-left corner of the snapshots (Figure 2-21(c)-(e)). Estimation error is within 2 cm when comparing to ground truth of the UAV positions using a measuring tape. Figure 2-22 illustrates the locations of the landed UAVs after repeating the test four times. All landing locations are within 5 cm (shown with dashed circle with 5 cm radius) from their desired locations.

After the human operator strikes the beam with a modal hammer, the wireless sensing nodes collect acceleration data at 100 Hz as shown in Figure 2-23(a) for the first

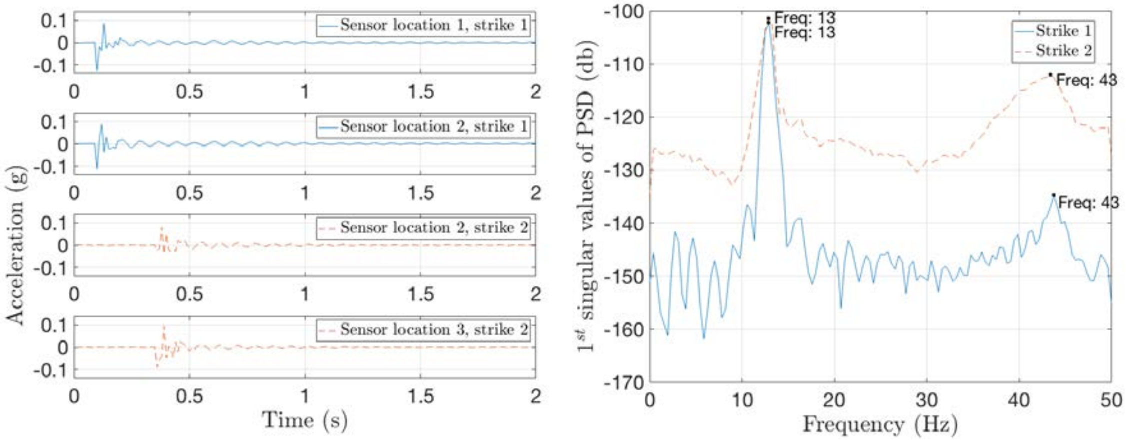

(a)

(b)

Figure 2-23. Modal analysis of the simply supported beam: (a) raw acceleration data collected by the Martlet sensing node; (b) 1st singular values of the PSD matrices.

test. The FDD method is then used to extract the natural frequencies and mode shapes of the beam from the collected time history data. Figure 2-23(b) shows the singular values of the power spectral density (PSD) function matrix for the first and second sensor locations of the first test. As it appears, the 1st and 2nd natural frequencies of the beam are at 13 Hz and 43 Hz.

The theoretical natural frequencies and mode shapes of a simply supported Euler-Bernoulli beam are computed as (See Appendix B for details):

$$f_n = \frac{n^2\pi}{2}\sqrt{\frac{EI}{\rho A L^4}}, \phi_n(x) = C\sin\frac{n\pi}{L}x\,, n = 1, 2, \ldots, \tag{2-11}$$

where E is the Young's modulus of the beam, I is the area moment of inertia of the beam's cross section, ρ is the mass density of the beam, A is the cross-section area of the beam, L is the length of the beam, x is the distance along the length of the beam from 0 to L, and C is any nonzero constant. Using the material and geometric parameters of the aluminum

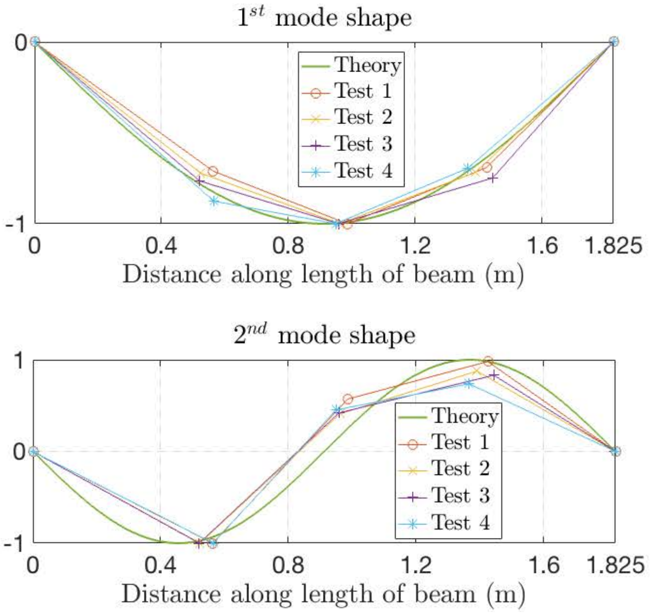

Figure 2-24. 1st and 2nd mode shapes of the beam.

beam ($E = 6.89 \times 10^{10}$ N/m^2, $I = 4.6785 \times 10^{-8}$ m^4, $\rho = 2.7 \times 10^{3}$ Kg/m^3, $A = 2.31 \times 10^{-3}$ m^2, $L = 1.825$ m). The theoretical 1st and 2nd natural frequencies are determined to be 10.7 Hz and 42.6 Hz, which are in strong agreement to the experimental results.

To get the complete mode shape of beam (Figure 2-24), mode shapes generated from the two strikes are stitched together using the common point sensor location 2. For the four different executions of the experiment, there is strong agreement between the mode shapes as well as the theoretical mode shapes.

2.5 Conclusion

The study presented herein explores the development of UAVs as an intelligent agent capable of deploying wireless sensor nodes autonomously for structural monitoring applications. The proposed UAV system can autonomously detect landing patterns, perform precision landing maneuvers, install accelerometers onto structures, and collect structural vibration data using only onboard sensors and computing units. Transition between different mission like pattern searching and precision landing is accomplished using a reliable finite-state machine embedded in the TX2 onboard computer of the UAVs. Precision positioning of a UAV in the outdoor environment is made possible by the integration of a customized fiducial marker pattern, a robust vision-IMU coupled estimation method, and a discrete Kalman filter. The landing pattern is designed to be universal for general use. The study reveals excellent landing and sensor positioning accuracy of less than 10 cm. The study features fully autonomous operations of UAVs and proves the feasibility of using UAVs as a viable sensor resource delivery and reconfiguration platform in a modal analysis application. Using two wireless sensors, the system is shown to be effective at precisely landing on a simply supported beam to within 5 cm of the desired location with accurate mode shapes determined.

Chapter 3 Integration of Wireless Geophones and Impulsive Source Generation with a UAV for Surface Wave Monitoring

3.1 Introduction

Seismic surveying is a technique used to determine the composition and structure of the subterranean areas based upon the analysis of how surface-generated seismic waves travel through different layers underground (Onajite 2014). Fundamentally, a seismic wave is generated with an energy source (e.g., explosives, vibrators, impact hammer), travels into the earth, and then picked up by a line or grid of sensors (e.g., geophones, hydrophones) as it bounces off subsurface formations such as layers, subsurface structures, and rock formations, just to name a few. Traditionally, the collection of seismic data is a time and labor consuming process requiring detailed planning by engineers well ahead of sensor deployment. Treacherous terrain and harsh weather pose serious challenges for seismic data acquisition (Selley and Sonnenberg 2015). Aside from these external environmental factors, the equipment used for seismic data collection is typically cumbersome and expensive which complicates seismic surveys conducted in the field. The method for near-surface site characterization is commonly referred to as the surface wave method (SWM), whose primary goal is to retrieve a 1D (depth) or 2D (depth and surface location) shear wave velocity (V_S) model of a site (Foti et al. 2017). Among various SWMs developed over the past century (Pelekis and Athanasopoulos 2011), two techniques—the spectral analysis of surface waves (SASW) method (Nazarian 1984; Stokoe et al. 1994) and the multichannel analysis of surface waves (MASW) method (Park, Miller, and Xia 1999)—have found widespread uses because of their relatively simple in-field operation and data processing routine. The SASW method requires the use of two geophones and a spectral analyzer to study the frequency and phase differences of the recorded signal pairs. While in the MASW method, a spread of geophones (typically 12 or more) is employed to collect data at multiple locations at the same time. Both methods estimate the dispersion properties of a site first and then undergo an inversion process to construct the V_S profile of the site.

3.1.1 Wireless Sensing for Seismic Surveying

The majority of the current seismic acquisition systems are cable-based. Modern-day seismic acquisition systems adopting the SASW or MASW method normally require the installation of long runs of coaxial cable to connect multiple external geophone sensors to an acquisition unit called seismograph that can digitize, amplify, filter, and synchronize the acquired analog signals. Additional external cables and connectors are extended from the geophones to hook them up to the main data acquisition unit. Most systems also require a long ethernet cable to subsequently transfer the digitized seismic data to a field PC for data storage and processing. The extensive use of cables and connectors introduces substantial weight and cost to field instrumentation, limiting survey flexibility and reliability. The excess weight introduced by cables may account for up to 20% of the operational cost of a typical land survey (Savazzi and Spagnolini 2008). This is especially true with high-density acquisition systems. A typical 4000-channel crew with a station spacing of 110 ft entails a strikingly 184-mile-long cable and more than 9300 connectors (Freed 2008). Another challenge associated with cable-based systems is the operating and maintenance costs pertaining to the cables and connectors. Surveyors oftentimes spend the better part of a day laying out bulky cables and troubleshooting connection problems. Worse still, these field components are vulnerable to damage from both natural and man-made sources, demanding recurrent maintenance and repair. Typically, a set of cables, connectors, and sensors can be used for five years (at best) before they must be replaced (Freed 2008). The final significant challenge linked to conventional seismic surveys is their heavy reliance on human labor to operate. Current seismic operations require field personnel manually placing geophones at different offsets away from an impulsive or vibratory source (e.g., in MASW, a sledgehammer is manually operated to deliver a seismic impulsive source in a repetitive fashion). As a result, cable-free acquisition systems embracing wireless technologies represent the future.

Recent technological innovations have made cableless seismic surveying solutions practical. Microprocessors and memory continue to decline in cost (MacK 2011), high-precision analog-to-digital converters (ADCs) continue to offer higher resolutions and higher sampling rates, advances in wireless network technology enable wireless (cable-free) communications. These trends in the embedded systems field have spurred innovation in high performing wireless sensors used in a variety of structural (Noel et al. 2017) and geotechnical (Muduli, Mishra, and Jana 2018) monitoring applications. By eliminating cables, wireless seismic monitoring systems have the potential to be lighter, more cost-effective, and offer easier access to difficult-to-reach or environmentally sensitive areas where deployment of wired systems is restricted. The proclivity towards wireless data collection systems has spurred many researchers (Dai et al. 2015; Martinez et al. 2017; Attia et al. 2020) and companies (Crice 2011; Mougenot 2012; Dean, Tulett, and Barnwell

2018) to develop and invest in wireless seismic acquisition approaches. As previously discussed in the first chapter, wireless sensors are essential to the development of MSN, especially those deployed by RAS platforms like UAVs. For example, Chapter 2 laid an illustrative foundation of the use of UAVs to deploy wireless sensors for structural monitoring in an MSN architecture tailored for modal analysis of structures. As this dissertation moves toward extending these accomplishments to geotechnical systems and seismic surveying, the demands to be placed on the wireless sensor increase due to the need to sense seismic waves with low amplitudes at high frequencies. Also, the high frequencies of seismic signals will demand high precision synchronization of wireless sensor clocks to ensure accurate phase information is maintained between sensing nodes.

This work proposes a completely self-contained wireless seismic sensing node comprising an SBC (for autonomous operations), a geophone sensor (to record velocity signals), a high-resolution ADC (to digitize geophone measurements), and a high-accuracy GPS module (to offer each node precise timing to a common GPS clock). Adopting a modular design, the wireless geophone node is lightweight, low-cost, and convenient to operate and maintain. The open-source software embedded in the wireless node separates it from its commercially available counterparts, whose closed-source software is impossible or hard to adapt leading to limited usages for research (most especially those using RAS platforms for sensor deployment and redeployment).

In this study, a wireless seismic sensor is developed for adoption in SASW and MASW tests. The objectives of this study are to: (1) design a wireless geophone node with the ability of capturing small-amplitude ground surface vibrations and performing interunit time synchronization; (2) quantify the performance of the wireless geophone node against a commercial seismic data acquisition system. While several wireless seismic sensors have been proposed for monitoring geo-structures as in the previously cited studies, the node proposed in this study is specifically designed to emphasize two critical features necessary to the MSN architecture: light weight and small size to be carried and deployed by a robot and open-source software to be integrated into the RAS system. This chapter presents detailed descriptions of the hardware and software architecture of the wireless geophone node. Detailed prices of all hardware components are also listed, proving the cost-effectiveness of the designed node. To illustrate the utility of the proposed wireless geophone sensor, two of the designed nodes are arranged in a SASW test topology to collect seismic waves generated by a sledgehammer. The study shows the quality of the data collected by the wireless geophone nodes comparable to a commercial wired data acquisition system. The development in this study makes advancement in the transition from cable-based seismic systems to cableless recording.

3.1.2 RAS Deployment of Seismic Source Weights

RAS platforms like UAVs can be developed to facilitate automation of in situ surveying with increased efficiency and reduced cost. While the design of a low-cost and energy-efficient cableless geophone unit is a necessary step to achieve mobility and automation, a UAV platform also needs to be developed to deploy wireless sensors and to deploy an impulsive source for seismic surveys such as SASW and MASW field tests. The UAV must be able to use vision to pick up and drop off a weight in an autonomous manner to generate surface waves during field surveying. Utilizing an UAV platform for test execution of a seismic survey is of great interest but has only been explored on a very limited basis (Greenwood, Lynch, and Zekkos 2019). UAV implementation in the geotechnical engineering domain has primarily focused on remote sensing making use of onboard sensors such as cameras and LiDARs. While UAVs as a data collection platform has revolutionized how the geometric characteristics of remote sites are documented using techniques such as surface imaging and photogrammetry (Puppala et al. 2018), its potential for subsurface characterization has not been fully realized. For instance, in a SASW or MASW seismic test, UAVs can serve as an active impact source by dropping from aloft an instrumented weight to act on the ground surface to generate seismic waves. Zekkos et al. (2014) and Greenwood et al. (2018) are two of the first to demonstrate the idea of UAV-dropped weights as an active impact source in both indoor and outdoor field tests. The UAV-dropped weight was found more advantageous than a traditional sledgehammer source due to the large amount of energy generated (Greenwood 2018). However, a major shortcoming of these field tests is the manual operation of the UAV and the need for a human-triggered payload release mechanism, limiting the automation of the method in remote sites. Additionally, for signal stacking and repeated testing at a site, a method of effectively retrieving the drop weight with the UAV needs to be developed for repeated testing using the same SASW and MASW sensor topologies.

A successful aerial grasping presents several challenges. First, a UAV mounted gripper needs to be lightweight due to restrictions on flight times associated with heavy payloads. Second, the gripper and the payload the gripper picks up may dramatically alter the flight dynamics of the UAV, requiring flexible yet robust flight controllers. For autonomous missions, additional feedback information about whether the payload is successfully picked up or not is also required. The UAV should be able to detect an unsuccessful grasp and make decisions about whether a second attempt to grab a weight is needed.

Different approaches to address these challenges exist in the literature. Thomas et al. (2013) analyzed the dynamics of a quadrotor equipped with a servomotor-driven gripper claw and designed control laws for the coupled system to achieve avian-like high-speed object retrieval. Gawel et al. (2017) proposed a novel gripper design that features an electro-permanent magnet coupled with a passively compliant mechanical structure, which could be used to pick up objects with partly ferrous surfaces. Utilizing a flock of autonomous UAVs equipped with grippers, several groups presented the autonomous assembly of small structures (Lindsey, Mellinger, and Kumar 2012; Augugliaro et al. 2014). There have also been research efforts on the design of more advanced non-linear controller tailored to stabilize UAVs equipped with multi-link dexterous manipulators (Jimenez-Cano et al. 2013; Heredia et al. 2014). However, most of the prior research published to date focuses on aerial grasping in indoor environments where an accurate motion capture localization system is used to provide reliable measurement of UAV pose. In an outdoor environment, it is difficult to estimate UAV dynamics and impose control due to environmental disturbances such as wind.

In this study, the aerial grasping problem is simplified in two ways. First, an electro-permanent magnetic gripper is integrated into the design of a UAV to pick up and drop off a steel plate (acting as a seismic source when dropped from a defined height). The magnetic gripper is attached to the bottom of the UAV without introduction of a robotic arm. The use of a multi-link arm is intentionally avoided because of its extra weight linked to the requirement of a large force and torque demands induced by the heavy weight. Another advantage of magnetic gripping is that it allows for a slightly higher tolerance on position error due to the magnetic field radiating a small distance away from the UAV. During payload pickup, the UAV will naturally encounter turbulence as it gets close to the ground, which makes the task difficult. The work addresses the challenge by separating aerial grasping into two steps: first the precision landing on top of the drop weight followed by magnetic gripping while the UAV is landed. The drop weight is featured with a unique color coupled with an AprilTag pattern. These visual attributes are able to provide continuous guidance to a UAV with a downward pointing camera throughout the precision landing process. Upon landing above the drop weight, the UAV will conduct a gripping attempt of it. A novel approach to identifying a successful grip event is implemented utilizing sound waves that define the snapping of the weight to the magnetic gripper surface.

Figure 3-1 shows the comparison of a state-of-the-practice human-deployed wired seismic sensing system and an envisioned UAV-enabled seismic monitoring system that is completely wireless and autonomous. In the envisioned application, the UAV will replace the human operator to not only deploy the sensor network and excite the sensing system, but also serve as an intelligent agent that can collect, store, and process the collected data in real-time to aid in instant decision-making such as reconfiguring the sensor network and dropping the weight from a different height to facilitate better data quality. As an indispensable component to this vision, a method of automating the payload pickup and drop-off process for the UAV is presented in this chapter. The use of a UAV as a means of deploying seismic sources is made possible through the integration of an EPM gripper that can lift and drop an instrumented weight from controlled heights. The UAV is also effective

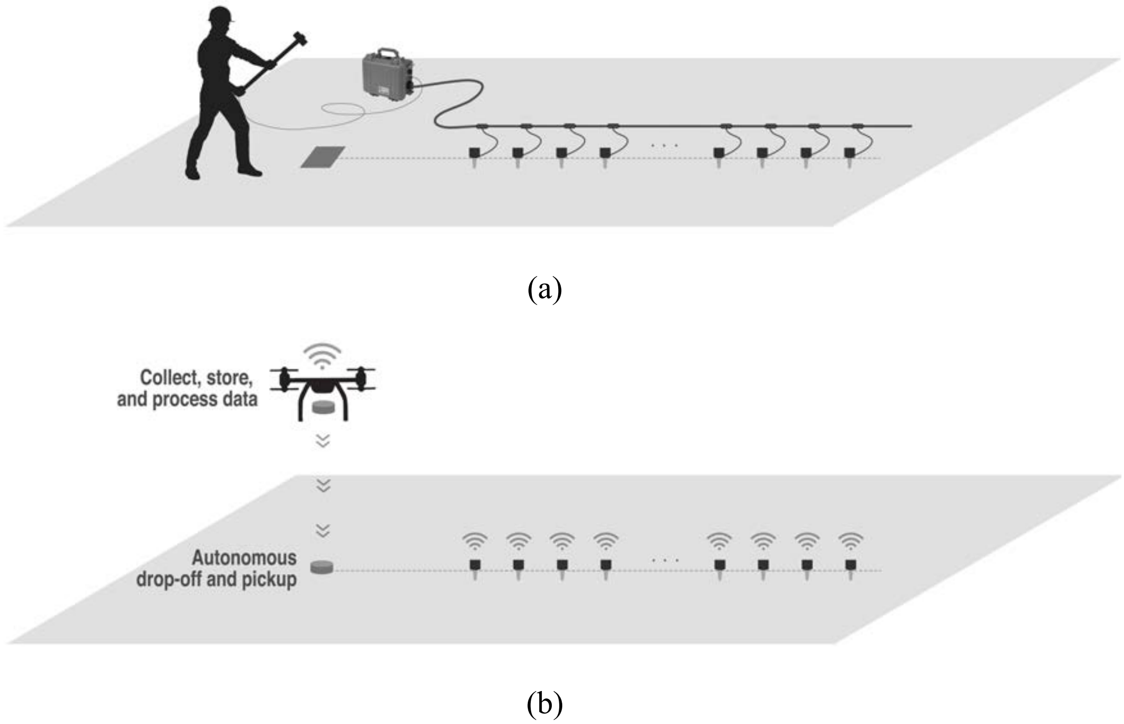

Figure 3-1. Comparison of a human-deployed wired seismic sensing system and a UAV-enabled wireless seismic monitoring system: (a) a wired sensing system with extensive uses of wires excited by a human operator manually striking a sledgehammer; (b) a wireless sensing system utilizing a UAV equipped with a robotic gripper to deploy wireless sensors and impulsive sources, command the sensor network, wirelessly collect data upon demand, and process data leading to onsite decision-making.

in autonomously tracking the location of the dropped weight and approaching it using onboard vision. The three intellectual contributions made in this study can be summarized as: (1) the integration of a robotic gripper with grasping feedbacks into the UAV system for object gripping and releasing; (2) the development of a tailored computer vision algorithm utilizing both fiducial marker patterns and color features for relative position estimation between the UAV and the drop weight; (3) the design of a fully autonomous architecture to control UAV operations in the payload pickup and drop-off application. These contributions will facilitate the development of a RAS solution for seismic surveying.

3.2 Design of the Wireless Geophone Node

The design of the wireless geophone node emphasizes ease of use and use of an open-source software architecture that can be easily modified to address particular research needs. The node is designed as a low-power and low-cost sensor node with all of its hardware components available off-the-shelf. To meet the needs of the specific application of using the node for SASW/MASW seismic monitoring, the following design requirements are specified ahead of its design (along with an explanation why):

- High frequency sampling to ensure the full range of signal bandwidths can be acquired (sampling rates as high as 1-2 KHz if not higher);
- High digital conversion resolution to collect low amplitude seismic signals with moderate to high signal-to-noise ratio (SNR);
- Be capable of synchronizing time to a GPS clock signal with sub-millisecond precision due to the need for precise phase assessment between independent nodes;
- Have a flexible wireless communication interface capable of communication to a base station and to other agents like a UAV;
- Be capable of being powered for the full duration of UAV flight using a standard battery pack (about 20-30 minutes);
- Weigh less than the payload capacity of a moderate to large UAV (e.g. X8) (less than 1 kg).

The wireless node design consists of four primary subsystems: a single-board computer, an ADC digitizer board, a GPS module for time synchronization, and a

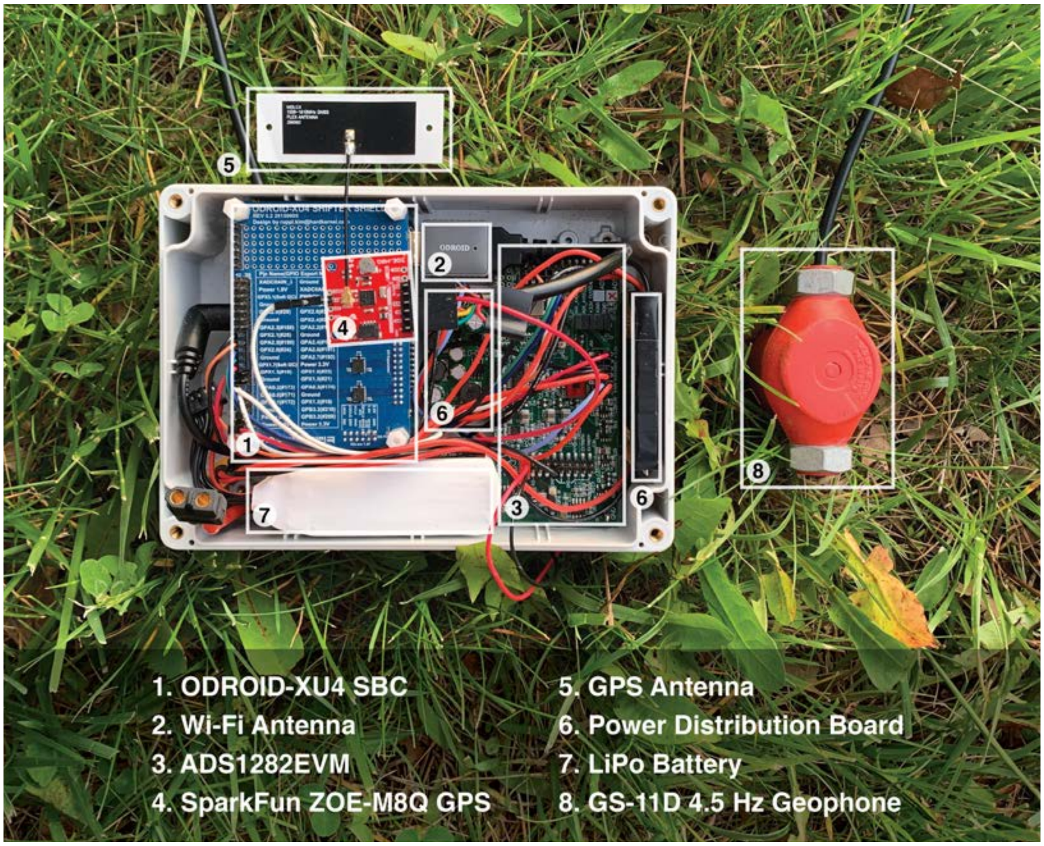

Figure 3-2. Wireless geophone node with key components highlighted.

Table 3-1. Technical specifications of the wireless geophone node.

Description	**Value**
Operating system	Interrupt-driven C++ program implemented in Linux (Ubuntu)
Memory	64GB
ADC	32-bit, 2-channel, 1000Hz sampling rate
GPS	72-channel GNSS receiver (30ns time pulse accuracy)
Wi-Fi	WLAN (2.4/5.0GHz)
Geophone	Vertical (4.5Hz)
Power supply	1000mAh 4S LiPo
Power consumption	~5W@14.8V (~340mA)
Size	170×120×50mm^3
Weight	810g with geophone, 495g without geophone

geophone sensor. Figure 3-2 shows the node components encapsulated within a sealed enclosure of limited dimension and size, and an externally connected geophone sensor. The system is powered by a four-cell 1,000 mAh LiPo battery. The amount of power required when all operational activities are executing has been experimentally measured to be about 5 W. More technical details of the designed wireless seismic node are listed in Table 3-1 and will be described in more depth in Section 3.2.1.

A major differentiator of the designed wireless seismic node from other commercial, ready-made ones such as those listed by Kendall (2015) is its high adaptability. The use of a single-board computer as the computing engine of the sensor node adds flexibility of user-defined onboard processing that can be written as scripts in the Linux operating system. This means that the time between data acquisition and data processing will be significantly reduced (i.e., in near real-time), leading to the transmission of information of increased value compared to raw data transmission. Meanwhile, unlike commercial seismic nodes where all system components are sealed in a heavy-duty enclosure (usually over 1.5 kg), the geophone node proposed in this study is lightweight (495 g without the geophone sensor and 810 g with one) ideally suited to be carried by as a UAV payload and contains only power-efficient components. Geophone sensors connected to the ADC interface and LiPo batteries powering the system can be either housed inside the node enclosure or connected to the node externally as will be explained in this dissertation. Another advantage of the designed wireless geophone node is its cost efficiency. Table 3-2 summarizes the total system cost; a single unit costs less than $500 while a commercial wireless counterpart is typically around $1,000, not to mention the cost of the bundling software that can easily exceed $3,000 (Global Sources 2021). Due to its

Table 3-2. A summary of total cost of the wireless geophone node.

Identification in Figure 3-2	**Name**	**Price (US$)**
1	ODROID-XU4 SBC	116.90
2	Wi-Fi antenna	8.90
3	ADS1282EVM	178.80
4	SparkFun ZOE-M8Q GPS Receiver	44.95
5	GPS antenna	3.95
6	Power regulator	21.00
7	1000 mAh LiPo battery	23.00
8	GS-11D 4.5Hz geophone	80.00
9	Node Enclosure	10.00
Total		**487.50**

low-power and low-cost design and its independence from proprietary software, the proposed wireless geophone node will be a great benefit to research on seismic data collection, especially those that require a wireless data acquisition platform. In particular, it can be deployed densely and adaptively as either a stationary or a mobile sensing unit in a wide range of demanding terrains such as congested areas, remote and hard-to-reach locations, and environmentally sensitive areas.

3.2.1 Hardware Architecture

The hardware design (Figure 3-3) of the wireless geophone node is separated into three primary components: the ODROID-XU4 single-board computer, the ADS1282EVM ADC, and the SparkFun ZOE-M8Q GPS module. A geophone sensor can be directly connected to the ADC module of the sensing node. Figure 3-3 provides a schematic overview of the hardware architecture of the wireless node, with technical details of the

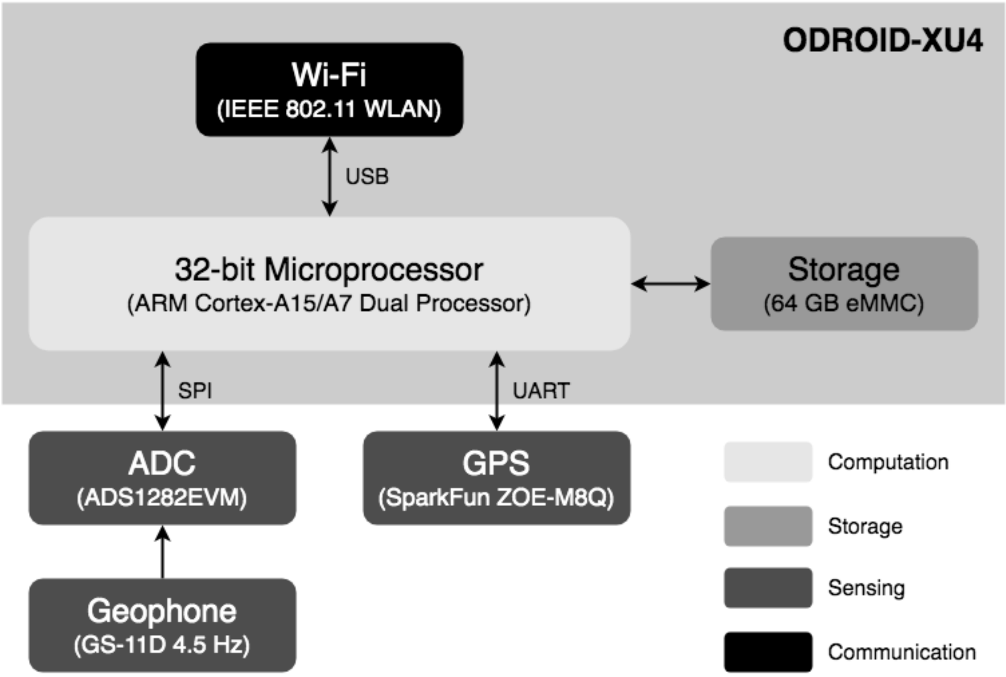

Figure 3-3. Hardware design for computational core, storage space, sensing interface, and wireless communication.

hardware parts listed in Table 3-3 (ODROID-XU4), Table 3-4 (ADS1282EVM ADC), and Table 3-5 (SparkFun GPS ZOE-M8Q). The following paragraphs define each functional module.

The main computing and data storage component of the mobile geophone is the ODROID-XU4 (Hardkernel 2016) SBC. The XU4 features two CPUs with a total number of eight cores: one ARM Cortex-A15 quad-core and another ARM Cortex-A7 quad-core, making it ideal for interrupt driven programming and multi-threaded behavior. Meanwhile, the XU4 has 2 GB LPDDR3 RAM and 64 GB embedded MultiMediaCard (eMMC) 5.0 HS400 Flash Storage, providing enough storage for both the operating system and the collected seismic data during field operations. In terms of support for peripherals, the XU4 offers 3 USB ports and various expansion ports (e.g., GPIO, UART, I²C, SPI (for serial

Table 3-3. Technical specifications of the ODROID-XU4 single-board computer as the compute engine of the wireless geophone node.

Description	**Value**
Operating system	Linux (Ubuntu 18.04)
CPU	Samsung Exynos5422 ARM Cortex-A15 Quad 2.0GHz and ARM Cortex-A7 Quad 1.4GHz
RAM	2GB LPDDR3 RAM PoP (750MHz, 12GB/s memory bandwidth, 2×32-bit bus)
Storage	64GB eMMC5.0 HS400 Flash Storage
Power consumption	1.5 to 10.0W@5V DC
Expansions	2×USB 3.0, 1×USB 2.0, 1×UART, 2×I^2C, 1×SPI, 12×GPIO, 1×ADC
Connectivity	USB IEEE 802.11 ac/b/g/n 1T1R WLAN, HDMI 1.4a, 10/100/1000Mbps Ethernet
Size	83×58×20mm^3
Weight	97g

peripheral interface)) for interfacing peripherals. As a result, a slew of breakout boards and sensory devices, such as an ADC board and a GPS module as done in this study, can be connected to the XU4 and interact with the external world. Data transfer and communication between the XU4 and a local field computer are established through the XU4's Wi-Fi module, which is an IEEE 802.11ac/a/b/g/n WLAN module with dual-band (2.4 GHz and 5 GHz) support. A Wi-Fi interface offers the node the most flexibility in how it interfaces to other components in an automated seismic monitoring system including a UAV and a base station (ground control station). The ability to deliver seismic data through a local Wi-Fi network in real-time substantially strengthens the performance of the node.

A geophone is a self-excited (i.e., does not require a power source) transducer which senses ground movement and converts vibration velocities into electrical signals.

Geophones are sensitive analog sensors requiring proper conditioning and processing of its electrical signals. In this study, an ADS1282EVM (TI 2009) is adopted as ADC and digital filter. As the name suggests, the evaluation model (EVM) is equipped with a ADS1282 ADC chip (TI 2007), which is a high-performance, delta-sigma (ΔΣ) ADC. The ADS1282 has a resolution of 32 bits, with a programmable-gain amplifier (PGA) gain up to 64× and a sampling rate selectable from 250 to 4,000 samples per second (SPS). A 1× PGA gain (resulting in a sensitivity of $\frac{5\text{ V}}{1\times(2^{32}-1)} = 1.164\text{ nV}$) and a sampling rate of 1000 SPS suits the needs of the application well. Following the PGA and ΔΣ modulator, the ADS1282 provides digital filtering options consisting of three cascaded stages: a sinc filter to attenuate the high-frequency noise of the ΔΣ modulator, a finite impulse response (FIR) low-pass filter, and a high-pass filter (HPF) implemented as an infinite impulse response (IIR) structure programmed by end-users. The output can be taken from one of the three filter blocks or directly from the modulator bypassing the build-in filters. The in-chip sinc and FIR filters are activated in this study, which provides more than 140 dB of attenuation above the Nyquist frequency of the output sampling frequency (500 Hz) (TI 2007). Together, the amplifier, modulator, and filter dissipate about 25 mW, making the ADS1282 a power-efficient chip suitable for energy exploration and seismic monitoring. The ADS1282EVM contains all support circuitry needed for the ADS1282 including an onboard high-accuracy 4.096 MHz clock and an OPA1632 buffer (TI 2003) which drives the ADC input terminals and provides a high-impedance input terminal for the geophone sensor. The ADS1282EVM exposes the SPI interface of the ADS1282 for configuration of ADC settings (e.g., sampling rate and filters used) and for the reading of data. There are fundamentally two ways to read data from the ADC: continuous mode and command mode.

Table 3-4. Technical specifications of the ADS1282EVM ADC board.

	Description	**Value**
ADS1282 Chip	Number of channels	2
	A/D resolution	32-bit
	Sampling rate	250, 500, 1000, 2000, or 4000SPS
	PGA gain	1, 2, 4, 8, 16, 32, or 64
	Available digital filter	Bypass or sinc + FIR + IIR (selectable)
	Signal-to-noise ratio	124dB (1000SPS)
	Integral nonlinearity	0.5ppm
	Power consumption	25mW
ADS1282EVM Board	Clock	4.096MHz crystal oscillator
	Temperature range	−45 to +125℃
	Analog supply	+5V, ±10 to ±15V
	Digital supply	3.3V
	Digital output	SPI interface
	Size	96×44×20mm^3
	Weight	29g

The continuous mode is adopted in this study. This mode generates data continuously and when a new sample is available, a "data ready (DRDY)" signal line goes low. The reading device (i.e., ODROID XU4) senses DRDY going low and knows to read the data point using the SPI protocol.

One of the most important components in the design of the wireless geophone is the inclusion of a low-cost GPS receiver. The GPS receiver is not used for position estimation (although it could), but instead as a synchronization clock to time-stamp seismic samples. The atomic clocks used on the GPS satellites offer one of the most precise timing

Table 3-5. Technical specifications of the SparkFun ZOE-M8Q GPS Breakout.

Description	**Value**
Time pulse accuracy	30ns
Update rate	Up to 18Hz
Time to first fix:	Cold: 26s; hot: 1s
Digital supply	3.3V
Current consumption	29mA
Digital output	UART or I^2C interface
Supported protocols	NMEA, UBX, and RTCM
Size	25.5×25.5×1mm^3
Weight	2g

signals that all nodes in an MSN could receive simultaneously, offering precise timing to within 100 billionths of a second (Bauch and Whibberley 2017). This accurate timing is critical for the elimination of a centralized radio systems attempting to synchronize distributed clocks and paves the way for truly autonomous recording (Mougenot 2010). In this study, each mobile geophone tracks timing independently through an accurate and miniaturized GPS receiver: the SparkFun ZOE-M8Q GPS Breakout. The u-blox ZOE-M8Q chip (U-blox 2018a) which is included in the SparkFun ZOE-M8Q board has an ultrasmall form factor (4.5×4.5×1.0 mm^3) with the entire SparkFun breakout board only about the size of a US quarter. The ZOE-M8Q chip includes a 72-channel GNSS positioning engine, meaning it can concurrently receive signals from multiple GNSS systems such as QZSS, GLONASS, Galileo, and BeiDou, thereby ensuring maximum performance even in GNSS-hostile environments (U-blox 2018b). Most importantly, the module provides a reliable pulse-per-second (PPS) signal accurate to within 30 ns. The PPS signal is sampled every second by the wireless geophone node so that geophone samples can be referenced to the global GPS time. Independent timing is acquired on each mobile geophone allowing interunit time synchronization to be performed after the collection of the geophone data. The GPS receiver is also equipped with a rechargeable coin cell battery that serves as a backup power supply. This design feature of SparkFun board significantly reduces the time to first fix (TTFF) from a cold start time of about 26 s to a hot start time of only 1 s. This is especially useful during field tests where the main power supply is sometimes turned off to save the battery life of the wireless geophone node. To complete the GPS system, a Molex GNSS Flex antenna is attached to the module. Even though the antenna has a small footprint of 4×1.5 cm^2 and is only as thick as a piece of paper, it covers a wide frequency band and supports all compatible GNSS signals. The ZOE-M8Q communicates with the XU4 through a UART serial interface and is connected to one of the XU4's USB ports using a UART to USB converter cable.

3.2.2 Software Architecture

The embedded software for the data acquisition and recording processes of the wireless geophone is written as a standalone C++ program sitting on the XU4's Linux OS and used an interrupt-like approach to its execution. Following an object-oriented design, each component (e.g., ADC and GPS) has its driver implemented as a class with the union of the classes forming an overarching class that represents a wireless node. The main loop of the embedded program operates on the wireless node class and iterates through each component to capture data and store them in a file until the recording time has passed. GPS timing and ADC sampling are driven based on real-time detection of the PPS and DRDY signal, respectively. Upon detection of a change in PPS or DRDY, interrupt service routines (ISRs) are executed almost immediately when a new GPS time or a new ADC

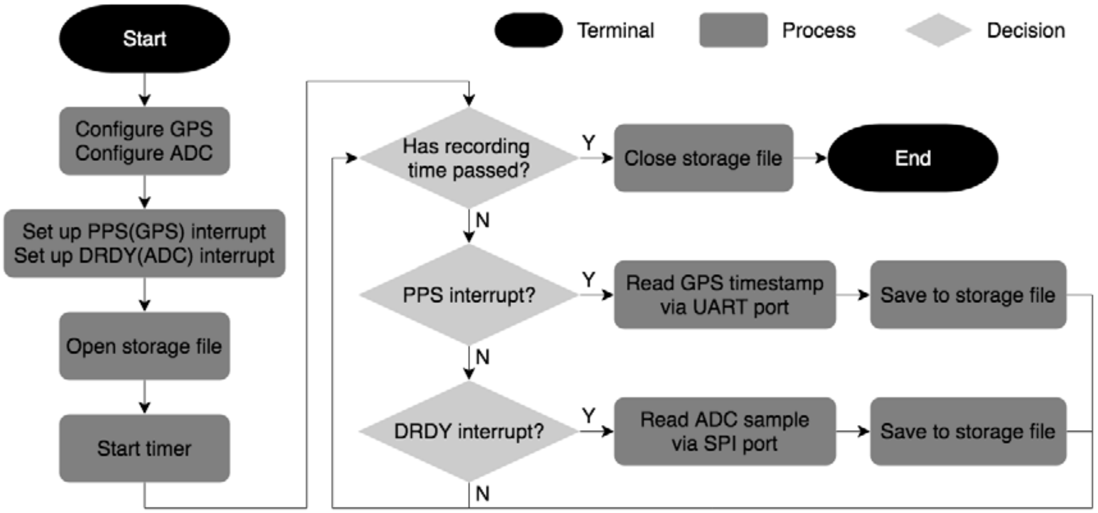

Figure 3-4. Flowchart of the data acquisition and recording processes.

sample is ready, respectively. Although the Ubuntu 18.04 running on XU4 is not a real-time operating system (RTOS), the ISRs are programmed cautiously so that they do not block other operations and precise GPS timing and the sampling rate (1,000 Hz) can be sustained. It should be noted that for sampling frequencies higher than 1,000 Hz, thorough testing will be required to determine whether the OS can handle the throughput with real-time attributes as has been confirmed at 1,000 Hz. Figure 3-4 shows a simplified diagram of the data collection architecture and how it provides real-time behavior at 1,000 Hz. More specifically, the software is able to carry out the following functions:

- Control overall survey parameters (e.g., recording duration and node ID).
- Configure GPS (e.g., update rate and protocol) and ADC (e.g., sampling rate, PGA gain, and filters) setting.
- Retrieve data from both sensing devices and reference ADC samples to GPS time.
- Manage the recording of data in memory (i.e., eMMC).
- Handle the file name assigned automatically to data records.

- Provide a CMake-based program build and configuration framework.

3.3 Design of the UAV and the Drop Weight

3.3.1 UAV platform

The UAV platform used in this study is the same 3DR X8 octocopter introduced in Chapter 2 with some modifications (Figure 3-5(a)). The X8 features two motors with inverted propellers on each of its four arms, generating twice the thrust of a normal quadcopter, and therefore has an enlarged payload capacity. Specifically, the UAV can carry up to a 1 kg payload in addition to its self-weight. Powered by a 16,000 mAh 4S LiPo battery, the X8 has a flight time of about 15 minutes when fully loaded (i.e., 1 kg payload), making it ideal for this study. In order to realize the functionality of autonomous weight pickup and drop-off needed in autonomous seismic surveying, two additional hardware components are incorporated into the UAV: a magnetic gripper and a laser-based rangefinder.

An OpenGrab electropermanent magnet (EPM) v3 gripper (Figure 3-5(b)) (Zubax Robotics 2016) is mounted to the bottom surface of the UAV. Connected to one of the Pixhawk's AUX OUT ports, the gripper accepts grabbing/releasing commands (i.e., two different PWM signals) encoded using the MAVLink protocol (MAVLink 2010). This small cuboid-shaped (about 4×4×2 cm^3) gripper is capable of securely holding up to 15 kg of cargo that has a ferrous surface it can attract. In this study, the cargo is a steel plate that weighs roughly 1 kg. The gripping and releasing of the steel plate are accomplished by the UAV delivering a short voltage pulse to an electromagnet inside the gripper, which reverses its field. Steady-state power consumption for the gripper is under 50 mW (Zubax

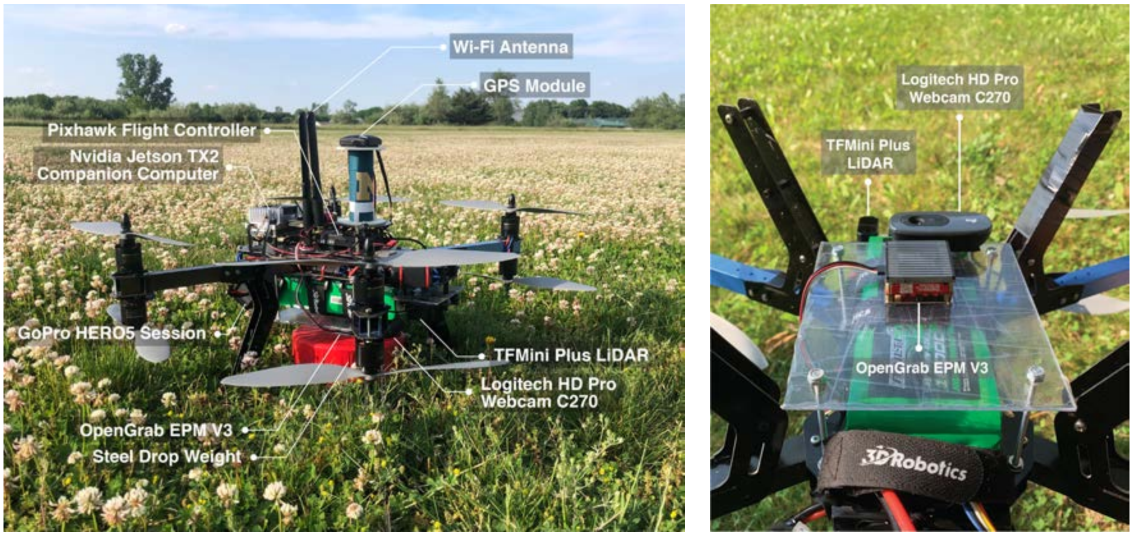

(a) (b)

Figure 3-5. The 3DR X8 UAV with key hardware components highlighted: (a) UAV sitting on grass and waiting to execute an autonomous weight drop-off and pickup mission; (b) zoom in view of the UAV bottom.

Robotics 2016). However, a significant amount of power is required when first gripping or releasing the cargo, but this lasts of less than one second, so it does not draw down the UAV battery quickly.

Sitting on the front of the UAV is a downward facing TFMini Plus LiDAR module (Figure 3-5(b)) (Benewake 2019). The TFMini Plus is a rangefinder sensor operating on the principle of time of flight (ToF). The sensor actively emits laser beams and measures the time difference between the emission of the light signal and the reception of it after being reflected from an object. The time of flight of the light signal can then be used to resolve the distance between the sensor and a remote object. The TFMini Plus has an operating range from 10 cm to 12 m and an accuracy of ±5 cm up to a distance of 6 m and ±1% when the distance is larger than 6 m. Measuring $35\times18.5\times21$ mm^3 and weighing only 11 g, the small and lightweight LiDAR sensor is integrated to the UAV system and

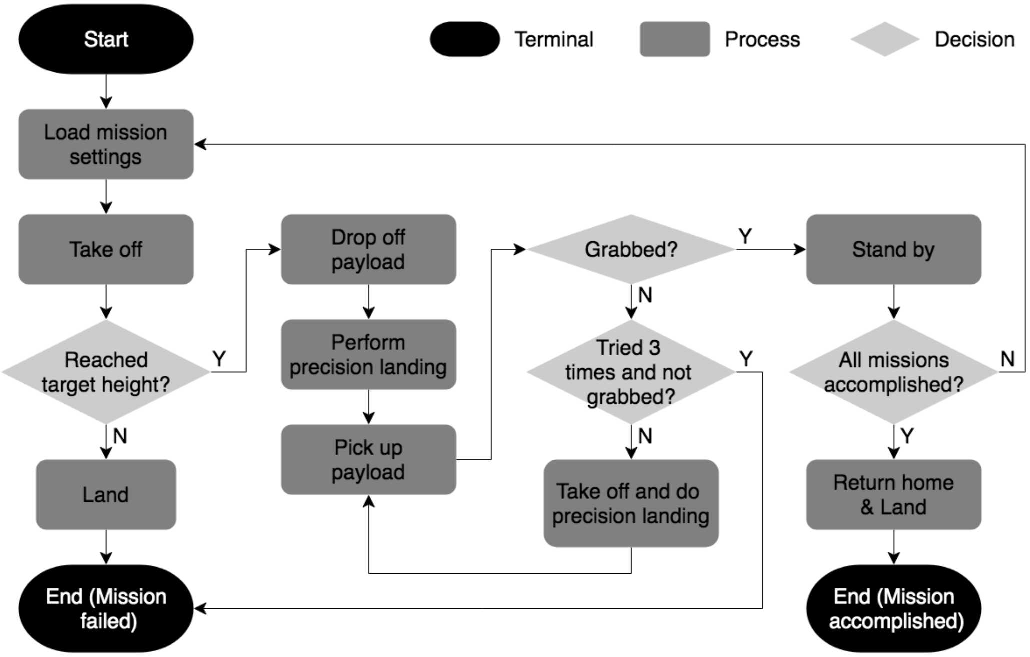

Figure 3-6. Finite-state machine for autonomous operation of a UAV engaged in payload drop-off and pickup.

connected to one of the Pixhawk's UART serial ports. It communicates to the flight controller through the UART communication protocol. Attached to the bottom of the UAV and facing the ground, the rangefinder is used as an altimeter in this study. As a valuable supplement to the GPS and barometer sensors embedded in the UAV flight controller that already provide height information of the UAV, laser-based measurements from the LiDAR are much more accurate and enable the UAV to hold a steady altitude even in heavy winds. This will be especially valuable for the weight dropping application since an accurate and consistent drop height is necessary to ensuring repeatability of the tests and benefits the calculation of impact energy delivered to the ground.

Equipped with the necessary hardware parts, the X8 follows a finite-state machine approach to partition the autonomous payload drop-off and pickup mission into a set of well-defined operations. The definition of different operations and interconnections between them are shown in Figure 3-6. The software system is divided into manageable pieces such as flying to a preset height, payload drop-off, and precision landing. Transitions between different sub-missions are clearly defined. A UAV starting from the “start” state would eventually reach the “end” state by either accomplishing or failing the mission. The most difficult step over all operations is the precision landing to pick up the payload. The precision landing maneuver aims to precisely land the UAV over the payload using only onboard sensing and computation. Unlike Chapter 2 where the UAV had a clean fiducial marker landing pad, in seismic monitoring such structured visual reference will not be available. The UAV will need to use only the weight itself to assist with its landing so higher errors in landing are expected. Should the UAV not succeed in grabbing the payload, the UAV would take off and attempt to do a precision landing again, thereby offering some resilience in its operation. Three trials are allowed for the payload pickup before the mission is counted as a “failure”.

As shown in Figure 3-6, an essential piece of fully autonomous operations of the UAV is to gather feedback information from the gripper about whether the payload is firmly seized or not. In the event of an unsuccessful grasping, flying the UAV to the drop height without carrying the payload is a complete waste of time and battery life so it is essential the UAV know it has the weight onboard or not. Out of the box, the EPM gripper does not provide any feedback for confirming a successfully grab attempt. Teams attending the Mohamed Bin Zayed International Robotics Challenge (MBZIRC) in 2017 provided a solution by installing Hall effect sensors to measure the magnetic field change when a ferrous object is attached (Loianno et al. 2018; Bähnemann et al. 2019). However, the installation of Hall effect sensors requires a customized interface board and the housing of

Hall effect sensors which adds extra weight and may complicate the gripper manipulation system.

In this study, a novel method that takes advantage of acoustic signature differences between a successful grip event and a failure is proposed. In the case of a successful grip, the magnetic force generated by the gripper keeps drawing the ferrous object closer until a firm contact between them is created. A loud click-like impulsive acoustic signature is generated when this tight contact is established. However, for an unsuccessful gripping attempt, there is no contact and thus only low-level background noise would be recorded. When a pickup command is issued from the flight controller to the gripper, the UAV is programmed to use onboard microphones included in the UAV webcam to start recording the ambient sound for one second.

3.3.2 Drop Weight and Visual Detection

The drop weight used in this study (Figure 3-7) is a steel plate that will naturally be usable with the magnetic gripping mechanism. The cylinder-shaped plate weighs 0.93 kg and has a radius of 7.62 cm and a height of 5.40 cm. An AprilTag with a side length of 2.80 cm is attached to both the top and bottom surfaces of the plate. This small marker is able to provide visual guidance to a landing UAV from a height of around 1.4 m down to 10 cm. Unfortunately, the short detection range can only assist in the very last stages of the landing approch. Because of the limited surface area of the plate, the addition of larger AprilTags as demonstrated in Chapter 2 is not feasible. To address this problem, a method utilizing color detection is adopted in this study. The drop weight therefore features a unique color that stands out against the background color of the ground (which is typically

Figure 3-7. The steel drop weight used in this study featuring a red color and an AprilTag attached to both the top and bottom surfaces.

a green or brown set of hues). In this study, the drop weight is wrapped with a red polymeric film, making it easily distinguishable in green and brown ground surfaces.

Generally, a color detection algorithm searches an image for pixels that have a specific range of RGB values. In this study, the HSV (for hue, saturation, value) color space instead of the RGB (for red, green, blue) model is used mainly because the HSV model is more robust under lighting variations (Schwarz, Cowan, and Beatty 1987). The RGB system is convenient for color display but struggles when it comes to object separation since the R (red), G (green), and B (blue) components are all correlated with the amount of light hitting the object. On the contrary, the HSV description separates color information (hue and saturation) of an image from its intensity information (value). In particular, the hue dimension represents basic colors and is determined by a color’s position in the spectrum; the saturation component is a measure of the purity of the color (and signifies the amount of white light mixed with the hue); and value describes the brightness of the

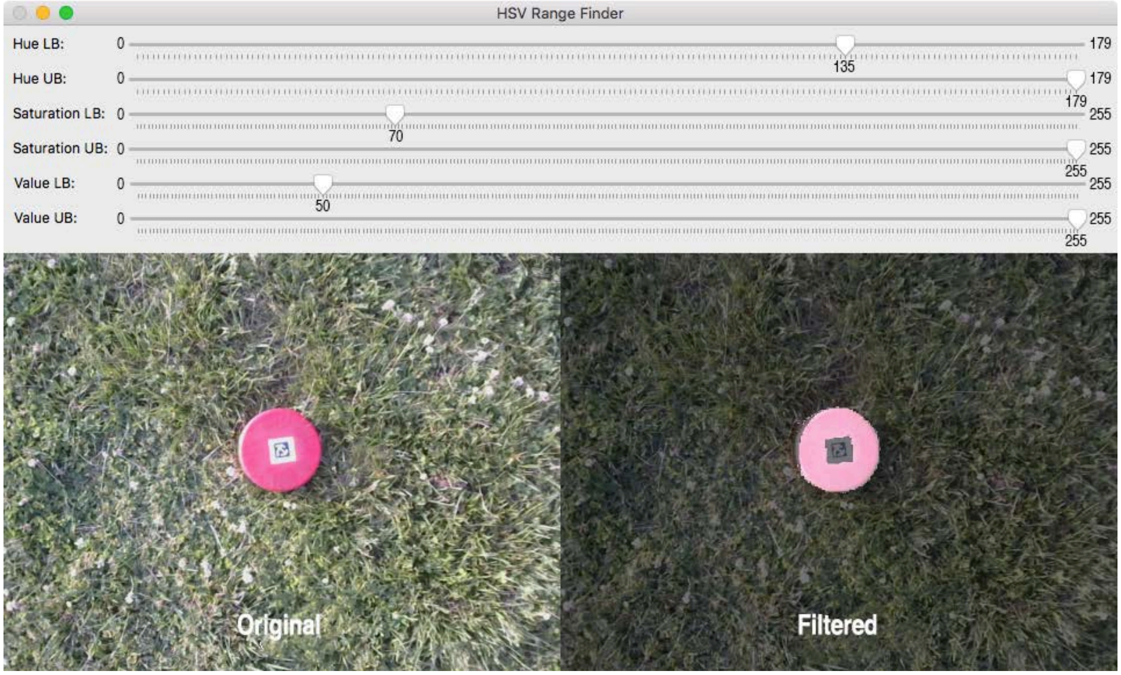

Hue LB: 0 135 179

Hue UB: 0 179 179

Saturation LB: 0 70 255

Saturation UB: 0 255 255

Value LB: 0 50 255

Value UB: 0 255 255

Figure 3-8. The interactive GUI designed to search for the best HSV ranges that are able to segment the drop weight from the ground in an image.

color (Cheng et al. 2001). Using the HSV color model, the color detection algorithm can search a downward view of the ground for color position and purity, therefore greatly improving the performance of object segmentation. In this study, a set of thresholds are applied to the H, S, and V components, respectively, to form a region that can represent the drop weight. An interactive graphical user interface (GUI) is developed as shown in Figure 3-8 to find the H, S, and V ranges that can best separate the red drop weight from green grass in an image. The ranges found in this study that best define the color blob of the drop weight are 135-179 for hue, 70-255 for saturation, and 50-255 for value.

With a successful detection of the drop weight, the relative position (of the UAV with respect to the drop weight) estimation algorithm used for precision landing follows the same design as illustrated in Chapter 2 with some modifications. As shown in Figure 3-9, four main coordinate frames (i.e., the *Ground* frame $P(x_p, y_p, z_p)$, the *UAV* frame

$Q(x_Q, y_Q, z_Q)$, the *Camera* frame $O(x_O, y_O, z_O)$, and the *Weight* frame $M(x_M, y_M, z_M)$) and transformations between them are illustrated. When the AprilTag on the weight surface is detected in an image, the landing point M is assigned to be the tag center; otherwise M is defined as the geometric center of the detected color blob of the drop weight. Recall that the objective is to find the landing point M's representation in the *Ground* frame, M^{Ground}, which can be derived from M's representation in the *Camera* frame, M^{Camera}, by applying two rigid motion transformations as shown in Equation (2-5). When the tag is detected, M^{Camera} is simply t_{World}^{Camera}, a direct result from the solvePnP algorithm. However, in the case of a color blob detection, t_{World}^{Camera} is no longer attainable from solving the PnP problem, because solvePnP requires at least four detected feature points from an image but the only one existing in a color blob is its geometric center M. The following is a method of computing M^{Camera} through a careful geometric deduction.

The derivation of M^{Camera} is separated into two parts: its direction $\frac{M^{Camera}}{\|M^{Camera}\|}$ and its magnitude $\|M^{Camera}\|$ (i.e., $\|\overrightarrow{OM}\|$ in Figure 3-9). First, $\frac{M^{Camera}}{\|M^{Camera}\|}$ can be derived following geometric relations shown in Figure 3-9:

$$\begin{aligned}\frac{M^{Camera}}{\|M^{Camera}\|} = \frac{N^{Camera}}{\|N^{Camera}\|} &= n\left([\|\overrightarrow{AI}\| \ \|\overrightarrow{AJ}\| \ \|\overrightarrow{OA}\|]^T\right) \\ &= n\left(\begin{bmatrix}\frac{\|\overrightarrow{AI}\|}{\|\overrightarrow{OA}\|} & \frac{\|\overrightarrow{AJ}\|}{\|\overrightarrow{OA}\|} & 1\end{bmatrix}^T\right) \\ &= n([\tan(\angle AOI) \ \tan(\angle AOJ) \ 1]^T),\end{aligned} \tag{3-1}$$

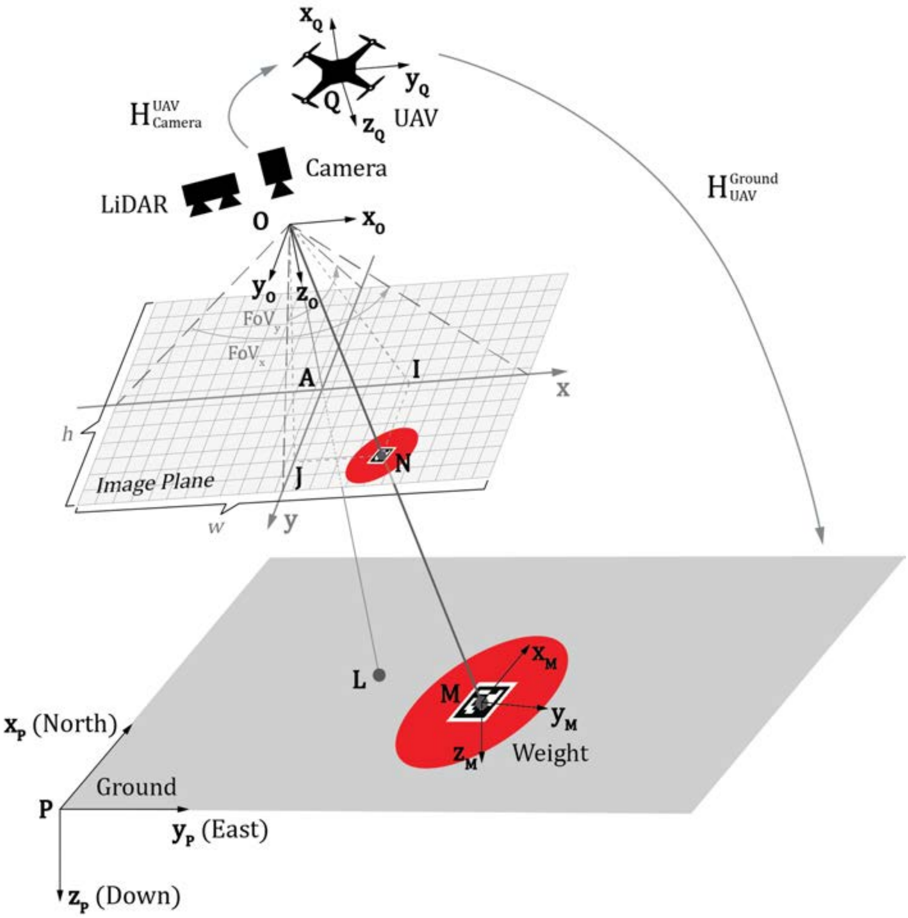

Figure 3-9. Diagram illustrating how to compute the relative position of the landing point M with respect to the UAV's CG, point Q.

where $n(\cdot)$ is a vector normalizing function, $\|\overrightarrow{AI}\|$ and $\|\overrightarrow{AJ}\|$ are the distances (in pixels) from the center of the image to the detected landing point N. Defining $\angle AOI$ and $\angle AOJ$ as $Offset_x$ and $Offset_y$, respectively; they are:

$$\begin{aligned} Offset_x &\triangleq \angle AOI = \frac{\|\overrightarrow{AI}\|}{w} FoV_x, \\ Offset_y &\triangleq \angle AOJ = \frac{\|\overrightarrow{AJ}\|}{h} FoV_y, \end{aligned} \tag{3-2}$$

where w and h (in pixels) are the width and height of the image, FoV_x and FoV_y (in radians) are the field of view in the camera's x_O and y_O directions, respectively (See Appendix A.3 for derivations of FoV_x and FoV_y). The magnitude of M^{Camera}, or $\|\overrightarrow{OM}\|$ in Figure 3-9, can be estimated as:

$$\|\overrightarrow{OM}\| \approx \|\overrightarrow{OL}\| \cdot \frac{\|\overrightarrow{ON}\|}{\|\overrightarrow{OA}\|} = \|\overrightarrow{OL}\| \cdot \sqrt{1 + \tan^2(\angle AOI) + \tan^2(\angle AOJ)}, \quad (3\text{-}3)$$

where $\|\overrightarrow{OL}\|$ is the measurement of distance from the LiDAR sensor, and $\angle AOI$ (i.e., $Offset_x$) and $\angle AOJ$ (i.e., $Offset_y$) are computed as in Equation (3-2). It should be noted that this approximation of $\|\overrightarrow{OM}\|$ is based on the assumption that the *Image* plane is parallel to the *Ground* plane, which does not hold true all of the time but works well in practice. The representation of the landing point M in the *Camera* frame can now be formulated as:

$$\begin{aligned} M^{Camera} &= \frac{M^{Camera}}{\|M^{Camera}\|} \cdot \|M^{Camera}\| \\ &= n\left(\left[\tan(Offset_x) \ \tan(Offset_y) \ 1\right]^T\right) \cdot \\ &\quad \|\overrightarrow{OL}\| \cdot \sqrt{1 + \tan^2(Offset_x) + \tan^2(Offset_y)} \\ &= \|\overrightarrow{OL}\| \cdot \left[\tan(Offset_x) \ \tan(Offset_y) \ 1\right]^T. \end{aligned} \quad (3\text{-}4)$$

3.4 Experiments and Results

3.4.1 Experimental Validation of the Wireless Geophone Node

To validate the functionality of the newly developed wireless geophone node, field tests were performed at the Scio Flyers Model Aircraft Club in Scio Township, MI. Two wireless geophone nodes were constructed per the design of Section 3.2 and used to verify their ability to record seismic waves and to synchronize their seismic signals between the node pair. A close-up view of the overall experiment setup and equipment layout is shown in Figure 3-10. The two wireless geophone nodes were placed at position *A* and *B*, respectively, with a 2 m inter-sensor spacing. The source target was placed along the line of the two geophones with an offset of 2 m from its nearest receiver. Seismic waves were generated by striking a 5.4 kg Dytran sledgehammer on a polyethylene plate. Ground vibrations recorded by the wireless geophone nodes were transmitted in real time to a field MacBook through a local Wi-Fi router. A commercial cabled seismic acquisition system was deployed side by side with the wireless system as the benchmark against which the wireless system should be compared. The commercial system included a Geometrics ES-3000 seismograph for geophone signal processing and a Panasonic field PC laptop for data storage. Geospace GS-11D 4.5 Hz geophones (natural frequency: 4.5 ± 0.75 Hz, coil resistance: 380 Ω, sensitivity: 32 V/m/s) were used for both the wired and wireless data recording system for direct comparison. Geophone sensors interfaced with the cabled seismic recorder were placed in close proximity (about 10 cm) to those attached to the wireless nodes.

During the field test, both wireless geophone nodes were commanded to register 30 seconds of data with a sampling frequency of 1,000 Hz (leading to a total of 30,000 signal samples for each node). Figure 3-11 illustrates the aligned time-domain geophone signals (blue curves) collected by the pair of wireless sensor nodes. The sledgehammer was manually stricken six times during the roughly 30 s time frame, which is manifested by the

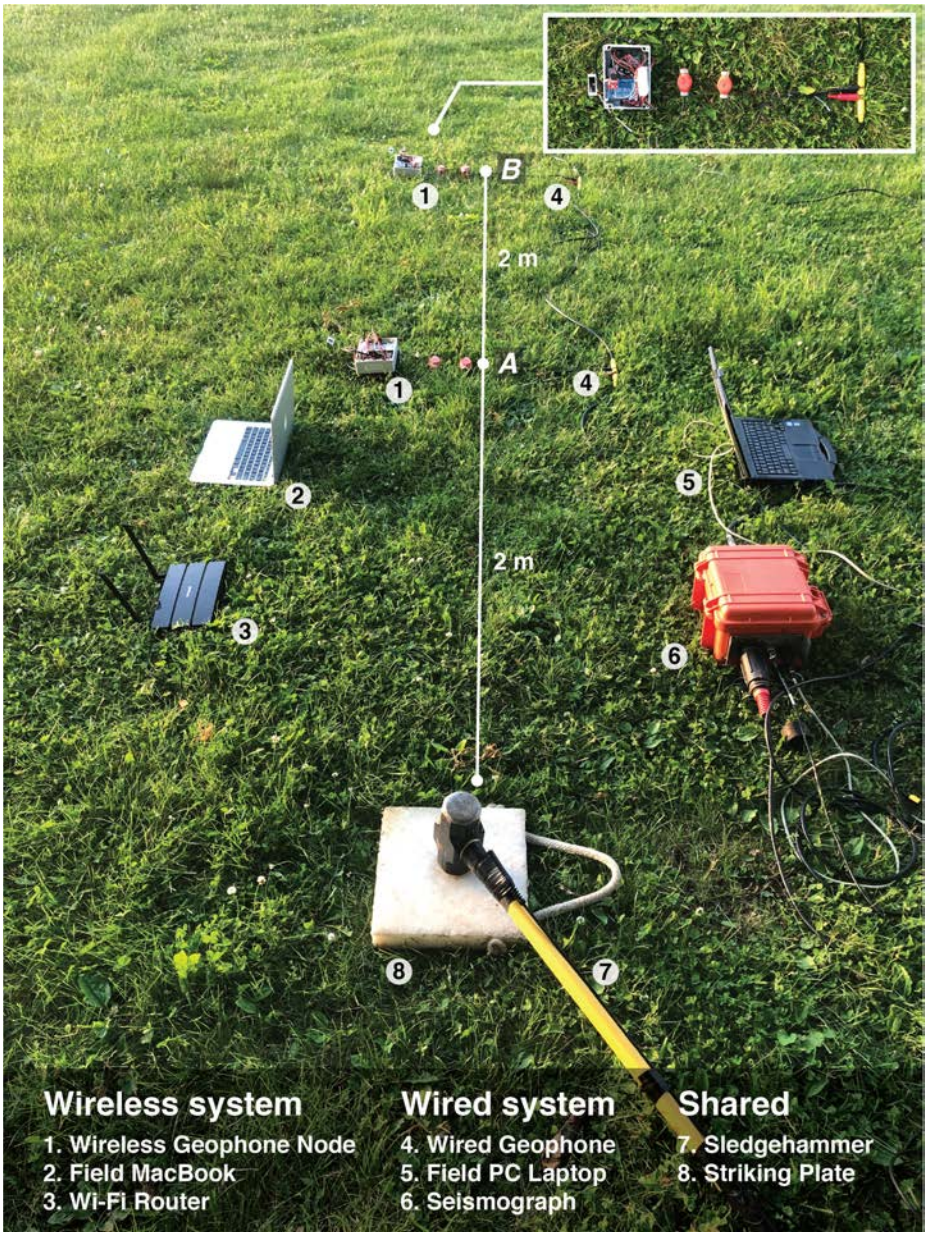

Figure 3-10. Experiment setup and equipment layout for validating the proposed wireless seismic recorder against a commercially available wired seismic monitoring system.

six peaks in both signal curves. PPS signals from the GPS sensor, indicated by green dashed vertical lines, are layered on top of each geophone signal to annotate time-instants. Accurate timestamps in the format of "minute:second" are labeled above each dashed line. These timestamps are crucial for synchronization of signals coming from different wireless

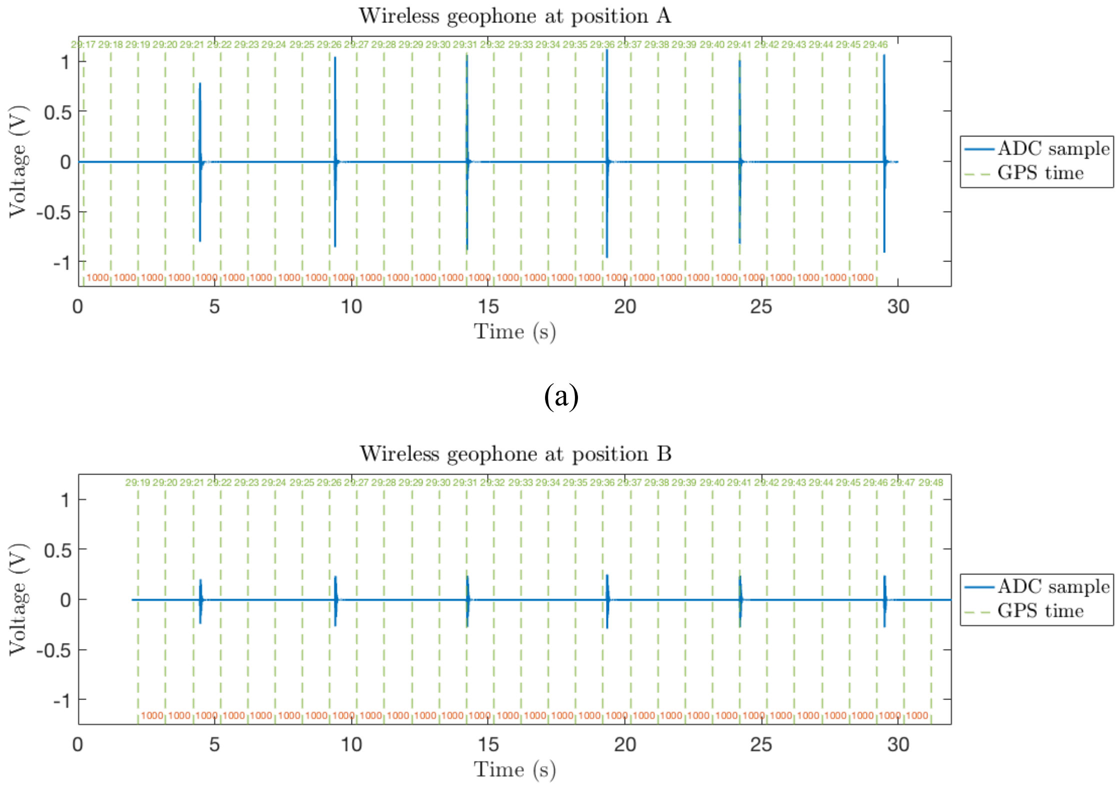

(a)

(b)

Figure 3-11. Time-domain signals coupled with GPS timestamps recorded by the wireless geophone node pair: (a) wireless geophone signal at position *A*; (b) wireless geophone signal at position *B*.

sensor nodes and are used in this figure to align the two geophone signal plots. The numbers in red labelled between each pair of neighboring green vertical lines represent the number of ADC samples between them. The constant counting of 1,000 ADC samples between any two consecutive PPS signals reveals the excellent performance of the XU4 SBC in handling data throughput at a sampling rate of 1,000 Hz.

A comparison between geophone signals recorded by the wireless sensor nodes and the wired seismic monitoring system in both the time and frequency domains is shown in Figure 3-12. Figure 3-12(a) and Figure 3-12(c) are zoom-in views of the second peak in

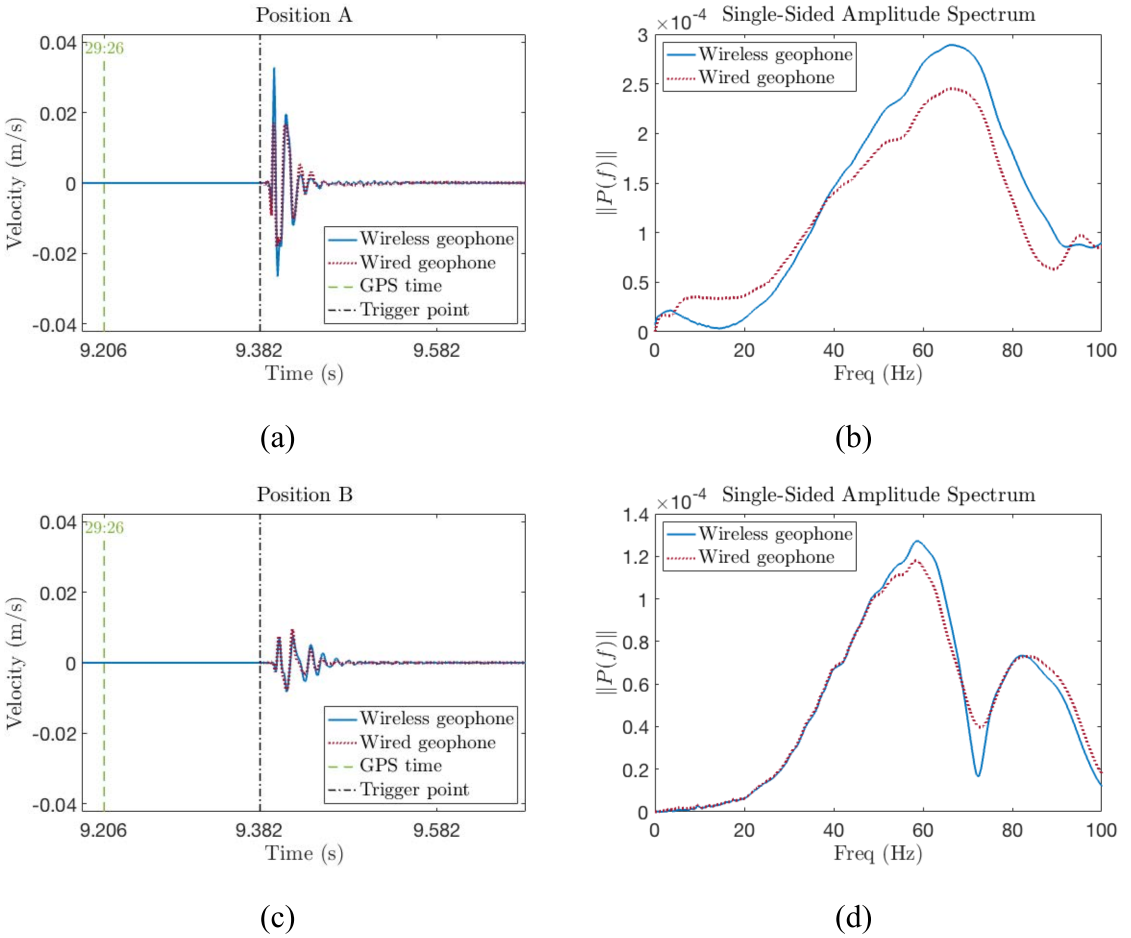

(a) (b)

(c) (d)

Figure 3-12. Comparison between measurements from the wireless geophones and recordings of the seismograph at locations *A* and *B* (Figure 3-10), respectively: (a) and (c) time histories; (b) and (d) frequency spectra.

Figure 3-11(a) and Figure 3-11(b), respectively. Raw signal voltage (in V) from each geophone is converted to ground movement velocity (in m/s) using the geophone's sensitivity of 32 V/m/s. Overlaid with the wireless geophone measurements (blue solid curve) are the wired system recordings (red dotted curve). The ES-3000 seismograph was configured to record seismic data at a sampling frequency of 1,000 Hz, same as the sampling rate of the wireless geophones, for a duration of two seconds. Triggering of the system, shown by the black dashdotted vertical line, was implemented via an inertial switch

Table 3-6. Lapse of time from position *A* to position *B* (Units are in seconds).

	Peak 1	**Peak 2**	**Peak 3**	**Peak 4**
Wired system	0.006	0.008	0.012	0.012
Wireless system	0.006	0.008	0.012	0.014

mounted on the sledgehammer handle. As shown in Figure 3-12(a) and Figure 3-12(c), at both position *A* and *B*, the alignment of time-domain signals collected by the wireless system and the wired one is fairly well, especially given the fact the two geophone sensors were not deployed at the exact same location. Specifically, Table 3-6 tabulates the lapse of time for the first four wave peaks in Figure 3-12(a) to travel from position *A* to *B* (Figure 3-12(c)). The wired and wireless systems report the same amount of travel time for the first three peaks and a slightly different (2 ms) travel time for the fourth peak. These impressive results underscore the effectiveness of the GPS receiver as a means of synchronizing time. The amplitudes of the geophone signals for the first 0.2 s since triggering (i.e., from 9.382 s to 9.582 s in Figure 3-12(a) and Figure 3-12(c)) have an RMS error of 0.0021 m/s and 0.0008 m/s at *A* and *B*, respectively. While this may be termed an error, given the fact that the wireless and wired geophone are not quite collocated, it would be expected the signals would not be identical. This successfully demonstrates the wireless geophone node's capability of recording accurate seismic data (on the level of a commercial cabled system) and annotating it with correct GPS time. Presented in Figure 3-12(b) and Figure 3-12(d) are the frequency spectra of the signals that were obtained following the fast Fourier transform (FFT) method. The resemblance of frequency spectra between the wired and wireless geophones further validates the functionality of the proposed wireless geophone node. This is an excellent finding as signal processing in SASW and MASW are often done in the frequency domain where there is very strong agreement.

3.4.2 Field Demonstration of Autonomous Payload Pickup and Drop-off of the UAV

The most difficult step among all autonomous UAV operations is the precision landing to pick up the drop weight, the results of which are reported herein. Figure 3-13 shows a sequence of snapshots from the onboard webcam during a typical precision landing, with (a)-(c) showcasing the spotting of color blob and (d)-(f) showing the detection of the AprilTag by the tailored onboard object detector. When the UAV was at relatively high altitudes, the color blob detection algorithm was used to segment the drop weight in the images. The target landing point M, which was computed as the geometric center of the color blob, is marked as a red cross marker in Figure 3-13(a)-(c). Displayed also on top of each image is $Offset_x$ and $Offset_y$ derived following the geometric method that were used to estimate relative UAV position. As the UAV gradually descended to the ground, the AprilTag detection algorithm came into effect at the height of about 1.39 m (Figure 3-13(d)). The landing point M in this case was assigned to be the center of the AprilTag. Estimations of M^{Camera} (i.e., t_1, t_2, and t_3) directly from the solvePnP algorithm are labelled in green at the top of the image. The UAV was able to land on top of the drop weight with a deviation from the weight center of only 2 cm (Figure 3-13(f)). The precision landing maneuver was tested thoroughly. Out of a total of 25 test flights, 19 were found to have a deviation of less than 7 cm. Of the other six, the deviation was greater than 7 cm making the magnetic gripping of the weight spatially infeasible. With future tweaking of the UAV controller, the landing accuracy can be improved.

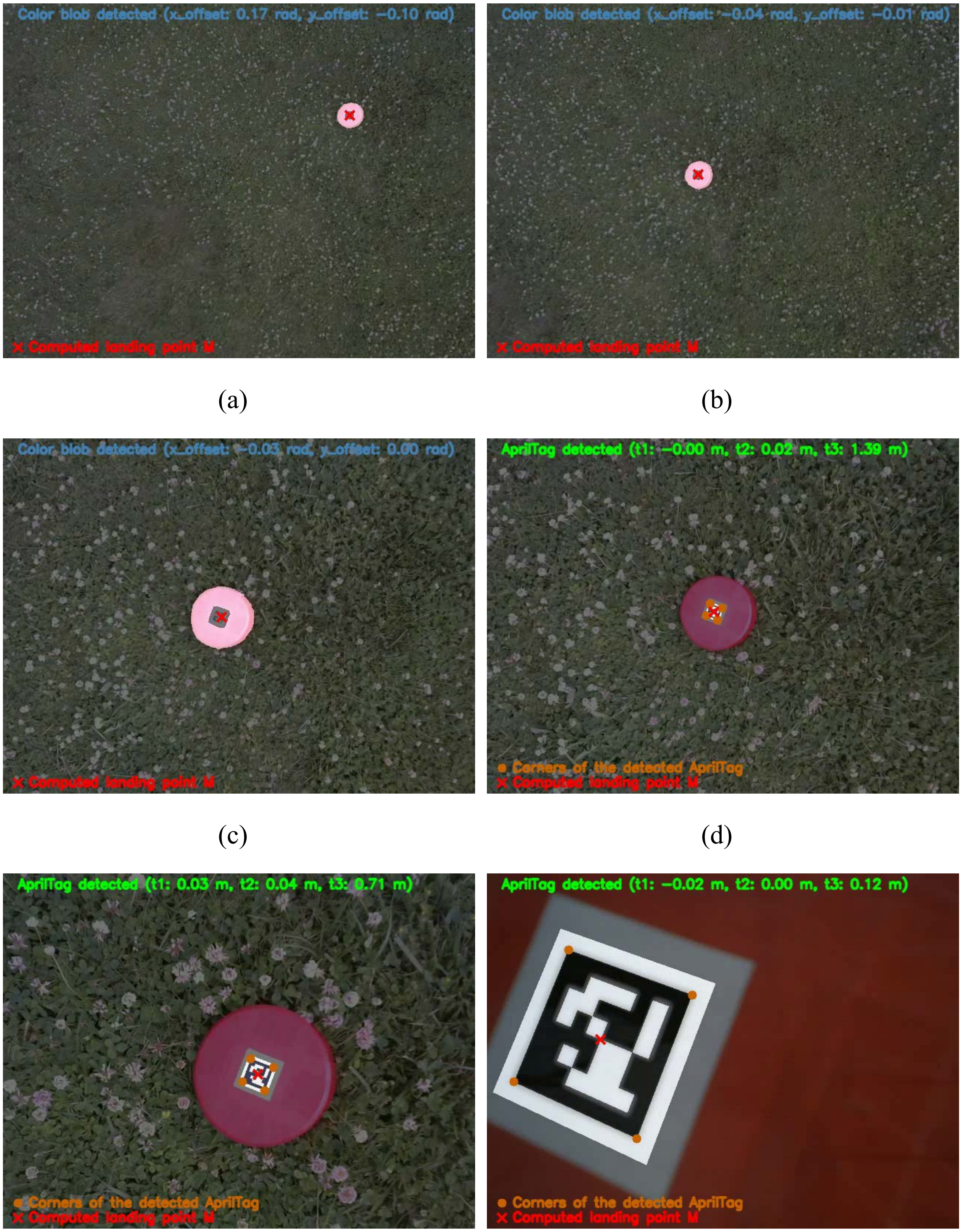

(a) (b) (c) (d) (e) (f)

Figure 3-13. A sequence of images streamed from the webcam during precision landing: (a)-(c) detection of the seismic weight as a color blob; (d)-(f) detection of the AprilTag on the weight.

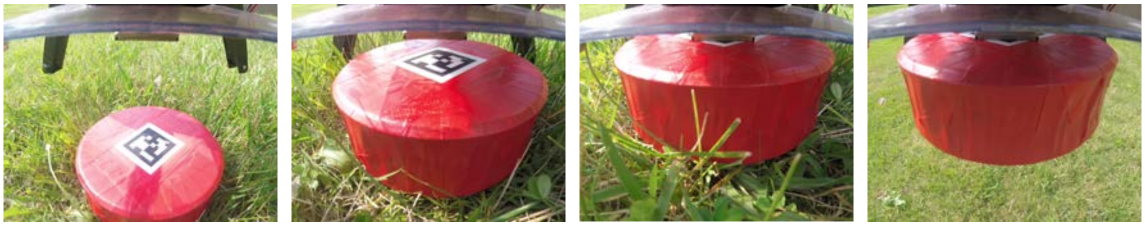

(a) (b) (c) (d)

Figure 3-14. A series of snapshots from the onboard GoPro camera showcasing a successful payload pickup action: (a)-(b) precision landing; (c) payload grasping; (d) takeoff with payload onboard.

Figure 3-14 illustrates the process of a successful drop weight pickup action observed from the onboard GoPro action camera. Following a precision landing maneuver, the UAV was able to successfully grab the weight and take off to drop the weight again. Experiments on determining whether a grasping attempt is successful were also conducted. The drop weight was manually put in various locations under the UAV. Upon issuing a gripping command to the gripper, ambient sound was recorded for one second, after which the gripping result was observed. Figure 3-15 shows the soundwaves in both the time and frequency domains for a typical successful grasp and an unsuccessful one. The three peaks in the plots arise from capacitors inside the EPM charging three times to create a strong magnetic field. The maximum soundwave amplitude for a successful grasp was found to be around 1 while that for an unsuccessful one was always below 0.25. A criterion based on this maximum sound amplitude was established to identify a successful grasping action. Figure 3-16 shows the relative positions of the drop weight after the UAV lands in four test flights. The UAV was able to successfully pick up the drop weight in (a)-(c), while failed in (d) and had to repeat the precision landing maneuver again according to the designed FSM. The overall success rate for picking up the drop weight is measured to be around 70% based on a total of 25 test flights.

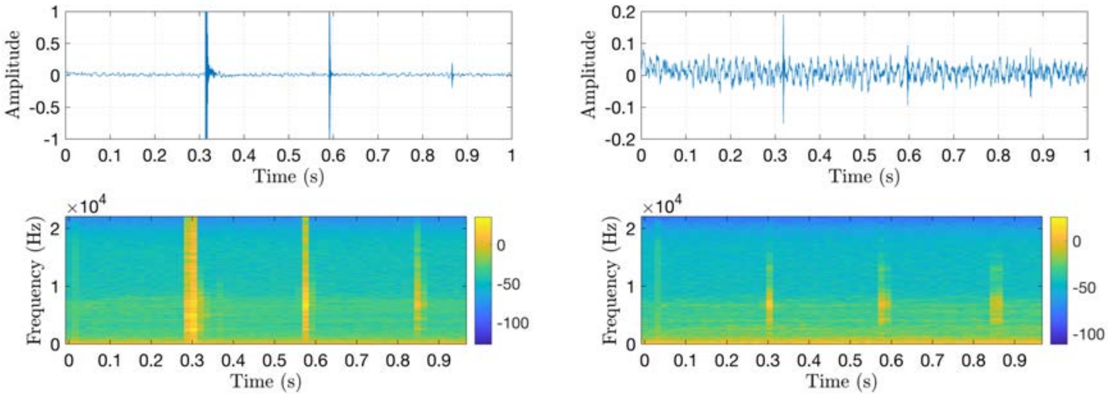

(a) (b)

Figure 3-15. Sound recorded in both time (up) and frequency (down) domain when a grip command is issued: (a) a successful grasp; (b) an unsuccessful one.

(a) (b) (c) (d)

Figure 3-16. Relative positions of the drop weight after the UAV lands, leading to: (a)-(c) successful grasps; (d) unsuccessful grasp.

3.5 Conclusion

This chapter presents two critical components that are necessary for the advancement of UAV-enabled automated subsurface characterization for remote or hard-to-reach sites. The proposed wireless geophone node is a stand-alone seismic recorder capable of collecting GPS-time-referenced seismic data. Featuring a modular design and open-source software, the designed wireless sensor node achieves great mobility and adaptability that meets growing research needs. Performance of the wireless sensor node is validated through side-by-side comparison with a commercial off-the-shelf (COTS) cabled seismic acquisition system. The wireless geophone is able to meet all the design requirements specified in Section 3.2. The combined functionality and affordability make the designed wireless geophone node an invaluable tool that can be densely deployed in challenging terrains where a cabled system would fail. The second piece of hardware introduced in this chapter is a UAV-based intelligent seismic source deployment system. Leveraging robust visual detection and precise position control, the UAV is able to drop off a weight and pick it up in a repeated and autonomous fashion. Results reveal excellent accuracy of less than 7 cm in the placement of the UAV on top of the drop weight and a success rate of 70% for grasping. A novel approach utilizing acoustic signatures to identify a successful gripping is also presented. The study proves the feasibility of using a UAV to actively deploy seismic sources and multiple wireless geophones to collect seismic responses. The two hardware components are geared towards a fully autonomous UAV system that can intelligently characterize earth subsurface stiffness, which will be shown in the next chapter.

Chapter 4 UAV-Enabled Automated Subsurface Characterization Using Spectral Analysis of Surface Waves

4.1 Introduction

The wireless geophone node developed in Chapter 3 marks a breakthrough from wired seismic recording to mobile wireless sensing. As an enhancement to the wireless sensing technology, an MSN architecture offers additional potential benefits such as reduced number of sensors within a network and increased data quality using configurable sensor network topologies. Integrating the wireless geophone node into a mobile UAV is a feasible and affordable means of realizing the MSN architecture. Advanced UAV technologies such as precision position control and autonomous operations, as illustrated in Chapter 2 and Chapter 3, have made UAVs a technologically matured RAS platform capable of geotechnical applications such as subsurface investigations of field sites. Built upon the technologies and devices developed in the previous two chapters, this chapter presents a RAS solution to shear wave velocity profiling of geotechnical sites.

4.1.1 Background of SWMs and SASW

Seismic surveys are a powerful tool to image subsurface formations using surface-induced seismic waves. Ever since the early years of the 20th century, when the first seismic surveying method was patented in 1919 by German scientist Ludger Mintrop (ETHW 2020), the development of surface methods to explore the earth subsurface has evolved rapidly. The goal of a SWM is to use the geometric dispersion of surface waves to infer the relevant medium properties by solving an inverse problem for parameter identification (Socco, Foti, and Boiero 2010). A variety of near-surface applications centered on the SWM prompted during the past few decades including earthquake site response (Foti et al. 2009; Comina et al. 2011), nondestructive pavement testing (Nazarian and Stokoe II 1984; Ryden et al. 2004), offshore site characterization (Luke and Stokoe II 1998), and underground anomaly detection (Nasseri-Moghaddam, Cascante, and Hutchinson 2005). The primary use of surface wave tests today is to determine the in situ shear wave velocity (V_S) profile (i.e., the variation of the shear wave velocity with depth) for earth subsurface characterization purposes. This is usually accomplished by first experimentally measuring the dispersion curve (i.e., the variation of Rayleigh phase velocity V_R with frequency) associated with a given site and subsequently going through an inversion process to derive a shear wave velocity profile. Depending on whether the surface waves are generated by a source for the purpose of profiling or not, surface wave methods can be divided into two categories: passive methods and active methods. Passive surface wave methods utilize naturally occurring microtremors (i.e., small-amplitude ground surface vibrations) to extract information for site characterization. The most commonly used methods for passive field data processing include spatial autocorrelation (SPAC) (Aki 1957) and minimum-variance distortionless look (MVDL) (Capon 1969). On the contrary, active surface wave methods rely on seismic pulses generated on purpose from artificial sources such as a sledgehammer, a drop weight, a thumper truck, or even explosives. The first active surface wave method developed for geotechnical site characterization was the steady-state Rayleigh method (Jones 1958) proposed in the 1950s. Later in the 1970s, the advent of portable sophisticated data acquisition and frequency analyzers led to two seminal works:

first the SASW (Nazarian 1984; Stokoe et al. 1994) and subsequently the MASW method (Park, Miller, and Xia 1999), which are widely adopted in field practice today. Both methods are non-invasive and non-destructive and can be performed in situ in a short time frame with relatively mature data processing routines. A comprehensive literature review on the development and technical details of SWMs can be found in the works of Socco et al. (2010), Pelekis et al. (2011), and Foti et al. (2011).

The SASW method is adopted in this work for surface wave analysis. Unlike the MASW method that requires an array of grid of typically more that 12 geophones (Pelekis and Athanasopoulos 2011), SASW only employs two geophones, rendering it ideal to use two mobile robots such as UAVs to carry and deploy the geophone pair. The SASW method is a nondestructive seismic method for near-surface profiling of sites based upon the dispersive characteristics of Rayleigh-type surface waves propagating in a layered medium. The general objective of an SASW test, as of any SWM test, is to measure the Rayleigh wave dispersion curve experimentally and then to obtain the V_S (stiffness) profile of a site through inversion of the dispersion curve. The inversion is accomplished by deriving a subsurface model that has a theoretical dispersion curve that closely matches the experimental one. Although a complete SASW test ends with the determination of the V_S profile, the chapter only investigates the acquisition of field data and the derivation of the experimental dispersion curve, allowing for a direct comparison between the conventional technique and the UAV technique without introducing additional variability due to the inversion process (Garofalo et al. 2016). The emphasis in this study is placed on automating the data collection process and quantifying the data quality through the constructed dispersion curve.

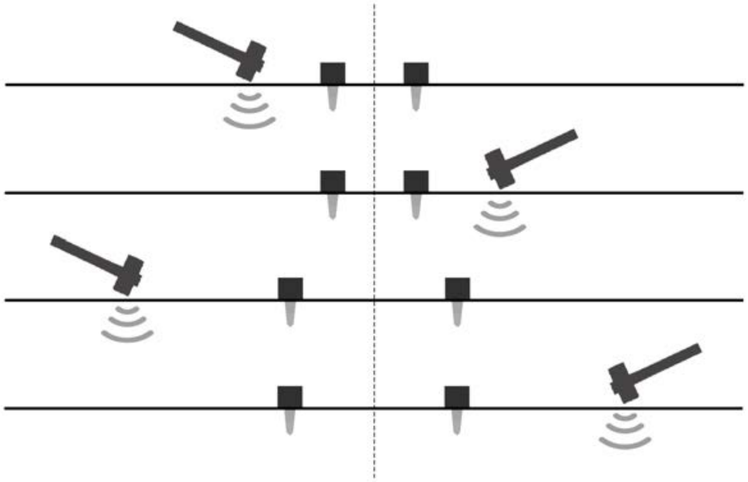

Figure 4-1. The CRMP scheme for two-station SASW testing.

A typical SASW test uses, most frequently, impulsive sources such as sledgehammers or steady-state sources such as electro-mechanical shakers to generate a seismic wave train that normally covers the frequency range of 5 to 200 Hz (Foti et al. 2011). Other sources have also been used, most recently a dropped mass using a UAV to generate the surface waves (Greenwood et al. 2018). Rayleigh waves are detected by a pair of vertically oriented receivers (e.g., geophones) that are deployed in a linear array along with the source. The inter-receiver distance is ordinarily kept equal to the distance between the source and its near receiver. By analyzing the phase of the cross-power spectrum (CPS) determined between the two receivers, dispersion curves showing surface wave velocities over frequency ranges are determined. The data collection and processing procedure is repeated with increasing inter-receiver spacings (usually ×2, ×4, ×8, …), with short spacings used to examine the shallow layers and long spacings for characterization at greater depths. The most common configuration of the SASW testing promoted in the literature is the Common Receiver MidPoint (CRMP) geometry (Foti 2000) as shown in Figure 4-1. In the CRMP geometry, the two receivers are moved away from a centerline located midway between the receivers. The source is placed at each side of the midpoint alternately to perform both forward and reverse profiling. The reversing of the source mostly serves to mitigate the effects of local material discontinuities or bedding inclination but also helps balance out internal phase distortion in the two geophones (Foti 2000).

4.1.2 UAV-Based Seismic Sensing

UAVs are aerial robots that can navigate autonomously or be remotely controlled by a human pilot. A vast number of civil engineering researchers and practitioners are embracing this emerging technology because UAVs provide an incomparable data acquisition capability in areas where conventional civil engineering tools would fail (Greenwood, Lynch, and Zekkos 2019). The agility and fast deployment of UAVs allow them easier and quicker access to traditionally difficult-to-reach areas such as remote sites and dangerous sites. Carrying a diverse range of onboard sensors such as cameras and LiDARs, UAVs can vastly increase the rate of data collection and improve data quality when necessary. Recent development of UAV autonomy further opens door to autonomous mission execution. The benefits presented by UAVs makes them potentially invaluable tools for geotechnical studies, especially those in hard-to-reach sites that occur in post-disaster scenarios. UAVs equipped with a RGB camera are most commonly used to document the damage to urban infrastructure after an extreme event occurs. Hundreds to thousands of high-resolution images can be captured over a broad perspective and stitched together to build a 3D point cloud model of a site using structure from motion (SfM) image processing techniques (Westoby et al. 2012; Schaefer et al. 2020). LiDAR is another sensor commonly incorporated into UAVs for mapping purposes. Airborne LiDAR systems have been deployed to generate high-resolution DTMs to help define damage patterns (Pellicani et al. 2019; Hirose et al. 2015), but are used less often due to their bulky size and high cost.

While site surface mapping is important to advance engineering practice and research, site subsurface exploration such as shear wave velocity profiling using SASW and MASW techniques remains a research frontier with a potentially significant impact in engineering practice. Conventional seismic surveying requires field teams placing wired geophone sensors in an array or grid configuration that covers the site under exploration and deploying an artificial seismic source such as a sledgehammer. As presented in Chapter 3, UAV can serve as a seismic source generator by dropping from aloft an instrumented weight to act on the ground surface and generate seismic waves that will be received by the geophones. Moreover, with the development of wireless geophone nodes shown in Chapter 3, UAVs can be employed, as a substitute for human operators, to deploy and retrieve sensor nodes following the MSN architecture. Most importantly, data collected from the geophones can be transmitted instantly to the UAVs or a base station through local wireless networks and get processed right away to provide invaluable subsequent planning insights. As a result, integrating a UAV platform to the seismic surveying framework may dramatically accelerate the time frames for reconnaissance teams to safely perform site subsurface investigations.

There have been some early but limited endeavors reported in the literature to develop a UAV-based autonomous system for subsurface sensing. Stewart et al. (2016) attached four 100 Hz spiked geophones to the bottom of a 3DR Solo quadcopter as the UAV's landing legs. The authors reported an average spike penetration depth of about 10 mm when the UAV landed on grass. The UAV-geophone pair demonstrated the ability to record reasonable seismic data but with an offboard seismograph which is designed for wired geophones, limiting the mobility and modularity of the prototype model. Sudarshan et al. (2017) proposed two robotic systems to automate seismic sensor deployment: a UAV capable of dropping dart-shaped geophone sensors that penetrate into soil and a ground hexapod robot with three of the legs replaced by spiked geophones. Although the paper showcased several successful tests of autonomous sensor placement, location accuracy was relatively low at the meter-scale level. Also, sensor retrieval conducted in the study was a manual process with the help of a human-piloted UAV. The geotechnical industry has also endorsed the view of dropping wireless seismic nodes from UAVs for seismic surveying (Rassenfoss 2017; Whaley 2018). These recorders, known as downfall air receiver technology (DART), are as the name implies, shaped like a dart and can penetrate into the ground and biodegrade after the survey without the need for retrieval. Challenges remain such as ensuring the landing sensors in a nearly vertical position and using completely biodegradable material to keep the DART's environmental footprint to a minimum.

4.1.3 UAV-Enabled Automated Seismic Surveying Using SASW

This study explores the usage of UAVs for performing automated seismic surveying using the SASW method. The work emphasizes truly autonomous operations across the full range of seismic surveying including placement of geophone sensors in an array pattern, triggering of a seismic event, and wireless collection of seismic data. Figure 4-2 provides a schematic overview of the proposed RAS solution to conduct SASW tests. Sensor deployment is accomplished by two autonomous UAVs flying to desired sensor installation locations following the CRMP scheme. A third UAV is used to deploy seismic

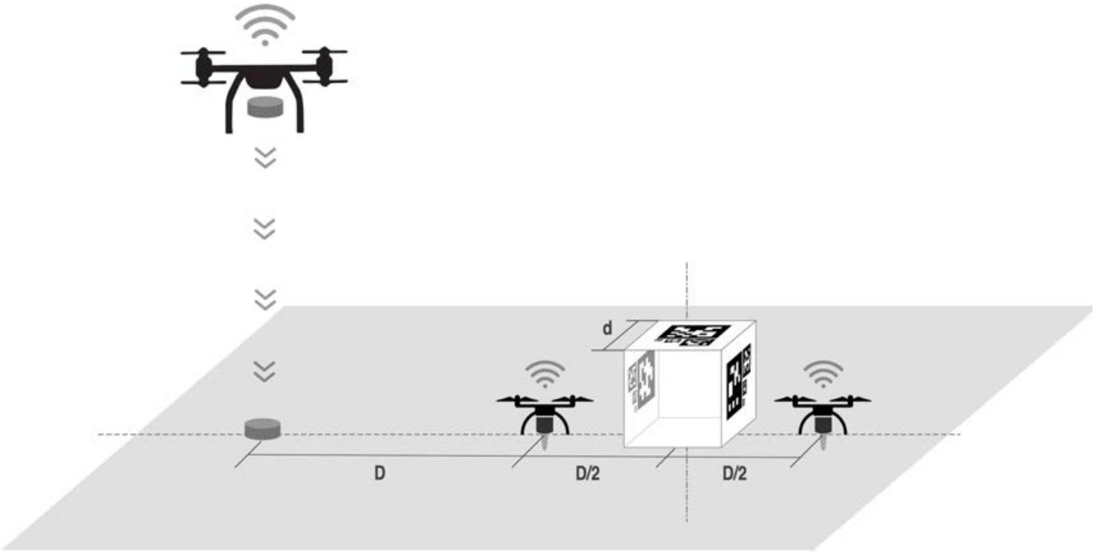

Figure 4-2. Overview of the proposed autonomous UAV system for automated seismic surveying using the MASW method with two smaller UAVs deploying two geophone sensors and a big UAV triggering a seismic event.

sources by dropping from aloft an instrumented weight as illustrated in Chapter 3 and presented by our research group in Greenwood et al. (2018) and (2021). The biggest challenge pertaining to realizing the CRMP geometry is the alignment of the seismic source and the two receivers and maintaining specific distances between the three components. This study fulfills these stringent geometric requirements of CRMP by using vison-aided precision control of the UAVs. Similar to Chapter 2, multi-resolution AprilTag patterns are adopted to provide reliable relative position estimations for the UAVs. The work proposes a cube shaped object with multi-resolution AprilTag patterns applied on three of its six faces that will be placed at the receiver midpoint serving as a landmark for position reference. The cube is supposed to be deployed by a UAV before the SASW test, thereby eliminating the need for human interventions. Table 4-1 summarizes the requirements and challenges associated with the proposed RAS solution. This chapter meets all key

Table 4-1. Requirements and challenges of UAV-enabled automated seismic surveying using the SASW method (✓: resolved in this study; ✕: unresolved and requiring future investigations)

	Requirements		**Challenges**	
Sensor placement	Moving receivers in a straight line consistently	✓	Ensuring tight ground coupling	✕
	Maintaining certain distances between the two receivers	✓	Maintaining a vertical position of the geophone sensor	✓
Seismic source deployment	Payload release mechanism	✓	Ideal size and shape of the drop weight	✕
	Payload release from a certain height	✓	Ideal drop weight	✕
	Payload retrieval	✓	Registering the landing location of the weight	✓
	Aligning the impact source on the line formed by the two receivers	✓		
	Keeping the distance between the source and near receiver equal to the distance between the two receivers	✓		
Data collection, storage, and processing	Wireless communication among receivers, the UAV, and the base station	✓	Verifying data quantity is sufficient	✕
	Dispersion curve construction	✓	Verifying data quality is sufficient	✕
	V_S profile generation	✕	Instant knowledge about ideal inter-receiver spacings	✕

requirements while leaving several challenges open for future research. The work aims to make three major intellectual contributions. First and foremost, the knowledge gap in automating seismic surveys using RAS is addressed. The RAS solution proposed in this research is the first of its kind that is intended for automated subsurface imaging in remote or dangerous environments. Second, this research showcases several advanced Stage 3 and

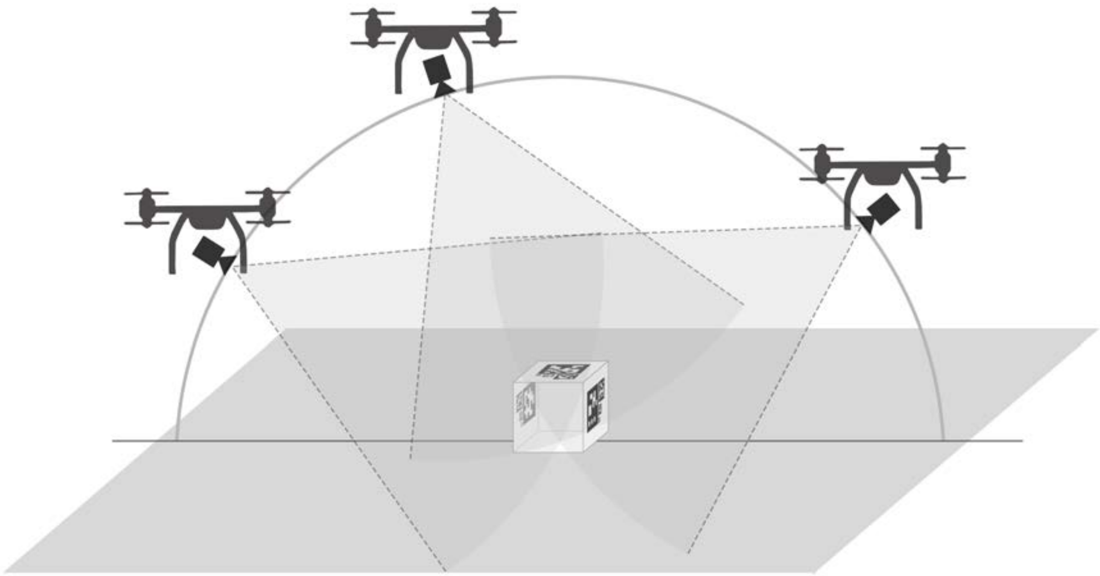

Figure 4-3. Detection zone of the cube using a camera with a one-axis elevation gimbal and a 60° field of view.

Stage 4 UAV technologies and the integration of them including vision-based precision position control and robotic manipulation. Third, seismic data collected by the RAS solution is used to construct a dispersion curve of the testing field, whose shape is shown to be similar to one constructed from a human-deployed wired data acquisition system.

4.2 UAV Platform: Hardware and Software

The UAV platforms adopted in this chapter is similar to those used in the previous two chapters (one 3DR X8 for weight dropping, and two Lumenier QAV210s for sensor deployment) with specific modifications of the onboard cameras to cater to the detection of the cube. Ideally, with a gimbaled camera capable of moving in the elevation (i.e., pitch) direction included in the UAV system, the cube can be detected in a semicircle shaped area as shown in Figure 4-3. The radius of the semicircle is dependent on the detection range of the AprilTag patterns on the cube faces, which is easily adjustable by using different sizes

(a) (b)

Figure 4-4. The QAV210 quadcopter used in this study to deploy wireless geophone nodes: (a) UAV landing in front of the cube with key hardware components highlighted; (b) the geophone sensor together with its three-spike base that are firmly attached to the bottom of the UAV.

of print. In this study, to speed up the development of the UAV systems, gimbaled cameras are not adopted. Instead, cameras with fixed orientations are installed on the UAVs with some sacrifice in the size of the detection area. However, these fixed cameras are still able to provide necessary visual estimations for precise localization of the UAVs during their autonomous operations. For instance, the smaller QAV210 has a forward-facing camera (Figure 4-4(a)) and uses the AprilTag pattern on the side face of the cube for position reference while flying relatively low to the ground. The X8 has two cameras installed onboard, one facing forward and the other facing downward in replacement of an elevation gimbal.

Installed on the QAV210 is also the wireless sensor node developed in Chapter 2. A Geospace GS-11D 4.5 Hz geophone is connected to the wireless node for recording ground vibration velocities. Typically, geophone sensors are mounted in an insulated enclosure with a spike attached to the bottom. The spike is meant to be inserted into the ground to ensure minimum transmission loss from seismic ground motion to the motion of the geophone. Geophone ground coupling is still not a well-understood problem regarding the ideal length, shape, and penetration depth of the spike (Krohn 1984; Drijkoningen 2000; Segarra et al. 2015). When using robotic systems such as UAVs to deploy the spiked geophones, specific challenges arise such as how to penetrate the spikes into the ground and how to maintain a vertical position of the geophone after its installation. In this study, these challenges are overcome by using a three-spike base for the geophone that also serves as landing legs for the UAV (Figure 4-4(b)). Geophone ground coupling relies on the self-weight of the UAV to push the spike ends into the ground after the UAV lands. During development and testing, the average penetration depth in a typical grass field was found to be about 1.0 cm with the 1.7 kg QAV210 UAV.

The UAV software is much like that articulated in the previous two chapters. The QAV210 adopts the same FSM design as shown in Figure 2-7 with some changes in the precision landing module. The desired landing point is now defined at the sensor installation location (a predefined distance, $\frac{D}{2} - \frac{d}{2}$, away from the vertical AprilTag plane as shown in Figure 4-2). The forward-facing camera on the QAV210 is able to detect the vertical multi-resolution AprilTag pattern and use it for precise relative position estimation during the entire landing process. The X8 follows the autonomous weight drop-off and pickup FSM defined in Figure 3-6 with an additional step of flying to the desired weight drop-off location after “Take off” and before “Drop off payload”. This weight drop-off location is defined based on the CRMP geometry and a preset height (Figure 4-2). Again, the X8 uses visual feedbacks from the cube and its internal cascaded PID controller to correct its position until it reaches the desired location for payload dropping. Similar to Chapter 2, a Kalman filter and a visual-inertial fusion method are employed to provide robust and reliable relative position estimations for the UAV. The overall software architecture for the two computing units on the X8 (i.e., the TX2 and the Pixhawk) is identical to that shown in Figure 2-5 with the exception that everything related to “precision landing” is modified to “precision loiter” so that the X8 can precisely loiter near the desired payload drop-off location before releasing the payload.

4.3 Dispersion Analysis

The experimental dispersion curve is derived from the phase of the CPS between the two receivers. This “folded” phase, ranging between $-\pi$ and $+\pi$, provides the relative lead or lag between the two signals detected by the pair of receivers. The cumulative phase shift between receivers is obtained from “unfolding” the phase plot by identifying phase jumps going from $-\pi$ to $+\pi$ (or $+\pi$ to $-\pi$) in the folded phase plot. The phase velocity V_R, as a function of frequency f, is obtained from the unfolded phase angle $\Phi(f)$ (in rads) together with the inter-receiver spacing D, using the following relationship:

$$V_R(f) = f \cdot \frac{2\pi}{\Phi(f)} \cdot D. \tag{4-1}$$

One important aspect of the above procedure is the influence of data quality. Portions of the phase plot with low SNR has to be eliminated to construct the correct dispersion curve. This is usually accomplished using the coherence function, whose value ranges between 0 (totally unrelated signals corrupted with noise) and 1 (linearly correlated signals without noise). The evaluation of the coherence function necessarily uses several pairs of signals from the two receivers, leading to a requirement for repeated testing on the same source-receiver layout. A small decline of the coherence function (e.g., less than 0.99) usually indicates large fluctuations in the phase. Therefore, frequency ranges corresponding to low values in the coherence function are rejected during the development of the dispersion curve. In addition to the coherence criterion, there are also restrictions for the acceptable range of wavelengths such as those suggested by Heisey (1982):

$$\frac{D}{2} < L_R(f) < 3D, \tag{4-2}$$

where $L_R(f) = \frac{V_R(f)}{f}$ is the wavelength. The dispersion curve is further screened following Equation (4-2) to avoid the near field and far field effects. The process of building dispersion curve is repeated using successively larger receiver spacings for signals with lower frequency and longer wavelength. These individual dispersion curves from different receiver spacings are stitched together to form a composite dispersion curve for the site.

4.4 Experiments and Results

Field experiments were performed at the Scio Flyers Model Aircraft Club in Scio Township, MI. The aims of the experiments were twofold. The first set of tests (experiment 1) was carried out to test if the proposed RAS solution can reliably realize the CRMP geometry. An inter-receiver spacing of 4 m was chosen and thoroughly tested. Tests were performed multiple times to build up a statistical basis for evaluating the positioning accuracy of system. The second set of tests (experiment 2) was conducted to investigate the usefulness of the ground-coupling measurements compared to data collected from a

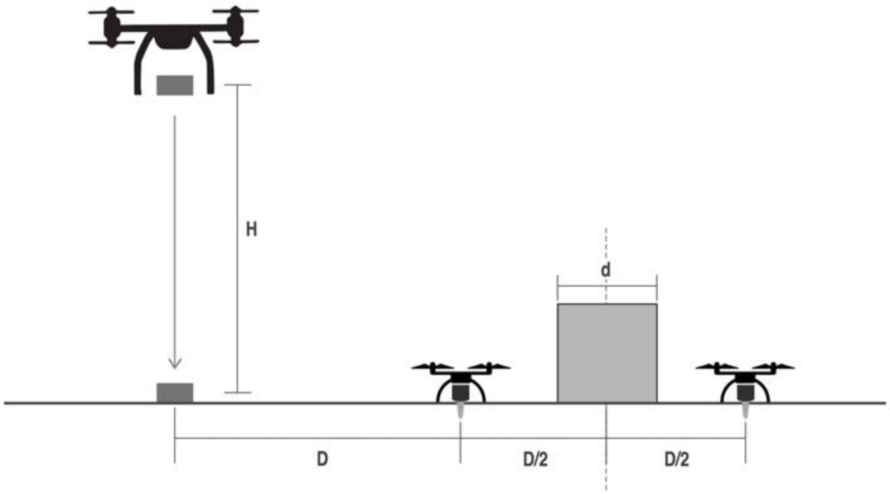

Figure 4-5. Schematic overview of experiment 1 ($D = 4$ m, $d = 0.5$ m, $H = 6$ m).

separate set of well-planted wired geophones. The aim was to see whether the same dispersion curve can be built from the measurements.

4.4.1 Experiment 1: Sensor Installation and Source Deployment Accuracy

As mentioned above, these tests were undertaken to evaluate the positioning accuracy of the proposed RAS. Figure 4-5 shows the schematic overview of the first experiment. For testing and validation purposes, a cube with a side length, d, of 0.5 m was used. Three unique multi-resolution AprilTag patterns were firmly attached on the left, right, and up faces of the cube. The AprilTag pattern adopted the same design as shown in Figure 2-10(b) including four tags with side lengths of 22.4 cm, 11.2 cm, 5.6 cm, and 2.8 cm. The pattern has a detection range of about 12 m when an image resolution of 640×480 px^2 is used. Extended range is achievable through the use of larger tags or higher resolution cameras. In this experiment, inter-receiver spacing, D, was set to be 4 m, and the drop weight height, H, was to set to be 6 m.

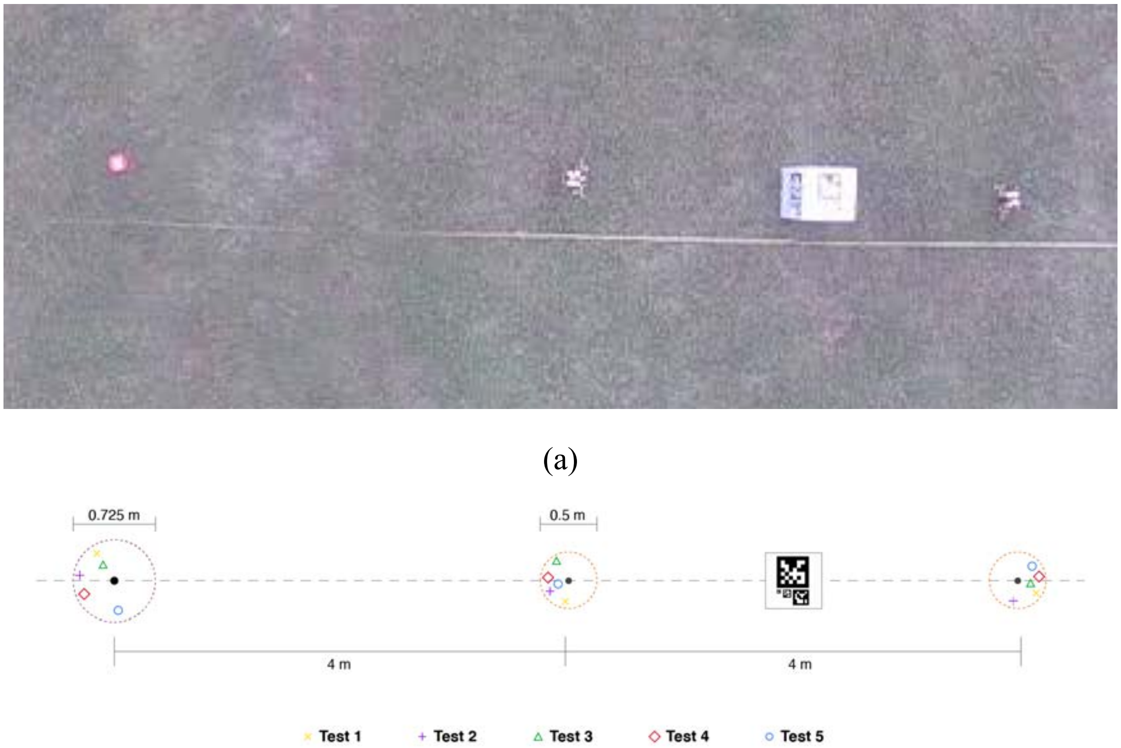

(a)

(b)

Figure 4-6. Sensor deployment and weight dropping accuracy: (a) bird's-eye view of a typical field test; (b) spatial accuracy of five field tests.

Figure 4-6 illustrates the locations of the landed UAVs and the dropped weight after repeating the test five times. All landing locations are within 0.5 m (shown with dashed orange circle with 0.5 cm radius) from their desired locations. Drop weight locations are within a slightly larger deviation of 0.725 m from their desired locations, although as discussed in Greenwood et al. (2021) this accuracy can be increased significantly, when necessary with a number of methods including RTK GPS, or other visual-based positioning control. However, for the purposes of this study, improving the accuracy of the drop location was not an objective. Another interesting finding from Figure 4-6 is that the positioning algorithm is precise (i.e., all measurements are close to each other) but not very accurate (i.e., measurements are not close to the true value). This behavior is expected as

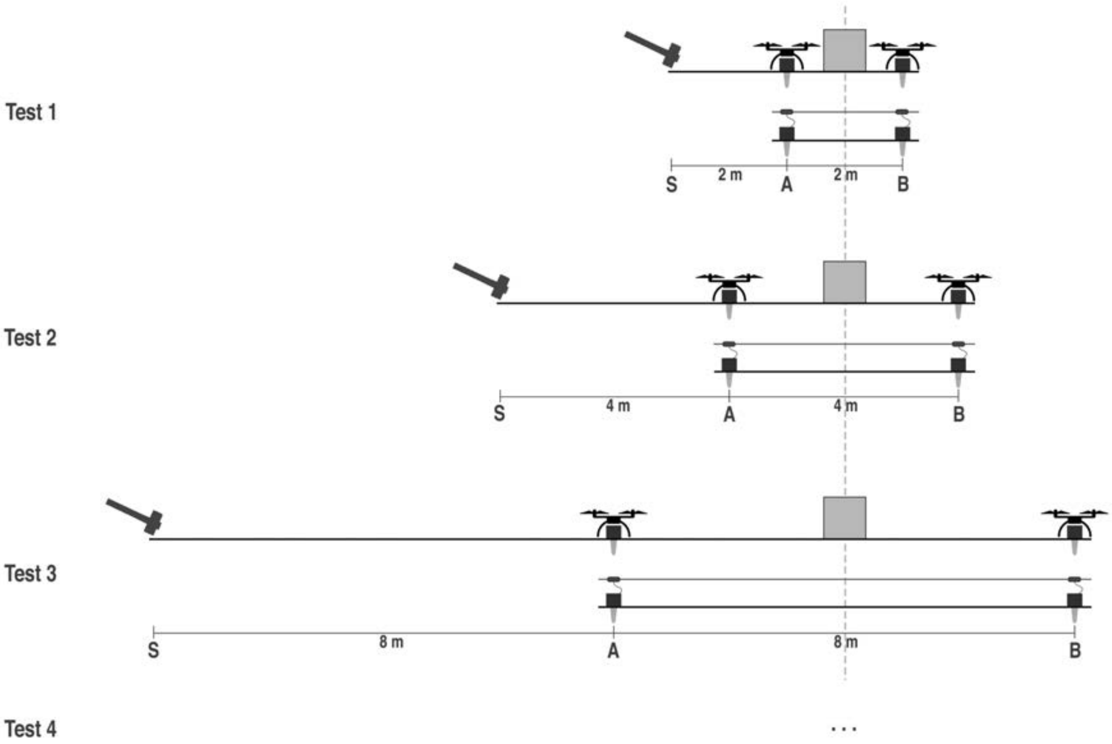

Figure 4-7. Schematic overview of experiment 2 (spacing between receivers of 2, 4, 8, and 16 m are used).

Figure 2-15(c) suggests that the accuracy of the AprilTag position estimation algorithm decreases as the camera moves away from the tag pattern. This reduced accuracy can be resolved by carefully calibrating the system before using it.

4.4.2 Experiment 2: Data Quality Assessment and Dispersion Analysis

In this set of tests, the usefulness of the data collected by UAV-deployed wireless geophones is investigated with respect to their use for dispersion analysis of the field site. The schematic overview of the second experiment is shown in Figure 4-7. A 5.4 kg sledgehammer was adopted as the seismic source instead of the UAV-dropped weight to increase the data acquisition speed and the quality of the seismic data collected. As Greenwood (2018) estimated, the 5.4 kg sledgehammer source has similar energy output to dropping a 4.7 kg mass from a 15 m height (approximate potential energy of 700 J), and the relatively light 0.93 kg drop weight adopted in this study is only “appropriate for testing where high frequency surface waves transmitted across short distances are of interest”. Also, during development and testing, it has been found that the steel plate used in this study has a tendency to bounce (i.e., recoil) after impacting the ground, resulting in poor data quality. Greenwood et al. (2021) has shown that the bounce on the ground is reduced when the mass is dropped from a higher elevation and that a sphere drop weight provides better quality data. Optimization of the drop weight was also outside the scope of this study. As shown in Figure 4-7, a total of four tests were conducted with inter-receiver spacings of 2, 4, 8, and 16 m, respectively. Each test was performed in three steps. First, two QAV210 UAVs were manually flown to the desired sensor installation locations, *A* and *B*, one at each side of the cube. The manual operations of the UAVs were to eliminate errors in positioning the UAVs and ensure accurate sensor installations. Then, two wired geophones (GS-11D 4.5 Hz vertical), same as those attached to the wireless nodes but with a single spike, were manually deployed besides the wireless geophone nodes for direct comparison. The wired geophones were connected to a commercial seismograph (Geometrics ES-3000) for seismic data collection. Finally, seismic waves were generated by manually operating the sledgehammer at the desired source location, *S*. The hammer was operated five times in each test to obtain five sets of data, which were stacked in later processing for improved SNR. Figure 4-8 illustrates the hardware layout of the SASW tests performed in the field site. In addition to the SASW tests, an MASW test was also conducted to provide a dispersion curve of the site as the baseline for comparison. The MASW test used a 2 m receiver spacing and 5 m nearest offset. The midpoint of the MASW

Figure 4-8. SASW field tests for comparison of data acquisition from UAV-deployed wireless geophones and a commercial wired system.

survey line coincided with the SASW-CRMP survey line so that the two tests share similar sampling range in the space. The seismic source in the MASW test was the same sledgehammer, which was applied five times on the strike plate for signal stacking.

Figure 4-9 to Figure 4-12 show the collected wireless and wired geophone measurements at position *A* and *B* in both the time and frequency domains. It can be observed that for the wireless-wired sensor pair close to the source, the single-spike wired geophone is more sensitive to ground vibrations at the moment of detection (larger wave amplitude) but also dissipates energy quicker than the three-spike wireless geophone. This phenomenon is not obvious though for the other sensor pair at the farther end of the source. In the frequency domain, the wired geophone almost always picks up more energy in the high frequency band (≥ 70 Hz) than the wireless geophone.

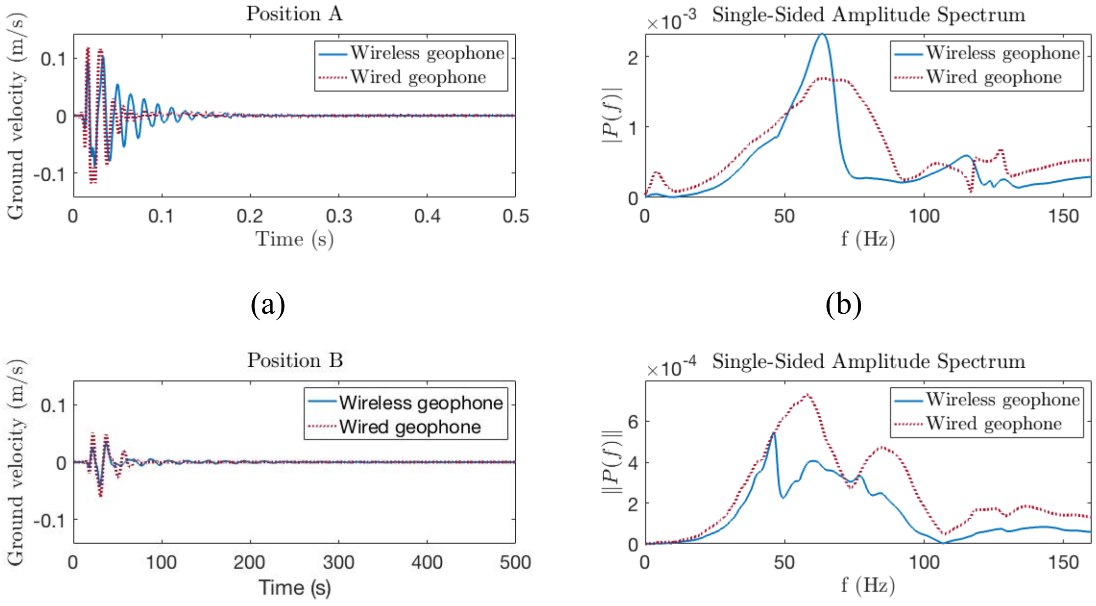

(a) (b)

(c) (d)

Figure 4-9. Comparison between wireless and wired geophone measurements at position *A* and *B* (Figure 4-7) with 2 m spacing in both the time and frequency domains.

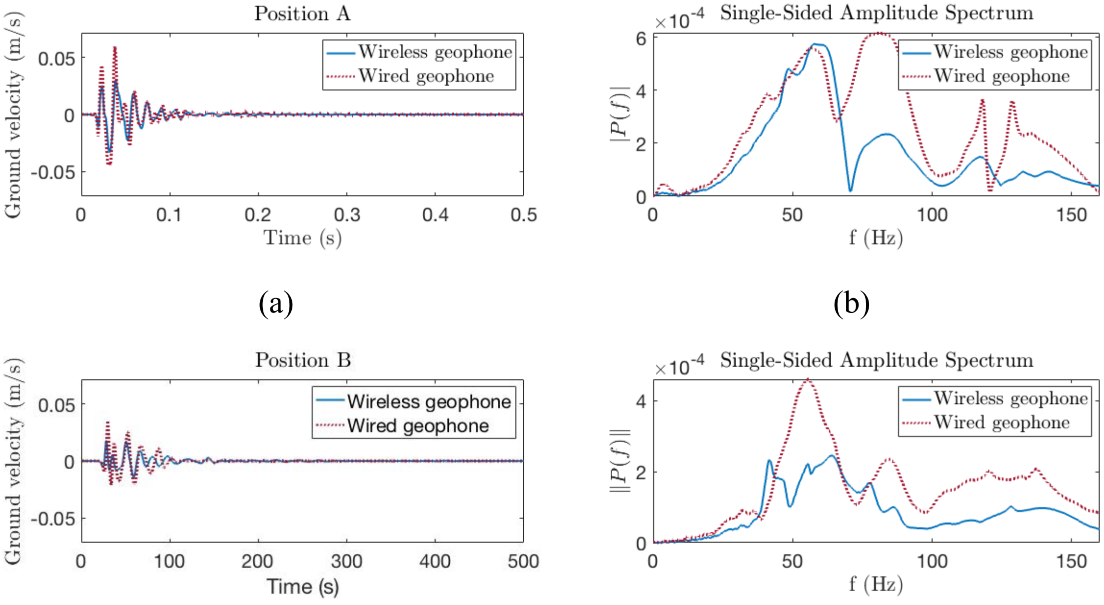

(a) (b)

(c) (d)

Figure 4-10. Comparison between wireless and wired geophone measurements at position *A* and *B* (Figure 4-7) with 4 m spacing in both the time and frequency domains.

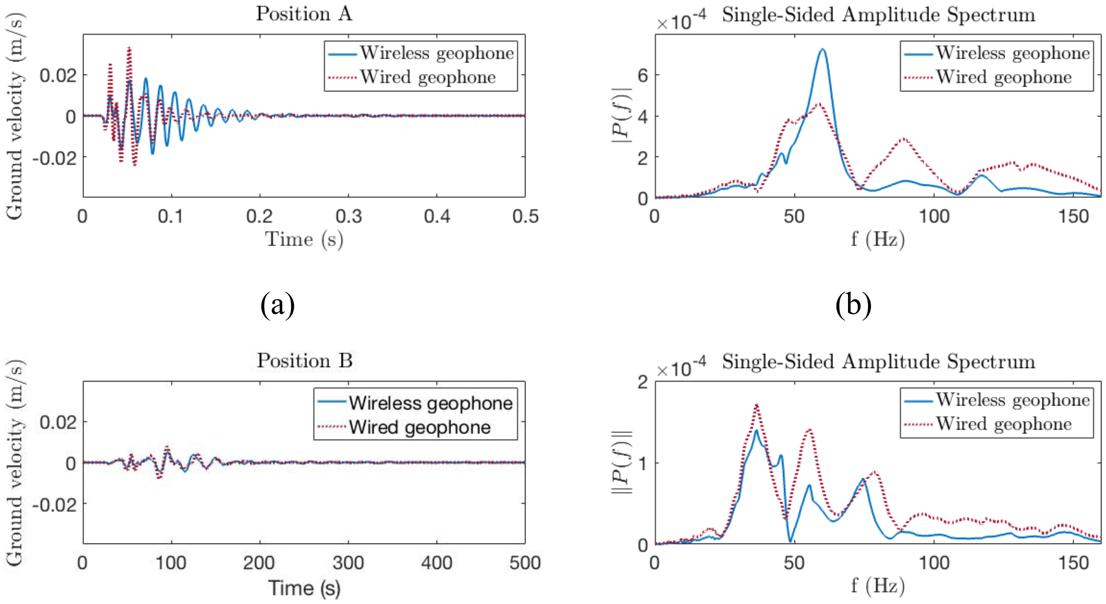

(a) (b)

(c) (d)

Figure 4-11. Comparison between wireless and wired geophone measurements at position *A* and *B* (Figure 4-7) with 8 m spacing in both the time and frequency domains.

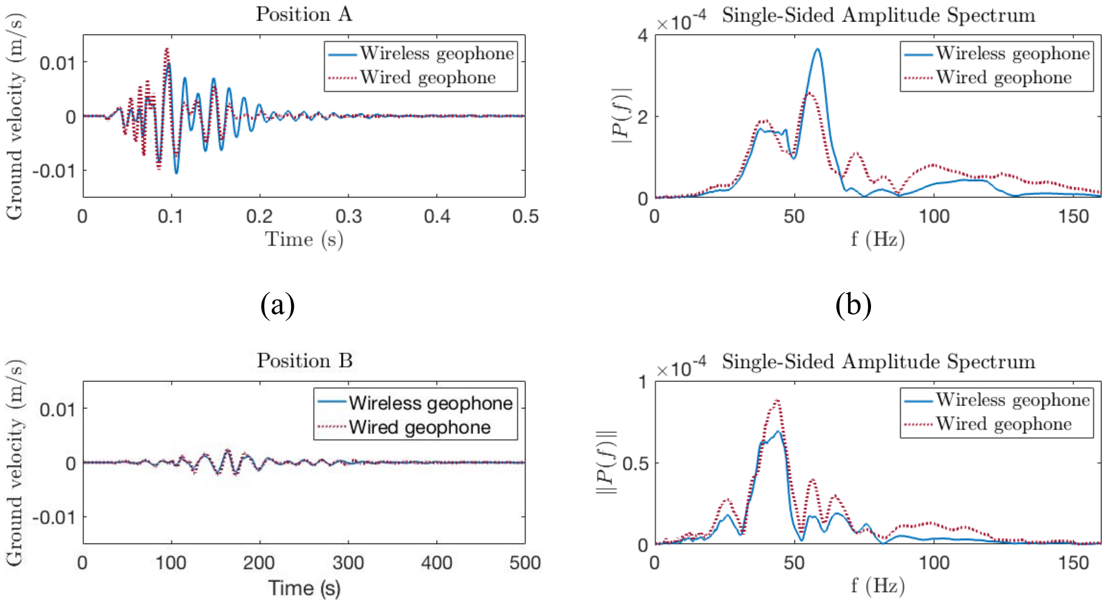

(a) (b)

(c) (d)

Figure 4-12. Comparison between wireless and wired geophone measurements at position *A* and *B* (Figure 4-7) with 16 m spacing in both the time and frequency domains.

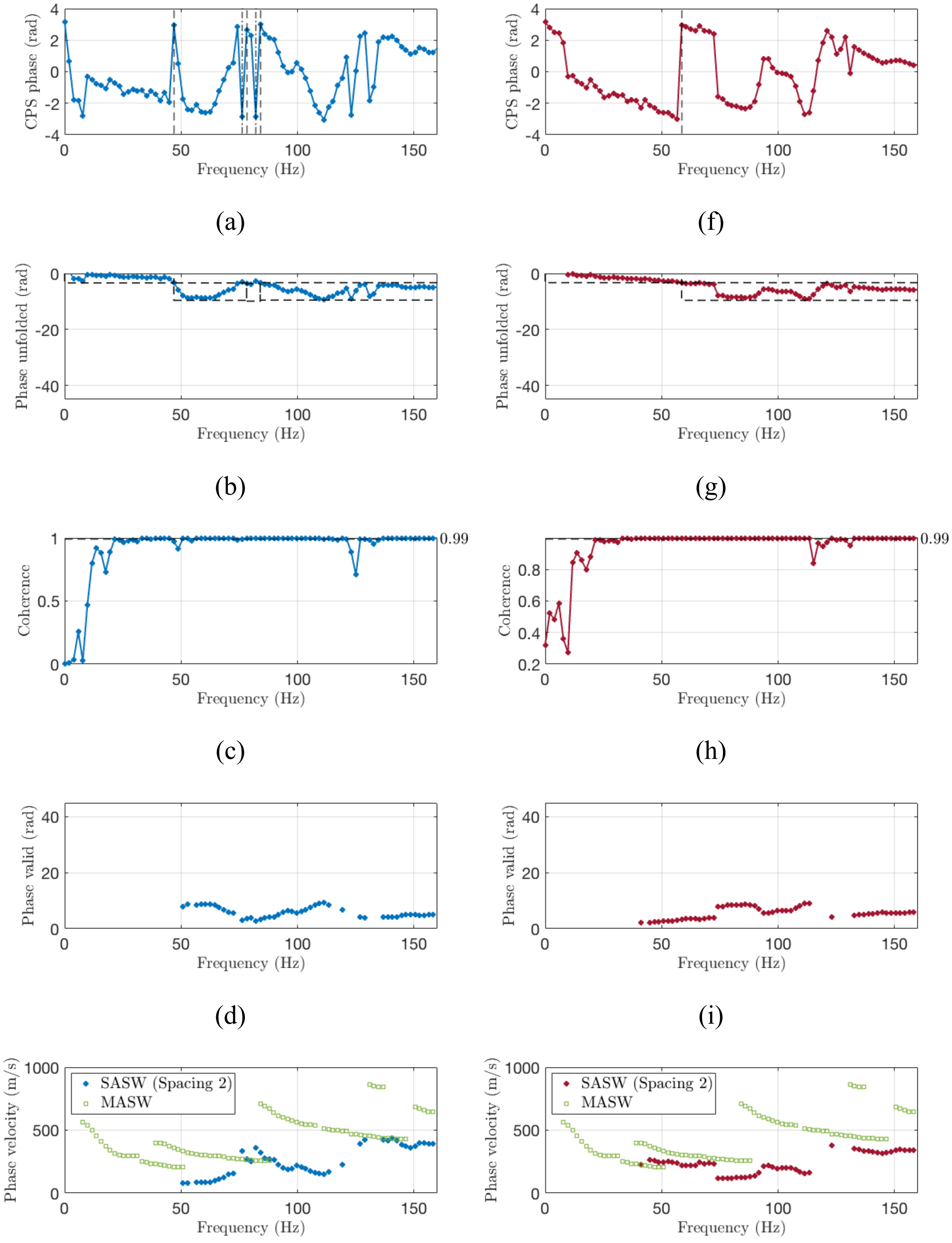

(a) (f)

(b) (g)

(c) (h)

(d) (i)

(e) (j)

Figure 4-13. Two-receiver data elaboration when inter-receiver spacing is 2 m: (a)-(e) wireless geophones; (f)-(j) wired geophones.

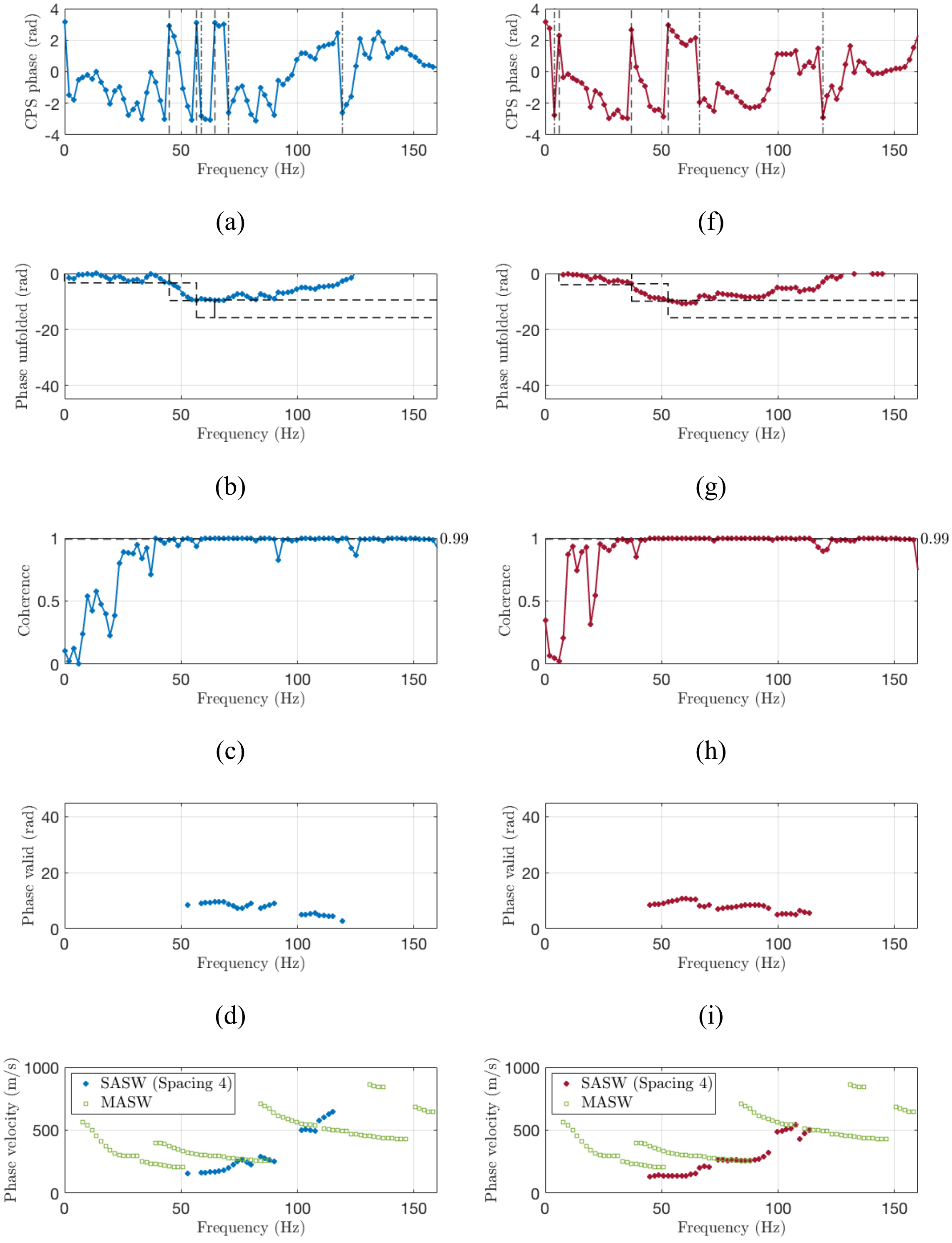

(a) (f)

(b) (g)

(c) (h)

(d) (i)

(e) (j)

Figure 4-14. Two-receiver data elaboration when inter-receiver spacing is 4 m: (a)-(e) wireless geophones; (f)-(j) wired geophones.

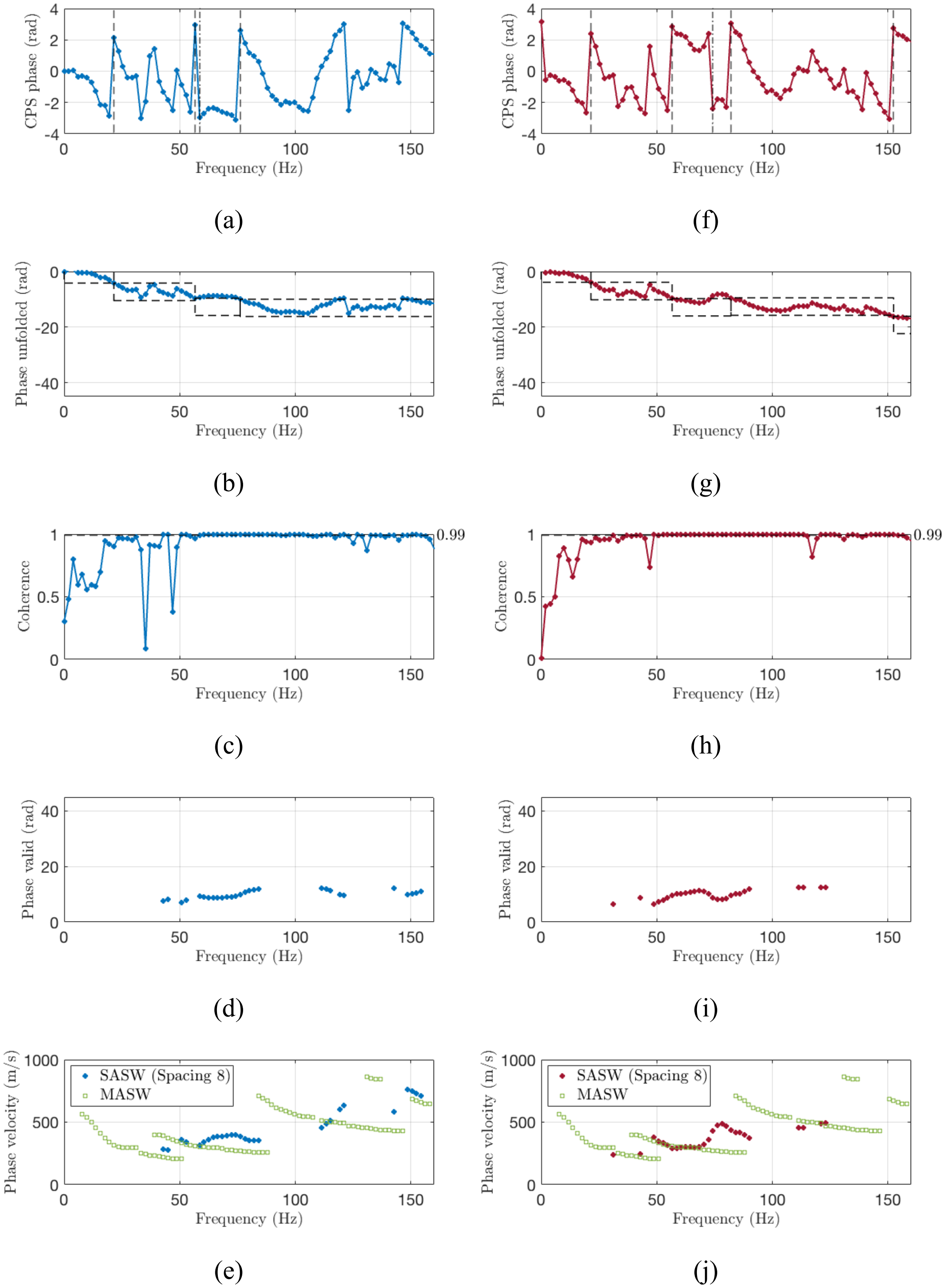

(a) (f)

(b) (g)

(c) (h)

(d) (i)

(e) (j)

Figure 4-15. Two-receiver data elaboration when inter-receiver spacing is 8 m: (a)-(e) wireless geophones; (f)-(j) wired geophones.

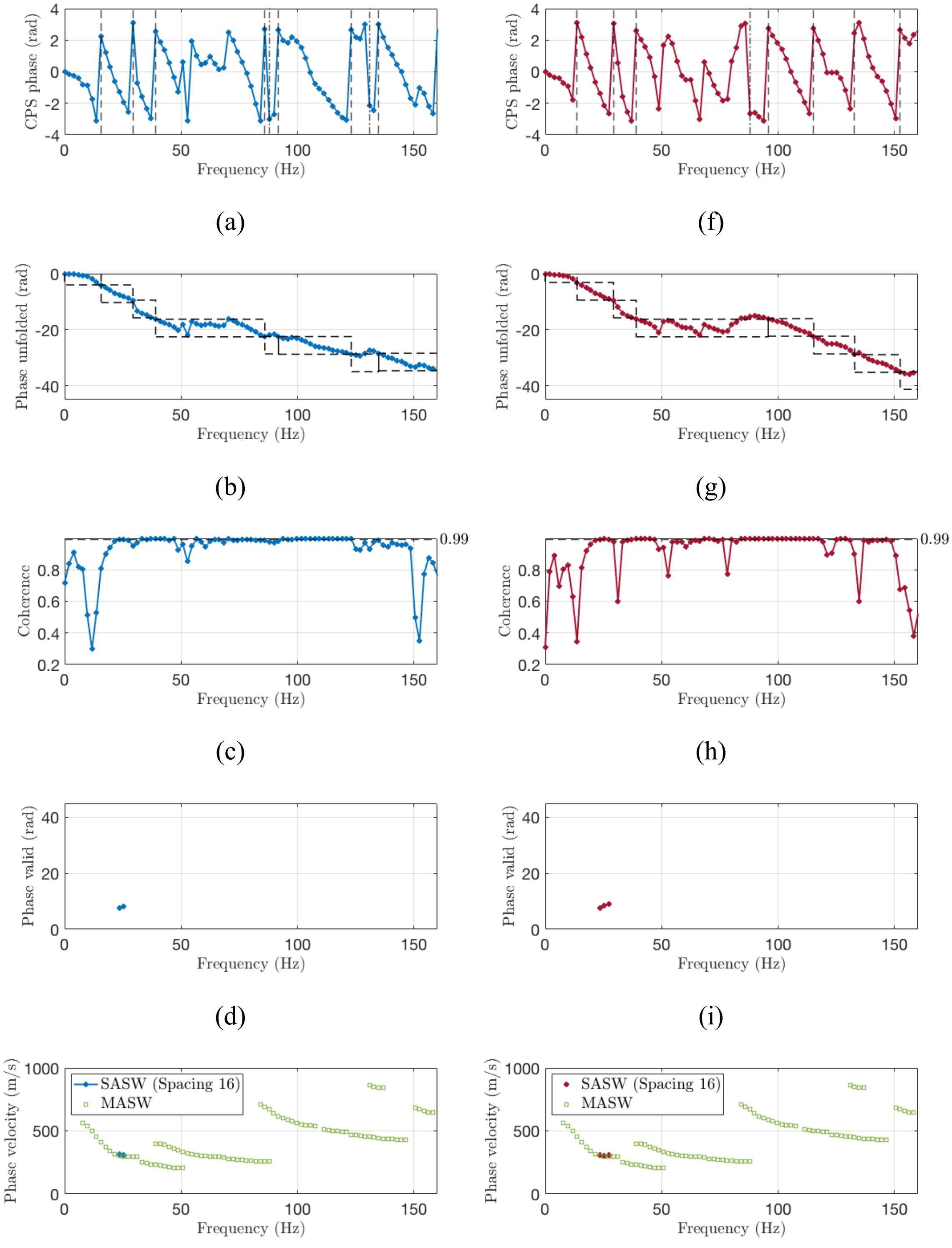

(a) (f)

(b) (g)

(c) (h)

(d) (i)

(e) (j)

Figure 4-16. Example of a two-receiver data elaboration when inter-receiver spacing is 16 m: (a)-(e) wireless geophones; (f)-(j) wired geophones.

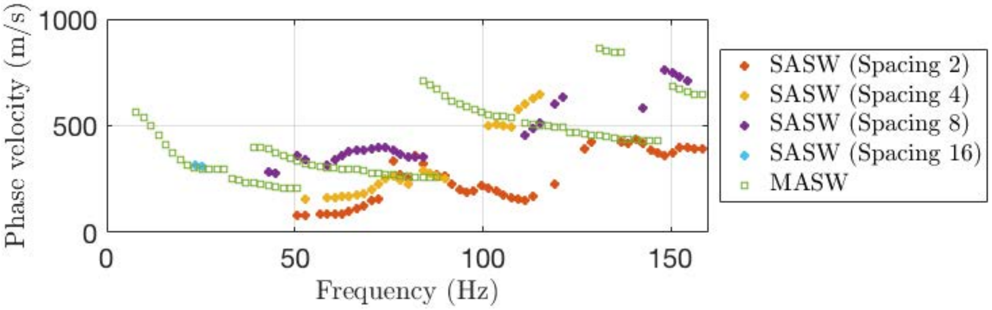

(a)

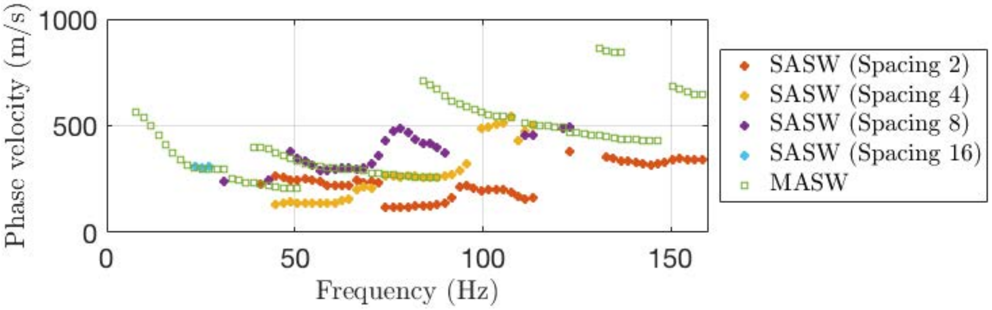

(b)

Figure 4-17. Comparison of dispersion curves constructed from the MASW method and those built from the SASW method using (a) wireless geophone measurements and (b) wired geophone data.

Figure 4-13 to Figure 4-16 illustrate the development of dispersion curves using both wireless and wired geophone data under each inter-receiver spacing. The process starts by computing the CPS phase (a and f) of the signal pair collected at position *A* and *B* and unfolding it (b and g). Data with a coherence score below 0.99 (c and h) and that not satisfying the wavelength criteria (Equation (4-2)) is then discarded to form the valid phase plot (d and i), from which the dispersion curve (e and j) can be constructed directly using Equation (4-1). The figures also provide a side-by-side comparison of each step built from data collected by the wireless and wired geophone sensors. The resulting dispersion curves of each spacing are closely matched, which validates the quality of data collected using the proposed UAV systems. Figure 4-17 shows the comparison of dispersion curves developed from the MASW and SASW techniques. The SASW data using the wireless geophones were successful in capturing the first and second modes.

4.5 Conclusion

An innovative RAS solution for subsurface characterization of geosystems using the SASW technique is introduced in this study. As a natural extension to the previous two chapters, this chapter combines the efforts and accomplishments already made into a feasible solution to fully automating seismic surveying in remote or dangerous areas. Three independent UAVs are adopted in the RAS and work collaboratively to install wireless geophone sensors, trigger seismic events, and collect seismic data. The work shows excellent positioning accuracy of the UAVs being able to meet the CRMP geometric requirements. The work verifies the quality of the data collected by the UAV-deployed wireless geophones comparable to that collected by well-planted single-spike wired geophones. The study also highlights the RAS's ability to construct complete in situ dispersion curves of a field site.

Chapter 5 Conclusions and Future Research Directions

5.1 Summary and Conclusions

As sensing technology has rapidly matured, the ability to deploy large arrays of sensors in various engineering applications has increased. In particular, the integration of miniaturized sensors, low-power embedded system components, and wireless telemetry has fueled the Internet of things (IoT) revolution. While these advances have undoubtedly created new opportunities for monitoring, the majority of current structural monitoring systems adopt permanently installed sensors that are manually deployed and remain in a fixed location indefinitely. Recent advances in robotics have made mobile robots increasingly suitable for field operations. Robot-operated sensor deployment has the potential to extend the scope of structural condition assessment far beyond the range of currently available mechanisms. Particularly, robots offer mobility to wireless sensors and enable easy configurations of the geometry of a WSN. Besides bringing mobility and adaptability to WSNs, autonomous robots also give possibility to automation of field monitoring operations, leading to increased efficiency and reduced cost. Given the significant potential of robotics and automation technologies, the overarching goal of this dissertation is to explore the feasibility of using autonomous UAVs to automate structural monitoring and geo-structural analysis of civil infrastructure systems.

The focus of the research presented in this dissertation is to build a UAV autonomy framework necessary to automated sensor deployment in response to the field's prevailing challenges: accurate UAV positioning in outdoor environments and extended sensing capabilities beyond photogrammetry. This is demonstrated in this dissertation through the development of a vision-aided control algorithm for outdoor UAV localization and the creation of several unique UAV-sensor pairs tailored for civil engineering applications such as structural analysis and geotechnical site characterization. Furthermore, the sensing systems feature fully autonomous deployments by UAVs to reduce their installation time and cost, so their adoption and proliferation are more practical. As a prerequisite to mobility, sensors deployed by UAVs need to be untethered, with the potential of obtaining data and transmitting them in real time over a wireless link to aid asset owners in onsite decision-making. Towards this end, a wireless geophone node capable of being deployed by a UAV and collecting GPS-time-annotated seismic vibrations is developed. The resulting seismic sensing platform and its autonomous deployment by UAVs will greatly facilitate seismic data collection in difficult-to-reach sites, particularly those occur in post-disaster scenarios. The contributions of the dissertation combine to assist automation of field monitoring operations, especially the arduous and repetitive ones, so that humans can focus on tasks that require creativity and critical thinking. The hope is that the UAV technologies developed in this dissertation and its applications in SHM will open door for a new civil infrastructure monitoring paradigm that is safe, efficient, and with minimal human intervention. The research results and contributions of each chapter are summarized as follows.

To confront the challenge that GPS-based UAV outdoor navigation lacks the accuracy necessary for precision placement of sensor payloads on structures, a vision-aided UAV localization algorithm was developed (described in Chapter 2). A calibrated camera combined with a set of four multi-resolution fiducial markers with known sizes are adopted to provide pose estimation for the UAV. Various sets of markers are attached to the surface of the structure that identify sensor placement locations. The UAV uses these artificial visual attributes as both navigation landmarks and precision landing targets. To compensate for cases where visual detections are not available, the chapter builds a robust visual-inertial fusion framework based on a discrete-time Kalman filter. Synchronization between the camera and IMU sensor is accomplished by cautiously measure delays in data transfer between the two computing components onboard the UAV: the Pixhawk flight controller and the Nvidia Jetson TX2 computer. Relative position and velocity estimations of the UAV with respect to the landing pad are integrated into the cascaded PID control law for precision landing. Validation of the proposed vision-aided control strategy of the UAV is performed in M-Air, a netted outdoor flying lab where a sophisticated motion capture IR system is installed and used as ground truth. The autonomous UAV landing achieves great accuracy; the UAV is able to land on a predefined landing point within 10 cm in 22 out of a total of 25 landing tests.

The UAV autonomy framework is shown (in Chapter 2) to be successful for control of UAV flight operations and sensor placement using only the onboard computing resources of the UAV. This is achieved through a dedicated FSM that is embedded on the onboard TX2 SBC. The FSM approach partitions a complicated system into a set of well-defined states with deterministic interconnections between them. One attractive attribute of this approach is its scalability: the UAV autonomy architecture can be easily extended to other autonomous applications by defining custom-built processes and transitions. In this chapter, the UAV autonomy framework is devoted to moving wireless accelerometers to locations on a beam structure. The UAV is able to explore the beam structure following a predetermined flight path, localize itself around the sensor installation locations defined by AprilTag patterns applied on the beam surface, and precisely land on top of the pattern for sensor placement. The case study proves the quality of the acceleration data collected by performing complete modal analysis of the monitored structure using reconfigurable sensor networks. It should be highlighted that the integrated UAV-enabled sensing system is fully autonomous where the only human intervention is impacting the beam with a modal hammer (which emulates ambient vibrations), although this latter process can also become autonomous.

A step forward in implementing UAV-based sensing of civil infrastructure is to allow UAVs to interact with the environment beyond flythroughs. One example of such interactions with geo-infrastructure is provided in Chapter 3, where a UAV is used to drop a payload to generate Rayleigh surface waves for subsurface characterization of the ground. Equipped with a downward facing LiDAR sensor acting as an altimeter and an EPM gripper, the UAV is able to hold a steady altitude and drop a weight up to 1 kg. The ability of the UAV to efficiently recover the drop weight is also investigated. A tailored visual detection algorithm built upon color detection techniques is devised to provide robust segmentation of the drop weight in an image. Relative position between the UAV and drop weight is estimated through a careful geometric deduction. Feeding the visual measurements into the vision-aided UAV control framework presented in Chapter 2, the UAV is capable of autonomously landing on top of the drop weight with an accuracy of 7 cm and successfully grasping it 70 percent of the time. For autonomous missions, confirmation of pickup is essential to ensure efficiency of field operations. This study proposes a novel approach to identify a successful grasping leveraging ambient sound differences between an effective grasping and a failed attempt. To conclude, the study proves the feasibility of using an autonomous UAV as a replacement for human operators to actively deploy seismic sources. The proposed approach can be readily applied in remote sites where human accessibility is restricted or impractical, but also has broader implication for autonomous characterization of the ground (in earth as well as in extraterrestrial applications).

A major premise of a mobile sensor is the elimination of long coaxial wires for data transmission and being able to communicate wirelessly. Recognizing this inherent requirement for mobility, a wireless geophone node was designed (Chapter 3) that aims at autonomous deployment by intelligent robots such as UAVs. The core of the design is a powerful SBC that is able to sample the geophone signals quick enough (1000 Hz) and reference the signals to accurate GPS timestamps. The Linux-based SBC allows flexibility of sensor-level data assimilation by the inclusion of a slew of open-source tools and custom written scripts for signal processing. The ADC board used to digitalize and filter the analog GPS signals provides 32-bit resolution and a sampling rate up to 4000 Hz, which is more than capable of seismic energy exploration. One highlight of the system is the integrated GPS module serving as an accurate time source that contributes to cross-unit synchronization. The performance of the proposed wireless seismic recorder is validated against a commercial wired seismic acquisition system. Field experiment results show fairly similar data quality of the two systems in both the time and frequency domains. The development of the wireless geophone node addresses the research need for a lightweight, low-cost, and nonproprietary seismic recorder that can be integrated into a robot-deployed monitoring system.

The previous development and findings enable the fully autonomous application of UAVs for subsurface characterization of geosystems (Chapter 4). A RAS solution tailored for the SASW method is proposed and validated. In the RAS solution, one X8 UAV with high payload capacity is used to deploy seismic sources while two custom-made QAV210s are employed to install wireless geophone sensors and record seismic data. The monitoring system features fully autonomous operations that is aimed for deployments in remote or hard-to-reach areas. To comply with the state-of-practice CRMP scheme regulating source-sensor layouts, the chapter adopts a unique design of an AprilTag-decorated cube that sits at the receiver midpoint and serves as a position reference landmark. The advanced vision-aided position controller embedded in the UAVs enables them to localize themselves around the cube with high accuracy. The UAV-geophone pair designed in this study highlights the use of a three-spike base for the geophone, which also functions as landing legs for the UAV. This stable structure ensures the vertical position of the geophone after the UAV lands on ground. Although ground-coupling can be improved, this study shows that data collected using the RAS has similar quality to that collected by well-planted single-spike geophones. The UAV experiments in this chapter are motivated by a strong desire to develop automated methods for performing MASW tests to assess subsurface material properties. The resulting RAS solution marks a breakthrough in unmanned seismic surveying, and from a broader perspective, provides a new paradigm on robot-aided monitoring of future civil infrastructure systems.

5.2 Recommendations for Future Research

Chapter 1 described some of the challenges associated with integrating robotics and autonomous systems into the inspection, maintenance, and repair of civil infrastructure and particularly challenges of UAV-enabled infrastructure monitoring. These challenges cannot be overcome by any single discipline working in isolation; impactful solutions will require multidisciplinary teams of researchers working in close collaboration. Future efforts will require civil engineers to develop strong linkages to researchers in robotics, computer science, social science, and public health, just to name a few, and will strongly emphasize purpose-driven robotic designs. It is shown in this dissertation that custom-made autonomous UAV systems can be applied to deploy and operate structural monitoring systems with great success. However, there are areas that this research does not directly address and are worthy of further investigation. Listed below are some research areas where additional contributions can be made.

Onboard decision-making: The proposed autonomous UAV sensor deployment system could be improved by incorporating on-the-fly decision-making capabilities. In the context of UAV-enabled seismic surface wave testing, some examples of onboard decision-making would be to determine if additional weight drops are needed for a certain inter-receiver spacing and to predict the next ideal inter-receiver spacing based on results from previous drop weight testing. The ability to quickly interpretate results and make decisions on next moves will greatly reduce both timelines and costs of the data acquisition process and improve data quality.

Advanced robot-environment interaction: When it comes to deployment of geophone sensors, good contact between the geophone spike and soil is important for obtaining quality data. Soil penetration in Chapter 4 is reliant on the self-weight of the UAV after landing; more research is needed on better geophone-ground coupling. One possible solution is to use counter-rotating propellers (Rotor Riot 2016) to generate a downward push that sinks the geophone spike into the ground. However, this method requires thrust inversion capabilities of the UAV and advanced control law that takes into account the ground reaction force to maintain the vertical position of the geophone sensor during the spike penetration process.

Reliability and robustness assessment of UAV systems: Reliability and robustness assessment is a key component of optimizing the design of UAV systems to identify potential system weaknesses and prevent catastrophic failures. Although this work demonstrates proof-of-concept trails of UAVs precisely landing on a multi-AprilTag pattern, system reliability and robustness is not well studied. The author has observed landing failures under environmental disturbances such as strong wind gusts and crumpled AprilTag sheet due to moisture. There is substantial research need of quantification of UAV susceptibility to environmental disturbances and improved UAV operational stability—including reliability, repeatability, and safety—in outdoor environments.

General-purpose UAV localization method: Fiducial markers offer accurate pose estimation of UAVs equipped with a calibrated camera but are not available in a natural environment. In general, there is substantial need for a reliable general-purpose UAV localization method in the field environment. RTK GPS is a promising high-accuracy positioning technology with proven applications such as drone light show (Intel 2021) but remains expensive and requires careful setup on a pre-surveyed base-station (Langley 1998). Complete UAV autonomy is likely a longer-term goal and remains an active research topic. Recent advancement in the visual-inertial SLAM technologies and deep leaning-based depth estimation methods provides promising opportunities for autonomous navigation of UAVs in an unknown environment.

UAV swarm sensing: A swarm of UAVs working together to deploy WSNs have obvious benefits such as increased coverage and higher speed of mission. However, deployment of physical UAV swarms is both a hardware and a software challenge requiring more basic research at the intersection of control, perception, and communication (Parker, Rus, and Sukhatme 2016). The field has expanded quickly in recent years but is still an active area of research with many open research issues remaining to be solved.

Appendix

A. Pinhole Camera Model

A.1 Geometry and Formulation

Considering the pinhole camera model in Figure A-1 with a point M in the 3D space and its projection point N in the 2D image,

$$M^{Camema} = [\text{-}a\ \text{-}b\ c]^T, N^{Camera} = [\text{-}d\ \text{-}e\ f]^T, \tag{A-1}$$

where f is the focal length (i.e., the distance from the optical center O to the image plane). Because the three points M, N, O are collinear, the following relationship holds:

$$\frac{a}{d} = \frac{b}{e} = \frac{c}{f}. \tag{A-2}$$

Therefore:

$$d = f\frac{a}{c}, e = f\frac{b}{c}. \tag{A-3}$$

Image coordinates of the projection point N (i.e., $[u\ v]^T$) can be computed from its representation in the *Camera* frame (i.e., $[\text{-}d\ \text{-}e]^T$) by applying a scaling (in pixel/meter) followed by a translation (in pixels), that is:

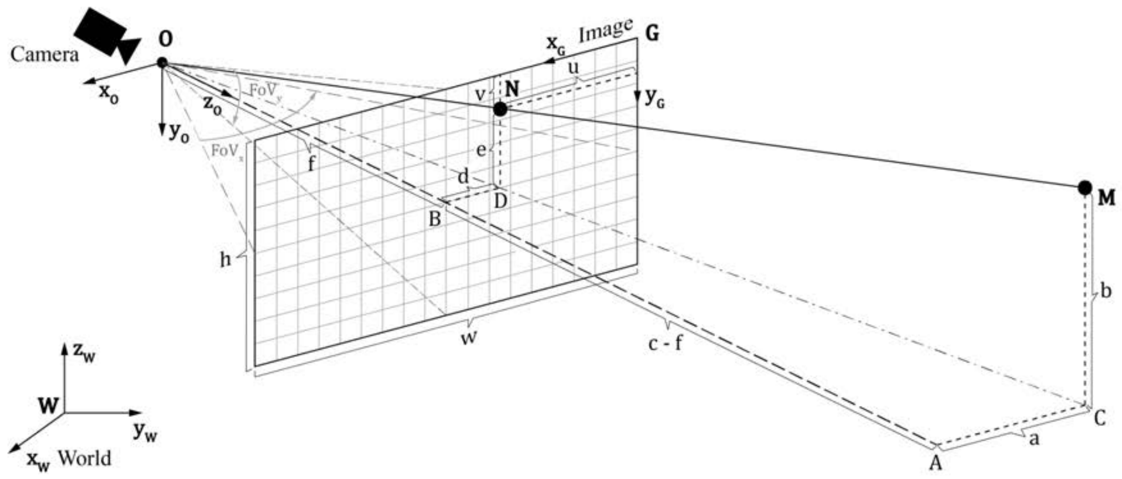

Figure A-1. Pinhole camera model showing a point M in the 3D world and its projection point N in the image plane through the camera lens center O.

$$\begin{bmatrix} u \\ v \end{bmatrix} = \begin{bmatrix} \alpha & 0 \\ 0 & \beta \end{bmatrix} \begin{bmatrix} -d \\ -e \end{bmatrix} + \begin{bmatrix} c_x \\ c_y \end{bmatrix} = \begin{bmatrix} -\alpha d + c_x \\ -\beta e + c_y \end{bmatrix} = \begin{bmatrix} -\alpha f \dfrac{a}{c} + c_x \\ -\beta f \dfrac{b}{c} + c_y \end{bmatrix}, \tag{A-4}$$

where α, β have units of pixel/meter, c_x, c_y have units of pixel, and $\alpha, \beta > 0$. Define:

$$f_x \triangleq \alpha f, f_y \triangleq \beta f, \tag{A-5}$$

both in pixels, Equation (A-4) can be written as:

$$\begin{bmatrix} u \\ v \end{bmatrix} = \begin{bmatrix} f_x \dfrac{-a}{c} + c_x \\ f_y \dfrac{-b}{c} + c_y \end{bmatrix}, \tag{A-6}$$

or in a more compact form:

$$\begin{bmatrix} u \\ v \\ 1 \end{bmatrix} = \frac{1}{c} \begin{bmatrix} f_x & 0 & c_x \\ 0 & f_y & c_y \\ 0 & 0 & 1 \end{bmatrix} \begin{bmatrix} -a \\ -b \\ c \end{bmatrix} \triangleq \frac{1}{c} K \begin{bmatrix} -a \\ -b \\ c \end{bmatrix}, \tag{A-7}$$

where K is defined as the camera intrinsic matrix.

The next step is to convert M's coordinates from the *Camera* frame to the *World* frame. From the theory of rigid motion transformation (Spong, Hutchinson, and Vidyasagar 2006), if a frame B is obtained from another frame A by first applying a rotation specified by R_B^A followed by a translation given (with respect to frame A) by t_B^A, then the coordinates of a point P in frame A are given by:

$$P^A = R_B^A P^B + t_B^A. \tag{A-8}$$

The rotation matrix R_B^A can be built by projecting the axes of frame B onto the coordinate axes of frame A, i.e.,

$$R_B^A = [x_B^A | y_B^A | z_B^A] = \begin{bmatrix} x_B \cdot x_A & y_B \cdot x_A & z_B \cdot x_A \\ x_B \cdot y_A & y_B \cdot y_A & z_B \cdot y_A \\ x_B \cdot z_A & y_B \cdot z_A & z_B \cdot z_A \end{bmatrix}. \tag{A-9}$$

The translation vector t_B^A contains important geometric implications: it is the coordinates of the origin of frame B with respect to the frame A.

Now assuming that the relative pose between the *Camera* frame and the *World* frame is known, i.e.,

$$M^{Camera} = RM^{World} + t, \tag{A-10}$$

or more specifically:

$$\begin{bmatrix} -a \\ -b \\ c \end{bmatrix} = R \begin{bmatrix} x \\ y \\ z \end{bmatrix} + t = [R|t] \begin{bmatrix} x \\ y \\ z \\ 1 \end{bmatrix}, \tag{A-11}$$

where $[R|t]$ is called the camera extrinsic matrix. Plugging Equation (A-11) into Equation (A-7) results in:

$$\begin{aligned}\begin{bmatrix}u\\v\\1\end{bmatrix} &= \frac{1}{c}K\begin{bmatrix}-a\\-b\\c\end{bmatrix} = \frac{1}{c}K[R|t]\begin{bmatrix}x\\y\\z\\1\end{bmatrix} \\ &= \frac{1}{c}\begin{bmatrix}f_x & 0 & c_x\\0 & f_y & c_y\\0 & 0 & 1\end{bmatrix}\begin{bmatrix}r_{11} & r_{12} & r_{13} & t_1\\r_{21} & r_{22} & r_{23} & t_2\\r_{31} & r_{32} & r_{33} & t_3\end{bmatrix}\begin{bmatrix}x\\y\\z\\1\end{bmatrix}.\end{aligned} \tag{A-12}$$

Equation (A-12) reveals the complete relationship between the coordinates of a 3D point in the *World* coordinate system and the coordinates of its projection point in pixels.

Comparing Equation (A-10) with Equation (A-8), it is clear that t in Equation (A-10) is actually t_{World}^{Camera}. In other words, t is the coordinates of the origin of the *World* frame with respect to the *Camera* frame. This interpretation of t is crucial for deriving the relative pose between the UAV and the landing pad as illustrated in Section 2.3.3.1.

A.2 Position Registration of Placed Wireless Sensor Node

Position registration of the placed sensor enclosure requires the detection of both the AprilTag on top of the UAV and at least one more AprilTag in the landing patterns that are attached to the beam. The objective is to find the unknown position of the sensor enclosure, which is represented by the AprilTag on top of the UAV, from the known 3D coordinates of AprilTags in the landing patterns. Consider the pinhole camera model with the origin of the *World* frame defined at any point on the beam surface. The camera extrinsic matrix $[R|t]$ can be found by solving the PnP problem using information from the detected AprilTags on the beam. The z coordinate of the AprilTag on top of the UAV can be measured in advance and is therefore known. In order to compute its remaining x and y

coordinates, a two-step method can be followed by first computing the scaling factor c in Equation (A-12) and then solving for x and y. Rewrite Equation (A-12) as:

$$cR^{-1}K^{-1}\begin{bmatrix}u\\v\\1\end{bmatrix} = R^{-1}t + \begin{bmatrix}x\\y\\z\end{bmatrix}. \qquad \text{(A-13)}$$

Note that c can be solved using only the third row of the left-hand side and right-hand side of Equation (A-13) because z is known. The solutions to x and y are immediate after plugging the computed c back into Equation (A-13).

A.3 Derivation of FoV_x and FoV_y

Additional findings can be drawn from the camera pinhole model, such as FoV_x and FoV_y shown in Figure A-1. Combining Equation (A-3) and Equation (A-5), it is easy to derive that:

$$\frac{\alpha d}{f_x} = \frac{a}{c}, \frac{\beta e}{f_y} = \frac{b}{c}. \qquad \text{(A-14)}$$

Note that αd and βe can be interpreted as distances d and e in Figure A-1 expressed in pixels, respectively. Considering the geometric relationship between the two similar triangles ΔOAC and ΔOBD in Figure A-1, Equation (A-14) implies that f_x and f_y are simply the focal length f interpreted in pixels, and they should be of the same value in theory. With this interpretation of f_x and f_y in mind, the camera's field of view in the x and y direction can be calculated as:

$$FoV_x = 2\arctan\frac{w}{2f_x}, FoV_y = 2\arctan\frac{h}{2f_y}. \qquad \text{(A-15)}$$

B. Theoretical Modal Analysis of a Simply Supported Beam

Considering a Euler-Bernoulli beam under the assumptions that plane sections remain plane and deformed beam angles (slopes) are small, the equation of the motion of beam can be written as:

$$EI\frac{\partial^4 v(x,t)}{\partial x^4}+\rho A\frac{\partial^2 v(x,t)}{\partial t^2}=0, \tag{B-1}$$

where v is the transverse displacement, x is the distance along the length of the beam from 0 to L, t is time, E is the Young's modulus of the beam, I is the area moment of inertia of the beam's cross section, ρ is the mass density of the beam, and A is the cross-section area of the beam. One form of solution to this equation can be obtained by separation of variables using:

$$v(x,t)=\phi(x)Y(t), \tag{B-2}$$

which suggests that the free-vibration motion of the beam is of a specific shape $\phi(x)$ having a time-dependent amplitude $Y(t)$. Plugging Equation (B-2) back into Equation (B-1) would yield two ordinary differential equations:

$$\ddot{Y}(t)+\omega^2Y(t)= 0, \tag{B-3}$$

$$\frac{d^4\phi(x)}{dx^4}-\frac{\omega^2\rho A}{EI}\phi(x)=0. \tag{B-4}$$

The solution to Equation (B-3) is:

$$Y(t)=Y(0)\cos\omega t+\frac{\dot{Y}(0)}{\omega}\sin\omega t. \tag{B-5}$$

Considering a simply supported beam with boundary conditions:

$$\phi(0) = \phi(L) = \ddot{\phi}(0) = \ddot{\phi}(L) = 0, \tag{B-6}$$

the solutions to Equation (B-4) are (Clough and Penzien 1993):

$$\omega_n = n^2\pi^2\sqrt{\frac{EI}{\rho A L^4}}, \phi_n(x) = C\sin\frac{n\pi}{L}x, n = 1, 2, \dots, \tag{B-7}$$

where ϕ_n is the n^{th} mode shape of the beam, and C is any nonzero constant. The n^{th} natural frequency of the beam is therefore:

$$f_n = \frac{\omega_n}{2\pi} = \frac{n^2\pi}{2}\sqrt{\frac{EI}{\rho A L^4}}. \tag{B-8}$$

Bibliography

Adler, Alan. 2018. “SkySpecs: A 10-Year Overnight Success.” https://michigantoday.umich.edu/2018/03/20/skyspecs-a-10-year-overnight-success/.

Air Force Print News (AFPN). 2006. “‘Reaper’ Moniker given to MQ-9 Unmanned Aerial Vehicle.” https://web.archive.org/web/20110914055555/http://www.af.mil/news/story.asp?storyID=123027012.

Aki, Keiiti. 1957. “Space and Time Spectra of Stationary Stochastic Waves, with Special Reference to Microtremors.” *Bulletin of the Earthquake Research Institute* 35: 415–56.

Akiyama, Nanoka, Satoshi Nishiyama, Koki Sakita, Junsheng Song, and Fumiaki Yamazaki. 2021. “River Levees Monitoring Using Three Dimensional Laser Point Clouds with SLAM Technology.” In *Civil Infrastructures Confronting Severe Weathers and Climate Changes Conference*, 14–22. Nanchang, China, July 19-21. https://doi.org/10.1007/978-3-030-79798-0_2.

Akyildiz, Ian F., Weilian Su, Yogesh Sankarasubramaniam, and Erdal Cayirci. 2002. “A Survey on Sensor Networks.” *IEEE Communications Magazine* 40 (8): 102–14. https://doi.org/10.1109/MCOM.2002.1024422.

Alonso-Mora, Javier, Ross Knepper, Roland Siegwart, and Daniela Rus. 2015. “Local Motion Planning for Collaborative Multi-Robot Manipulation of Deformable Objects.” In *2015 IEEE International Conference on Robotics and Automation (ICRA)*, 5495–5502. Seattle, WA, May 26-30. https://doi.org/10.1109/ICRA.2015.7139967.

American Society of Civil Engineers (ASCE). 2021a. “2021 Report Card for American’s Infrastructure.” American Society of Civil Engineers, Reston, VA.

———. 2021b. “Failure to Act: Economic Impacts of Status Quo Investment across Infrastructure Systems.” American Society of Civil Engineers, Reston, VA.

Araar, Oualid, Nabil Aouf, and Ivan Vitanov. 2017. “Vision Based Autonomous Landing of Multirotor UAV on Moving Platform.” *Journal of Intelligent & Robotic Systems* 85 (2): 369–84. https://doi.org/10.1007/s10846-016-0399-z.

ArduPilot. 2011a. “ArduPilot EKF.” https://ardupilot.org/copter/docs/common-apmnavigation-extended-kalman-filter-overview.html.

———. 2011b. “ArduPilot Project.” *GitHub Repository*. https://github.com/ArduPilot/ardupilot.

———. 2011c. “ArduPilot Simulation.” https://ardupilot.org/dev/docs/simulation-2.html.

Attia, Hussein, Sagiru Gaya, Abdullah Alamoudi, Fahad M. Alshehri, Abdulrahman Al-Suhaimi, Nawaf Alsulaim, Ahmad M. Al Naser, et al. 2020. “Wireless Geophone Sensing System for Real-Time Seismic Data Acquisition.” *IEEE Access* 8: 81116–28. https://doi.org/10.1109/ACCESS.2020.2989280.

Augugliaro, Frederico, Sergei Lupashin, Michael Hamer, Cason Male, Markus Hehn, Mark W. Mueller, Jan Sebastian Willmann, Fabio Gramazio, Matthias Kohler, and Raffaello D’Andrea. 2014. “The Flight Assembled Architecture Installation: Cooperative Construction with Flying Machines.” *IEEE Control Systems Magazine* 34 (4): 46–64. https://doi.org/10.1109/MCS.2014.2320359.

Auterion. 2020. “The Story of PX4 and Pixhawk.” https://auterion.com/company/the-history-of-pixhawk/.

Bähnemann, Rik, Michael Pantic, Marija Popović, Dominik Schindler, Marco Tranzatto, Mina Kamel, Marius Grimm, Jakob Widauer, Roland Siegwart, and Juan Nieto. 2019. “The ETH-MAV Team in the MBZ International Robotics Challenge.” *Journal of Field Robotics* 36 (1): 78–103. https://doi.org/10.1002/rob.21824.

Bailey, Tim, and Hugh Durrant-Whyte. 2006. “Simultaneous Localization and Mapping (SLAM): Part II.” *IEEE Robotics and Automation Magazine* 13 (3): 108–17. https://doi.org/10.1109/MRA.2006.1678144.

Bajwa, Waheed, Jarvis Haupt, Akbar Sayeed, and Robert Nowak. 2006. “Compressive Wireless Sensing.” In *Proceedings of the 5th International Conference on Information Processing in Sensor Networks*, 134–42. Nashville, TN, April 19-21. https://doi.org/10.1145/1127777.1127801.

Bar-Shalom, Yaakov, X. Rong Li, and Thiagalingam Kirubarajan. 2004. *Estimation with Applications to Tracking and Navigation: Theory Algorithms and Software*. John Wiley & Sons, New York, NY.

Barin, Amirreza, Igor Dolgov, and Zachary O. Toups. 2017. “Understanding Dangerous Play: A Grounded Theory Analysis of High-Performance Drone Racing Crashes.” In *Proceedings of the Annual Symposium on Computer-Human Interaction in Play*, 485–96. Amsterdam, The Netherlands, October 15–18. https://doi.org/10.1145/3116595.3116611.

Bauch, Andreas, and Peter Whibberley. 2017. “Reliable Time from GNSS Signals.” *Inside GNSS* 44: 38–44.

Beautiful Destinations. 2019. “Johnny FPV x Beautiful Destinations - Turkey.” *YouTube Video*. https://www.youtube.com/watch?v=f3lv65BFmaA.

Bein, Doina, Wolfgang Bein, Ashish Karki, and Bharat B. Madan. 2015. “Optimizing Border Patrol Operations Using Unmanned Aerial Vehicles.” In *2015 12th International Conference on Information Technology - New Generations*, 479–84. Las Vegas, NV, April 13-15. https://doi.org/10.1109/ITNG.2015.83.

Benewake. 2019. “TFmini Plus LiDAR Module Short-Range Distance Sensor.” *Data Sheet*. Benewake, Beijing, China.

Benowitz, David. 2021. “The Rise of Open-Source Drones.” https://droneanalyst.com/2021/05/30/rise-of-open-source-drones.

Berenson, Dmitry, Siddhartha S. Srinivasa, Dave Ferguson, and James J. Kuffner. 2009. “Manipulation Planning on Constraint Manifolds.” In *2009 IEEE International Conference on Robotics and Automation*, 625–32. Kobe, Japan, May 12-17. https://doi.org/10.1109/ROBOT.2009.5152399.

Bergen, Peter, Melissa Salyk-Virk, and David Sterman. 2020. “World of Drones.” New America, Washington, DC.

Bertinetto, Luca, Jack Valmadre, João F. Henriques, Andrea Vedaldi, and Philip H.S. Torr. 2016. “Fully-Convolutional Siamese Networks for Object Tracking.” In *European Conference on Computer Vision 2016 Workshops*, 850–65. Amsterdam, The Netherlands, October 8-10 and 15-16. https://doi.org/10.1007/978-3-319-48881-3_56.

Bloesch, Michael, Sammy Omari, Marco Hutter, and Roland Siegwart. 2015. “Robust Visual Inertial Odometry Using a Direct EKF-Based Approach.” In *2015 IEEE/RSJ International Conference on Intelligent Robots and Systems (IROS)*, 298–304. Hamburg, Germany, September 28-October 2. https://doi.org/10.1109/IROS.2015.7353389.

Bloomberg Quicktake. 2016. “Go inside the World’s First $1 Million Drone Race.” *YouTube Video*. https://www.youtube.com/watch?v=pZ0viMxYDA4.

Borowczyk, Alexandre, Duc-Tien Nguyen, André Phu-Van Nguyen, Dang Quang Nguyen, David Saussié, and Jerome Le Ny. 2017. “Autonomous Landing of a Multirotor Micro Air Vehicle on a High Velocity Ground Vehicle.” *Ifac-Papersonline* 50 (1): 10488–94. https://doi.org/10.1016/J.IFACOL.2017.08.1980.

Bouabdallah, Samir, Pierpaolo Murrieri, and Roland Siegwart. 2004. “Design and Control of an Indoor Micro Quadrotor.” In *IEEE International Conference on Robotics and Automation, 2004. Proceedings. ICRA ’04. 2004*, 5:4393–98. New Orleans, LA, April 26-May 1. https://doi.org/10.1109/robot.2004.1302409.

Bradski, G. 2000. “The OpenCV Library.” *Dr. Dobb’s Journal of Software Tools* 25: 120–

25. https://doi.org/10.1109/MRA.2009.933612.

Brescianini, Dario, and Raffaello D'Andrea. 2016. "Design, Modeling and Control of an Omni-Directional Aerial Vehicle." In *2016 IEEE International Conference on Robotics and Automation (ICRA)*, 3261–66. Stockholm, Sweden, May 16-21: IEEE. https://doi.org/10.1109/ICRA.2016.7487497.

Brincker, Rune, Lingmi Zhang, and Palle Andersen. 2000. "Modal Identification from Ambient Responses Using Frequency Domain Decomposition." In *IMAC 18: Proceedings of the International Modal Analysis Conference (IMAC)*, 625–30. San Antonio, Texas, February 7-10.

Bristeau, Pierre Jean, François Callou, David Vissière, and Nicolas Petit. 2011. "The Navigation and Control Technology inside the AR.Drone Micro UAV." In *IFAC Proceedings Volumes*, 44:1477–84. Milano, Italy, August 28-September 2. https://doi.org/10.3182/20110828-6-IT-1002.02327.

Burke, Claire, Paul R. McWhirter, Josh Veitch-Michaelis, Owen McAree, Harry A.G. Pointon, Serge Wich, and Steve Longmore. 2019. "Requirements and Limitations of Thermal Drones for Effective Search and Rescue in Marine and Coastal Areas." *Drones* 3 (4): 78. https://doi.org/10.3390/drones3040078.

Capon, Jack. 1969. "High-Resolution Frequency-Wavenumber Spectrum Analysis." *Proceedings of the IEEE* 57 (8): 1408–18. https://doi.org/10.1109/PROC.1969.7278.

Çelebi, Mehmet. 2002. "Seismic Instrumentation of Buildings (with Emphasis on Federal Buildings)." *Technical Report No. 0-7460-68170*. United States Geological Survey, Menlo Park, CA.

Chan, Brodie, Hong Guan, Jun Jo, and Michael Blumenstein. 2015. "Towards UAV-Based Bridge Inspection Systems: A Review and an Application Perspective." *Structural Monitoring and Maintenance* 2 (3): 283–300. https://doi.org/10.12989/smm.2015.2.3.283.

Chaves, Stephen M, Ryan W Wolcott, and Ryan M Eustice. 2015. "NEEC Research: Toward GPS-Denied Landing of Unmanned Aerial Vehicles on Ships at Sea." *Naval Engineers Journal* 127 (1): 23–35.

Chen, Siyuan, Debra F. Laefer, Eleni Mangina, S. M. Iman Zolanvari, and Jonathan Byrne. 2019. "UAV Bridge Inspection through Evaluated 3D Reconstructions." *Journal of Bridge Engineering* 24 (4): 05019001. https://doi.org/10.1061/(ASCE)BE.1943-5592.0001343.

Cheng, H. D., X. H. Jiang, Y. Sun, and Jingli Wang. 2001. "Color Image Segmentation: Advances and Prospects." *Pattern Recognition* 34 (12): 2259–81. https://doi.org/10.1016/S0031-3203(00)00149-7.

Cho, Byung Hak, Seung Hyun Byun, Joon Young Park, and Jin Seok Kim. 2006.

"Development of Automatic Inspection Robot for Live-Line Insulators." In *ESMO 2006 - 2006 IEEE 11th International Conference on Transmission & Distribution Construction, Operation and Live-Line Maintenance*. Albuquerque, NM, October 15-19. https://doi.org/10.1109/TDCLLM.2006.340743.

Cho, Kyeong Ho, Ho Moon Kim, Young Hoon Jin, Fengyi Liu, Hyungpil Moon, Ja Choon Koo, and Hyouk Ryeol Choi. 2013. "Inspection Robot for Hanger Cable of Suspension Bridge: Mechanism Design and Analysis." *IEEE/ASME Transactions on Mechatronics* 18 (6): 1665–74. https://doi.org/10.1109/TMECH.2013.2280653.

Chung, Timothy H., and Joel W. Burdick. 2007. "A Decision-Making Framework for Control Strategies in Probabilistic Search." In *Proceedings 2007 IEEE International Conference on Robotics and Automation*, 4386–93. Rome, Italy, April 10-14. https://doi.org/10.1109/ROBOT.2007.364155.

Clark, Richard M. 1999. "Uninhabited Combat Aerial Vehicles: Airpower by the People, for the People, but Not with the People." *Thesis*. School of Advanced Airpower Studies, Air University, Maxwell AFB, AL.

Clough, Ray W., and Joseph Penzien. 1993. *Dynamics of Structures*. McGraw-Hill, New York, NY.

Comina, C., S. Foti, D. Boiero, and L. V. Socco. 2011. "Reliability of VS, 30 Evaluation from Surface-Wave Tests." *Journal of Geotechnical and Geoenvironmental Engineering* 137 (6): 579–86. https://doi.org/10.1061/(asce)gt.1943-5606.0000452.

Computing Research Association (CRA). 2016. "A Roadmap for US Robotics: From Internet to Robotics, 2016 Edition." Computing Research Association, Washington, DC.

Crice, Doug. 2011. "Seismic Surveys without Cables." https://www.geoexpro.com/articles/2011/10/seismic-surveys-without-cables.

Crocker, R. Ian, James A. Maslanik, John J. Adler, Scott E. Palo, Ute C. Herzfeld, and William J. Emery. 2012. "A Sensor Package for Ice Surface Observations Using Small Unmanned Aircraft Systems." *IEEE Transactions on Geoscience and Remote Sensing* 50 (4): 1033–47. https://doi.org/10.1109/TGRS.2011.2167339.

Cura, Rémi, Julien Perret, and Nicolas Paparoditis. 2017. "A Scalable and Multi-Purpose Point Cloud Server (PCS) for Easier and Faster Point Cloud Data Management and Processing." *ISPRS Journal of Photogrammetry and Remote Sensing* 127: 39–56. https://doi.org/10.1016/J.ISPRSJPRS.2016.06.012.

D'Andrea, Raffaello. 2013. "The Astounding Athletic Power of Quadcopters." *TED Talk*. https://www.ted.com/talks/raffaello_d_andrea_the_astounding_athletic_power_of_quadcopters.

———. 2016. "Meet the Dazzling Flying Machines of the Future." *TED Talk*.

https://www.ted.com/talks/raffaello_d_andrea_meet_the_dazzling_flying_machines_of_the_future.

Dai, Kaoshan, Xiaofeng Li, Chuan Lu, Qingyu You, Zhenhua Huang, and H. Felix Wu. 2015. "A Low-Cost Energy-Efficient Cableless Geophone Unit for Passive Surface Wave Surveys." *Sensors* 15 (10): 24698–715. https://doi.org/10.3390/s151024698.

Dean, Tim, John Tulett, and Richard Barnwell. 2018. "Nodal Land Seismic Acquisition: The next Generation." *First Break* 36 (1): 47–52. https://doi.org/10.3997/1365-2397.n0061.

Debenest, Paulo, Michele Guarnieri, and Shigeo Hirose. 2014. "PipeTron Series-Robots for Pipe Inspection." In *Proceedings of the 2014 3rd International Conference on Applied Robotics for the Power Industry*, 1–6. Foz do Iguacu, Brazil, October 14-16. https://doi.org/10.1109/CARPI.2014.7030052.

Debenest, Paulo, Michele Guarnieri, Kensuke Takita, Edwardo F. Fukushima, Shigeo Hirose, Kiyoshi Tamura, Akihiro Kimura, Hiroshi Kubokawa, Narumi Iwama, and Fuminori Shiga. 2008. "Expliner - Robot for Inspection of Transmission Lines." In *2008 IEEE International Conference on Robotics and Automation*, 3978–84. Pasadena, CA, May 19-23. https://doi.org/10.1109/ROBOT.2008.4543822.

Delmerico, Jeffrey, and Davide Scaramuzza. 2018. "A Benchmark Comparison of Monocular Visual-Inertial Odometry Algorithms for Flying Robots." In *2018 IEEE International Conference on Robotics and Automation (ICRA)*, 2502–9. Brisbane, QLD, Australia, May 21-25. https://doi.org/10.1109/ICRA.2018.8460664.

Dijkstra, Edsger W. 1959. "A Note on Two Problems in Connexion with Graphs." *Numerische Mathematik* 1 (1): 269–71.

Drijkoningen, Guy G. 2000. "The Usefulness of Geophone Ground-coupling Experiments to Seismic Data." *Geophysics* 65 (6): 1780–87. https://doi.org/10.1190/1.1444862.

DroneKit. 2014. "DroneKit-Python: Library for Communicating with Drones via MAVLink." https://github.com/dronekit/dronekit-python.

Durrant-Whyte, Hugh, and Tim Bailey. 2006. "Simultaneous Localization and Mapping: Part I." *IEEE Robotics and Automation Magazine* 13 (2): 99–110. https://doi.org/10.1109/MRA.2006.1638022.

Ebeid, Emad, Martin Skriver, and Jie Jin. 2017. "A Survey on Open-Source Flight Control Platforms of Unmanned Aerial Vehicle." In *2017 Euromicro Conference on Digital System Design (DSD)*, 396–402. Vienna, Austria, August 30-September 1. https://doi.org/10.1109/DSD.2017.30.

Ellenberg, A., A. Kontsos, F. Moon, and I. Bartoli. 2016. "Bridge Related Damage Quantification Using Unmanned Aerial Vehicle Imagery." *Structural Control and Health Monitoring* 23 (9): 1168–79. https://doi.org/10.1002/STC.1831.

Engineering and Technology History Wiki (ETHW). 2020. "Ludger Benedikt Mintrop." https://ethw.org/Ludger_Benedikt_Mintrop.

Erdelj, Milan, Enrico Natalizio, Kaushik R. Chowdhury, and Ian F. Akyildiz. 2017. "Help from the Sky: Leveraging UAVs for Disaster Management." *IEEE Pervasive Computing* 16 (1): 24–32. https://doi.org/10.1109/MPRV.2017.11.

Erhart, Sebastian, and Sandra Hirche. 2015. "Internal Force Analysis and Load Distribution for Cooperative Multi-Robot Manipulation." *IEEE Transactions on Robotics* 31 (5): 1238–43. https://doi.org/10.1109/TRO.2015.2459412.

Eschmann, C, C.-M Kuo, C.-H Kuo, and C Boller. 2012. "Unmanned Aircraft Systems for Remote Building Inspection and Monitoring." In *6th European Workshop on Structural Health Monitoring*, 1–8. Dresden, Germany, July 3-6.

Escobar-Wolf, Rüdiger, Thomas Oommen, Colin N. Brooks, Richard J. Dobson, and Theresa M. Ahlborn. 2018. "Unmanned Aerial Vehicle (UAV)-Based Assessment of Concrete Bridge Deck Delamination Using Thermal and Visible Camera Sensors: A Preliminary Analysis." *Research in Nondestructive Evaluation* 29 (4): 183–98. https://doi.org/10.1080/09349847.2017.1304597.

Fahrney, Delmar S. 1980. "The Birth of Guided Missiles." In *United States Naval Institute Proceedings*, 56–57. https://www.usna.com/NetCommunity/Document.Doc?&id=93.

Fan, Linxi, Yuke Zhu, Jiren Zhu, Zihua Liu, Orien Zeng, Anchit Gupta, Joan Creus-Costa, Silvio Savarese, and Li Fei-Fei. 2018. "Surreal: Open-Source Reinforcement Learning Framework and Robot Manipulation Benchmark." In *2nd Conference on Robot Learning*, 767–82. Zurich, Switzerland, October 29-31. http://proceedings.mlr.press/v87/fan18a.html.

Farrar, Charles R. 2001. "Historical Overview of Structural Health Monitoring." *Lecture Notes on Structural Health Monitoring Using Statistical Pattern Recognition*. Los Alamos Dynamics, Los Alamos, NM.

Farrar, Charles R., and Keith Worden. 2010. "An Introduction to Structural Health Monitoring." In *New Trends in Vibration Based Structural Health Monitoring*, 1–17. Springer, Vienna. https://doi.org/10.1007/978-3-7091-0399-9_1.

Federal Aviation Administration (FAA). 2020a. "FAA Aerospace Forecast, Fiscal Years 2020-2040." Federal Aviation Administration, Washington, D.C.

———. 2020b. "Unmanned Aircraft System Traffic Management (UTM)." https://www.faa.gov/uas/research_development/traffic_management/.

———. 2021. "UAS Remote Identification Overview." https://www.faa.gov/uas/getting_started/remote_id/.

Fernández-Caramés, Tiago M., Oscar Blanco-Novoa, Iván Froiz-Míguez, and Paula Fraga-Lamas. 2019. "Towards an Autonomous Industry 4.0 Warehouse: A UAV and Blockchain-Based System for Inventory and Traceability Applications in Big Data-Driven Supply Chain Management." *Sensors* 19 (10): 2394. https://doi.org/10.3390/S19102394.

Fincky. 2019. "Filming Drifting Live for Red Bull TV." *YouTube Video*. https://www.youtube.com/watch?v=8OJxaEc2Sbg.

Floreano, Dario, and Robert J. Wood. 2015. "Science, Technology and the Future of Small Autonomous Drones." *Nature* 521 (7553): 460–66. https://doi.org/10.1038/nature14542.

Flyability. 2016. "Flyability Presentation - Elios, the Collision-Tolerant Drone for Industrial Inspection." *YouTube Video*. https://www.youtube.com/watch?v=s96Q2GXgoeE.

Forster, Christian, Luca Carlone, Frank Dellaert, and Davide Scaramuzza. 2016. "On-Manifold Preintegration for Real-Time Visual-Inertial Odometry." *IEEE Transactions on Robotics* 33 (1): 1–21. https://doi.org/10.1109/TRO.2016.2597321.

Foti, S., C. Comina, D. Boiero, and L. V. Socco. 2009. "Non-Uniqueness in Surface-Wave Inversion and Consequences on Seismic Site Response Analyses." *Soil Dynamics and Earthquake Engineering* 29 (6): 982–93. https://doi.org/10.1016/j.soildyn.2008.11.004.

Foti, Sebastiano. 2000. "Multistation Methods for Geotechnical Characterization Using Surface Waves." *PhD Dissertation*. Department of Geotechnical Engineering, Polytechnic University of Turin, Turin, Italy.

Foti, Sebastiano, Fabrice Hollender, Flora Garofalo, Dario Albarello, Michael Asten, Pierre-Yves Bard, Cesare Comina, et al. 2017. "Guidelines for the Good Practice of Surface Wave Analysis: A Product of the InterPACIFIC Project." *Bulletin of Earthquake Engineering* 16 (6): 2367–2420. https://doi.org/10.1007/S10518-017-0206-7.

Foti, Sebastiano, Stefano Parolai, Dario Albarello, and Matteo Picozzi. 2011. "Application of Surface-Wave Methods for Seismic Site Characterization." *Surveys in Geophysics* 32 (6): 777–825. https://doi.org/10.1007/s10712-011-9134-2.

Franco, Carmelo Di, and Giorgio Buttazzo. 2015. "Energy-Aware Coverage Path Planning of UAVs." In *2015 IEEE International Conference on Autonomous Robot Systems and Competitions*, 111–17. Vila Real, Portugal, April 8-10. https://doi.org/10.1109/ICARSC.2015.17.

Freed, Dennis. 2008. "Cable-Free Nodes: The next Generation Land Seismic System." *The Leading Edge* 27 (7): 878–81. https://doi.org/10.1190/1.2954027.

Froese, Michelle. 2018. “How to Choose the Right Drone-Inspection Service.” SkySpecs, Ann Arbor, MI.

Fuad, N. A., Z. Ismail, Z. Majid, N. Darwin, M. F.M. Ariff, K. M. Idris, and A. R. Yusoff. 2018. “Accuracy Evaluation of Digital Terrain Model Based on Different Flying Altitudes and Conditional of Terrain Using UAV LiDAR Technology.” In *IOP Conference Series: Earth and Environmental Science*, 169:012100. Kuala Lumpur, Malaysia, April 24–25. https://doi.org/10.1088/1755-1315/169/1/012100.

Fujino, Yozo, and Dionysius M. Siringoringo. 2020. “Recent Research and Development Programs for Infrastructures Maintenance, Renovation and Management in Japan.” *Structure and Infrastructure Engineering* 16 (1): 3–25. https://doi.org/10.1080/15732479.2019.1650077.

Garofalo, F., S. Foti, F. Hollender, P. Y. Bard, C. Cornou, B. R. Cox, M. Ohrnberger, et al. 2016. “InterPACIFIC Project: Comparison of Invasive and Non-Invasive Methods for Seismic Site Characterization. Part I: Intra-Comparison of Surface Wave Methods.” *Soil Dynamics and Earthquake Engineering* 82: 222–40. https://doi.org/10.1016/J.SOILDYN.2015.12.010.

Garrido-Jurado, S., R. Muñoz-Salinas, F. J. Madrid-Cuevas, and M. J. Marín-Jiménez. 2014. “Automatic Generation and Detection of Highly Reliable Fiducial Markers under Occlusion.” *Pattern Recognition* 47 (6): 2280–92. https://doi.org/10.1016/j.patcog.2014.01.005.

Gawel, Abel, Mina Kamel, Tonci Novkovic, Jakob Widauer, Dominik Schindler, Benjamin Pfyffer von Altishofen, Roland Siegwart, and Juan Nieto. 2017. “Aerial Picking and Delivery of Magnetic Objects with MAVs.” In *2017 IEEE International Conference on Robotics and Automation (ICRA)*, 5746–52. Singapore, May 29-June 3. https://doi.org/10.1109/ICRA.2017.7989675.

Giones, Ferran, and Alexander Brem. 2017. “From Toys to Tools: The Co-Evolution of Technological and Entrepreneurial Developments in the Drone Industry.” *Business Horizons* 60 (6): 875–84. https://doi.org/10.1016/j.bushor.2017.08.001.

Global Sources. 2021. “SmartSolo Wireless Seismic Sensor - Seismic Acquisition Nodal Geophone for Land Exploration.” *Oneline Marketplace*. https://www.globalsources.com/Vibration-sensor/Wireless-Seismic-Sensor-1179747979p.htm#1179747979.

Goel, Puneet, Goksel Dedeoglu, Stergios I. Roumeliotis, and Gaurav S. Sukhatme. 2000. “Fault Detection and Identification in a Mobile Robot Using Multiple Model Estimation and Neural Network.” In *Proceedings 2000 ICRA. Millennium Conference. IEEE International Conference on Robotics and Automation. Symposia Proceedings (Cat. No.00CH37065)*, 3:2302–9. San Francisco, CA, April 24-28. https://doi.org/10.1109/ROBOT.2000.846370.

Gómez, Cristina, and David R. Green. 2017. “Small Unmanned Airborne Systems to

Support Oil and Gas Pipeline Monitoring and Mapping." *Arabian Journal of Geosciences* 10 (9): 202. https://doi.org/10.1007/s12517-017-2989-x.

Gong, Chunhe, Jingxia Yuan, and Jun Ni. 2000. "Nongeometric Error Identification and Compensation for Robotic System by Inverse Calibration." *International Journal of Machine Tools and Manufacture* 40 (14): 2119–37. https://doi.org/10.1016/S0890-6955(00)00023-7.

Gopalakrishnan, Kasthurirangan, Hoda Gholami, Ankit Agrawal, Akash Vidyadharan, and Alok Choudhary. 2018. "Crack Damage Detection in Unmanned Aerial Vehicle Images of Civil Infrastructure Using Pre-Trained Deep Learning Model." *International Journal for Traffic and Transport Engineering* 8 (1): 1–14. https://doi.org/10.7708/ijtte.2018.8(1).01.

Gordon, Daniel, Ali Farhadi, and Dieter Fox. 2018. "Re3: Real-Time Recurrent Regression Networks for Visual Tracking of Generic Objects." *IEEE Robotics and Automation Letters* 3 (2): 788–95. https://doi.org/10.1109/LRA.2018.2792152.

Greene, W. Nicholas, Kyel Ok, Peter Lommel, and Nicholas Roy. 2016. "Multi-Level Mapping: Real-Time Dense Monocular SLAM." In *2016 IEEE International Conference on Robotics and Automation (ICRA)*, 833–40. Stockholm, Sweden, May 16-21. https://doi.org/10.1109/ICRA.2016.7487213.

Greenwood, William W. 2018. "UAV-Enabled Surface and Subsurface Characterization for Post-Earthquake Geotechnical Reconnaissance." *PhD Dissertation*. Department of Civil and Environmental Engineering, University of Michigan.

Greenwood, William W., Jerome P. Lynch, and Dimitrios Zekkos. 2019. "Applications of UAVs in Civil Infrastructure." *Journal of Infrastructure Systems* 25 (2): 04019002. https://doi.org/10.1061/(asce)is.1943-555x.0000464.

Greenwood, William W., Dimitrios Zekkos, and Jerome P. Lynch. 2021. "UAV-Enabled Subsurface Characterization Using Multichannel Analysis of Surface Waves." *Journal of Geotechnical and Geoenvironmental Engineering (in Press).*

Greenwood, William W., Hao Zhou, Dimitrios Zekkos, and Jerome P. Lynch. 2018. "Experiments Using a UAV-Deployed Impulsive Source for Multichannel Analysis of Surface Waves Testing." In *Geotechnical Earthquake Engineering and Soil Dynamics V: Slope Stability and Landslides, Laboratory Testing, and In Situ Testing*, 443–51. Austin, TX, June 10–13. https://doi.org/10.1061/9780784481486.046.

Griffin, Brent, and Carrick Detweiler. 2012. "Resonant Wireless Power Transfer to Ground Sensors from a UAV." In *2012 IEEE International Conference on Robotics and Automation*, 2660–65. Saint Paul, MN, May 14-18. https://doi.org/10.1109/ICRA.2012.6225205.

Gucunski, Nenad, Seong-Hoon Kee, Hung La, Basily Basily, and Ali Maher. 2015. "Delamination and Concrete Quality Assessment of Concrete Bridge Decks Using a

Fully Autonomous RABIT Platform." *Structural Monitoring and Maintenance* 2 (1): 19–34. http://dx.doi.org/10.12989/smm.2015.2.1.019.

Hachicha, Saber, Chiheb Zaoui, Habib Dallagi, Samir Nejim, and Aref Maalej. 2019. "Innovative Design of an Underwater Cleaning Robot with a Two Arm Manipulator for Hull Cleaning." *Ocean Engineering* 181: 303–13. https://doi.org/10.1016/J.OCEANENG.2019.03.044.

Haddal, Chad C., and Jeremiah Gertler. 2010. "Homeland Security: Unmanned Aerial Vehicles and Border Surveillance." *CRS Report for Congress*. Congressional Research Service, Washington, DC.

Ham, Youngjib, Kevin K. Han, Jacob J Lin, and Mani Golparvar-Fard. 2016. "Visual Monitoring of Civil Infrastructure Systems via Camera-Equipped Unmanned Aerial Vehicles (UAVs): A Review of Related Works." *Visualization in Engineering* 4 (1): 1–8. https://doi.org/10.1186/s40327-015-0029-z.

Hardkernel. 2016. "ODROID-XU4 User's Manual." *User's Manual*. Hardkernel, Anyang, Gyeonggi, South Korea.

Hare, Sam, Stuart Golodetz, Amir Saffari, Vibhav Vineet, Ming Ming Cheng, Stephen L. Hicks, and Philip H.S. Torr. 2016. "Struck: Structured Output Tracking with Kernels." *IEEE Transactions on Pattern Analysis and Machine Intelligence* 38 (10): 2096–2109. https://doi.org/10.1109/TPAMI.2015.2509974.

Heisey, J. S. 1982. "Determination of In Situ Shear Wave Velocity from Spectral-Analysis-of-Surface-Waves." *Master's Thesis*. Department of Civil Engineering, The University of Texas, Austin, TX.

Heredia, G., A. E. Jimenez-Cano, I. Sanchez, D. Llorente, V. Vega, J. Braga, J. A. Acosta, and A. Ollero. 2014. "Control of a Multirotor Outdoor Aerial Manipulator." In *2014 IEEE/RSJ International Conference on Intelligent Robots and Systems*, 3417–22. Chicago, IL, September 14-18. https://doi.org/10.1109/IROS.2014.6943038.

Hirose, Mitsuhito, Yong Xiao, Zhiyuan Zuo, Vineet R. Kamat, Dimitrios Zekkos, and Jerome Lynch. 2015. "Implementation of UAV Localization Methods for a Mobile Post-Earthquake Monitoring System." In *2015 IEEE Workshop on Environmental, Energy, and Structural Monitoring Systems (EESMS) Proceedings*, 66–71. Trento, Italy, July 9-10. https://doi.org/10.1109/EESMS.2015.7175854.

Hodgson, Jarrod C., Shane M. Baylis, Rowan Mott, Ashley Herrod, and Rohan H. Clarke. 2016. "Precision Wildlife Monitoring Using Unmanned Aerial Vehicles." *Scientific Reports* 6 (1): 1–7. https://doi.org/10.1038/srep22574.

Hoskere, Vedhus, Jong Woong Park, Hyungchul Yoon, and Billie F. Spencer. 2019. "Vision-Based Modal Survey of Civil Infrastructure Using Unmanned Aerial Vehicles." *Journal of Structural Engineering* 145 (7): 04019062. https://doi.org/10.1061/(ASCE)ST.1943-541X.0002321.

How, Jonathan P., Brett Bethke, Adrian Frank, Daniel Dale, and John Vian. 2008. "Real-Time Indoor Autonomous Vehicle Test Environment." *IEEE Control Systems Magazine* 28 (2): 51–64. https://doi.org/10.1109/MCS.2007.914691.

Huang, Haomiao, Gabriel M. Hoffmann, Steven L. Waslander, and Claire J. Tomlin. 2009. "Aerodynamics and Control of Autonomous Quadrotor Helicopters in Aggressive Maneuvering." In *2009 IEEE International Conference on Robotics and Automation*, 3277–82. Kobe, Japan, May 12-17. https://doi.org/10.1109/ROBOT.2009.5152561.

Huston, Dryver R., Brain Esser, Jonathan Miller, and Xiaoguang Wang. 2003. "Robotic and Mobile Sensor Systems for Structural Health Monitoring." In *Proceedings of the 4th International Workshop on Structural Health Monitoring*. Vol. 1517. Stanford, CA, September 15-17.

Huston, Dryver R., Jonathan Miller, and Brian Esser. 2004. "Adaptive, Robotic, and Mobile Sensor Systems for Structural Assessment." In *Smart Structures and Materials 2004: Sensors and Smart Structures Technologies for Civil, Mechanical, and Aerospace Systems*, edited by Shih-Chi Liu, 5391:189–96. San Diego, CA, March 15-18. https://doi.org/10.1117/12.546606.

Innocente, Mauro S., and Paolo Grasso. 2019. "Self-Organising Swarms of Firefighting Drones: Harnessing the Power of Collective Intelligence in Decentralised Multi-Robot Systems." *Journal of Computational Science* 34: 80–101. https://doi.org/10.1016/J.JOCS.2019.04.009.

Inoue, Fumihiro, Satoru Doi, Tatsuya Ishizaki, Yasuhiro Ikeda, and Yutaka Ohta. 2010. "Study on Automated Inspection Robot and Quantitative Detection of Outer Tile Wall Exfoliation by Wavelet Analysis." In *ICCAS 2010*, 994–99. Gyeonggi-do, South Korea, October 27-30. https://doi.org/10.1109/iccas.2010.5669653.

Intel. 2021. "Intel Drone Light Show Premium Fact Sheet." In . Intel, Santa Clara, CA.

Inzerillo, Laura, Gaetano Di Mino, and Ronald Roberts. 2018. "Image-Based 3D Reconstruction Using Traditional and UAV Datasets for Analysis of Road Pavement Distress." *Automation in Construction* 96 (December): 457–69. https://doi.org/10.1016/j.autcon.2018.10.010.

Jang, Shinae, Hongki Jo, Soojin Cho, Kirill Mechitov, Jennifer A. Rice, Sung Han Sim, Hyung Jo Jung, Chung Bang Yun, Billie F. Spencer, and Gul Agha. 2010. "Structural Health Monitoring of a Cable-Stayed Bridge Using Smart Sensor Technology: Deployment and Evaluation." *Smart Structures and Systems* 6 (5_6): 461–80. https://doi.org/10.12989/sss.2010.6.5_6.439.

Jimenez-Cano, A. E., J. Martin, G. Heredia, A. Ollero, and R. Cano. 2013. "Control of an Aerial Robot with Multi-Link Arm for Assembly Tasks." In *2013 IEEE International Conference on Robotics and Automation*, 4916–21. Karlsruhe, Germany, May 6-10. https://doi.org/10.1109/ICRA.2013.6631279.

Johnson, Nephi R., Jerome P. Lynch, and Matthew D. Collette. 2018. "Response and Fatigue Assessment of High Speed Aluminium Hulls Using Short-Term Wireless Hull Monitoring." *Structure and Infrastructure Engineering* 14 (5): 634–51. https://doi.org/10.1080/15732479.2017.1380676.

Jones, Ronald. 1958. "In-Situ Measurement of the Dynamic Properties of Soil by Vibration Methods." *Geotechnique* 8 (1): 1–21. https://doi.org/10.1680/geot.1958.8.1.1.

Jordan, Sophie, Julian Moore, Sierra Hovet, John Box, Jason Perry, Kevin Kirsche, Dexter Lewis, and Zion Tsz Ho Tse. 2018. "State-of-the-Art Technologies for UAV Inspections." *IET Radar, Sonar & Navigation* 12 (2): 151–64. https://doi.org/10.1049/IET-RSN.2017.0251.

Kalra, Love P., Jason Gu, and Max Meng. 2006. "A Wall Climbing Robot for Oil Tank Inspection." In *2006 IEEE International Conference on Robotics and Biomimetics*, 1523–28. Kunming, China, December 17-20. https://doi.org/10.1109/ROBIO.2006.340155.

Kane, Michael, Dapeng Zhu, Mitsuhito Hirose, Xinjun Dong, Benjamin Winter, Mortiz Häckell, Jerome P. Lynch, Yang Wang, and A. Swartz. 2014. "Development of an Extensible Dual-Core Wireless Sensing Node for Cyber-Physical Systems." In *Sensors and Smart Structures Technologies for Civil, Mechanical, and Aerospace Systems 2014*, 9061:90611U. San Diego, CA, March 10-13. https://doi.org/10.1117/12.2045325.

Kanistras, Konstantinos, Goncalo Martins, Matthew J. Rutherford, and Kimon P. Valavanis. 2013. "A Survey of Unmanned Aerial Vehicles (UAVs) for Traffic Monitoring." In *2013 International Conference on Unmanned Aircraft Systems (ICUAS)*, 221–34. Atlanta, GA, May 28-31. https://doi.org/10.1109/ICUAS.2013.6564694.

Kato, H., and M. Billinghurst. 1999. "Marker Tracking and Hmd Calibration for a Video-Based Augmented Reality Conferencing System." In *Proceedings 2nd IEEE and ACM International Workshop on Augmented Reality (IWAR'99)*, 85–94. San Francisco, CA, October 20-21. https://doi.org/10.1109/IWAR.1999.803809.

KBV Research. 2020. "Global Autonomous Mobile Robots Market by Offering, by End User, by Region, Industry Analysis and Forecast, 2020 - 2026." KBV Research, New York, NY.

Ke, Ruimin, Zhibin Li, Jinjun Tang, Zewen Pan, and Yinhai Wang. 2018. "Real-Time Traffic Flow Parameter Estimation from UAV Video Based on Ensemble Classifier and Optical Flow." *IEEE Transactions on Intelligent Transportation Systems* 20 (1): 54–64. https://doi.org/10.1109/TITS.2018.2797697.

Keane, John F., and Stephen S. Carr. 2013. "A Brief History of Early Unmanned Aircraft." *Johns Hopkins APL Technical Digest* 32 (3): 558–71.

Kendall, Rob. 2015. “Cableless Seismic Acquisition.” In *GeoConvention 2015: New Horizons*. Calgary, AB, Canada, May 4-8.

Kim, Si Jung, Yunhwan Jeong, Sujin Park, Kihyun Ryu, and Gyuhwan Oh. 2018. “A Survey of Drone Use for Entertainment and AVR (Augmented and Virtual Reality).” In *Augmented Reality and Virtual Reality*, edited by Timothy Jung and M. Claudia tom Dieck, 339–52. Springer, Cham. https://doi.org/10.1007/978-3-319-64027-3_23.

Kim, Sukun, Shamim Pakzad, David Culler, James Demmel, Gregory Fenves, Steven Glaser, and Martin Turon. 2007. “Health Monitoring of Civil Infrastructures Using Wireless Sensor Networks.” In *2007 6th International Symposium on Information Processing in Sensor Networks*, 254–63. Cambridge, MA, April 25-27. https://doi.org/10.1109/IPSN.2007.4379685.

Krishnappa, Yathin S., and Wendy C. Turner. 2014. “Software for Minimalistic Data Management in Large Camera Trap Studies.” *Ecological Informatics* 24: 11–16. https://doi.org/10.1016/J.ECOINF.2014.06.004.

Krohn, Christine E. 1984. “Geophone Ground Coupling.” *Geophysics* 49 (6): 722–31. https://doi.org/10.1190/1.1441700.

Kuffner, James, and Jing Xiao. 2016. “Motion for Manipulation Tasks.” In *Springer Handbook of Robotics*, edited by Bruno Siciliano and Oussama Khatib. Springer, Berlin/Heidelberg, Germany.

Kumar, Vijay. 2012. “Robots That Fly ... and Cooperate.” *TED Talk*. https://www.ted.com/talks/vijay_kumar_robots_that_fly_and_cooperate.

———. 2015. “The Future of Flying Robots.” *TED Talk*. https://www.ted.com/talks/vijay_kumar_the_future_of_flying_robots.

Kumar, Vijay, Daniela Rus, and Sanjiv Singh. 2004. “Robot and Sensor Networks for First Responders.” *IEEE Pervasive Computing* 3 (4): 24–33. https://doi.org/10.1109/MPRV.2004.17.

Kümmerle, Rainer, Bastian Steder, Christian Dornhege, Michael Ruhnke, Giorgio Grisetti, Cyrill Stachniss, and Alexander Kleiner. 2009. “On Measuring the Accuracy of SLAM Algorithms.” *Autonomous Robots* 27 (4): 387–407. https://doi.org/10.1007/S10514-009-9155-6.

Kurata, Narito, Billie F. Spencer, and Manuel Ruiz-Sandoval. 2005. “Risk Monitoring of Buildings with Wireless Sensor Networks.” *Structural Control and Health Monitoring: The Official Journal of the International Association for Structural Control and Monitoring and of the European Association for the Control of Structures* 12 (3–4): 315–27. https://doi.org/10.1002/STC.73.

La, Hung M., Ronny S. Lim, Basily Basily, Nenad Gucunski, Jingang Yi, Ali Maher, Francisco A. Romero, and Hooman Parvardeh. 2013. “Autonomous Robotic System for High-Efficiency Non-Destructive Bridge Deck Inspection and Evaluation." In *2013 IEEE International Conference on Automation Science and Engineering (CASE)*, 1053–58. Madison, WI, August 17-20. https://doi.org/10.1109/COASE.2013.6653886.

Lange, Sven, Niko Sünderhauf, and Peter Protzel. 2009. "A Vision Based Onboard Approach for Landing and Position Control of an Autonomous Multirotor UAV in GPS-Denied Environments." In *2009 International Conference on Advanced Robotics*, 1–6. Munich, Germany, June 22-26.

Langley, Richard B. 1998. "RTK GPS." *Gps World* 9 (9): 70–76.

Lattanzi, David, and Gregory Miller. 2017. "Review of Robotic Infrastructure Inspection Systems." *Journal of Infrastructure Systems* 23 (3): 04017004. https://doi.org/10.1061/(ASCE)IS.1943-555X.0000353.

Law, Kincho H., and Jerome P. Lynch. 2019. "Smart City: Technologies and Challenges." *IT Professional* 21 (6): 46–51. https://doi.org/10.1109/MITP.2019.2935405.

Leon-Rodriguez, Hernando, Salman Hussain, and Tariq Sattar. 2012. "A Compact Wall-Climbing and Surface Adaptation Robot for Non-Destructive Testing." In *2012 12th International Conference on Control, Automation and Systems*. Jeju, South Korea, October 17-21. https://ieeexplore.ieee.org/abstract/document/6393473.

Lepetit, Vincent, Francesc Moreno-Noguer, and Pascal Fua. 2009. "EPnP: An Accurate O(n) Solution to the PnP Problem." *International Journal of Computer Vision* 81 (2): 155–66. https://doi.org/10.1007/s11263-008-0152-6.

Leutenegger, Stefan, Simon Lynen, Michael Bosse, Roland Siegwart, and Paul Furgale. 2015. "Keyframe-Based Visual–Inertial Odometry Using Nonlinear Optimization." *The International Journal of Robotics Research* 34 (3): 314–34. https://doi.org/10.1177/0278364914554813.

Levenberg, Kenneth. 1944. "A Method for the Solution of Certain Non-Linear Problems in Least Squares." *Quarterly of Applied Mathematics* 2 (2): 164–68. https://doi.org/10.1090/qam/10666.

Li, Yundong, Han Dong, Hongguang Li, Xueyan Zhang, Baochang Zhang, and Zhifeng Xiao. 2020. "Multi-Block SSD Based on Small Object Detection for UAV Railway Scene Surveillance." *Chinese Journal of Aeronautics* 33 (6): 1747–55. https://doi.org/10.1016/j.cja.2020.02.024.

Lin, Jacob J., Kevin K. Han, and Mani Golparvar-Fard. 2015. "A Framework for Model-Driven Acquisition and Analytics of Visual Data Using UAVs for Automated Construction Progress Monitoring." In *Computing in Civil Engineering 2015*, 156–64. Austin, Texas, June 21-23. https://doi.org/10.1061/9780784479247.020.

Lin, Yucong, and Srikanth Saripalli. 2017. "Sampling-Based Path Planning for UAV

Collision Avoidance.” *IEEE Transactions on Intelligent Transportation Systems* 18 (11): 3179–92. https://doi.org/10.1109/TITS.2017.2673778.

Linchant, Julie, Jonathan Lisein, Jean Semeki, Philippe Lejeune, and Cédric Vermeulen. 2015. “Are Unmanned Aircraft Systems (UASs) the Future of Wildlife Monitoring? A Review of Accomplishments and Challenges.” *Mammal Review* 45 (4): 239–52. https://doi.org/10.1111/MAM.12046.

Lindsey, Quentin, Daniel Mellinger, and Vijay Kumar. 2012. “Construction of Cubic Structures with Quadrotor Teams.” In *Robotics: Science & Systems VII*, 177–84.

Loianno, Giuseppe, Vojtech Spurny, Justin Thomas, Tomas Baca, Dinesh Thakur, Daniel Hert, Robert Penicka, et al. 2018. “Localization, Grasping, and Transportation of Magnetic Objects by a Team of Mavs in Challenging Desert-like Environments.” *IEEE Robotics and Automation Letters* 3 (3): 1576–83. https://doi.org/10.1109/LRA.2018.2800121.

Loke, Seng W. 2015. “The Internet of Flying-Things: Opportunities and Challenges with Airborne Fog Computing and Mobile Cloud in the Clouds.” *Internet of Things Journal*. http://arxiv.org/abs/1507.04492.

Lottes, Philipp, Raghav Khanna, Johannes Pfeifer, Roland Siegwart, and Cyrill Stachniss. 2017. “UAV-Based Crop and Weed Classification for Smart Farming.” In *2017 IEEE International Conference on Robotics and Automation (ICRA)*, 3024–31. Singapore, May 29-June 3. https://doi.org/10.1109/ICRA.2017.7989347.

Lu, Chien Ping, Gregory D. Hager, and Eric Mjolsness. 2000. “Fast and Globally Convergent Pose Estimation from Video Images.” *IEEE Transactions on Pattern Analysis and Machine Intelligence* 22 (6): 610–22. https://doi.org/10.1109/34.862199.

Luke, Barbara A., and Kenneth H. Stokoe II. 1998. “Application of SASW Method Underwater.” *Journal of Geotechnical and Geoenvironmental Engineering* 124 (6): 523–31. https://doi.org/10.1061/(asce)1090-0241(1998)124:6(523).

Lupashin, Sergei, Markus Hehn, Mark W. Mueller, Angela P. Schoellig, Michael Sherback, and Raffaello D’Andrea. 2014. “A Platform for Aerial Robotics Research and Demonstration: The Flying Machine Arena.” *Mechatronics* 24 (1): 41–54. https://doi.org/10.1016/j.mechatronics.2013.11.006.

Lydgate, Anthony. 2018. “How Zipline Helps Remote Regions Get Blood From a Drone.” https://www.wired.com/story/wired25-anne-wojcicki-keller-rinaudo-zipline-medical-drones/.

Lynch, Jerome P., and Kenneth J. Loh. 2006. “A Summary Review of Wireless Sensors and Sensor Networks for Structural Health Monitoring.” *Shock and Vibration Digest* 38 (2): 91–130. https://doi.org/10.1177/0583102406061499.

Lynch, Jerome P., Yang Wang, Kenneth J. Loh, Jin Hak Yi, and Chung Bang Yun. 2006. "Performance Monitoring of the Geumdang Bridge Using a Dense Network of High-Resolution Wireless Sensors." *Smart Materials and Structures* 15 (6): 1561–75. https://doi.org/10.1088/0964-1726/15/6/008.

Ma, Xiaobai, Ziyuan Jiao, Zhenkai Wang, and Dimitra Panagou. 2016. "Decentralized Prioritized Motion Planning for Multiple Autonomous UAVs in 3D Polygonal Obstacle Environments." In *2016 International Conference on Unmanned Aircraft Systems (ICUAS)*, 292–300. Arlington, VA, June 7-10. https://doi.org/10.1109/ICUAS.2016.7502596.

Mac, Ryan. 2016. "Behind the Crash of 3D Robotics, North America's Most Promising Drone Company." 2016. https://www.forbes.com/sites/ryanmac/2016/10/05/3d-robotics-solo-crash-chris-anderson/.

MacK, Chris A. 2011. "Fifty Years of Moore's Law." *IEEE Transactions on Semiconductor Manufacturing* 24 (2): 202–7. https://doi.org/10.1109/TSM.2010.2096437.

Mahony, Robert, Vijay Kumar, and Peter Corke. 2012. "Multirotor Aerial Vehicles: Modeling, Estimation, and Control of Quadrotor." *IEEE Robotics and Automation Magazine* 19 (3): 20–32. https://doi.org/10.1109/MRA.2012.2206474.

Major, Richard. 2012. "RQ-2 Pioneer: The Flawed System That Redefined US Unmanned Aviation." *Research Report*. Air Command And Staff College, Air University, Maxwell AFB, AL.

Marquardt, Donald W. 1963. "An Algorithm for Least-Squares Estimation of Nonlinear Parameters." *Journal of the Society for Industrial and Applied Mathematics* 11 (2): 431–41. https://doi.org/10.1137/0111030.

Martinez, Kirk, Jane K. Hart, Philip J. Basford, Graeme M. Bragg, Tyler Ward, and David S. Young. 2017. "A Geophone Wireless Sensor Network for Investigating Glacier Stick-Slip Motion." *Computers and Geosciences* 105: 103–12. https://doi.org/10.1016/j.cageo.2017.05.005.

Marvin, Simon, Aidan While, Mateja Kovacic, Andy Lockhart, and Rachel Macrorie. 2018. "Urban Robotics and Automation: Critical Challenges, International Experiments and Transferable Lessons for the UK." The Engineering and Physical Sciences Research Council (EPSRC) UK Robotics and Autonomous Systems Network (UK-RAS Network). https://doi.org/10.13140/RG.2.2.16976.56321.

MAVLink. 2010. "MAVLink: Micro Air Vehicle Message Marshalling Library." *GitHub Repository*. https://github.com/mavlink/mavlink.

Menendez, Elisabeth, Juan G. Victores, Roberto Montero, Santiago Martínez, and Carlos Balaguer. 2018. "Tunnel Structural Inspection and Assessment Using an Autonomous Robotic System." *Automation in Construction* 87: 117–26.

https://doi.org/10.1016/j.autcon.2017.12.001.

Merz, Torsten, Simone Duranti, and Gianpaolo Conte. 2006. “Autonomous Landing of an Unmanned Helicopter Based on Vision and Inertial Sensing.” In *Experimental Robotics IX*, 343–52. Springer, Berlin/Heidelberg, Germany. https://doi.org/10.1007/11552246_33.

Michael, Nathan, Daniel Mellinger, Quentin Lindsey, and Vijay Kumar. 2010. “The GRASP Multiple Micro-UAV Testbed.” *IEEE Robotics and Automation Magazine* 17 (3): 56–65. https://doi.org/10.1109/MRA.2010.937855.

Mogili, Um Rao, and B. B.V.L. Deepak. 2018. “Review on Application of Drone Systems in Precision Agriculture.” *Procedia Computer Science* 133: 502–9. https://doi.org/10.1016/J.PROCS.2018.07.063.

Mollica, Christian M. 2020. *FPV Flight Dynamics: Mastering Acro Mode on High-Performance Drones*. Vespula Ventures LLC, Wilton, CT.

Mougenot, Denis. 2010. “Land Cableless Systems: Use & Misuse.” In *EAGE Workshop on Developments in Land Seismic Acquisition for Exploration*, cp-159. Cairo, Egypt, May 17-19. https://doi.org/10.3997/2214-4609-pdb.159.d02.

———. 2012. “UNITE Cableless System and Its Real-Time Capabilities.” https://www.sercel.com/products/Lists/ProductPublication/UNITE cableless system and its real-time capabilities_Jan13.pdf.

Mourikis, Anastasios I., and Stergios I. Roumeliotis. 2007. “A Multi-State Constraint Kalman Filter for Vision-Aided Inertial Navigation.” In *Proceedings 2007 IEEE International Conference on Robotics and Automation*, 3565–72. Rome, Italy, April 10-14. https://doi.org/10.1109/ROBOT.2007.364024.

Muduli, Lalatendu, Devi Prasad Mishra, and Prasanta K. Jana. 2018. “Application of Wireless Sensor Network for Environmental Monitoring in Underground Coal Mines: A Systematic Review.” *Journal of Network and Computer Applications* 106: 48–67. https://doi.org/10.1016/J.JNCA.2017.12.022.

Mulcahy, Chris. 2013. “DJI Innovations Phantom RTF - Review.” https://www.rcgroups.com/forums/showthread.php?1811071-DJI-Innovations-Phantom-RTF-Review&highlight=Phantom#post23839219.

Nagarajan, Balaji, Yu Li, Zeyi Sun, and Ruwen Qin. 2019. “A Routing Algorithm for Inspecting Grid Transmission System Using Suspended Robot: Enhancing Cost-Effective and Energy Efficient Infrastructure Maintenance.” *Journal of Cleaner Production* 219: 622–38. https://doi.org/10.1016/J.JCLEPRO.2019.02.088.

Nasseri-Moghaddam, A., G. Cascante, and J. Hutchinson. 2005. “A New Quantitative Procedure to Determine the Location and Embedment Depth of a Void Using Surface Waves.” *Journal of Environmental & Engineering Geophysics* 10 (1): 51–64.

https://doi.org/10.2113/JEEG10.1.51.

Nassiraei, Amir A.F., Yoshinori Kawamura, Alireza Ahrary, Yoshikazu Mikuriya, and Kazuo Ishii. 2007. "Concept and Design of a Fully Autonomous Sewer Pipe Inspection Mobile Robot 'KANTARO.'" In *Proceedings 2007 IEEE International Conference on Robotics and Automation*, 136–43. Rome, Italy, April 10-14. https://doi.org/10.1109/ROBOT.2007.363777.

National Research Council (NRC). 2006. *Improved Seismic Monitoring - Improved Decision-Making: Assessing the Value of Reduced Uncertainty*. National Academies Press, Washington, DC.

Nazarian, Soheil. 1984. "In Situ Shear Wave Velocities from Spectral Analysis of Surface Wave." In *Proceedings of 8th Conference on Earthquake Engineering*. San Francisco, CA.

Nazarian, Soheil, and Kenneth H Stokoe II. 1984. "Nondestructive Testing of Pavements Using Surface Waves." *Transportation Research Record* 993: 67–79.

Newcombe, Richard A., Steven J. Lovegrove, and Andrew J. Davison. 2011. "DTAM: Dense Tracking and Mapping in Real-Time." In *2011 International Conference on Computer Vision*, 2320–27. Barcelona, Spain, November 6-13. https://doi.org/10.1109/ICCV.2011.6126513.

Noel, Adam B., Abderrazak Abdaoui, Tarek Elfouly, Mohamed Hossam Ahmed, Ahmed Badawy, and Mohamed S. Shehata. 2017. "Structural Health Monitoring Using Wireless Sensor Networks: A Comprehensive Survey." *IEEE Communications Surveys and Tutorials* 19 (3): 1403–23. https://doi.org/10.1109/COMST.2017.2691551.

Oleynikova, Helen, Zachary Taylor, Marius Fehr, Roland Siegwart, and Juan Nieto. 2017. "Voxblox: Incremental 3d Euclidean Signed Distance Fields for on-Board Mav Planning." In *2017 IEEE/RSJ International Conference on Intelligent Robots and Systems (IROS)*, 1366–73. Vancouver, Canada, September 24-28. https://doi.org/10.1109/IROS.2017.8202315.

Olson, Edwin. 2011. "AprilTag: A Robust and Flexible Visual Fiducial System." In *2011 IEEE International Conference on Robotics and Automation*, 3400–3407. Shanghai, China, May 9-13. https://doi.org/10.1109/ICRA.2011.5979561.

Onajite, Enwenode. 2014. *Seismic Data Analysis Techniques in Hydrocarbon Exploration*. Elsevier, Amsterdam, The Netherlands. https://doi.org/10.1016/C2013-0-09969-0.

OpenCV. 2019. "Camera Calibration and 3D Reconstruction, OpenCV 2.4.13.7 Documentation." https://docs.opencv.org/2.4/modules/calib3d/doc/camera_calibration_and_3d_reconstruction.html?highlight=solvepnp#bool%2520solvePnP(InputArray%2520objectPoints,%2520InputArray%2520imagePoints,%2520InputArray%2520cameraMatrix,%

2520InputArray%2520distCoeffs.

Palomba, J. V. 2017. "Unmanned Aereial Veichle Inspections and Environmental Benefits." In *15th Asia Pacific Conference for Non-Destructive Testing*. Singapore, November 13-17. http://www.ndt.net/?id=22272.

Park, Choon B., Richard D. Miller, and Jianghai Xia. 1999. "Multichannel Analysis of Surface Waves." *Geophysics* 64 (3): 800–808. https://doi.org/10.1190/1.1444590.

Parker, Lynne E., Daniela Rus, and Gaurav S. Sukhatme. 2016. "Multiple Mobile Robot Systems." In *Springer Handbook of Robotics*, edited by Bruno Siciliano and Oussama Khatib. Springer, Berlin/Heidelberg, Germany.

Pearson, Lee. 1969. "Developing the Flying Bomb." In *Naval Aviation in World War I*, 70–73. University Press of the Pacific, Honolulu, HI.

Pelekis, P. C., and G. A. Athanasopoulos. 2011. "An Overview of Surface Wave Methods and a Reliability Study of a Simplified Inversion Technique." *Soil Dynamics and Earthquake Engineering* 31 (12): 1654–68. https://doi.org/10.1016/j.soildyn.2011.06.012.

Pellicani, Roberta, Ilenia Argentiero, Paola Manzari, Giuseppe Spilotro, Cosimo Marzo, Ruggero Ermini, and Ciro Apollonio. 2019. "UAV and Airborne LiDAR Data for Interpreting Kinematic Evolution of Landslide Movements: The Case Study of the Montescaglioso Landslide (Southern Italy)." *Geosciences* 9 (6): 248. https://doi.org/10.3390/geosciences9060248.

Pittelkau, Mark E. 2003. "Rotation Vector in Attitude Estimation." *Journal of Guidance, Control, and Dynamics* 26 (6): 855–60. https://doi.org/10.2514/2.6929.

Pizzoli, Matia, Christian Forster, and Davide Scaramuzza. 2014. "REMODE: Probabilistic, Monocular Dense Reconstruction in Real Time." In *2014 IEEE International Conference on Robotics and Automation (ICRA)*, 2609–16. Hong Kong, China, May 31-June 7: IEEE. https://doi.org/10.1109/ICRA.2014.6907233.

Popper, Ben. 2016. "Amazon's Drone Delivery Launches in the UK." https://www.theverge.com/2016/12/14/13952240/amazon-drone-delivery-launch-uk.

Pouliot, Nicolas, Pierre Luc Richard, and Serge Montambault. 2015. "LineScout Technology Opens the Way to Robotic Inspection and Maintenance of High-Voltage Power Lines." *IEEE Power and Energy Technology Systems Journal* 2 (1): 1–11. https://doi.org/10.1109/JPETS.2015.2395388.

Prabakaran, Veerajagadheswar, Anh Vu Le, Phone Thiha Kyaw, Rajesh Elara Mohan, Prathap Kandasamy, Tan Nhat Nguyen, and Madhukumar Kannan. 2020. "Hornbill: A Self-Evaluating Hydro-Blasting Reconfigurable Robot for Ship Hull Maintenance." *IEEE Access* 8: 193790–800. https://doi.org/10.1109/ACCESS.2020.3033290.

Puppala, Anand J., Surya S. C. Congress, Tejo V. Bheemasetti, and Santiago R. Caballero. 2018. "Visualization of Civil Infrastructure Emphasizing Geomaterial Characterization and Performance." *Journal of Materials in Civil Engineering* 30 (10): 04018236. https://doi.org/10.1061/(ASCE)MT.1943-5533.0002434.

Qin, Tong, Peiliang Li, and Shaojie Shen. 2018. "VINS-Mono: A Robust and Versatile Monocular Visual-Inertial State Estimator." *IEEE Transactions on Robotics* 34 (4): 1004–20. https://doi.org/10.1109/TRO.2018.2853729.

Quarini, J, and S Shire. 2007. "A Review of Fluid-Driven Pipeline Pigs and Their Applications." *Proceedings of the Institution of Mechanical Engineers, Part E: Journal of Process Mechanical Engineering* 221 (1): 1–10. https://doi.org/10.1243/0954408JPME108.

Queralta, Jorge Pena, Jussi Taipalmaa, Bilge Can Pullinen, Victor Kathan Sarker, Tuan Nguyen Gia, Hannu Tenhunen, Moncef Gabbouj, Jenni Raitoharju, and Tomi Westerlund. 2020. "Collaborative Multi-Robot Search and Rescue: Planning, Coordination, Perception, and Active Vision." *IEEE Access* 8: 191617–43. https://doi.org/10.1109/ACCESS.2020.3030190.

Ragi, Shankarachary, and Edwin K.P. Chong. 2013. "UAV Path Planning in a Dynamic Environment via Partially Observable Markov Decision Process." *IEEE Transactions on Aerospace and Electronic Systems* 49 (4): 2397–2412. https://doi.org/10.1109/TAES.2013.6621824.

Raoult, V., and T. F. Gaston. 2018. "Rapid Biomass and Size-Frequency Estimates of Edible Jellyfish Populations Using Drones." *Fisheries Research* 207: 160–64. https://doi.org/10.1016/J.FISHRES.2018.06.010.

Rassenfoss, Stephen. 2017. "The Vision of Onshore Seismic May Look Strange at First." *Journal of Petroleum Technology* 69 (09): 30–32. https://doi.org/10.2118/0917-0030-jpt.

Ratliff, Nathan, Matt Zucker, J. Andrew Bagnell, and Siddhartha Srinivasa. 2009. "CHOMP: Gradient Optimization Techniques for Efficient Motion Planning." In *2009 IEEE International Conference on Robotics and Automation*, 489–94. Kobe, Japan, May 12-17: IEEE. https://doi.org/10.1109/robot.2009.5152817.

Real Engineering. 2019. "How Rwanda Built a Drone Delivery Service." *YouTube Video*. https://www.youtube.com/watch?v=jEbRVNxL44c.

Rees, Caroline. 2013. "PX4 and 3D Robotics Launch New Pixhawk Autopilot for UAVs." https://www.unmannedsystemstechnology.com/2013/08/px4-and-3d-robotics-launch-new-pixhawk-autopilot-for-uavs/.

Richards, Christina. 2014. "Will Internet Access via Drones Ever Fly?" https://www.wired.com/insights/2014/11/internet-access-drones/.

Richardson, Robert, Raul Fuentes, Tim Chapman, Michael Cook, James Scanlan, Zhibin Li, and David Flynn. 2017. “Robotic and Autonomous Systems for Resilient Infrastructure.” The Engineering and Physical Sciences Research Council (EPSRC) UK Robotics and Autonomous Systems Network (UK-RAS Network). https://doi.org/10.31256/WP2017.2.

Robinson, Amy. 2006. “FAA Authorizes Predators to Seek Survivors.” https://www.af.mil/News/Article-Display/Article/130220/faa-authorizes-predators-to-seek-survivors/.

Robotics Today. 2021. “‘Skydio Autonomy’ - Adam Bry and Hayk Martiros.” *YouTube Video*. https://www.youtube.com/watch?v=ncZmnfIRIWE.

Romano, Matthew, Yuxin Chen, Owen Marshall, and Ella Atkins. 2019. “Nailed It: Autonomous Roofing with a Nailgun-Equipped Octocopter.” *ArXiv Preprint ArXiv:1909.08162*.

Rossi, Maurizio, and Davide Brunelli. 2016. “Autonomous Gas Detection and Mapping with Unmanned Aerial Vehicles.” *IEEE Transactions on Instrumentation and Measurement* 65 (4): 765–75. https://doi.org/10.1109/TIM.2015.2506319.

Rotor Riot. 2016. “3D Flying with Zoe FPV.” *YouTube Video*. https://www.youtube.com/watch?v=_AvXYvwhwVs.

Rudol, Piotr, and Patrick Doherty. 2008. “Human Body Detection and Geolocalization for UAV Search and Rescue Missions Using Color and Thermal Imagery.” In *2008 IEEE Aerospace Conference*, 1–8. Big Sky, MT, March 1-8. https://doi.org/10.1109/AERO.2008.4526559.

Ryden, Nils, Choon B. Park, Peter Ulriksen, and Richard D. Miller. 2004. “Multimodal Approach to Seismic Pavement Testing.” *Journal of Geotechnical and Geoenvironmental Engineering* 130 (6): 636–45. https://doi.org/10.1061/(asce)1090-0241(2004)130:6(636).

Sa, Inkyu, Mina Kamel, Michael Burri, Michael Bloesch, Raghav Khanna, Marija Popovic, Juan Nieto, and Roland Siegwart. 2017. “Build Your Own Visual-Inertial Drone: A Cost-Effective and Open-Source Autonomous Drone.” *IEEE Robotics and Automation Magazine* 25 (1): 89–103. https://doi.org/10.1109/MRA.2017.2771326.

Salvo, Giuseppe, Luigi Caruso, and Alessandro Scordo. 2014. “Urban Traffic Analysis through an UAV.” *Procedia - Social and Behavioral Sciences* 111: 1083–91. https://doi.org/10.1016/j.sbspro.2014.01.143.

Sankarasrinivasan, S., E. Balasubramanian, K. Karthik, U. Chandrasekar, and Rishi Gupta. 2015. “Health Monitoring of Civil Structures with Integrated UAV and Image Processing System.” *Procedia Computer Science* 54: 508–15. https://doi.org/10.1016/J.PROCS.2015.06.058.

Saripalli, Srikanth, James F. Montgomery, and Gaurav S. Sukhatme. 2003. “Visually Guided Landing of an Unmanned Aerial Vehicle.” *IEEE Transactions on Robotics and Automation* 19 (3): 371–80. https://doi.org/10.1109/TRA.2003.810239.

Savazzi, Stefano, and Umberto Spagnolini. 2008. “Wireless Geophone Networks for High-Density Land Acquisition: Technologies and Future Potential.” *The Leading Edge* 27 (7): 882–86. https://doi.org/10.1190/1.2954028.

Schaefer, Martin, Richard Teeuw, Simon Day, Dimitrios Zekkos, Paul Weber, Toby Meredith, and J. Van Westen Cees. 2020. “Low-Cost UAV Surveys of Hurricane Damage in Dominica: Automated Processing with Co-Registration of Pre-Hurricane Imagery for Change Analysis.” *Natural Hazards* 101: 755–84. https://doi.org/10.1007/s11069-020-03893-1.

Schäfer, Björn E., Davide Picchi, Thomas Engelhardt, and Dirk Abel. 2016. “Multicopter Unmanned Aerial Vehicle for Automated Inspection of Wind Turbines.” In *2016 24th Mediterranean Conference on Control and Automation (MED)*, 244–49. Athens, Greece, June 21-24. https://doi.org/10.1109/MED.2016.7536055.

Schempf, Hagen, Brian Chemel, and Nathan Everett. 1995. “Neptune: Above-Ground Storage Tank Inspection Robot System.” *IEEE Robotics and Automation Magazine* 2 (2): 9–15. https://doi.org/10.1109/100.392414.

Schroth, Lukas. 2020. “DRONEII: The Drone Market Size 2020-2025, Five Key Takeaways.” https://droneii.com/the-drone-market-size-2020-2025-5-key-takeaways.

Schut, Antonius G.T., Pierre C.Sibiry Traore, Xavier Blaes, and Rolf A. de By. 2018. “Assessing Yield and Fertilizer Response in Heterogeneous Smallholder Fields with UAVs and Satellites.” *Field Crops Research* 221: 98–107. https://doi.org/10.1016/j.fcr.2018.02.018.

Schwarz, Michael W., William B. Cowan, and John C. Beatty. 1987. “An Experimental Comparison of RGB, YIQ, LAB, HSV, and Opponent Color Models.” *ACM Transactions on Graphics (TOG)* 6 (2): 123–58. https://doi.org/10.1145/31336.31338.

Segarra, P., J. A. Sanchidrián, R. Castedo, L. M. López, and I. Del Castillo. 2015. “Performance of Some Coupling Methods for Blast Vibration Monitoring.” *Journal of Applied Geophysics* 112: 129–35. https://doi.org/10.1016/J.JAPPGEO.2014.11.012.

Selley, Richard C., and Stephen A. Sonnenberg. 2015. *Elements of Petroleum Geology (Third Edition)*. Academic Press, Cambridge, MA. https://doi.org/10.1016/B978-0-12-386031-6.00003-5.

Shaw, Ian G. R. 2014. “The Rise of the Predator Empire: Tracing the History of U.S. Drones.” https://understandingempire.wordpress.com/2-0-a-brief-history-of-u-s-drones/.

Shen, Shaojie, Nathan Michael, and Vijay Kumar. 2011. "Autonomous Multi-Floor Indoor Navigation with a Computationally Constrained MAV." In *2011 IEEE International Conference on Robotics and Automation*, 20–25. Shanghai, China, May 9-13. https://doi.org/10.1109/ICRA.2011.5980357.

Shontell, Alyson. 2014. "A Hot-Shot Magazine Editor And A Tijuana Teenager Met Online And Made $5 Million Building Drones." https://www.businessinsider.com/how-3d-robotics-founders-chris-anderson-and-jordi-munoz-met-2014-12.

Siebert, Sebastian, and Jochen Teizer. 2014. "Mobile 3D Mapping for Surveying Earthwork Projects Using an Unmanned Aerial Vehicle (UAV) System." *Automation in Construction* 41: 1–14. https://doi.org/10.1016/j.autcon.2014.01.004.

Skydio. 2020a. "Introducing Skydio 3D Scan™." *YouTube Video*. https://www.youtube.com/watch?v=VxLXTeycyeE.

———. 2020b. "Introducing Skydio House Scan™." *YouTube Video*. https://www.youtube.com/watch?v=MSy_06aOBzg.

Socco, Laura Valentina, Sebastiano Foti, and Daniele Boiero. 2010. "Surface-Wave Analysis for Building near-Surface Velocity Models—Established Approaches and New Perspectives." *Geophysics* 75 (5): 75A83–102. https://doi.org/10.1190/1.3479491.

Sohraby, Kazem, Daniel Minoli, and Taieb Znati. 2007. *Wireless Sensor Networks: Technology, Protocols, and Applications*. John Wiley & Sons, Hoboken, NJ.

Song, Byung Duk, and Young Dae Ko. 2017. "Quantitative Approaches for Economic Use of Emerging Technology in the Tourism Industry: Unmanned Aerial Vehicle Systems." *Asia Pacific Journal of Tourism Research* 22 (12): 1207–20. https://doi.org/10.1080/10941665.2017.1378689.

Sony, Sandeep, Shea Laventure, and Ayan Sadhu. 2019. "A Literature Review of Next-Generation Smart Sensing Technology in Structural Health Monitoring." *Structural Control and Health Monitoring* 26 (3): e2321. https://doi.org/10.1002/STC.2321.

Spencer, Billie F., Vedhus Hoskere, and Yasutaka Narazaki. 2019. "Advances in Computer Vision-Based Civil Infrastructure Inspection and Monitoring." *Engineering* 5 (2): 199–222. https://doi.org/10.1016/j.eng.2018.11.030.

Spong, Mark W., Seth Hutchinson, and M. Vidyasagar. 2006. *Robot Modeling and Control*. John Wiley & Sons, New York, NY.

Stachniss, Cyrill, John J. Leonard, and Sebastian Thrun. 2016. "Simultaneous Localization and Mapping." In *Springer Handbook of Robotics*, edited by Bruno Siciliano and

Oussama Khatib. Springer, Berlin/Heidelberg, Germany.

Stewart, Robert R., Li Chang, Srikanth K.V. Sudarshan, Aaron T. Becker, and Li Huang. 2016. “An Unmanned Aerial Vehicle with Vibration Sensing Ability (Seismic Drone).” In *SEG Technical Program Expanded Abstracts*, 225–29. https://doi.org/10.1190/segam2016-13973407.1.

Stibinger, Petr, George Broughton, Filip Majer, Zdenek Rozsypalek, Anthony Wang, Kshitij Jindal, Alex Zhou, et al. 2021. “Mobile Manipulator for Autonomous Localization, Grasping and Precise Placement of Construction Material in a Semi-Structured Environment.” *IEEE Robotics and Automation Letters* 6 (2): 2595–2602. https://doi.org/10.1109/LRA.2021.3061377.

Stokoe, K. H., S. G. Wright, J. A. Bay, and J. M. Roesset. 1994. “Characterization of Geotechnical Sites by SASW Method.” In *Geophysical Characterization of Sites*, 15–25. A.A. Balkema, Rotterdam, The Netherlands.

Straser, Erik Gregory. 1998. “A Modular, Wireless Damage Monitoring System for Structures.” *PhD Dissertation*. Department of Civil and Environmental Engineering, Stanford University, Stanford, CA.

Sudarshan, Srikanth K.V., Victor Montano, An Nguyen, Michael McClimans, Li Chang, Robert R. Stewart, and Aaron T. Becker. 2017. “A Heterogeneous Robotics Team for Large-Scale Seismic Sensing.” *IEEE Robotics and Automation Letters* 2 (3): 1328–35. https://doi.org/10.1109/LRA.2017.2666300.

Sui, Zhiqiang, Zheming Zhou, Zhen Zeng, and Odest Chadwicke Jenkins. 2017. “SUM: Sequential Scene Understanding and Manipulation.” In *2017 IEEE/RSJ International Conference on Intelligent Robots and Systems (IROS)*, 3281–88. Vancouver, BC, Canada, September 24-28. https://doi.org/10.1109/IROS.2017.8206164.

Swartz, R. Andrew, Jerome P. Lynch, Stephan Zerbst, Bert Sweetman, and Raimund Rolfes. 2010. “Structural Monitoring of Wind Turbines Using Wireless Sensor Networks.” *Smart Structures and Systems* 6 (3): 183–96. https://doi.org/10.12989/SSS.2010.6.3.183.

Swatbotics. 2016. “Apriltag.” *GitHub Repository*. https://github.com/swatbotics/apriltag.

Tayebi, Abdelhamid, and Stephen McGilvray. 2006. “Attitude Stabilization of a VTOL Quadrotor Aircraft.” *IEEE Transactions on Control Systems Technology* 14 (3): 562–71. https://doi.org/10.1109/TCST.2006.872519.

Texas Instruments (TI). 2003. “OPA1632High-Performance, Fully-Differential AudioOperational Amplifier.” *Data Sheet*. Texas Instruments, Dallas, TX.

———. 2007. “ADS1282 High-Resolution Analog-to-Digital Converter.” *Data Sheet*. Texas Instruments, Dallas, TX.

———. 2009. “ADS1282EVM and ADS1282EVM-PDK User’s Guide.” *User’s Guide*. Texas Instruments, Dallas, TX.

Thomas, Justin, Joe Polin, Koushil Sreenath, and Vijay Kumar. 2013. “Avian-Inspired Grasping for Quadrotor Micro UAVs.” In *ASME 2013 International Design Engineering Technical Conferences and Computers and Information in Engineering Conference*, 6A:V06AT07A014. Portland, OR, August 4–7. https://doi.org/10.1115/DETC2013-13289.

Tomic, Teodor, Korbinian Schmid, Philipp Lutz, Andreas Domel, Michael Kassecker, Elmar Mair, Iris Grixa, Felix Ruess, Michael Suppa, and Darius Burschka. 2012. “Toward a Fully Autonomous UAV: Research Platform for Indoor and Outdoor Urban Search and Rescue.” *IEEE Robotics and Automation Magazine* 19 (3): 46–56. https://doi.org/10.1109/MRA.2012.2206473.

Tucker, Sepncer C., Priscilla Roberts, Paul G. Pierpaoli Jr., David Zabecki, and Sherifa Zuhur, eds. 2008. *The Encyclopedia of the Arab-Israeli Conflict: A Political, Social, and Military History*. ABC-Clio, Santa Barbara, CA.

Turner, Darren, Arko Lucieer, and Steven M. De Jong. 2015. “Time Series Analysis of Landslide Dynamics Using an Unmanned Aerial Vehicle (UAV).” *Remote Sensing* 7 (2): 1736–57. https://doi.org/10.3390/rs70201736.

U-blox. 2018a. “U-Blox 8 / u-Blox M8 Receiver Description Including Protocol Specification.” *Data Sheet*. U-blox, Thalwil, Switzerland.

———. 2018b. “ZOE-M8 Series Ultra Small u-Blox M8 GNSS SiPs.” *Product Summary*. U-blox, Thalwil, Switzerland.

Valls Miro, Jaime, Nalika Ulapane, Lei Shi, Dave Hunt, and Michael Behrens. 2018. “Robotic Pipeline Wall Thickness Evaluation for Dense Nondestructive Testing Inspection.” *Journal of Field Robotics* 35 (8): 1293–1310. https://doi.org/10.1002/rob.21828.

Villa, Tommaso, Farhad Salimi, Kye Morton, Lidia Morawska, and Felipe Gonzalez. 2016. “Development and Validation of a UAV Based System for Air Pollution Measurements.” *Sensors* 16 (12): 2202. https://doi.org/10.3390/s16122202.

Wagner, William, and William P. Sloan. 1992. *Fireflies and Other UAVs (Unmanned Aerial Vehicles)*. Aerofax.

Wait, Jeannette R., Neal A. Tanner, Hoon Sohn, and Charles R. Farrar. 2002. “Application of a Wireless Sensor Module as a Distributed Structural Health Monitoring Solution.” In *Proceedings of the Third World Conference on Structural Control*, 2:35–41.

Wallace, Luke, Arko Lucieer, Christopher Watson, and Darren Turner. 2012. “Development of a UAV-LiDAR System with Application to Forest Inventory.” *Remote Sensing* 4 (6): 1519–43. https://doi.org/10.3390/rs4061519.

Wang, Xiaoli, Aakanksha Chowdhery, and Mung Chiang. 2017. "Networked Drone Cameras for Sports Streaming." In *2017 IEEE 37th International Conference on Distributed Computing Systems (ICDCS)*, 308–18. Atlanta, GA, June 5-8. https://doi.org/10.1109/ICDCS.2017.200.

Wang, Yu, and Chang-Hua Wu. 2007. "Robot-Assisted Sensor Network Deployment and Data Collection." In *2007 International Symposium on Computational Intelligence in Robotics and Automation*, 467–72. Jacksonville, FL, June 20-23. https://doi.org/10.1109/CIRA.2007.382919.

Wawrla, Lukas, Omid Maghazei, and Torbjørn Netland. 2019. "Applications of Drones in Warehouse Operations." *Whitepaper*. ETH Zurich, Zurich, Switzerland.

Westoby, M. J., J. Brasington, N. F. Glasser, M. J. Hambrey, and J. M. Reynolds. 2012. "'Structure-from-Motion' Photogrammetry: A Low-Cost, Effective Tool for Geoscience Applications." *Geomorphology* 179: 300–314. https://doi.org/10.1016/j.geomorph.2012.08.021.

Whaley, Jane. 2018. "DARTs and Drones: The Future of Onshore Seismic." *GEO ExPro* 5 (2).

Whittle, Richard. 2013. "The Man Who Invented the Predator." https://www.airspacemag.com/flight-today/the-man-who-invented-the-predator-3970502/.

———. 2015. "Hellfire Meets Predator." https://www.airspacemag.com/flight-today/hellfire-meets-predator-180953940/.

Yapp, Justin, Remzi Seker, and Radu Babiceanu. 2016. "UAV as a Service: Enabling on-Demand Access and on-the-Fly Re-Tasking of Multi-Tenant UAVs Using Cloud Services." In *2016 IEEE/AIAA 35th Digital Avionics Systems Conference (DASC)*, 1–8. Sacramento, CA, September, 25-29. https://doi.org/10.1109/DASC.2016.7778007.

Yoo, Wonsang, Eun Yu, and Jaemin Jung. 2018. "Drone Delivery: Factors Affecting the Public's Attitude and Intention to Adopt." *Telematics and Informatics* 35 (6): 1687–1700. https://doi.org/10.1016/J.TELE.2018.04.014.

Yoon, Hyungchul, Vedhus Hoskere, Jong Woong Park, and Billie F. Spencer. 2017. "Cross-Correlation-Based Structural System Identification Using Unmanned Aerial Vehicles." *Sensors* 17 (9): 2075. https://doi.org/10.3390/s17092075.

Yu, Seung Nam, Jae Ho Jang, and Chang Soo Han. 2007. "Auto Inspection System Using a Mobile Robot for Detecting Concrete Cracks in a Tunnel." *Automation in Construction* 16 (3): 255–61. https://doi.org/10.1016/J.AUTCON.2006.05.003.

Zaloga, Steven J. 2011. *V-1 Flying Bomb 1942–52: Hitler's Infamous "Doodlebug."* Bloomsbury Publishing, London, UK.

Zekkos, Dimitrios, William Greenwood, Jerome Lynch, John Manousakis, Adda Athanasopoulos-Zekkos, Marin Clark, Kristen L. Cook, and Charalampos Saroglou. 2018. "Lessons Learned from the Application of UAV-Enabled Structure-from-Motion Photogrammetry in Geotechnical Engineering." *International Journal of Geoengineering Case Histories* 4 (4): 254–74. https://doi.org/10.4417/IJGCH-04-04-03.

Zekkos, Dimitrios, Jerome P. Lynch, Andhika Sahadewa, Mitsuhito Hirose, and Danny Ellis. 2014. "Proof-of-Concept Shear Wave Velocity Measurements Using an Unmanned Autonomous Aerial Vehicle." In *Geo-Congress 2014: Geo-Characterization and Modeling for Sustainability*, 953–62. Atlanta, GA, February 23-26. https://doi.org/10.1061/9780784413272.093.

Zekkos, Dimitrios, J. Manousakis, William Greenwood, and Jerome P Lynch. 2016. "Immediate Uav-Enabled Infrastructure Reconnaissance Following Recent Natural Disasters: Case Histories from Greece." In *International Conference on Natural Hazards and Infrastructure*. Chania, Greece, June 28-30. https://www.researchgate.net/publication/304578569.

Zhang, Yilan, Sean M. O'Connor, Gwendolyn W. van der Linden, Atul Prakash, and Jerome P. Lynch. 2016. "SenStore: A Scalable Cyberinfrastructure Platform for Implementation of Data-to-Decision Frameworks for Infrastructure Health Management." *Journal of Computing in Civil Engineering* 30 (5): 04016012. https://doi.org/10.1061/(ASCE)CP.1943-5487.0000560.

Zhou, Boyu, Fei Gao, Luqi Wang, Chuhao Liu, and Shaojie Shen. 2019. "Robust and Efficient Quadrotor Trajectory Generation for Fast Autonomous Flight." *IEEE Robotics and Automation Letters* 4 (4): 3529–36. https://doi.org/10.1109/LRA.2019.2927938.

Zhou, Hao, Mitsuhito Hirose, William Greenwood, Yong Xiao, Jerome Lynch, Dimitrios Zekkos, and Vineet Kamat. 2016. "Demonstration of UAV Deployment and Control of Mobile Wireless Sensing Networks for Modal Analysis of Structures." In *Sensors and Smart Structures Technologies for Civil, Mechanical, and Aerospace Systems 2016*, 9803:98031X. Las Vegas, NV, March 21-24. https://doi.org/10.1117/12.2223441.

Zhou, Hao, Jerome P. Lynch, and Dimitrios Zekkos. 2019. "Vision-Based Precision Localization of UAVs for Sensor Payload Placement and Pickup for Field Monitoring Applications." In *Sensors and Smart Structures Technologies for Civil, Mechanical, and Aerospace Systems 2019*, 10970:1097007. Denver, CO, March 4-7. https://doi.org/10.1117/12.2516049.

Zhu, Dapeng. 2014. "Decentralized Structural Damage Detection and Model Updating with Mobile and Wireless Sensors." *PhD Dissertation*. School of Civil and Environmental Engineering, Georgia Institute of Technology, Atlanta, GA.

Zhu, Dapeng, Jiajie Guo, Chunhee Cho, Yang Wang, and Kok Meng Lee. 2012. "Wireless

Mobile Sensor Network for the System Identification of a Space Frame Bridge." *IEEE/ASME Transactions on Mechatronics* 17 (3): 499–507. https://doi.org/10.1109/TMECH.2012.2187915.

Zubax Robotics. 2016. "OpenGrab EPM V3." *GitHub Repository*. https://github.com/Zubax/opengrab_epm_v3.